UNIVERSITY OF TRENTO

Doctoral School in Civil, Environmental and Mechanical Engineering

Curriculum 3. Modelling and Simulation

Himanshu Nautiyal

Electronic structure calculations of Thermoelectric Materials

$$\left(-\frac{1}{2}\nabla^2 + v_{eff}\right)\phi_i^{KS} = \varepsilon_i \phi_i^{KS}$$

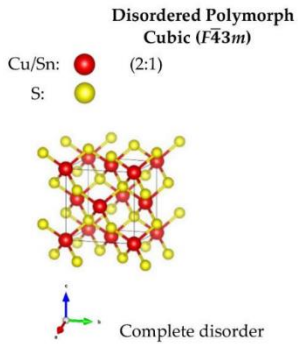

Ternary CTS

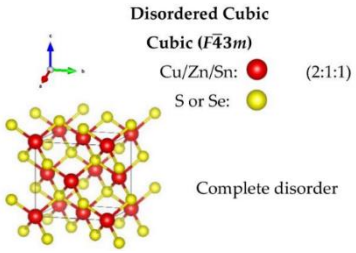

Quaternary CZTS/Se

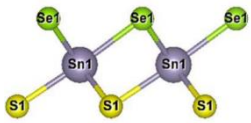

Janus SnSSe

2023 – Doctoral thesis

UNIVERSITY OF TRENTO - Italy
Department of Civil, Environmental and Mechanical Engineering

Doctoral School in Civil, Environmental and Mechanical Engineering
Topic 3. Modelling and Simulation - 35º cycle 2019/2023

Doctoral Thesis – March 2023

Himanshu Nautiyal

Electronic structure calculation of Thermoelectric materials

Supervisor
Prof. Paolo Scardi, University of Trento

University of Trento
Doctoral School in Civil, Environmental and Mechanical Engineering
http://web.unitn.it/en/dricam
Via Mesiano 77, I-38123 Trento
Tel. +39 0461 282670 / 2611 - *dicamphd@unitn.it*

कर्मण्येवाधिकारस्ते मा फलेषु कदाचन।
मा कर्मफलहेतुर्भूर्मा ते सङ्गोऽस्त्वकर्मणि॥

karmaṇy-evādhikāras te mā phaleṣhu kadāchana
mā karma-phala-hetur bhūr mā te saṅgo 'stvakarmaṇi

You have a right to perform your prescribed duties, but you are not entitled to the fruits of your actions. Never consider yourself to be the cause of the results of your activities, nor be attached to inaction.

(Bhagvad Geeta-Chapter 2 verse 47)

Acknowledgements

First and foremost, I would like to express my deepest gratitude to my PhD supervisor, Prof. Paolo Scardi, for his guidance, support, and encouragement, which were essential for the completion of my thesis. His expertise, supervision, and constructive feedback were invaluable in shaping my research.

I would also like to thank my colleagues and lab members, Dr Narges Ataollahi, Dr Ketan Lohani, Dr Mirco D'Incau, Marcello Malagutti, Eleonora Tomasino, Varun D. N. and Sergio Setti for the supportive academic environment we shared.

Furthermore, I want to acknowledge the academic support of Dr Binayak Mukherjee, Dr Carlo Fanciulli, Dr Eleonora Isotta, Dr Emmanuel Guilmeau, Dr Ilaria Pallecchi, Dr Ilya Sergueev, Mr Krishnendu Maji, Dr Luca Rebuffi, Dr Marina Putti, Dr Martin Etter, Dr Raju Edla, Dr Scott T. Misture, Dr Sebastian Bette and Dr Ubaidah Syafiq.

I would also like to thank all my teachers, especially Dr Awadhesh Kumar Dubey and Dr Jaswant Kumar.

My thanks also go to my friends Abiskar, Ashish, Ayushi, Dalip, Pleasant, Purna, Priya, and Salman.

My family has been my support and source of motivation throughout my academic career. Their unwavering love, encouragement, and sacrifices have made this thesis possible, and I am very grateful for their support.

Finally, I would like to thank the University of Trento for the scholarships that have supported my research.

Thank you all for your support and encouragement.

Abstract

Thermoelectric semiconductors can convert temperature differences into electricity or electricity into temperature differences. This offers great potential for the use of wasted heat or cooling. These materials can be used in a variety of fields, from healthcare to space exploration. The effectiveness of the materials is evaluated by their thermoelectric properties such as the Seebeck coefficient, electrical conductivity, and thermal conductivity.

The aim of this PhD thesis is to investigate the electronic structure using first-principle methods for potential thermoelectric applications. Materials of interest include Copper and Tin based ternary /quaternary compounds, and monolayers of SnS_2, $SnSe_2$ and Janus SnSSe. Density functional theory, ab initio molecular dynamics and Boltzmann transport theory are used to study the electronic and phonon transport properties.

In the first part of the thesis, electronic structure calculations were performed on both monoclinic and disordered cubic forms of Cu_2SnS_3(CTS). The impact of structural disorder on thermoelectric properties was examined through these simulations. The results, obtained through first-principle calculations, revealed the existence of band tails in the electronic density of states for the disordered structure, and low-lying optical modes in the disordered cubic structure. This was found to be caused by a significant variation in Sn bonding, leading to strong anharmonicity as measured by the Grüneisen parameter. The findings from the first principle calculations were supported by Nuclear inelastic scattering experiments. Furthermore, the effect of grain size on Cu_2SnS_3 was studied using first-principles calculations on various ordered and disordered surfaces. The density of states (DOS) revealed that the surface of CTS is conductive due to the presence of dangling bonds. Furthermore, calculations of the formation energy showed that the stoichiometric CTS, Cu-vacant and Cu-rich systems are energetically more favourable, while the formation of Sn-vacant and Sn-rich systems is less likely. In the subsequent study, the impact of Ag substitution at the Sn site at various concentrations was investigated. The Fermi level for Ag-substituted systems was found to lie deep within the valence band, with the shift of the Fermi level inside the valence band increasing with substitution increasing the carrier concentration.

The incorporation of Ag into the system decreases the root mean squared displacement of the other cations and anions, which reduces the scattering of phonons and thereby increases the lattice thermal conductivity. A comparative study of various polymorphs of CTS, Cu_2ZnSnS_4 and $Cu_2ZnSnSe_4$ was done. *Ab-initio* molecular dynamics was performed on CTS, CZTS and CZTSe. The root mean squared displacement value for the disordered polymorph was higher than for the ordered phase, indicating increased static disorder. This corresponds to the static (temperature-independent) distortion of the crystalline lattice due to the disorder of the cations and is associated with higher anharmonicity and bond inhomogeneity in the disordered phase, which is then directly responsible for the ultra-low thermal conductivity.

In the final part of the thesis, thermoelectric properties of dichalcogenide monolayer of SnS_2, $SnSe_2$ and Janus SnSSe was performed. Density functional theoretical calculations points out the hexagonal Janus SnSSe monolayer as a potential high-performing thermoelectric material. Results for the Janus SnSSe monolayer show an ultra-low thermal conductivity originating from the low group velocity of the low-lying optical modes, leading to superior zT values of 0.5 and 3 at 300 K and 700 K for the p-type doping, respectively.

The successful calculation of properties for materials shows that the computational work done in this thesis can be used for further research into thermoelectricity.

Table of Contents

1. Introduction

Throughout human history, the availability and utilization of energy sources have undergone significant transformations. Initially, conventional biomass sources such as wood, agricultural waste, and charcoal were the primary sources of energy. The Industrial Revolution marked a new era, where coal emerged as the primary energy source, following that, oil and gas were discovered in the subsequent years, collectively known as fossil fuels.[1]

Today, fossil fuels play a dominant role in meeting our energy demands, contributing to about 80% of the world's energy requirements.[1] This is due to their unmatched energy efficiency, convenience, and logistical feasibility. Nonetheless, there is a growing concern over the negative impact of fossil fuels on our environment, from greenhouse gas emissions to the depletion of non-renewable resources. To address these challenges and create a sustainable future, it is essential that we transition to renewable and green energy sources. The generation and transmission of electricity inevitably produces excess heat as a by-product. Numerous studies show that a significant portion, estimated at 66 %, of the energy generated is lost in the form of waste heat and remains unused.[2,3]

One promising approach to improving sustainability is through the recovery of waste heat. By capturing and utilizing the excess heat generated by industrial processes, we can reduce energy waste and create a more efficient, sustainable energy system. Thermoelectric (TE) technology offers a promising way to extract clean energy from dissipated heat by facilitating the conversion of a thermal gradient into electric current or vice versa.

1.1 Background

In 1821, a scientist named T. Seebeck made an important discovery that has since played a significant role in the development of thermoelectric technology. Seebeck found that when two dissimilar materials are connected via a junction and kept at different temperatures, a voltage difference appears between the junctions. This voltage is proportional to the temperature difference between the two junctions.

The intrinsic property of the materials that determines this voltage difference is called the Seebeck coefficient (S). The ratio between the developed voltage and the temperature gradient ($\Delta V/\Delta T$) is directly related to the Seebeck coefficient. This discovery is the basis of thermocouples, which are widely used for temperature measurements.

To understand how thermocouples work, consider a finite rod of conducting material that is heated at one end. The presence of a temperature gradient causes charge carriers (electrons or holes) to experience a force that drives them from the hot end to the cold end. If the rod consists of two dissimilar conductors and a temperature gradient is present, a voltage is produced at the junction between the two conductors. This voltage is the result of the Seebeck effect.

The magnitude of the voltage generated by the thermocouple is directly proportional to the Seebeck coefficient of the materials and the temperature gradient between the two junctions. Thus, by measuring the voltage generated by a thermocouple, one can determine the temperature difference between the two junctions.

The Seebeck effect is a fundamental principle underlying TE technology. Its discovery paved the way for the development of thermocouples and other thermoelectric devices used to measure temperature and power generation.

A second effect was discovered 13 years later, in 1834, by J.C. Peltier. Peltier found that when an electric current flows through the junction of two dissimilar materials, heat is either absorbed or released at the junction, depending on the direction of the current. This phenomenon came to be known as the Peltier effect. Essentially, the Peltier effect can be thought of as the opposite of the Seebeck effect. While the Seebeck effect describes how a difference in temperature creates an electric current, the Peltier effect describes how an electric current can create a flow of heat.

This discovery had a significant impact on the development of TE devices, as it demonstrated that heat flow could be controlled by the flow of electricity. Peltier's work laid the foundation for the development of TE cooling and heating systems, which are used in a wide range of applications.

1.2 Performance of TE materials and devices

The performance of a TE material is determined by the figure of merit zT of the material,[4] which is given by a combination of transport coefficients:

$$zT = \frac{S^2\sigma T}{\kappa} = \frac{S^2\sigma T}{\kappa_e + \kappa_L} \quad \dots (1.1)$$

where S, σ, T, κ, κ_e and κ_L are the Seebeck coefficient, electrical conductivity, temperature, total thermal conductivity, thermal conductivity of electrons and phonons, respectively. $S^2\sigma$ is collectively referred as Power Factor (PF). The higher the material figure of merit is, the higher the performance of the device. The figure of merit is linked to the efficiency[5] of the device by:

$$\eta = \frac{T_{Hot} - T_{Cold}}{T_{Hot}} \frac{\sqrt{1+zT} - 1}{\sqrt{1+zT} + \frac{T_{Hot}}{T_{cold}}} \quad \dots (1.2)$$

here T_{Hot} and T_{Cold} are the temperature of hot and cold side, respectively.

Early work in the field of thermoelectricity resulted in very small values of zT because they focussed mainly on metal-based thermoelectric materials, which have a high σ, but a relatively small S and a high κ. In the mid-twentieth century, semiconducting materials began to attract the attention of the research community. Later, it was discovered that semiconducting materials such as Bi_2Te_3,[6] PbTe,[7] and SiGe[8] had excellent TE performance due to their large S values.

Since the 1970s, TE materials with different operating temperatures have appeared, e.g., clathrates,[9] half-Heusler,[10,11] skutterudites,[12] oxides,[13,14] diamond-like compounds[15] etc., which shows relatively high TE performance. An ideal high performing TE material should have a typical "phonon-glass-electron-crystal" (PGEC) behaviour (proposed by Slack in 1995),[16] with a high P.F. and a low κ_l, where the structure of the compound provides conducting paths for electrons by behaving like a crystal, and at the same time scatters phonons by behaving like glass or amorphous solid. In addition to high TE performance, TE materials should be environment friendly, economical, non-toxic, and sustainable.

1.3 Applications of thermoelectricity

The application of thermoelectric in space technology is one of the most remarkable achievements. NASA has employed radioisotope thermoelectric generators (RTGs) to power various spacecraft, including Voyager 1, Voyager 2, Galileo, Ulysses, Cassini, and New Horizons.[17] The reason for this is that conventional energy sources, such as photovoltaics, are not feasible in deep space missions.[18]

Modern electronics rely heavily on voltage regulators and microprocessors, which often operate at or near their maximum temperature limits. This can have a negative impact on both performance and lifespan. Traditionally, heat sinks have been used to dissipate heat from these components, but now thermoelectric coolers (TEC) offer a more localised cooling solution.

Thermoelectric refrigerators are also useful in the transport of biological products, as maintaining a certain temperature range is crucial for the preservation of vaccines, blood serums, and other biological substances during transport.[18] A portable thermoelectric medical refrigerator controlled by a microprocessor is one such application developed for the preservation of human blood during transport.[19]

Recently, the application of thermoelectric technology to generate energy from body heat has also proven to be an extremely innovative and efficient means of powering a variety of electronic devices.[18] Body sensors, medical devices, implantable devices, low-consumption wearables, and smart clothing are just some of the many potential applications.[20,21]

1.4 Structure of the thesis

Remarkable technological advancements in computer architecture have facilitated the study of material properties through modeling and simulation. The use of computer simulations has gained significant importance in various fields, including physics, chemistry, materials science, climate science, and biology. The development of computational theories, including ab initio methods, semi-empirical methods, atomistic simulation methods, mesoscale methods, and continuum methods, in materials science has resulted in an

interdisciplinary research field known as "Computational Materials Science." One of the aim of computational materials is to explore new materials and investigate the behavior and mechanisms of electron and phonon transport.

The present thesis takes advantage of first-principle calculations as implemented in density functional theory, density functional perturbation theory (DFPT), ab initio molecular dynamics (AIMD) and Boltzmann transport theory. The aim is to gain understanding of the electron and phonon transport of materials in relation to the thermoelectric phenomenon. The results were compared with experiments, in close collaboration with experimentalists.

Chapter 2 provides an overview of the theoretical methods used in this work, including density functional theory (DFT), electronic transport, phonon transport, and *ab initio* molecular dynamics.

Chapter 3 focuses on a first-principles study of experimentally prepared Cu_2SnS_3 (CTS) polymorphs, examining the effects of structural disorder on the electronic and phononic properties of both ordered monoclinic and disordered cubic phases. The analysis includes calculations of the electronic density of states, phonon dispersion curve, phonon density of states, mode Grüneisen parameter, and electron localisation function.

Chapter 4 investigates the effect of grain size on CTS through modeling of various surface and density of states calculations were performed using DFT. Additionally, energy of formation calculations are performed for stoichiometric CTS, Cu-vacant, Cu-rich, Sn-vacant, and Sn-rich systems.

Chapter 5 examines the impact of Ag doping on CTS at different doping levels using DFT and DFPT, calculating the electronic density of states and the vibrational density of states. AIMD is also used to study the time evolution of the structure at different temperatures, via determining mean square displacement and vibrational density of states from the trajectories.

Chapter 6 includes a comparative study of electronic and thermal transport of various polymorphs of CTS, Cu_2ZnSnS_4 and $Cu_2ZnSnSe_4$. *Ab-initio* molecular dynamics was performed on CTS, CZTS and CZTSe. The electronic structure calculations were performed using hybrid functional. The disorder was quantified in terms of root mean squared displacement. Additionally, the results were validated by temperature-dependent synchrotron X-ray diffraction (SXRD) and Raman spectroscopy.

In Chapter 7, 2-dimensional metal dichalcogenides monolayers of SnS_2, $SnSe_2$ and Janus SnSSe has been explored for thermoelectric applications. The electron and phonon transport have been studied using the DFT and Boltzmann transport theory.

Finally, Chapter 8 concludes the thesis and proposes some future perspectives to be explored.

2. Theory and Methodology

2.1 Electronic Structure Theory

After Schrödinger's wave equation for quantum mechanics had been formalized in 1926, Paul Dirac declared: "The underlying physical laws necessary for the mathematical theory of a large part of physics and the whole of chemistry are thus completely known, and the difficulty is only that the exact application of these laws leads to equations much too complicated to be soluble. It therefore becomes desirable that approximate practical methods of applying quantum mechanics should be developed, which can lead to an explanation of the main features of complex atomic systems without too much computation." The goal of electronic structure theory is to solve the non-relativistic time independent many-body Schrödinger equation.

2.2 Many-body problem

The many-body problem involves a collection of atomic nuclei and electrons that interact through Coulomb forces. In materials science, if one is concerned only with the system's ground state and not its time evolution, it is adequate to solve the time-independent Schrödinger equation:

$$H\psi = E\psi \quad \ldots (2.1)$$

here ψ represents the many-body wave function that contains information about the spatial coordinates of the nuclei as well as the spatial and spin coordinates of the electrons. The Hamiltonian operator of the system is denoted by H, while E represents the energy eigenvalue that represents the system's total energy.

The complete non-relativistic quantum many-body Hamiltonian (H) of interacting nuclei (M) and electrons (N) has the following form in reduced units:

$$H = -\frac{1}{2}\sum_{i=1}^{N}\nabla_i^2 - \sum_{I=1}^{M}\frac{1}{2M_I}\nabla_I^2 - \sum_{i=1}^{N}\sum_{I=1}^{M}\frac{Z_I}{|\boldsymbol{r_i}-\boldsymbol{R_I}|} + \frac{1}{2}\sum_{i\neq j}\frac{1}{|\boldsymbol{r_i}-\boldsymbol{r_j}|} + \frac{1}{2}\sum_{I\neq J}\frac{Z_I Z_J}{|\boldsymbol{R_I}-\boldsymbol{R_J}|} \quad \dots (2.2)$$

here $\boldsymbol{r_i}$ is the spatial coordinate of the ith electron, $\boldsymbol{R_I}$ is the spatial coordinates of the Ith nucleus, and Z_I is the atomic number of the Ith nucleus. The above equation can be written in the simpler form:

$$H = T_e + T_n + V_{e-n} + V_{e-e} + V_{n-n} \quad \dots (2.3)$$

Here, T_e is kinetic energy of the electrons, T_n is the kinetic energy of the nuclei, V_{e-n} is the interaction between nuclei and electrons, V_{e-e} is the electrostatic repulsion between electrons, and last term V_{n-n} is the Coulomb-interaction between the nuclei.

The many-body Schrödinger equation is too complex to solve in most cases, except for simple systems such as Hydrogen or Helium atoms. To obtain solutions for systems containing numerous particles, one must rely on approximations. The electron-electron interaction term represented by V_{e-e}, is the primary obstacle in solving the many-body Schrödinger equation.

2.2.1 Born-Oppenheimer approximation

The Born-Oppenheimer approximation assumes that the kinetic energy term for the nuclei is much smaller than the kinetic energy term for the electrons because the nuclear masses are many times larger than the electronic masses $\left({}^{M_I}/_{m_e} \gg 1\right)$. This approximation considers the atomic nuclei are in fixed positions and that the electrons move in the

field of these atomic nuclei. Mathematically, we can separate the wave function of the electrons and nuclei.

$$\psi = \psi_{elelctrons} \times \psi_{nuclie} \quad \dots (2.4)$$

With this approximation we can omit T_n and V_{n-n} and obtain the electronic Schrödinger equation,

$$H_e\psi_{electron} = \left[-\frac{1}{2}\sum_{i=1}^{N}\nabla_i^2 - \sum_{i=1}^{N}\sum_{I=1}^{M}\frac{Z_I}{|\boldsymbol{r_i}-\boldsymbol{R_I}|} + \frac{1}{2}\sum_{i\neq j}\frac{1}{|\boldsymbol{r_i}-\boldsymbol{r_j}|}\right]\psi_{electron} = E\psi_{electron} \quad \dots (2.5)$$

Although the Born-Oppenheimer approximation simplifies the problem, the Schrödinger equation remains unsolvable for systems containing more than a few atoms.

2.3 Density functional theory

Density functional theory (DFT) is a theoretical framework that emphasises the importance of electron density in describing the behaviour of many-body systems such as atoms, molecules, and solids. Unlike methods based on wave functions, DFT reduces the complexity of the equations by using electron density as a key parameter, which has a fixed dimensionality of 3, independent of the number of atoms in the system. By reducing the number of degrees of freedom from 3N to 3, DFT enables the study of large systems containing hundreds or thousands of atoms making it widely accepted method in condensed matter physics.

The fundamental assumption underlying DFT is that the electron density in the ground state provides all the necessary information to characterise the system properties. DFT methods enables the accurate solution of Schrödinger equation for large systems with reasonable computational cost. The notion of using the electron density instead of

the wave function was first proposed by Thomas and Fermi in 1927 and subsequently refined by Hohenberg and Kohn in 1964. State of the art DFT is based on Kohn and Sham's theory. In recognition of his pioneering contributions to the establishment of DFT, Walter Kohn was awarded the Nobel Prize in Chemistry in 1998.

2.3.1 Thomas Fermi model:

In 1927, Thomas and Fermi first proposed the electronic density as a basic quantity instead of the complicated *N*-electron wave functions to solve the Schrödinger equation. The electronic density is defined as

$$\rho(\boldsymbol{r}) = N \int d\boldsymbol{r_1} \dots \int d\boldsymbol{r_N} |\psi(\boldsymbol{r_1}, \dots, \boldsymbol{r_N})|^2 \quad \dots (2.6)$$

Thomas and Fermi proposed that the motion of electrons is uncorrelated, and the kinetic energy of the system can be written as an explicit functional of the density of electrons in a homogeneous electron gas. In this model, the kinetic energy of the electrons is expressed as follows:

$$T_{TF}[\rho(\boldsymbol{r})] = \frac{3}{10}(3\pi^2)^{2/3} \int \rho^{\frac{5}{3}}(\boldsymbol{r}) d\boldsymbol{r} \quad \dots (2.7)$$

The total energy of a Thomas-Fermi (TF) system can be determined by adding the interactions between the electrons and nuclei and the electron-electron interactions. This expression for the total energy is often used in the local density approximation (LDA).

$$E_{TF}[\rho(\boldsymbol{r})] = \frac{3}{10}(3\pi^2)^{\frac{2}{3}} \int \rho^{\frac{5}{3}}(\boldsymbol{r}) d\boldsymbol{r} - \int \frac{\rho(r)}{\boldsymbol{r}} d\boldsymbol{r} + \frac{1}{2} \iint \frac{\rho(\boldsymbol{r})\rho(\boldsymbol{r'})}{|\boldsymbol{r}-\boldsymbol{r'}|} d\boldsymbol{r} d\boldsymbol{r'} \quad \dots (2.8)$$

The second and third terms in the energy expression represent the potential energy due to electron-nucleus interactions and the Hartree energy due to electron-electron interactions, respectively. The energy of the system can be determined by minimizing the $E_{TF}[\rho(\boldsymbol{r})]$ using the Lagrange multiplier method. However, it is important to note that the

TF model does not account for all aspects of the physics involved. In particular, the model neglects the electronic exchange-correlations, which can lead to in errors in the calculated total energy and density divergence. To address these limitations, Hohenberg and Kohn later proposed a reformulation of the TF method that provides an exact description of the system.

2.3.2 Hohenberg Kohn theorem:

In 1964, Hohenberg and Kohn (HK) established the groundwork for DFT by demonstrating how the electronic Hamiltonian can be expressed as a functional of density.[22] The HK approach formulates DFT as an exact theory of many-electron systems, wherein the Hamiltonian of interacting particles is represented as follows:

$$H = -\frac{1}{2}\sum_{i=1}^{N}\nabla_i^2 + \sum_I \frac{Z_I}{|\boldsymbol{r_i}-\boldsymbol{R_J}|} - \sum_{i\neq j}\frac{1}{|\boldsymbol{r_i}-\boldsymbol{r_j}|} \quad \dots (2.9)$$

$$v_{ext}(r) = \sum_I \frac{Z_I}{|\boldsymbol{r_i}-\boldsymbol{R_J}|} \quad \dots (2.10)$$

Here $v_{ext}(r)$ is an external potential that includes interactions between electrons and nuclei. The two HK theorems dependent on electron density ρ(**r**) of electrons in an external potential.

Theorem 1: For any system of interacting particles in an external potential $v_{ext}(r)$, the potential $v_{ext}(r)$ is determined uniquely, except for a constant, by the ground-state particle density ρ_0(r).

Theorem 2: A universal functional for the energy $E[\rho(r)]$ in terms of the density ρ(r) can be defined, valid for any external potential $v_{ext}(r)$. For any $v_{ext}(r)$, the exact ground-state energy of the system is the global minimum value of this functional, and the density ρ(r) that minimizes the functional is the exact ground-state density ρ_0(r).

As a result, the energy functional has the following form:

$$E[\rho(r)] = \int v_{ext}(r)\rho(r)dr + F_{HK}[\rho(r)] \quad \text{... (2.11)}$$

here $F_{HK}[\rho(r)]$ functional is defined as

$$F_{HK}[\rho(r)] = T[\rho(r)] + V_{e-e}[\rho(r)] \quad \text{... (2.12)}$$

In this expression $T[\rho(r)]$ is the kinetic-energy functional and $V_{e-e}[\rho(r)]$ is the electron-electron interaction functional.

The HK theorems demonstrate that there exists a one-to-one correspondence between the external potential and the ground-state density. This implies that a universal functional can be defined for any density. By minimizing this functional, one can accurately determine the exact density and energy of the interacting many-body system. Specifically, one can obtain the lower bound of the true interacting many-body system energy, such that: $E_0[\rho_0(r)] \leq E_0[\rho(r)]$.

Despite its usefulness, the HK theorem encounters a conceptual issue regarding the representability of density due to the unknown form of the functional $F[\rho(r)]$. To address this problem, Kohn and Sham developed a method to perform DFT calculations.

2.3.3 Kohn-Sham Method

Kohn and Sham developed a method based on the HK theorems that allows one to minimize the functional by varying $\rho(r)$ over all densities of N electrons.[23] Essentially, the universal functional F_{HK}, is separated into a set of energy components, each of which has a clear physical origin, and some of which have explicit forms. Approximation is only required for the components that cannot be readily evaluated.

The method employs an imaginary auxiliary system to simulate the true many-electron system. This hypothetical system consists of independent electrons, each subjected to the same external potential (otherwise known as the effective potential). This approach assumes

that the ground-state density of a non-interacting system, denoted as $\rho_{KS}(r)$ corresponds to the actual ground−state density $\rho(r)$ of the system. Under this assumption, the system's ground-state wave function can be expressed in terms of single-particle wave functions.

Kohn and Sham wrote the F_{HK} in three terms, resulting in the energy functional as:

$$E[\rho_{KS}(r)] = \underbrace{T_{KS}[\rho_{KS}(r)] + \frac{1}{2}\iint \frac{\rho_{KS}(r)\rho_{KS}(r')}{|r-r'|}drdr' + E_{XC}[\rho_{KS}(r)]}_{F_{HK}} + \int v_{ext}(r)\rho_{KS}(r)dr \quad \text{... (2.13)}$$

The energy functional can be expressed in the following form[24]:

$$E[\rho_{KS}(r)] = T_{KS} + E_H + E_{XC} + E_{ext} \quad \text{... (2.14)}$$

Here T_{KS} represents the kinetic energy of noninteracting electrons, while E_H represents the Hartree energy corresponding to electron-electron interaction. E_{XC} refers to the exchange-correlation energy and E_{ext} represents the external potential energy of electrons due to the nuclei.

For a system of N electrons, the wave function can be constructed from the single-particle Kohn-Sham orbitals $\phi_i^{KS}(r)$(i = 1, 2, . . . , N). The kinetic energy and electron density of the system can then be determined as follows:

$$T_{KS} = -\frac{1}{2}\sum_{i=1}^{N}\left\langle \phi_i^{KS}\middle|\nabla^2\middle|\phi_i^{KS}\right\rangle \quad \text{... (2.15)}$$

$$\rho_{KS}(r) = \sum_{i=1}^{N}|\phi_i^{KS}(r)|^2 \quad \text{... (2.16)}$$

in terms of single-particle orbitals, one can arrive at the central equation in KS-DFT expressed as

$$H_i^{KS}\phi_i(r) = \varepsilon_i\phi_i^{KS}(r) \quad \text{... (2.17)}$$

with the one-electron Hamiltonian in the following form

$$H_i^{KS} = -\frac{1}{2}\nabla^2 + v_H(\rho_{KS}) + v_{XC}(\rho_{KS}) + v_{ext}(r) \quad \text{... (2.18)}$$

here $v_H(\rho_{KS})$ is Hartree potential, $v_{XC}(\rho_{KS})$ is the exchange-correlation potential and $v_{ext}(r)$ is the external potential.

$$v_{eff}(\rho_{KS}) = v_H(\rho_{KS}) + v_{XC}(\rho_{KS}) + v_{ext}(\boldsymbol{r}) \quad \text{... (2.19)}$$

with the exchange-correlation potential $v_{XC}(r)$ given by

$$v_{XC}(\rho_{KS}) = \frac{\delta E_{XC}[\rho_{KS}(r)]}{\delta \rho_{KS}(r)} \quad \text{... (2.20)}$$

one can rewrite the KS equation as

$$\left(-\frac{1}{2}\nabla^2 + v_{eff}\right)\phi_i^{KS} = \varepsilon_i \phi_i^{KS} \quad \text{... (2.21)}$$

The above single particle like Kohn-Sham equations is solved self-consistently by assessing the effective potential $v_{eff}(\rho_{KS})$, starting from the trial electron density $\rho_{KS}(r)$ as an input.

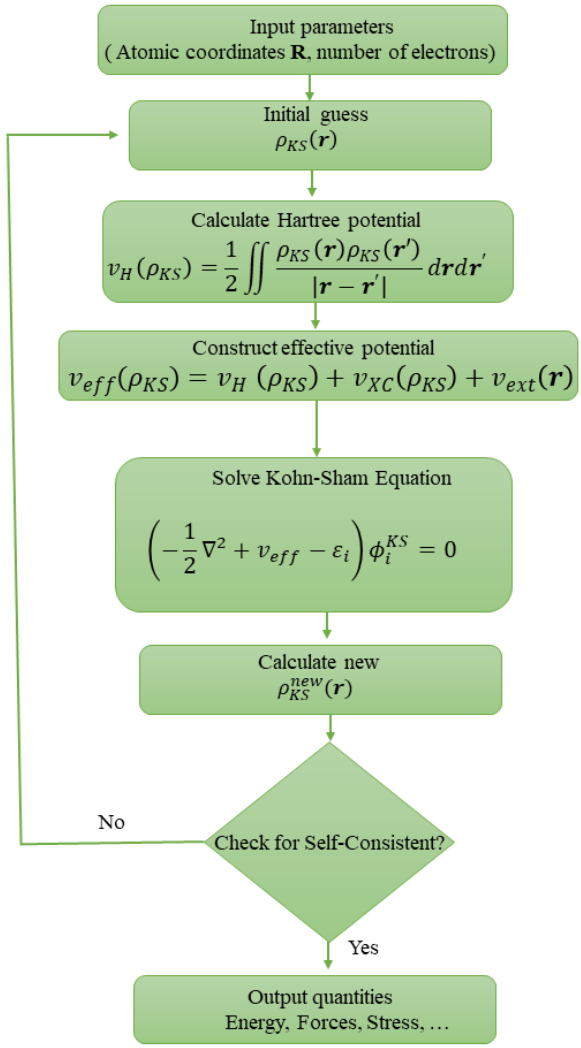

Figure 2.1. The schematic diagram of the self-consistent loop for solution of the Kohn–Sham equations.

2.3.4 Exchange correlation energy:

To arrive at the solution the KS equation, one must know the form of exchange-correlation energy functional ($E_{XC}[\rho_{KS}(r)]$). The exchange-correlation energy is divided into two parts: the exchange energy, and the correlation energy.

$$E_{XC}[\rho_{KS}(r)] = E_X[\rho_{KS}(r)] + E_C[\rho_{KS}(r)] \quad \text{... (2.22)}$$

Exchange energy ($E_X[\rho_{KS}(r)]$): This term comes into picture due to the antisymmetric nature of electronic wavefunction. Since electron are fermions, they follow Pauli's exclusion principle. This leads to a spatial separation between the electrons and give rise to the Exchange energy.

Correlation energy ($E_C[\rho_{KS}(r)]$): The origin of the correlation energy is due to the electron-electron interaction.

The exact analytical or mathematical form of $E_{XC}[\rho_{KS}(r)]$ is not known. Therefore, various approximations have been introduced to find the best accuracy potential.

Local density Approximation (LDA)

In LDA, the exchange and correlation energy is determined by integrating the energy density over the entire space, with the assumption that the energy density at each point is equal to that of a homogeneous electron gas with corresponding density.[25]

The LDA method introduced by Kohn-Sham, the exchange correlation term was approximated as

$$E_{XC}^{LDA}[\rho_{KS}(r)] = \int \rho_{KS}(r)\, \varepsilon_{XC}^{unif}\big(\rho_{KS}(r)\big) dr \quad \text{... (2.23)}$$

where $\varepsilon_{XC}^{unif}\big(\rho_{KS}(r)\big)$ is the exchange-correlation energy per particle of the infinite uniform electron gas with the density $\rho_{KS}(r)$.

The LDA is accurate for high densities or slowly varying charge density systems, but tends to overestimate binding energies, making it an inadequate descriptor for some materials. LDA is most effective in computing ground state energy of the system. However, for systems with rapidly varying electron densities, LDA performs poorly, resulting

in an underestimation of the band gaps of semiconductors and similar materials.

Generalized gradient approximation (GGA)

The GGA[26] approach was the next logical progression beyond the LDA. In GGA, the functional depends not only on the electron density, but also on the magnitude of its gradient ($\nabla\rho_{KS}(r)$), making it is a semi-local method.

In the GGA method, the exchange-correlation energy is approximated as follows:

$$E_{XC}^{GGA}[\rho_{KS}(r)] = \int \rho_{KS}(r)\, \varepsilon_{XC}^{GGA}\big(\rho_{KS}(r), \nabla\rho_{KS}(r)\big)dr \quad \ldots (2.24)$$

Compared to LDA, GGA provide better results in determination of structural properties and ground state energies of the system. The GGA functional also improves the accuracy of calculations such as bond lengths and lattice constant.

However, being an approximation GGA has limitation in capturing the electron-electron interactions. Consequently, the band gaps are often underestimated. GGA tends to overestimate the delocalization of electrons. This means that the electrons are less confined to the atoms and more spread out, which lead to a reduction in the band gap.

Hybrid functional

Hybrid functionals are, as the name suggests, advanced functionals obtained by combining part of the exact Hartree-Fock exchange (a predecessor of DFT) with the semi-local exchange-correlation functional used in GGA or LDA.[27] By including the HF exchange term, hybrid functions can better account for electron-electron interactions that are not fully captured by GGA or LDA. This improved treatment

of exchange correlation effects often leads to more accurate predictions of band gaps and electronic structures.

In the HSE method, the exchange-correlation energy is approximated as follows:

$$E_{XC}^{HSE}[\rho_{KS}(r)] = aE_{XC}^{HF} + (1-a)E_{X}^{GGA} + E_{C}^{GGA} \quad \text{... (2.25)}$$

here a is mixing parameter, E_{XC}^{HF} nonlocal Hartree-Fock exchange energy, E_{X}^{GGA} is exchange energy and E_{C}^{GGA} is correlation energy.

2.3.5 Plane wave basis set

Expanding the KS orbitals using a suitable basis set is essential to solve the Kohn-Sham equations. For systems that can be described using periodic boundary conditions, a plane wave (PW) basis set is a popular choice due to its efficiency in reciprocal space representation. Additionally, PWs can be easily transformed from real to reciprocal space through fast Fourier transform (FFT) which form complete basis sets composed of simple mathematical functions. By utilizing a PW basis set, the single particle KS orbital in equation can be expressed as:

$$\phi_{i}^{KS}(\boldsymbol{r}, \boldsymbol{k}) = \frac{1}{\sqrt{V}} \sum_{\vec{G}} \boldsymbol{C}_{i,\vec{G}}(\vec{k})\, \boldsymbol{e}^{\boldsymbol{i}(\vec{k}+\vec{G}).\vec{r}} \quad \text{... (2.26)}$$

Where V is the volume of the cell, $\vec{G}$ refers to the reciprocal lattice vector and $\boldsymbol{C}_{\boldsymbol{i},\vec{G}}$ denotes the coefficients of the PW basis set. In principle, an infinite number of plane waves are required for the expansion. In practise, the plane wave basis sets are truncated to include only those PWs that have kinetic energies smaller than E_{cut}, where,

$$E_{cut} = \frac{1}{2}|\vec{k} + \vec{G}|^2 \quad \text{... (2.27)}$$

2.3.6 Pseudopotential

Unlike valence electrons, which have a significant impact on the ground state properties due to their strong interaction with neighbouring atoms, core electrons have a negligible effect on the ground state properties as they interact weakly with neighbouring atoms. In addition, core electrons are more localised and have deeper energy levels in the host atomic potential compared to valence electrons, which further reduces their interaction with valence electrons.

In DFT, pseudopotentials are used to account for this reduced interaction by considering only the valence electrons in the calculation of material properties. This reduces the complexity of the calculations without sacrificing accuracy. Pseudopotentials are constructed to produce orbital wave functions that mimic the exact valence orbital wave functions. However, in cases where certain core electrons have a strong interaction with valence electrons and affect the ground state properties, they must also be considered in the construction of the pseudopotential. The accuracy of the system can be improved by choosing a small cut-off radius, but this increases the computational costs. Conversely, a large cut-off radius lowers the computational costs, but also reduces the predictive power of the material model.

2.4 Electron Transport

Boltzmann transport theory is a useful tool to calculate various transport properties of real materials. The thermoelectric and transport properties were evaluated using a semiclassical Boltzmann transport theory with constant relaxation time approximation (CRTA) and rigid band approximation (RBA) as implemented in the BoltzTrap2 code.[28] In CRTA, we assume that the scattering time is almost independent of the energy and that both the group velocity of the charge carriers and DOS contribute to the transport function. RBA assumes that changing the

temperature or doping of the system, does not change the band structure. The group velocity (v_α) of the charge carriers in a given band can be described as

$$v_\alpha(i,\boldsymbol{k}) = \frac{1}{\hbar^2}\frac{\partial \epsilon_{i,\boldsymbol{k}}}{\partial \boldsymbol{k}_\alpha} \quad \text{... (2.28)}$$

The group velocity can be obtained by the derivatives of the smoothed Fourier interpolated electronic bands. To calculate the thermoelectric properties, we need to evaluate the conductivity tensor, which is given by,

$$\sigma_{\alpha\beta}(i,\boldsymbol{k}) = e^2\tau_{i,\boldsymbol{k}}v_\alpha(i,\boldsymbol{k})v_\beta(i,\boldsymbol{k}) \quad \text{... (2.29)}$$

here, *e* is the charge of the electron, i is the band index, ***k*** is the direction of the wave vector, and $\tau_{i,\boldsymbol{k}}$ is the relaxation time.

According to the semi-classical BTE, the Seebeck coefficient tensors $S_{\alpha\beta}(T,\epsilon_f)$, the electrical conductivity tensors $\sigma_{\alpha\beta}(T,\epsilon_f)$, and the electronic thermal conductivity tensor $k^{el}_{\alpha\beta}(T,\epsilon_f)$ are given:

$$\sigma_{\alpha\beta}(T,\epsilon_f) = \frac{1}{\mathrm{V}}\int e^2\tau_{i,\boldsymbol{k}}v_\alpha(i,\boldsymbol{k})v_\beta(i,\boldsymbol{k})\left[-\frac{\partial f_0(T,\epsilon,\epsilon_f)}{\partial\epsilon}\right]d\epsilon \quad \text{... (2.30)}$$

$$S_{\alpha\beta}(T,\epsilon_f) = \frac{1}{eT}\frac{\int v_\alpha(i,\boldsymbol{k})v_\beta(i,\boldsymbol{k})(\epsilon-\epsilon_f)\left[-\frac{\partial f_0(T,\epsilon,\epsilon_f)}{\partial\epsilon}\right]d\epsilon}{\int v_\alpha(i,\boldsymbol{k})v_\beta(i,\boldsymbol{k})\left[-\frac{\partial f_0(T,\epsilon,\epsilon_f)}{\partial\epsilon}\right]d\epsilon} \quad \text{... (2.31)}$$

$$k^{el}_{\alpha\beta}(T,\epsilon_f) = \frac{1}{TV}\int e^2\tau_{i,\boldsymbol{k}}v_\alpha(i,\boldsymbol{k})v_\beta(i,\boldsymbol{k})(\epsilon-\epsilon_f)^2\left[-\frac{\partial f_0(T,\epsilon,\epsilon_f)}{\partial\epsilon}\right]d\epsilon \quad \text{... (2.32)}$$

where V, ϵ_f, and f_0 are the volume of the unit cell, the Fermi level of the charge carriers, and the carrier Fermi–Dirac distribution function, respectively.

2.5 Phonon Transport

In quantum mechanics, lattice vibrations are characterised by quasiparticles, known as phonons. These phonons help to gather the information on the dynamic stability of the system. The phonon modes

are represented in the form of phonon dispersion curve, which gives the relationship between the phonon frequency (ω) and the wave vector (***k***). The slope of the dispersion relation gives the group velocity of phonons (v_g). To determine the phonon dispersion relation, one can solve the classical equations of motion of atoms that are perturbed by small displacements from their respective equilibrium positions.

The potential energy V($\boldsymbol{R}$) of a system of N atoms, depends on the equilibrium positions $\boldsymbol{R}_{j,\beta}$, and the displacements from these positions $\mathbf{u}_{j,\beta}$, where j, β denote index of atom and the Cartesian x, y, z coordinates. V($\boldsymbol{R}$, u) can be expanded in a Taylor series.

$$V = V_o + \sum_{j,\beta} \frac{\partial V}{\partial \boldsymbol{u}_{j,\beta}} \boldsymbol{u}_{j,\beta} + \frac{1}{2} \sum_{j,\beta,j'.\beta'} \boldsymbol{u}_{j,\beta} \frac{\partial^2 V}{\partial \boldsymbol{u}_{j,\beta} \partial \boldsymbol{u}_{j',\beta'}} \boldsymbol{u}_{j',\beta'} + \cdots \ \ldots \quad (2.33)$$

Since at equilibrium there is no force acting on the atom, the first order derivative is zero. If the displacement from the equilibrium position is small, the third and higher order terms can also be neglected, which is known as the harmonic approximation. The second order derivative of the energy is known as the force constant.

$$\Phi^{j,j'}_{\beta,\beta'} = \frac{\partial^2 V}{\partial \boldsymbol{u}_{j,\beta} \partial \boldsymbol{u}_{j',\beta'}} \boldsymbol{u}_{j',\beta'} \Big|_{u=0} \quad \ldots (2.34)$$

To proceed, it is necessary to express the displacements in relation to a plane wave about the cell coordinates, which can be achieved as follows:

$$\boldsymbol{u}_{j,\beta} = \boldsymbol{e}_{\boldsymbol{lq},j\beta} \boldsymbol{e}^{\boldsymbol{i}(\boldsymbol{q}.\boldsymbol{R}_{j,\beta} - \boldsymbol{\omega}_{\boldsymbol{lq}} \boldsymbol{t})} \quad \ldots (2.35)$$

where $\boldsymbol{l}$ is the index of the phonon modes, $\boldsymbol{q}$ represents phonon wave vector, ω is the angular frequency of the wave and $\boldsymbol{e}_{\boldsymbol{lq},j\beta}$ is the polarisation vector of the phonon mode labelled by $\boldsymbol{lq}$.

The lattice vibrations (phonons) can be evaluated by using the following the eigenvalue problem:

$$D^{j,j'}_{\beta,\beta'}(\boldsymbol{q})\boldsymbol{e}_{\boldsymbol{lq},j\beta} = \boldsymbol{\omega}^{\boldsymbol{2}}_{\boldsymbol{lq}}\boldsymbol{e}_{\boldsymbol{lq},j\beta} \quad \text{... (2.36)}$$

the dynamical matrix $D^{j,j'}_{\beta,\beta'}(\boldsymbol{q})$ is defined as

$$D^{j,j'}_{\beta,\beta'}(\boldsymbol{q}) = \frac{1}{\sqrt{M_j M_{j'}}}\sum \Phi^{j,j'}_{\beta,\beta'}\, \boldsymbol{e}^{\boldsymbol{iq.R_{j,\beta}}} \quad \text{... (2.37)}$$

here M is the mass of the atom.[29,30]

Once from the above eigen value equation phonon frequency is determined the vibrational density of states can be evaluated using the following relation:

$$VDOS = \frac{1}{N}\sum_{q,j} \delta(\omega - \omega_{\boldsymbol{lq}}) \quad \text{... (2.38)}$$

From the phonon dispersion curves under the quasi harmonic approximation (by changing volume, phonon properties vary since the potential is an anharmonic function of volume). The mode Grüneisen parameter ($\gamma_{q,i}$), which is a measure of anharmonicity, can be calculated by

$$\gamma_{q,i}(V) = -\frac{V}{\omega_{\boldsymbol{lq}}}\frac{\partial \omega_{\boldsymbol{lq}}}{\partial V} \quad \text{... (2.39)}$$

here $\boldsymbol{l}$ is the band index and V is the volume of a unit cell.

The force constant for the phonon calculations can be determined using either the finite difference method (frozen phonon approach) or the linear response method (density functional perturbation theory approach).

In order to determine the lattice thermal conductivity, it is necessary to consider third order force constants. The calculation of the lattice

thermal conductivity involves solving the linearized Boltzmann transport equation using the single-mode relaxation time (SMRT) approximation. The phono3py code implements an expression for the lattice thermal conductivity.[31]

$$\kappa_l = \frac{1}{NV}\sum_\lambda C_\lambda v_\lambda^2 \tau_\lambda^{SMRT} \quad \text{... (2.40)}$$

here V is the volume of a unit cell, and v_λ and τ_λ^{SMRT} are the

group velocity and SMRT of the phonon mode λ, respectively. C_λ is the mode dependent heat capacity defined as:

$$C_\lambda = k_B \left(\frac{\hbar\omega_\lambda}{k_B T}\right)^2 \frac{exp\left(\frac{\hbar\omega_\lambda}{k_B T}\right)}{\left(exp\left(\frac{\hbar\omega_\lambda}{k_B T}\right)-1\right)^2} \quad \text{... (2.41)}$$

2.6 Ab-initio Molecular dynamics

In classical molecular dynamics the atoms are treated as classical point-like particles, and their motions is studied by Newton's laws. In Ab-initio molecular dynamics (AIMD) the forces are obtained directly from electronic structure calculations. In AIMD the forces are calculated from the Hellmann-Feynman Theorem[30] and is written as

$$\boldsymbol{F} = -\langle\psi\left|\frac{\partial H}{\partial \boldsymbol{R}}\right|\psi\rangle = -\frac{d(E[\rho_{KS}(r)]+V_{n-n})}{d\boldsymbol{R}} \quad \text{... (2.42)}$$

Where **R** is the nuclear spatial coordinate and the energy **E** can be obtained by solving the KS equations.

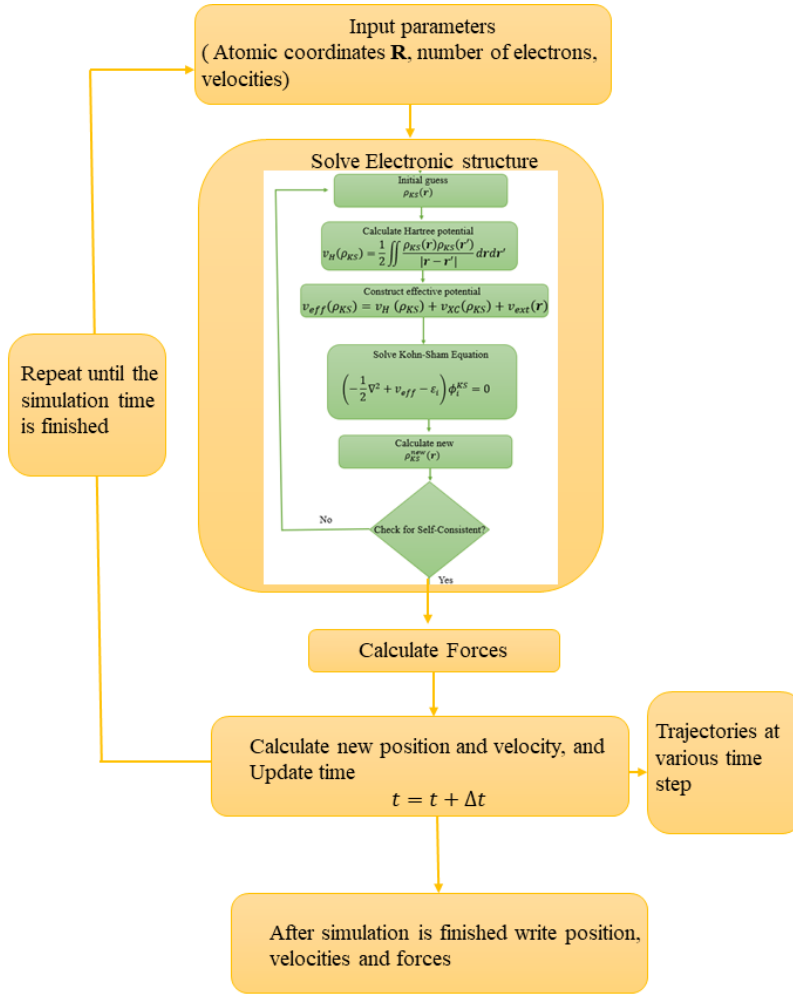

Figure 2.2. Schematic diagram of the AIMD calculation

Ab-initio molecular dynamics is extremely heavy computationally, and many ideas to improve its performance has been suggested. The main problem with AIMD simulations is of course that in each timestep the electronic structure problem is solved and this take a considerable amount of time.

2.6.1 Root mean squared displacement:

Root Mean Squared Displacement (RMSD) is a mathematical measure that quantifies the deviation of the position of a particle with respect to a reference position over time.

Using the atomic coordinates of N atoms obtained from the various trajectories of the AIMD simulation, the RMSD can be calculated with the following formula:

$$RMSD = \sqrt{\langle u^2 \rangle} = \sqrt{\frac{1}{N}\sum_i^N |r_i(t + \Delta t) - r_i(t)|} \quad \text{... (2.43)}$$

here $r_i(t)$ is the position coordinate of the i^{th} atom at time t.

Experimentally, the root mean squared displacement (RMSD) can be determined using the Debye-Waller coefficient (B_{iso}), which measures the intensity of a Bragg peak in a diffraction pattern resulting from thermal motion. B_{iso} is related to RMSD through the following equation:

$$B_{iso} = \frac{8\pi^2}{3}\langle u^2 \rangle \quad \text{... (2.44)}$$

2.6.2 Vibrational density of states:

The vibration density of states of the system can also be determined via the AIMD trajectories. This can be achieved by first calculating the velocity autocorrelation function (VACF). The VACF quantifies the degree to which the velocity of a particle is correlated with its past velocities.

The VACF is defined as,

$$C(t) = \frac{\sum_i^N \langle v_i(t+\Delta t).v_i(t) \rangle}{\sum_i^N \langle v_i(t).v_i(t) \rangle} \quad \text{... (2.45)}$$

here, here $v_i(t)$ is the velocity of the ith atom at time t, and the angle bracket denotes average over the time.

From the VACF the vibrational density of states is computed by taking its Fourier transform.

$$VDOS = \int_{-\infty}^{\infty} C(t) e^{-i\omega t}\, dt \quad \ldots (2.46)$$

3. Experimental and Ab Initio Study of Cu_2SnS_3 Polymorphs for Thermoelectric Applications

This section is taken from[32]: Lohani, K.; Nautiyal, H.; Ataollahi, N.; Fanciulli, C.; Sergueev, I., Etter, M., Scardi, P.* "Experimental and Ab Initio Study of Cu_2SnS_3 (CTS) Polymorphs for Thermoelectric Applications. J. Phys. Chem. C **2021**, 125, 178– 188. https://doi.org/10.1021/acs.jpcc.0c09139"

*Correspondence: paolo.scardi@unitn.it

Abstract

Cu_2SnS_3 (CTS) is a medium-temperature, eco-friendly, p-type thermoelectric material known for phonon-glass-electron-crystal characteristic. In the present work, ordered and disordered CTS samples were prepared from elemental powders, and their electronic and vibrational properties were systematically investigated by experimental methods and ab initio calculations. The disordered CTS polymorph presents a higher power factor, PF ~ 1.5 μW/K^2 cm, than the ordered and stable phase, PF ~ 0.5 μW/K^2 cm, above 700 K, as an effect of a smaller band gap and higher carrier concentration. Most importantly, the disordered CTS shows an ultralow thermal conductivity, k ~ 0.4−0.2 W/m K, as compared to ordered, k ~ 1.0−0.4W/m K, in the temperature range of 323−723 K. The combined effect of a higher PF and lower k results in a higher figure of merit, zT ~ 0.5 at 723 K, obtained for disordered CTS without resorting to chemical alloying. It turns out that structural disorder contributes to the suppression of thermal conductivity. While group velocity of acoustic phonons, as shown both by experiments and ab initio calculations, is similar in the two polymorphs, a strong anharmonicity characterizes the disordered

CTS, resulting in the presence of low-lying optical modes acting as traps for heat transmission. Density functional perturbation theory simulations and nuclear inelastic scattering combined with high-resolution diffraction studies of the lattice parameters reveal details of phonon−phonon interactions in CTS with unprecedented effectiveness.

3.1 Introduction

Thermoelectric (TE) materials attract increasing interest in applications involving thermal gradients for durable, noise-free, and scalable solid-state power generators and coolers.[33–36] Performing TE devices require an optimal combination of properties Seebeck coefficient (S), electrical conductivity (σ), and thermal conductivity (κ) to maximize the figure of merit, $zT = S^2\sigma T/\kappa$. Therefore, an ideal TE material would require a high power factor ($PF = S^2\sigma$) and a low k (involving an electronic (κ_e) and a lattice (κ_l) component). In particular, obtaining an ultralow thermal conductivity is one of the main goals of the current research on TE materials.[37–39]

The Cu_2SnS_3 mineral phase was first reported in 1983, as a new sulphide with a triclinic structure (SG: P1).[40] It has been widely studied as an absorber material for photovoltaic devices owing to its high (∼104 cm^{-1}) optical absorption coefficient and tunable band gap spanning from 0.7 to 1.6 eV.[41–46] In recent years, CTS has attracted interest from the TE community for its 3D hole conductive network and ultralow thermal conductivity, a so-called "phonon-glass-electron-crystal" characteristic.[46] At first, in 2016, Tan et al.[47] and Shen et al.[48] reported CTS as a potential TE material, using In and Zn doping, respectively. Other researchers have reported Mn,[49] Ni,[50] Fe,[51] and Co[52] doping to enhance the TE performance of CTS.

The experimental literature suggests that undoped CTS forms an ordered monoclinic (SG: Cc) phase.[53] However, this ordered CTS polymorph has high electrical resistivity (ρ) and κ values, resulting in a low zT.[51] One way to lower k is to hinder the propagation of phonon waves,[33] and to do this, some researchers produced a disordered cubic (SG:$F\bar{4}3m$) polymorph.[52] This, however, required acceptor cation doping, except in our recent work,[54] where we have shown how to stabilize the disordered CTS polymorph using a bottom-up (reactive milling) production technique that does not require any doping.

CTS polymorphs are a variant of the zinc blende (ZnS) structure (Figure 3.1a), made of tetrahedral cages (Figure 3.1b) of S (Wyckoff position 4c) with a cation (Zn) positioned in the middle (4a). For ordered (Figure 1c) and disordered (Figure 3.1d) CTS, the Zn cation is stoichiometrically replaced by Cu and Sn, respectively, in an ordered and in a random manner. This results in a partial cation occupancy of 2/3, and 1/3, for Cu and Sn, respectively.[55] These polymorphs can also be understood as an assembly of S coordination motifs, in which each S anion is connected to four (Cu/Sn) cations, making tetrahedral motifs. Zawadzki et al.[56] have put forward that cations in CTS structures contain five possible S−Cu_iSn_{4-i} motifs, where i ϵ {0, ..., 4}, but the S−Cu_4,S−$CuSn_3$, and S−Sn_4 motifs are energetically unlikely to form. The ordered CTS has a regular distribution of S−Cu_2Sn_2 and S−Cu_3Sn motifs, while in disorder CTS, S−Cu_2Sn_2 motifs form nanometer-scale clusters. Additionally, because the octet rule is not locally respected in these structures, all of this brings the crystal structure, especially in the disordered phase, close to instability. In the present work, the abovementioned clustering effect was not considered for ab initio calculations because of the limitation of computational resources, rather two, Sn-rich and Sn-poor disordered cells. Zhai et al.[57] have discussed

the difficulty in the *ab initio* simulation of similar Cu_2SnX_3 (X = S/Se) disordered structures, and how this limits the electronic information from band structures. However, the electronic bands for the ordered phase are diffusely discussed in the literature.[44,57,58] In the similar CTSe system,[59] the disordered polymorph shows a lower band gap energy than the corresponding ordered phase, which promotes a higher carrier concentration (n), resulting in a higher PF. Recently, we have shown that the disordered CTS polymorph without acceptor doping presents a higher PF ~ 1.1 $\mu W/K^2$ cm than the ordered polymorph, PF ~ 0.1 $\mu W/K^2$ cm, above 700 K. In fact, the disordered polymorph has a lower Seebeck (S ~ 250−325 μV/K) and resistivity (ρ ~ 1.5−1.0 Ω cm) than the ordered polymorph (S ~ 600−700 μV/K, ρ ~ 27−30 Ω cm), in the temperature range of 323−723 K.[60]

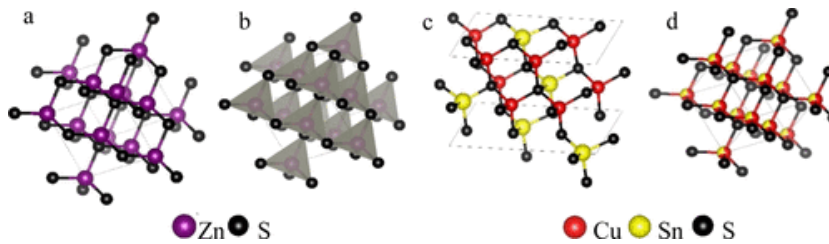

Figure 3.1. ZnS structure (a) with tetrahedral drawn (d) and monoclinic (SG: *Cc*) ordered (a), cubic (SG: *F4̄3m*) disordered (b) CTS.

Both polymorphs show a decreasing k trend with increasing temperature, indicating the presence of a dominating phonon−phonon interaction.[52] However, it is the ultralow thermal conductivity (k < 0.5 W/K m) shown by the disordered polymorph which is particularly interesting[49] and still little studied. Several mechanisms could be at the origin of this much-desired behavior, such as an enhanced phonon scattering because of the increase in crystal symmetry, cation disorder, soft bonds, alloy scattering, and possible suppression of normal phonon

scattering process because of random cations and dopant distribution.[48,51]

In this work, ordered and disordered CTS polymorphs were produced in a highly controlled environment from elemental powders (Cu, Sn, and S) using a high-energy reactive ball-mill, followed by sintering at various temperatures. We started from the experimental results for PF and thermal conductivity for both the phases, stating the higher performance of the disordered form of CTS. Therefore, we have investigated the mechanisms leading to the improvements observed, looking for a full understanding of the CTS system. The work presents a unique mix of experimental analyses and theoretical calculations that can achieve a description of the CTS property depending on the structural phase disorder. We have studied electronic and vibrational properties using density functional theory (DFT) and density functional perturbation theory (DFPT) simulations, respectively. The ab initio calculations provide insights on the possible origin of the ultralow k, which is identified as a distinct behavior of the cations in the disordered structure. By investigating the vibrational density of states (DOS) and phonon dispersion curves and correlating them with the mode Grüneisen parameters (γ_i) and electron localization function (ELF) curves, we unveil the vibrational properties of CTS. Nuclear inelastic scattering (NIS) from Sn provides direct experimental evidence on the vibrational DOS, validating the DFPT results, and in particular, the mechanism underlying the ultralow thermal conductivity of the cubic disordered CTS phase. Moreover, by combining NIS and high-resolution X-ray diffraction (XRD) measurements, Grüneisen parameters were experimentally calculated for the disordered sample. The investigation proposed in this work, covering most of the material

characteristics, can be the base for the design of novel solutions for the development of materials based on CTS with improved TE properties.

3.2 Experimental and computational methodology

3.2.1 Experimental Methods:

Elemental powders of Cu, Sn, and S, procured from Sigma-Aldrich (99% pure) were fed in ball-mill vials made of WC, and anhydrous C2H5OH (100 µlt.) was added to the mixture as a lubricant. High-energy ball- milling Fritsch P4 was used for the milling. The mill was operated for 30 and 60 min, with a fixed main disk and spinning speed of 300 rpm and −540 rpm, respectively. Two circular pellets (thickness ∼1.5 mm, diameter ∼16 mm) were prepared using a manual cold press. One sample was sintered at 500 °C, and the other was sintered at 650 °C, for 2 h in Ar flux. The entire synthesis process was performed in a highly controlled environment (O2 and H2O < 10 ppm). XRD was performed on as-milled powders and sintered disks, in Bragg−Brentano geometry using a Rigaku PMG powder diffractometer equipped with a graphite bent-crystal monochromator, and Cu Kα source operated at 40 kV and 30 mA. The optical properties of CTS polymorphs were investigated using a PerkinElmer spectrophotometer (Perki- nElmer, Milan, Italy), model LAMBDA 750, equipped with a 150 mm integrating sphere. The polycrystalline samples were dispersed in ethanol and sonicated for 1 h, and the optical absorption spectra were collected. Mobility (µ) and carrier concentration (n) were measured with an MMR K-20 and an H-50 measurement system by applying a magnetic field of 6720 Gauss, in temperature range 300−450 K. The absolute Seebeck coefficient (S) was measured using a Pt Standard, while resistivity (ρ) was measured by four-contact measure ments using a Linseis LSR-3 instrument. Thermal diffusivity (D) was measured using a Linseis LFA-500. S, ρ, and D measurements were performed

over the temperature range of 323−723 K. To verify our theoretical findings, we have used NIS with 119Sn nuclear resonance. The method provides the partial phonon-DOS (pDOS) of Sn atoms. Experiments were carried out at the dynamic's beamline P01 at PETRAIII (DESY, Hamburg) using a high-resolution monochromator with 1.4 meV energy resolution at 23.9 keV, the energy of the ^{119}Sn nuclear transition. The measurements were performed on samples with natural enrichment by 119Sn (8.6%) inserted into the closed cycle He cryostat and kept at 43 and 295 K. The nuclear resonance signal was separated in time from electronic X-ray fluorescence and measured using a Si avalanche photodiode detector. This measurement was combined with high-resolution XRD studies of the lattice parameters between 100 and 300 K at the beamline P02.1 at PETRAIII. The combination of the phonon and lattice parameter measurements provides the possibility to obtain the mode Grüneisen parameters.

3.2.2 Computational Methods

The electronic structures were studied using DFT as implemented in the Vienna ab initio simulation package.[61,62] The interaction between the electron ion was described using the projector augmented wave method. The generalized gradient approximation with Perdew−Burke−Ernzerhof (PBE)[26] electron exchange−correlation was employed for band structure and DOS calculations.

The ternary ordered and disordered CTS polymorphs present *Cc* and $F\bar{4}3m$ structural symmetry, respectively. As already pointed out, in the ordered CTS, each S anion is tetrahedrally bonded by four cations (Cu/Sn), forming S− Cu_2Sn_2 and S−Cu_3Sn motifs. The disordered CTS system is possible when the cations (Cu/Sn) randomly replace Zn with an occupancy of 66.66 and 33.33%, respectively, in a diamond- like ZnS structure. This partial occupancy leads to a primitive cell that

cannot be simulated exactly.[57] To satisfy the partial occupancy and respect the stoichiometry, one needs to make large cells that are computationally nonviable to solve. To overcome this limitation, two disordered cells were modelled by a slight alteration of the partial occupancy of Cu and Sn, respectively. The first cell was modelled with Cu (65.625%) and Sn (34.375%), and the second cell was modelled with Cu (68.75%) and Sn (31.25%). Hereafter, the first and second disordered cells are referred to as disordered Sn-rich and disordered Sn-poor, respectively.

The plane wave cut-off and electronic convergence were set to 500 eV and 10^{-6} eV, respectively. All the structures were relaxed until the force on each atom was <0.01 eV/Å, using a Gaussian smearing with σ = 0.05. Two k-point mesh of 4 × 3 × 4 and 4 × 4 × 4 were used for ordered and disordered systems, respectively, using the Monkhorst−Pack technique centered at the Γ-point.[63] For single-point self-consistent field calculation, the tetrahedron method and Blöch corrections[64] were considered. The high symmetry path was provided by Seek- Path.[65] The DOS was calculated on a dense k-mesh of 12 × 12 × 12 and 8 × 8 × 8 grids.

The phonon dispersion curve and pDOS were calculated using the Phonopy code.[29] For DFPT calculations, local density approximation[66] was used with a 10^{-8} eV convergence criteria. These calculations were performed on the ordered supercell (2 × 2 × 2), whereas, for both the disordered cells, a much larger, 64-atom cell was used. The mode Grüneisen parameter (γ_i) was calculated using a quasi-harmonic approximation, by expanding and contracting the relaxed cell volume by ±1%.

3.3 Results

3.3.1 Structural Analysis

XRD measurements were performed on elemental powder milled for 30 and 60 min, and samples were sintered at 500 and 650 °C (shown in Figure 3.2). The 30 min milled powder was observed as a blend of partially formed CTS, binary sulphides (SnS and CuS), and metallic elements (Cu and Sn). With a longer milling time of 60 min, the CTS (SG: $F\bar{4}3m$) formation was complete, although one weak Sn peak ($2\theta \sim 32^{o}$) could still be observed. Because of the use of WC vials for the milling, traces of WC (SG: $P\bar{6}m2$) were present in the as-milled powder. Broad peaks with diffuse background for the as-milled powder suggests the presence of small crystalline domains and a possibly amorphous fraction. As expected, the sintering step increases both crystallinity and grain size. The CTS sample sintered at 500 °C shows a disordered cubic structure alike as-milled CTS, identified by three characteristic peaks at $2\theta \sim 28.5$, 47, and 56°, representing planes (111), (220), and (311), respectively. However, the sample sintered at 650 °C shows three additional peaks located at $2\theta \sim 16$, 18, and 21°, respectively, representing planes (110), ($11\bar{1}$), and (021), characteristic of the ordered monoclinic structure (SG: Cc).

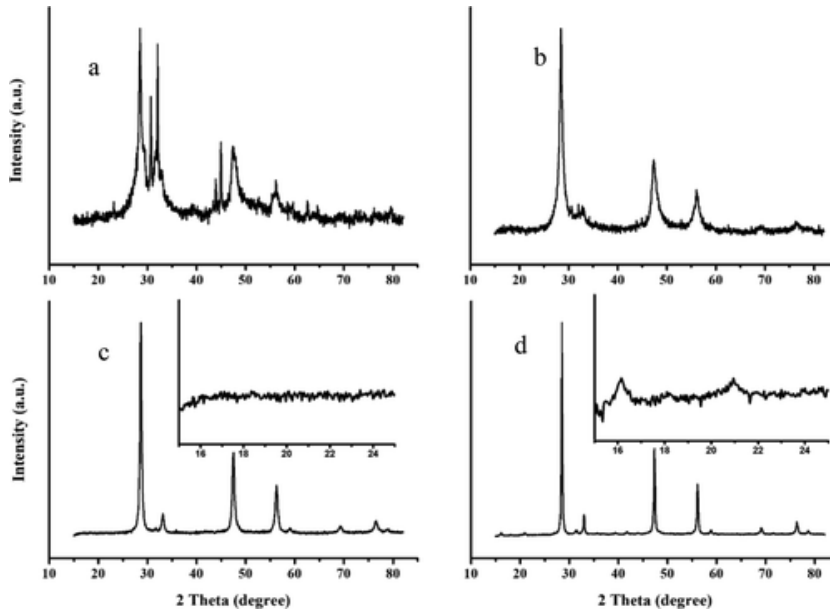

Figure 3.2. XRD pattern of CTS samples after 30 (a), and 60 min milling (b); then, in the sintered disordered (c) and ordered (d) forms. The insets show details of the distinctive peaks of the monoclinic phase.

To confirm the crystallographic structure and to get quantitative information on the crystallite size, the Rietveld refinement[67] was performed using the whole powder pattern modeling[68] approach, as implemented in the recent release of the software TOPAS 7.[69] The underlying assumption is that the crystalline domains are approximated by spheres with a lognormal distribution of diameters. Modeling results are shown in Figure 3.3 and Table 3.1.

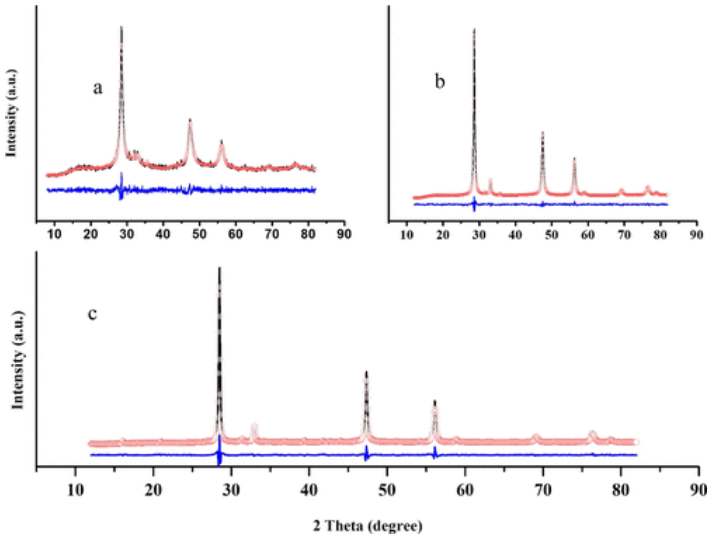

Figure 3.3. Rietveld refinement performed on 60 min milled powder (a), disordered (b), and ordered (c) sintered CTS samples. Experimental data (circle), model (line) and their difference, or residual (line below).

Table 3.1. Lattice Parameter and Average Crystallite Size for 60 min Milled Powder, Disordered, and Ordered Sintered CTS Samples (Figure 3.3 a, b, c, Respectively)

sample	**lattice parameters (±0.01 Å)**	**angle (deg)**	**average crystallite size (±10 nm)**
60 min milled	$a = b = c = 5.44$	$\alpha = \beta = \gamma = 90$	20
disordered	$a = b = c = 5.44$	$\alpha = \beta = \gamma = 90$	50
ordered	$a = 6.66$, $b = 11.5$, $c = 6.66$	$\alpha = \gamma = 90$, $\beta = 109.39$	200

The formation of tin oxides is a known problem for this family of materials, which deteriorates the TE performance in temperature.[70] These oxide phases are hard to eliminate because of the low partial pressure for tin oxide formation.[71] Comparatively, a higher amount (2−5% weight fraction) of tin oxides was observed in CTS samples prepared using binary sulphides (CuS and SnS). Rather, the present

samples prepared from elemental powders (Cu, Sn, and S) processed in a strictly controlled environment do not show the formation of secondary phase oxides in the disordered CTS, which is a substantial improvement from previous studies.[60] Nevertheless, a small amount of SnO2 (<1% in weights) was observed in the ordered CTS.

3.3.2 Electronic Transport:

Figure 3.4a shows the electrical resistivity and Seebeck coefficient for the CTS polymorphs. Both phases show an overall decreasing trend of resistivity with the temperature, while S has positive values and an increasing trend, typical of nondegenerate p-type semiconductors. Nevertheless, the ordered sample shows a decrease in S above ~600 K, likely caused by thermal excitation of bipolarons.[52] The disordered sample presents a lower ~0.99 and ~0.95 eV for the ordered and disordered samples, respectively. A lower band gap promotes a higher carrier concentration, and indeed, the average value of carrier concentration for the disordered sample ($n \sim 1.9 \times 10^{18}$ cm^{-3}) is 10-fold higher than the ordered ($n \sim 2.7 \times 10^{17}$ cm^{-3}). The two polymorphs show similar mobility ($\mu \sim 20$ cm^2/V s) and values compatible with those expected for the stable CTS phase (spanning from 1 to 80 cm^2/V s[72]) (shown in Figure 3.S2, Supporting Information). According to the Mott equation,[34] both n and μ have an inverse relation with the Seebeck coefficient, and this explains the lower S (~320−500 μV/K) for the disordered sample. Overall, above 700 K, the disordered CTS presents a higher PF (~1.5 $\mu W/K^2cm$) than the ordered polymorph (~0.5 $\mu W/K^2cm$); see Figure 3.4b.

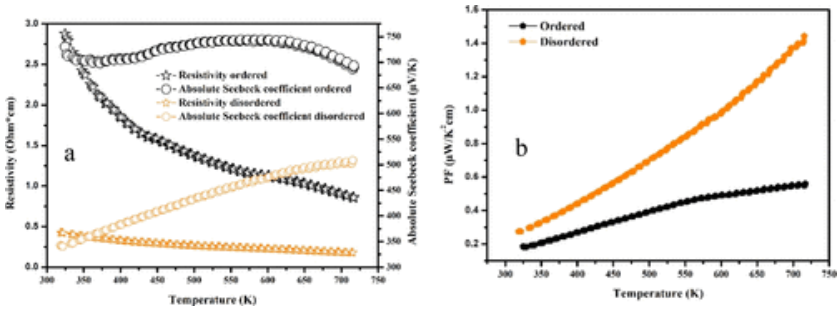

Figure 3.4. Resistivity (star) and absolute Seebeck coefficient (circle) for ordered (black) and disordered (orange) phases (a); corresponding power factor calculated as PF = S^2/ρ for ordered (black) and disordered (orange) CTS (b).

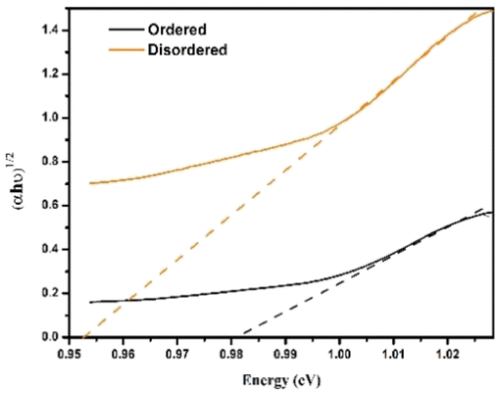

Figure 3.5. Band gap (E_g) estimated by linear extrapolation in the Tauc plot, using the equation $\alpha h\nu = A(h\nu - E_g)^{1/2}$, where α, h, ν, A, and E_g are absorption coefficient, Planck constant, frequency, transition constant, and band gap, respectively (optical absorption spectra is shown in the appendix 2.2.7 file, Figure S 2.2.1).

In order to further understand the differences between the results obtained for ordered and disordered samples, the electronic properties were investigated by DFT. As already pointed out, the ordered structure was simulated with its exact stoichiometry, using 24-atoms (8-Cu, 4-Sn, and 12-S), whereas for the disordered phase, the constraint of occupancy and the structure[57] led us to simulate two slightly off-stoichiometric structures, Sn-rich (21-Cu, 11-Sn, and 32-S) and Sn-poor (22- Cu, 10-Sn, and 32-S), respectively. Total and atomic

projected electronic DOS are shown in Figure 3.6 for both CTS structures.

The total DOS is higher in the valence band (VB) side than in the conduction band (CB), for all the structures, confirming the p-type nature of CTS. In VB, the main contribution to the projected-atomic DOS is given by Cu 3d and S 3p orbitals, whereas the CB is composed of Sn 5s and S 3p orbitals. Band structures are shown in Figure 3.S3 of the Appendix. This for the ordered CTS is in agreement with the literature,[57,73] also showing a largely underestimated band gap value. This is even more relevant for the cubic phase, where no band gap is observed in the DFT results, as it has also been found for analogous simulations of the disordered copper−tin−selenide system.[59] The random distribution of Cu and Sn atoms in the disordered structures causes band tailing, which points out the presence of available states in the DOS curve near the Fermi energy.[55] It is likely that the structures in the gap region and the tailing of the DOS at the Fermi energy play a role in enhancing the carrier concentration, as we observed experimentally. Even if the PBE exchange−correlation tends to underestimate the band gap,[74] the band tailing reduces the band gap, in agreement with the optical absorption results of Figure 3.5.

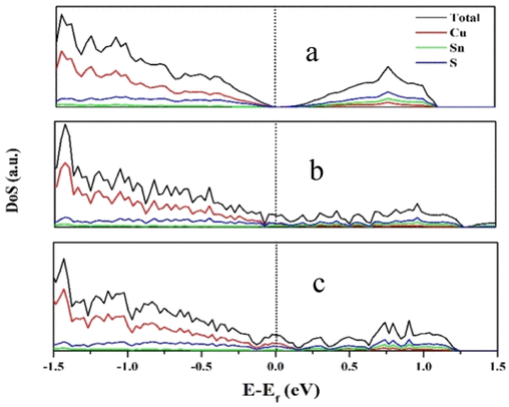

Figure 3.6. Total DOS and atomic projected DOS for ordered (a), Sn-rich disordered (b), and Sn-poor disordered (c) cells; the Fermi energy is shown by the dotted line.

3.3.3 Thermal Transport:

Thermal conductivity was calculated as k = DdCp, where D, d, and Cp are thermal diffusivity, density, and specific heat capacity, respectively. Thermal diffusivity and density were measured using a xenon flash instrument and Archimedes' method, respectively, while the value of Cp was taken from our previous work.[54]

As shown in Figure 3.7, the thermal conductivity of the ordered CTS ranges from 1.0 to 0.45 W/m K, whereas it is ultralow for the disordered CTS, with values 0.45−0.20 W/m K, in the temperature range 323−723 K. The trend of κ decreases with temperature, indicative of increased phonon−phonon interactions. The present values of κ are lower than in CTS prepared by high-temperature solid-state reactions.[49] Reasons are likely related to the bottom-up production method, which limits the grain growth, as well as to a lower density. However, the effect of the lower density on thermal conductivity can be ignored for the comparison between samples of the two polymorphs because they have similar densities (~3.7 g/cm^3), lower than theoretical (~4.85 g/cm^3). Furthermore, near room temperature (T = 323 K), the lattice component

of thermal conductivity was estimated using the single parabolic band (SPB) approximation (calculations used are shown in the Appendix). As it happens in highly resistive semiconductors, the thermal conductivity is dominated by the lattice part. For ordered and disordered samples, the κ_l is ~0.44 and ~0.99 W/m K, respectively; such values are close to the experimentally measured values for total thermal conductivity, confirming the main role of phonon contribution to thermal transport. However, the difference between the values achieved by the two samples suggests a relevant discrepancy in the pDOS for the two structures.

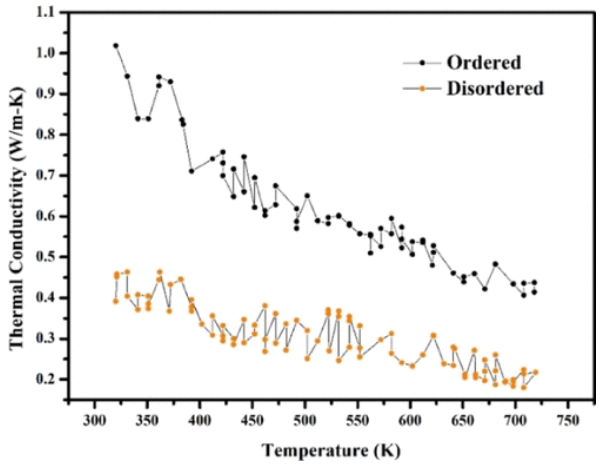

Figure 3.7. Thermal conductivity for CTS polymorphs in the temperature range of 323–723 K.

The phonon dispersion curves were investigated using first principle calculations to shed light on the lower kl of the disordered polymorph. The primitive cell of the ordered CTS has 12 atoms, whereas the disordered cells were simulated with 64 atoms. Therefore, the phonon dispersion curves show 3N (N = number of atoms), 36 and 192, branches of vibrational modes, respectively (see Figure 3.8a−c). Three low-frequency modes are acoustical, rest (3N-3) of the branches correspond to the optical modes. The low-frequency modes in all three

cells are dominated by heavy Cu and Sn, while S, a much lighter atom, dominates the high-frequency modes. The difference in atomic-projected pDOS can be observed in a frequency of < 1 THz, in ordered and Sn-poor cells; these modes are dominated by Cu vibrations, whereas Sn vibrations dominate in the Sn-rich cell.[75] The acoustic modes in the disordered Sn-rich cell are softer as compared to the ordered. Additionally, simulations show a weak bonding and a strong anharmonicity along the Γ−M and Γ−Z directions,[76] whereas these effects are less evident for the Sn-poor cell. The vibrational modes for the disordered cells are shifted to lower frequencies (see Figure 3.8d), and the gap between low- and high-lying optical modes is narrower with higher population of low-lying optical modes. Moreover, optical modes cut the acoustical modes at a lower (~1.1 THz) frequency in the disordered cells than in the ordered (~1.9 THz), suppressing the lattice thermal conductivity by scattering the heat-carrying acoustic modes.[75]

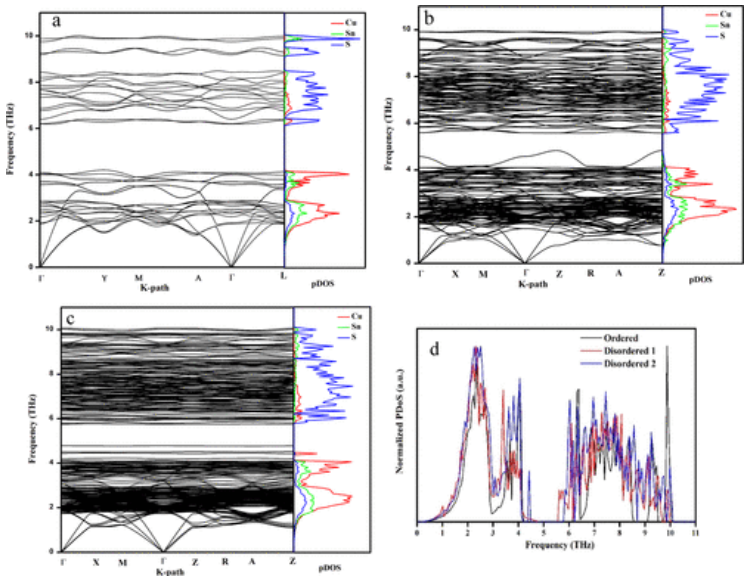

Figure 3.8. Phonon dispersion curves (ω *vs k*) and atomic-projected pDOS for ordered (a), disordered Sn-rich (b), disordered Sn-poor (c) cells, and a comparison among normalized total pDOS (d).

The optical phonon branches in the disordered cells are flatter than the ordered cell, suggesting a lower group velocity of optical phonons. The mode level phonon group velocity ($v_g = d\omega/dk$) is shown in Figure 3.S4 of the Supporting Information file. The acoustic modes of all three cells show a similar $v_g \sim 50$ THz Å. However, the experimentally obtained k for the disordered CTS has an approximately twofold lower value than that of the ordered, which cannot be explained in terms of a lower Vg only. This suggests the possibility of heat being trapped in low-velocity optical modes, as discussed with the phonon dispersion curves.[77]

Moreover, a strong anharmonic effect in bonding contributes to a low lattice thermal conductivity. The mode Grüneisen parameter (γ_i), shown for all cells in Figure 3.9 is a measure of lattice anharmonicity, as it reflects the extent of deviations of phonon vibrations from the harmonic oscillations.

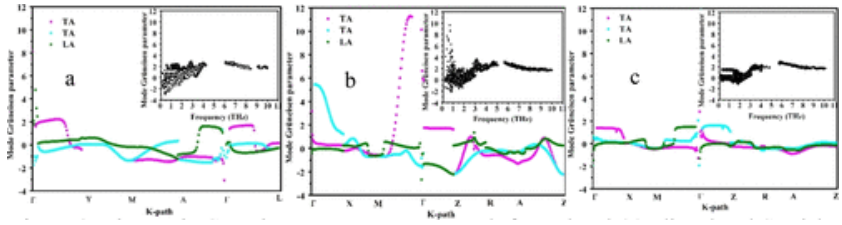

Figure 3.9. Mode Grüneisen parameter *vs K*-path for ordered (a), disordered Sn-rich, (b), and disordered Sn-poor (c) cells; the corresponding Grüneisen parameter *vs* frequency (ω) is shown in the insets.

For all cells, the fluctuation in the values of the mode Grüneisen parameter decreases for increasing frequency (shown in the insets of Figure 3.9), indicating a weak interaction between different vibrations at higher frequencies.[78] The Sn-rich cell shows a much higher mode Grüneisen parameter, whereas comparatively lower values were observed for the ordered and Sn-poor cells, suggesting the anharmonicity in the disordered structures is highly dependent on the

concentration of Sn-atoms. It is worth noting that the stoichiometry of the disordered Sn-rich system is closer to the exact CTS than that of the Sn-poor cell.

The atomic bonds were investigated by the ELF plots (Figure 3.10). Cu−S and Sn−S bonds show an ionic and covalent nature, respectively.[79] All Sn-atoms have similar electron localization (Figure 3.10a) in the ordered cell because of the regular arrangement of S−Cu_2Sn_2 and S−$CuSn_3$ motifs. However, a variation in electron localization is observed in the disordered cells (Figure 3.10 b,c), indicating the inhomogeneous nature of Sn−S bonds[80] (see Figure S5 of the Supporting Information file for the contribution of every Cu and Sn atom to the atomic pDOS). In low frequencies (1−3 THz), an identical contribution of Sn can be observed for the ordered cell, whereas it is dispersed for disordered cells. These observations suggest a distinct nature of Sn atoms in the disordered cells, that might scatter phonons more efficiently than in the structure of the stable ordered CTS.

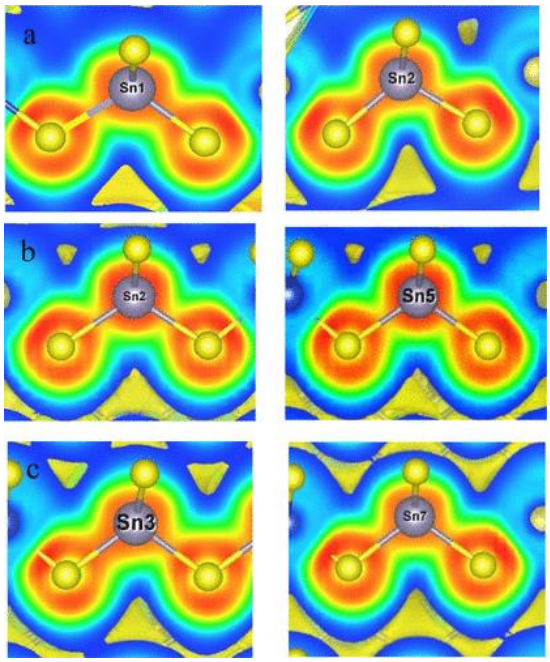

Figure 3.10. Magnified view of ELF plots for Sn atoms in ordered (a), disordered Sn-rich (b), and disordered Sn-poor (c) cells.

To validate the above conclusions on the Sn pDOS obtained by DFPT, NIS experiments (Figure 3.11) were performed at 43 K on both samples; an additional measurement was performed on the disordered sample at 295 K. The Debye energy was calculated by fitting the reduced pDOS (pDOS/E^2) in the range 0.5−1.2 THz, using the parabolic function, pDOS(E)/E^2 = 3/E_D^3 + bE^2 , where E, ED, and b are energy, Debye energy, and a fitting parameter, respectively.[81] The Debye energy together with other parameters obtained from Sn pDOS are presented in Table 3.2.

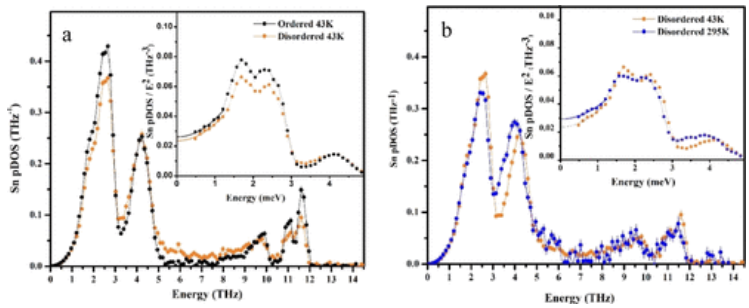

Figure 3.11. Sn pDOS-ordered and disordered CTS samples at 43 K (a) and disordered CTS samples at 43 and 295 K (b). Reduced Sn pDOS plots are shown in the inset for both figures.

Table 3.2. Parameters Obtained from the Sn VDOS of the Samples Measured at 43 and 295 K: The Lamb–Mössbauer Factor (f_{LM}), the Sn Atomic Displacement Parameter (U_{eq}), the Mean Force Constant (F), the Debye Energy (E_D), and the Mean Sound Velocity V

	f_{LM}	U_{eq} (A^2)	F (N/m)	E_D (THz)	V (km/s)
ordered at 43 K	0.754 (1)	0.00180 (2)	224 (2)	5.13 (5)	2.69
disordered at 43 K	0.769 (1)	0.00193 (2)	221 (1)	5.02 (5)	2.81
disordered at 295 K	0.291 (4)	0.00844 (5)	196 (5)	4.67 (5)	2.62

The experimentally observed trend of Sn pDOS at 43 K agrees with the theoretical results for both samples. The disordered sample shows a broad phonon band (5−9 THz), consistently with the atomic-projected pDOS and individual atomic pDOS of Figure 3.8. The value of the Debye energies and mean sound velocities (see Table 3.2) are similar for both polymorphs, suggesting similar group velocities, as observed from mode level group velocity calculations.

The NIS measurement performed at 295 K on a disordered CTS sample reveals significant phonon mode softening for the acoustical part of the pDOS and a higher Debye level compared with the low T measurement. The relative energy shifts ΔE/E of the specific peaks can be obtained from the pDOS measured at 43 and 295 K using the procedure described in refs [82] and [83]. XRD measurements were performed from 300 to 100 K with a step of 20 K (shown in the Supporting Information file), and the relative volume change ΔV/V = 0.0065 between 43 and 295 K was estimated by fitting a parabolic function (see Figure 3.12b). Thus, using both relative volume and energy change Grüneisen parameters for specific phonon peaks were obtained and are shown in Figure 3.12a, which agrees with the results obtained via ab initio calculations presented in Figure 3.9. In particular, the high Grüneisen

parameter was observed for the 0 energy and 4 THz peak. The 0-energy value of the Grüneisen parameter was obtained by comparison of the Debye energy.

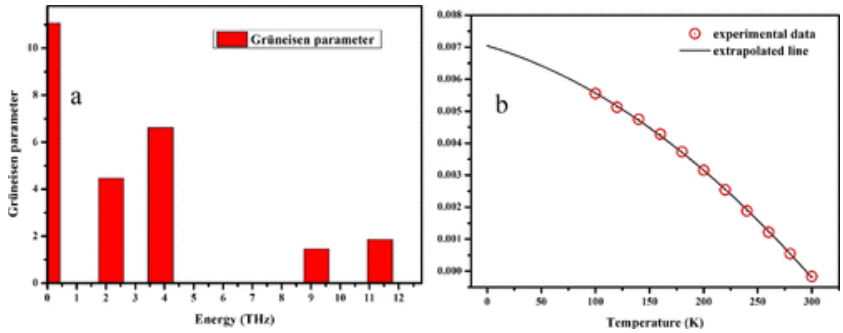

Figure 3.12. Grüneisen parameters of the specific phonon peaks of the disordered compound obtained from the NIS measurements at 43 and 295 K (a) and relative volume change $\Delta V/V_{295K}$ from the XRD data collected in temperature range 300–100 K (b).

Hence, from the analyses performed on the samples and the good agreement achieved with the theoretical calculations, the ultralow thermal conductivity in the disordered sample is shown to be because of the random arrangement of Sn and Cu atoms, which not only blocks the normal phonon scattering but also shows strong anharmonicity for the inhomogeneous nature of the Sn−S bonds. The low-lying optical modes support acoustical-optical phonon scattering, and the higher value of the Grüneisen parameter obtained from DFPT and NIS results confirm the higher anharmonicity in the disordered structure. However, a lower mode Grüneisen parameter was observed in the Sn-poor cell, suggesting that anharmonicity in the disordered system is largely dependent on the Sn-atoms. Moreover, a small crystallite size (< 100 nm) and the coexistence of secondary phases (WC, SnO, and SnO2) should also serve to additional phonon scattering.

The results achieved up to here are well summarized combining the electric and thermal transport properties in the dimensionless figure of merit, zT (Figure 3.13). For the ordered sample, zT ~ 0.05 is in agreement with the values commonly reported in literature,[51] whereas zT ~ 0.5 was observed for the disordered CTS polymorphs above 700 K, which is fairly high for an undoped material.[36] In particular, as demonstrated by our results, the enhanced zT for the disordered CTS is an attribute of its high PF and ultralow thermal conductivity.

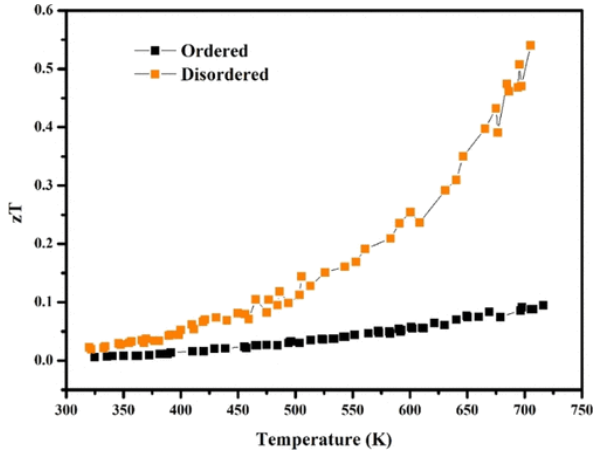

Figure 3.13. Calculated *zT* for ordered and disordered CTS samples.

3.4 Conclusion

In this work, a study of the dependence of TE properties of CTS by structural characteristics has been presented. In particular, the effect of structural disorder on electronic and thermal transport properties have been investigated, taking advantage of different experimental techniques. The disordered CTS polymorph shows a better TE performance than the ordered and stable CTS phase, mainly because of an enhanced carrier concentration and ultralow thermal conductivity observed in the former phase. In the present study, we have experimentally determined Seebeck coefficient, resistivity, and thermal

conductivity and correlated them with the band gap, mobility, and carrier concentration obtained also from experimental measurements. First-principle simulations disclose the presence of low-lying optical modes in the disordered cubic structure, with significant variation in the Sn bonding, leading to a strong anharmonicity. A variation in values of the mode Grüneisen parameter for Sn-rich and Sn-poor disordered cells confirms that the anharmonicity is dependent on the Sn-atoms. The overall picture emerging from DFT and DFPT simulations finds confirmation in NIS experiments, as the Sn-pDOS agrees with the ab initio results. NIS experiments performed at low (43 K) and near-room temperature (295 K) show evidence of a strong anharmonicity, presence of softer modes, and a higher Debye level in the disordered polymorph. The results presented in this work cover most of the material characteristics providing a detailed understanding of the mechanisms promoting a relevant improvement in TE properties of CTS-based materials. In particular, the structural disorder results to have a major impact on the enhancement of material performance. Therefore, these results suggest the strategy for the design of novel solutions for the development of materials based on CTS with improved TE properties.

Appendix:

The optical absorption spectra for the ordered and disordered CTS samples.

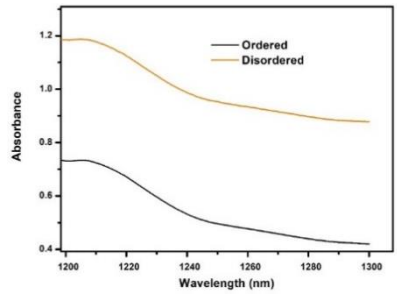

Figure 3.S1. optical absorption spectra for the ordered and disordered CTS samples.

Carrier concentration (n) and mobility (μ) measured from in temperature range 300-450 K:

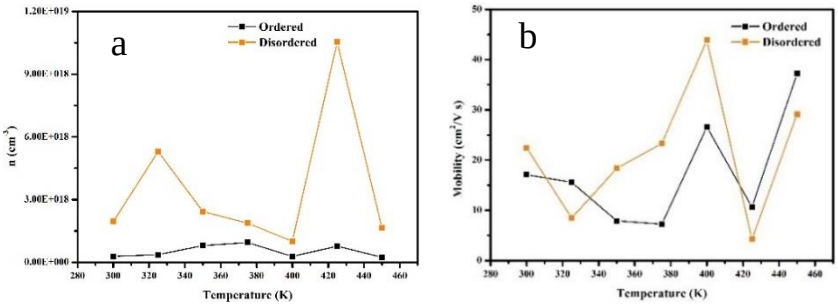

Figure 3.S2. Carrier concentration (a), and mobility (b) for ordered and disordered CTS samples.

Band structures: Band structures for the ordered , Sn-rich disordered, and Sn-poor disordered cells are shown in figure 3.S3, the band structures for the Ordered CTS are in agreement with the literature [8444].

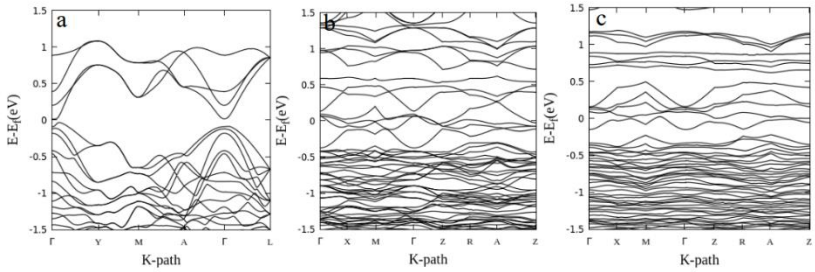

Figure 3.S3. Band structures for ordered (a), Sn-rich disordered (b), and Sn-poor disordered (c) cells.

Mode level phonon group velocity (v_g): The mode level phonon group velocity ($v_g = d\omega/dk$) curves are shown in figure 2.2.S4. Three low frequency (< 2 THz) peaks green, orange, and blue are corresponding to the acoustical modes, showing a similar v_g, for all three cells.

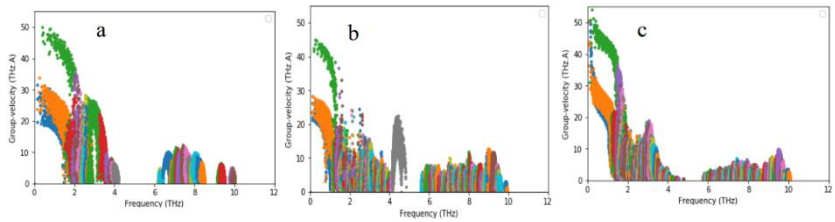

Figure 3.S4. Mode level phonon group velocity (Vg) vs. frequency (ν) plots for ordered (a), Sn- rich disordered (b) and, Sn-poor disordered (c) CTS cells.

The contribution of every Cu and Sn atom on individual atomic pDOS is shown in figure 3.S5.

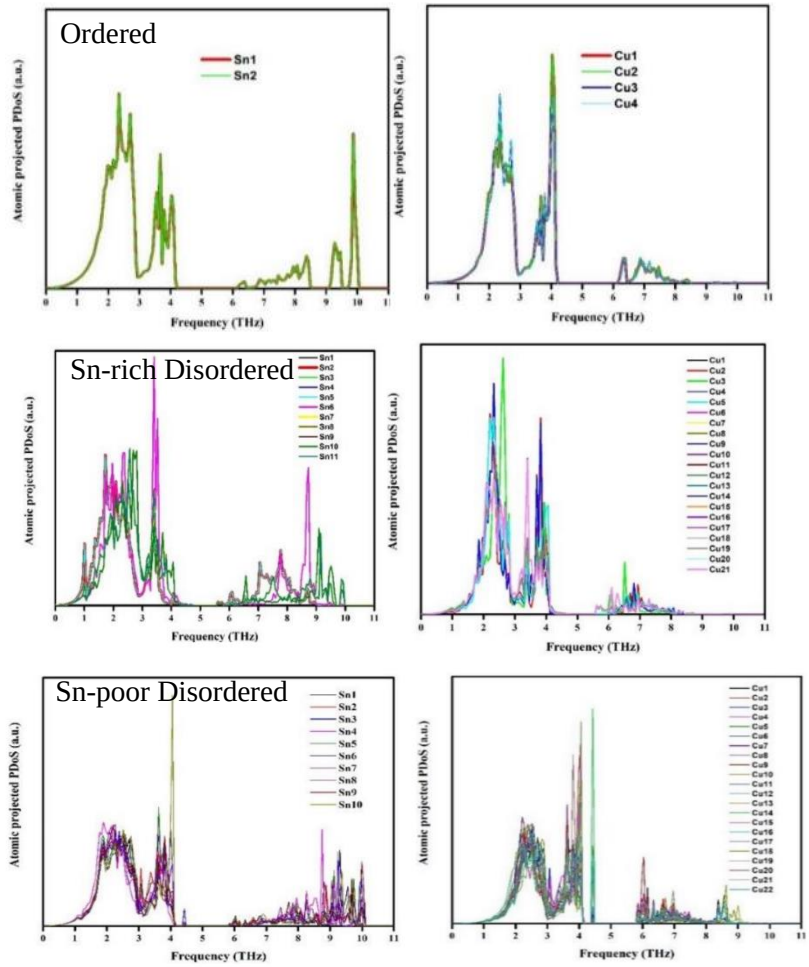

Figure 3.S5. Each Sn and Cu atom contribution in the individual pDOS for ordered, Sn-rich disordered, and Sn-poor disordered CTS cells.

Lattice thermal conductivity (κ_l) calculations using Single Parabolic Band (SPB) approximation:

Total thermal conductivity: $\kappa = \kappa_e + \kappa_l$

Electronic thermal conductivity: $\kappa_e = \kappa - \kappa_l$

Wiedemann-Franz law: $\kappa_e = LT\sigma$

We have estimated the Lorenz number, L, by fitting the Seebeck coefficient (S) to the reduced chemical potential.

$$L = \left(\frac{k_B}{e}\right)^2 \frac{3F_0(\eta)F_2(\eta) - 4F_1^2(\eta)}{F_0^2(\eta)}$$

$$S = \left(\frac{k_B}{e}\right)\left(\frac{2F_1(\eta)}{F_0(\eta)} - \eta\right)$$

$$F_n(\eta) = \int_0^\infty \frac{x^n}{1 + e^{x-\eta}}\, dx$$

Where k_B, e, η, *and* $F_n(\eta)$ are Boltzmann constant, charge of electron, reduced Fermi energy, and Fermi integral of order n, respectively [85].

High-resolution X-ray diffraction studies of the lattice parameters in the temperature range 295 K to 100 K at the beamline P02.1 at PETRAIII synchrotron source: High-resolution X-ray powder diffraction data were collected at a wavelength of 0.20761 Å on a disordered CTS sample in a glass capillary with 0.8 mm diameter (manufacturer WJM, Berlin). The sample was spun during the measurement and cooled with an Oxford Cryostreamer. The beam size was 1x1 mm². Data was collected on PerkinElmer XRD1621 area detector (200×200 μm^2 pixel size, 2048 x 2048 pixel area). The 2D data sets were azimuthally

integrated to 1D data using the DAWN Science package[86]. The lattice parameters of the disordered CTS sample were then determined by Rietveld refinements using the TOPAS software.

Table 3.S1. Lattice parameter (a) and cell volume (V) for the disordered (cubic) CTS in temperature range 300 K to 100 K.

Temperature	**Lattice Parameter**		**Cell Volume**	
K	a (Å)	e.s.d.	V (Å^3)	e.s.d.
300	5.43614	2.80E-04	160.64699	0.02444
280	5.43485	2.70E-04	160.53262	0.02408
260	5.43364	2.70E-04	160.42521	0.02374
240	5.43243	2.60E-04	160.31784	0.02332
220	5.43123	2.60E-04	160.212	0.02292
200	5.43012	2.60E-04	160.11347	0.02256
180	5.42907	2.50E-04	160.02093	0.02225
160	5.42806	2.50E-04	159.93181	0.02196
140	5.42722	2.40E-04	159.85763	0.02156
120	5.42654	2.40E-04	159.79713	0.02133
100	5.42576	2.40E-04	159.72824	0.02095

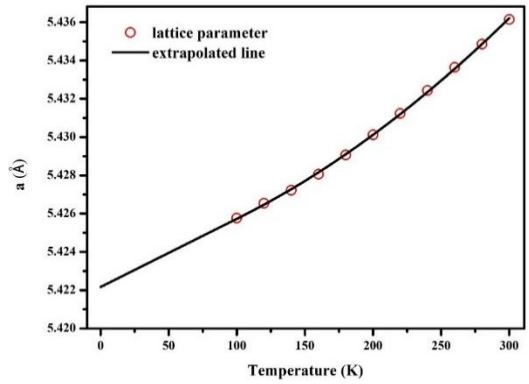

Figure 3.S6. The lattice parameter of disordered (cubic) CTS in temperature range 300K to 100 K shown in table 2.2.S1 with a parabolic fit.

4. Effects of Grain Size on the Thermoelectric Properties of Cu_2SnS_3:An Experimental and First-Principles Study

This section is taken from[32]: Lohani, K.; Nautiyal, H.; Ataollahi, N.; Maji, K.; Guilmeau, E.; Scardi, P. "Effects of Grain Size on the Thermoelectric Properties of Cu_2SnS_3: An Experimental and First-Principles Study. ACS Appl. Energy Mater. 4 (11), 12604–12612. https://doi.org/10.1021/acsaem.1c02377."

*Correspondence: paolo.scardi@unitn.it

Abstract

Cu−Sn-based sulphides are earth-abundant and nontoxic compounds of special interest for low-cost energy harvesting applications. In the present work, we have investigated the effect of grain size on the thermoelectric properties of Cu_2SnS_3 (CTS). Three dense CTS samples with nanometric grains were produced by mechanical alloying combined with spark plasma sintering, preserving the small size of crystalline domains to 12, 25, and 37 nm, respectively. The experimental results show that the Seebeck coefficient (S) and electrical resistivity (ρ) decrease with decreasing domain sizes, while the thermal conductivity (κ) increases. A smaller domain size correlates with a lower resistivity and a degenerate semiconductor-like behavior due to higher carrier concentration. At the same time, our synthesis method leads to materials with very low lattice thermal conductivity, thanks to the nanometric size of grains and structural disorder. As a result, the sample with the smallest grain size exhibits the highest zT of ∼0.4 at 650 K. First-principles density functional theory (DFT) simulations on various CTS crystallite surfaces revealed localized states near the Fermi

level and the absence of band gap, indicating the metallic nature of the surfaces. Various CTS systems were tested by DFT, showing the following order of increasing formation energy: stoichiometric CTS, Cu vacancy, Cu-rich, Sn vacancy, and Sn-rich.

4.1 Introduction

Most commercially available thermoelectric (TE) devices use toxic and scarce materials, making them expensive and potentially hazardous, for example, Sb_2Te_3, Bi_2Te_3, and so forth. In recent years, the search for high-performance, nontoxic, ecofriendly, and earth-abundant TE materials has led to the exploration of multinary sulfides.[34,87] Chalcogenides[88], colusites,[89,90] and other metal-based sulfides[91,92] could be viable alternatives to existing materials[93]. Cu-based sulfides have low formation energy so that it is possible to produce them by short-period reactive milling using a planetary or vibrating mill. As also shown in the present work, high-energy reactive ball milling, also called mechanical alloying, can be employed with success to synthesize new and disordered phases. In addition, milling offers the advantage of facile and scalable production for industrial use.[94]

The energy conversion efficiency of a TE material is determined by a dimensionless figure of merit (zT) expressed as $zT = S^2/\rho\kappa^*T$, where S, ρ, κ, and T are the Seebeck coefficient, electrical resistivity, thermal conductivity, and absolute temperature, respectively. S^2/ρ is referred to as the power factor (PF). The Seebeck coefficient and electrical resistivity are strongly dependent on the carrier concentration (n), mobility (μ), and effective mass of the charge carriers (m^*) (see equation 4.1 and 4.2 below). A low carrier concentration and high effective mass of charge carriers can increase the Seebeck coefficient, but it also penalizes the electrical conductivity (σ) and vice versa[34,95]

$$S = Am^*(\frac{\pi}{3n})^{\frac{2}{3}}T \ldots (4.1)$$

$$\sigma = ne\mu \ldots (4.2)$$

$$\kappa_e = \frac{LT}{\rho} \ldots (4.3)$$

where A, e, and L represent a constant, charge of an electron, and the Lorenz number, respectively.

Besides high PF, TE materials also require low thermal conductivity (κ), composed of a lattice (κ_l) and an electronic contribution (κ_e), combined as $\kappa = \kappa_l + \kappa_e$. The lattice contribution can be decreased by increasing the grain boundary density, vacancies, defects, impurities, strain, and so forth. Differently, κe shows a strong dependence on the electrical resistivity, as in the Wiedemann–Franz law (see eq 3).[90] More recently, the determination of the TE quality factor (β) given by $\beta \propto \mu_0 m_{dos}^{*3/2}/\kappa_l$ (where μ_0 and m_{dos}* are the nondegenerate mobility and density of state effective mass, respectively) is in practice for the simultaneous optimization of all TE parameters.[96,97]

$Cu_{2+x}Sn_{1-x}S_3$(CTS) polymorphs are studied for many applications such as photovoltaics, transistors, LEDs, and TE materials. A recent study has also suggested a potential use of CTS quantum dots for photodetector applications.[98] CTS polymorphs have been extensively studied as *p*-type TE materials showing moderately high PF with high or low thermal conductivity, depending on whether the crystal structure is ordered or disordered.[60,85,99] To increase the TE performance, different cationic substitutions have been investigated with the aim to tune the carrier concentration and to introduce structural disorder. Among the various studies, Zhao et al. have reported the highest $zT \sim 0.9$ (at $T > 700$ K) so far by simultaneous cobalt and antimony doping.[50]

Zhai et al.[84] and Shigemi et al.[73] have shown that the hybridization of Cu *3d* and S *3p* orbitals in the valence band (VB) is responsible for the p-type nature of CTS. Heavy acceptor doping due to unfilled *d*-orbitals of Co,[52] Cu,[100] Ni,[50] Fe,[51] and Mn[49] enhances the density-of-state (DOS) effective mass of carriers (holes) and electrical conductivity, resulting in a high $PF \sim 10$ $\mu W/cmK^2$ around 700 K. Cationic substitution also transforms the CTS crystal structure from ordered (monoclinic *Cc*),[101] to tetragonal $I\bar{4}2m$ and disordered (cubic: $F\bar{4}3m$).[85] In most of the cases, a mixture of different phases is obtained. Deng et al.[100] have shown the influence of the Cu/Sn ratio in $Cu_{2+x}Sn_{1-x}S_3$ on the electrical and thermal properties. More recently, Pavan Kumar et al.[99] have discovered a new ordered monoclinic structure $Cu_5Sn_2S_7$ by increasing the Cu/Sn ratio up to $x = 0.15$, leading to a specific ordering of Cu and Sn in the structure. In summary, the hole doping in CTS compounds, induced by the substitution of Cu, Sn, or S by aliovalent cations, or by Cu for Sn substitution, increases the carrier concentration. Disordering phenomena, usually induced by the cationic/anionic substitution, scatter the phonon waves more effectively, resulting in a higher TE figure of merit.

The disordered cubic CTS and Cu_2SnSe_3 (CTSe) phases can also be produced and stabilized without chemical alteration.[32,59,60] The optical absorption measurements revealed a lower band gap for the disordered CTS/Se polymorphs. The lower band gap enhances the carrier concentration, resulting in a higher PF compared to its ordered polymorph. Furthermore, in a theoretical study, Baranowski et al.[102] have also reported band tailing and midgap states for the disordered CTS phase.[32,102] The structural disorder introduces potential energy fluctuations in the lattice that allow energy levels within the forbidden gap, responsible for the band tailing and reduced band gap.

Moreover, Dahule et al.[103] have studied the electronic structure properties of (200) and (−131) surfaces of monoclinic CTS and have shown their metallic character. It is worth mentioning that the metallic character was confirmed using different potentials, including the Heyd–Scuseria–Ernzerhof potential, which results in a better estimation of the band gap.

In terms of synthesis, the literature suggests a three-step top-down approach to produce CTS samples for TE applications. First, CTS is produced from the elemental powders (Cu, Sn, S, and dopant elements) using an extended high-temperature solid-state reaction[85]. In the second step, the grain size is sometimes reduced by ball milling. Finally, high-density pellets are produced using spark-plasma sintering (SPS) or hot pressing. This approach results in highly crystalline materials with average domain sizes ranging from half to several microns. This synthesis method requires a long annealing time at high temperatures, which is time- and resource-consuming.

Alternatively, CTS compounds, as many other Cu-based sulfides, can be produced by combined high-energy reactive ball milling (mechanical alloying) and SPS or hot pressing.[99,104] Mechanical alloying allows us to produce fine, homogeneous, precrystallized, and highly reactive powders, which usually lead to high-purity, crystalline, and dense samples after sintering with small grain and crystallite sizes. Furthermore, a highly dense disordered CTS polymorph can be stabilized without any chemical substitution.[94]

The present work aims to shed light on the degenerate semiconductor-like behavior of nanocrystalline CTS samples. Three dense CTS samples were produced using powder synthesized by high-energy reactive ball milling and SPS. We have investigated the effects of grain size on the TE properties. Structural and microstructural analyses suggested a stoichiometry deviation in CTS phases sintered at low

temperature, together with a very small crystallite and grain size. Ab initio calculations using density functional theory (DFT) indicated the metallic nature of CTS surfaces, leading to a degenerate semiconductor-like trend with temperature. Further evidence is presented on the formation energies for various CTS systems with vacancies and chemical deviations.

4.2 Experimental and computational methodology

4.2.1 Experimental Methods

Elemental powders (Cu, Sn, and S) were weighted in a stochiometric ratio and fed in WC vials with WC balls. A Fritsch PULVERISETTE-4 mill was operated for 1 h, producing ~6 g of the as-milled CTS powder. The entire production process was performed in a glovebox with an argon-filled environment. During the milling, no lubricant was introduced to avoid any contamination. The production of CTS powder by high-energy ball milling of elemental powders and binary sulfides is discussed in detail elsewhere.[32,105]

The as-milled powder was sintered using a SPS machine (FCT HPD 25) at various temperatures and pressures to optimize the sintering conditions (Table 4.1). The relative densities of the samples are 86, 96, and 94% for sample A, B, and C, respectively.

Table 4.1. Sample Names, sintering conditions, densities, phase purity, and average grain size for various CTS samples.

Sample name	Sinte-ring die	Sinte-ring pressure (MPa)	Sinte-ring temp. (°C)	Dwell time (min)	Den-sity (g/cm^3)	Weight fraction (±1%)		Avera ge domai n size (±10 nm)
						CTS	SnO_2	
A	WC	500	400	60	4.06	99	1	12
B	graphite	64	512	30	4.52	100		25
C	graphite	64	500	30	4.45	99	1	37

Structural analysis was performed using X-ray diffraction (XRD). XRD data were collected in *θ/2θ* Bragg–Brentano geometry using a PANalytical X'Pert Pro diffractometer equipped with a *Cu Kα (λ = 1.5406 Å)* source. Micrographs and energy-dispersive X-ray (EDX) spectroscopy analyses were collected using a JEOL JSM 7200F scanning electron microscope equipped with an EDX X-Flash Bruker detector.

The electrical resistivity (ρ) and Seebeck coefficient (S) were measured simultaneously from 300 up to 700 K on bar-shaped samples of typical dimensions 2 × 3 × 10 mm^3 using an ULVAC-ZEM3 instrument under partial helium pressure. A NETZSCH LFA-457 apparatus was used for measuring the thermal diffusivity under argon flow. The thermal conductivity (κ) was determined as the product of the geometrical density, the thermal diffusivity, and the theoretical heat capacity using the Dulong–Petit approximation. The lattice contribution to the thermal conductivity (κ_l) was determined by subtracting the estimated electronic component (κ_e) from the measured total thermal conductivity, κ. The measurement uncertainties are estimated to be 6% for the Seebeck

coefficient, 8% for the electrical resistivity, 11% for the thermal conductivity, and 16% for the final dimensionless figure of merit.

Hall effect measurements at RT were carried out using a physical property measurement system (Quantum Design) under an applied magnetic field of 9 T.

4.2.2 Computational Methods

The electronic structure calculations were performed using DFT as implemented in the Vienna ab initio simulation package[61,62]. The interaction between electrons and ions was described using the projector-augmented-wave (PAW) method. The generalized gradient approximation with Perdew–Burke–Ernzerhof [26] electron exchange–correlation was used for the calculations.

We have performed the calculations for (001), (010), and (100) slabs of monoclinic CTS and two disordered CTS cells with sulfur termination. We considered two cases for the disordered cell, one with the Cu-rich and the other with Sn-rich atomic layer below the terminating sulfur layer. For all the calculations, CTS stoichiometry was preserved. A vacuum of 15 Å was created to minimize the interaction between the periodic copies. In the disordered cells, the atoms of the lower four layers were fixed in a position, whereas the atoms of the upper four layers were free to move. Relaxation was performed with a plane-wave kinetic energy cutoff and an electronic convergence of 350 and $10–5$ eV, respectively. The involvement of core electrons was seized by freezing. Only $3d_{10}4s_1$, $4d_{10}5s_25p_2$, and $3s_23p_4$ electrons were treated as valence electrons for Cu, Sn, and S, respectively. The cell parameters were fixed, whereas the atomic position was allowed to change for relaxation. The electronic convergence was set to 10^{-6} eV for DOS

calculations. Brillion zone sampling was performed on a k-point grid of 9 × 9 × 1 and 5 × 5 × 1 for monoclinic slabs and disordered cells, respectively. The k-mesh was reduced for the disordered cell due to its larger size.

The formation energy calculations were performed on Cu-rich, Cu-vacant, Sn-rich, and Sn-vacant cells. For these calculations, the plane wave kinetic energy cutoff and electronic convergence were changed to 400 and 10^{-6} eV, respectively. A Monkhorst–Pack[63] k-point mesh of 7 × 7 × 7 (centered at the gamma point) was used to integrate the Brillion zone. One atom was removed from the supercell, and the remaining atoms were allowed to relax for the vacancy calculations. The off-stoichiometry calculations were performed on a supercell of 72 atoms with a stable monoclinic phase, where one Cu atom was replaced by one Sn atom and vice versa, respectively, for the Sn-rich and Cu-rich simulations.

4.3 Results and Discussion

XRD patterns collected on the as-milled powder with increasing milling times are shown in Figure 4.1. Due to its low formation energy, short milling of 15 min led to the formation of binary sulphides, especially CuS. As the milling time was increased to 30 min, the appearance of diffraction peaks of sphalerite-type structures can be noticed. However, unreacted SnS and Sn powder were still present in the sample. With the further increase of the milling time to 1 h, the as-milled powder showed four broad diffraction peaks, implying the formation of a sphalerite-type crystal structure. It is worth mentioning here that, among all the elements, Sn incorporated last in the CTS system. Broad Bragg-peaks with diffuse backgrounds imply that the one-hour milled powder consists of less crystalline CTS grains with a small domain size.

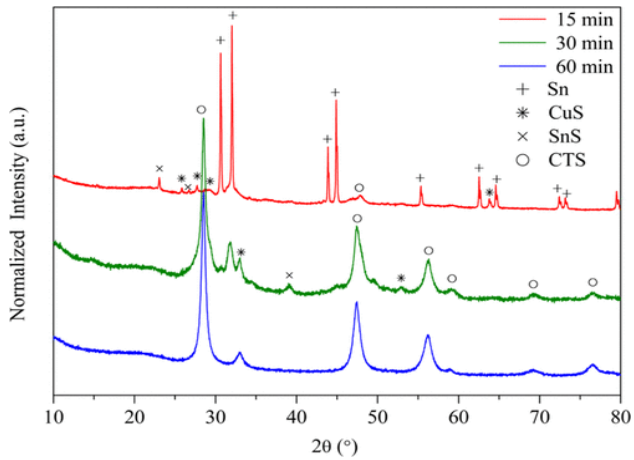

Figure 4.1. XRD patterns for the powder milled for 15, 30, and 60 min.

SEM−EDX data collected on 60 min milled powder at full frame image showed the presence of stoichiometric CTS. On the same sample, various micrographs and EDX data were collected at different magnifications from different parts of the SEM grid. It indicated that the as-milled powder has a nonhomogeneous chemical distribution with a small domain size, which tends to agglomerate in larger particles (Figure 4.S1).

High-density bulk CTS samples were produced by SPS under different sintering conditions (listed in Table 4.1). Sintered samples maintained the same Bragg-peak positions as the as-milled powder. However, sharper Bragg peaks for sintered samples indicate an increased crystallinity and crystallite size. XRD line profile analysis was performed by the Rietveld method[106] using Topas 7 software.[69] We employed the whole powder pattern modeling macro[68] to simulate the peak profile. The instrumental profile was obtained from a LaB_6 standard sample.[107] A nine-point Chebyshev polynomial and a $1/x$-function were used to simulate the background and low-angle intensity, respectively. Subsequently, zero shift and other parameters

were systematically refined.[67] During the refinement, the variation of the Debye–Waller coefficients (thermal factors) was restricted between 0 and 2 for all atoms. For all the samples discussed below, the goodness of fit was ~1.1–1.3.

Disordered CTS has a zinc-blende (ZnS)-like (cubic) close-packed face-centered structure, which arranges its atoms in the (216) space group. The *4a* Wyckoff position is occupied by Cu and Sn atoms with occupancy 2/3 and 1/3, respectively, while the 4*c* site is occupied by S atoms with occupancy 1. The lattice parameter, phase density, and cell volume determined from Rietveld refinement were 5.43 Å, 4.71 g/cm^3, and 160.50 Å^3, respectively. No microstrain was observed for any sample. The average domain size and the weight fraction of CTS and secondary phases are listed in Table 4.1 for different sintering conditions. All the samples showed disordered cubic CTS structures. However, a small amount (weight fraction <0.5%) of SnO_2 was observed for samples A and C. For sample B (see Figure 4.2 (a)), two Bragg peaks around $2\theta \sim 16$ and ~31° were observed. Sample B may have a small amount of the monoclinic phase. However, the two peaks are quite broad which makes it hard to quantify the monoclinic phase reliably, and it is certainly below 1% in weight.

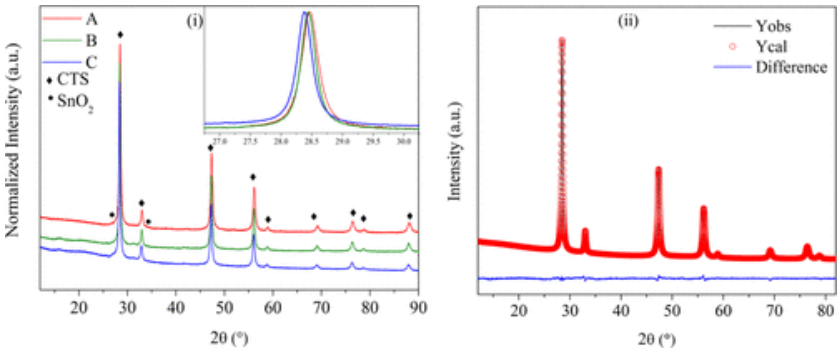

Figure 4.2. (i) XRD patterns of samples sintered under various conditions.; (ii) Rietveld refinement data for sample A collected (Y_{obs}), calculated (Y_{cal}), difference (difference) pattern. See Figure 3.S2 for the Rietveld refinement data for samples B and C.

The sizes of crystalline domains were estimated as 12 ± 10, 25 ± 10, and 37 ± 10 nm for samples A, B, and C, respectively. The reported average grain size for high-density CTS samples prepared by the three-step method (discussed in the Introduction) is in the range of 500–600 nm,[47] and in some cases, micron-size grains are also reported.[52] In contrast, traditionally sintered samples (without applying pressure) showed smaller grains, domain size ranging from ∼50 nm to a few 100 nm, and low density.[105] The mechanical alloying combined with the SPS method proposed here constrained the grain size below 50 nm[104] while promoting densification at a relatively low sintering temperature.

SEM micrographs on bulk samples reveal a dense microstructure, that is, highly intact grains with almost no porosity (shown in Figure 4.3, 4.S3 and 4.S4). Unlike the as-milled powder, EDX analysis on the sintered samples revealed a homogeneous chemical distribution, with the exception of sample A, in which a small amount of SnS was found, likely due to an incomplete reaction at 400 °C (Figures 4.3i, 4.S3, and 4.S5). Some bright spots in the micrographs revealed traces of WC particles. However, WC and SnS signals were not observed in the XRD patterns because of their small weight fraction, which was below the detection limit (≪1%). Comparative SEM–EDX analysis was performed on samples A and B (before and after polishing), and SEM–EDX data are shown in the Appendix (Figures 4.S3–S6). Sample A has a higher amount of the SnS phase compared to sample B, probably due to a lower sintering temperature. However, the matrix composition for both samples is similar, suggesting that stoichiometric deviation in CTS

grains is quite small. These micrographs also confirm that the average grain size is much smaller than the magnification of the microscope allows to see.

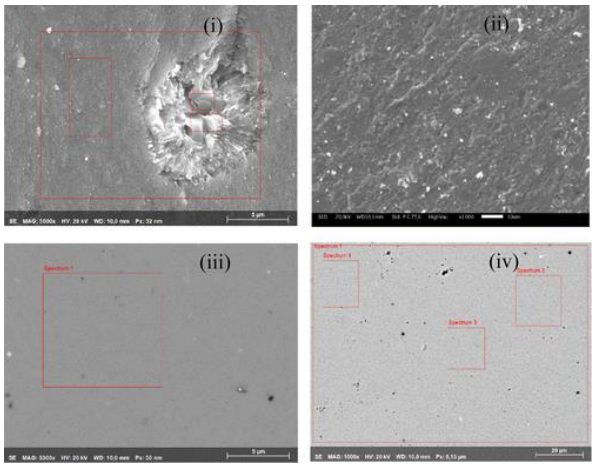

Figure 4.3. (i) SEM micrograph of the surface of SPS sintered sample A showing a compact sample with almost no pores and the presence of SnS; (ii) WC particles on one of the samples (bright spots in the micrograph, identified by EDX); (iii) micrographs of polished samples A and (iv) B. EDX data are provided in Table 4.S1

Figures 4.4 (i,ii) shows the absolute Seebeck coefficient (S) and resistivity (ρ), respectively, for the CTS samples in Table 4.1. Although there is a variation in the values of S, all the samples show a positive Seebeck coefficient increasing with temperature. Samples A, B, and C present $S \sim 100$, 180, and 160 μV/K, respectively, at room-temperature (RT), which are lower than the reported RT values for the CTS compound ($S \sim 500$–700 μV/K).[32,60,100] A general trend of increasing values of the Seebeck coefficient with increasing sintering temperature and grain size can be observed. The Cu–Sn–S-based systems exist in numerous phases, such as Cu_2SnS_3,[60] Cu_3SnS_4,[108] $Cu_5Sn_2S_7$,[99]

$Cu_7Sn_3S_{10}$,[109] and so forth.[87] Mostly, these systems show a p-type semiconducting nature due to the unfilled Cu 3d-orbitals. Additionally, Cu–S bonds in Cu–Sn–S-based systems form a three-dimensional conduction network which enhances their electrical conductivity.[85]

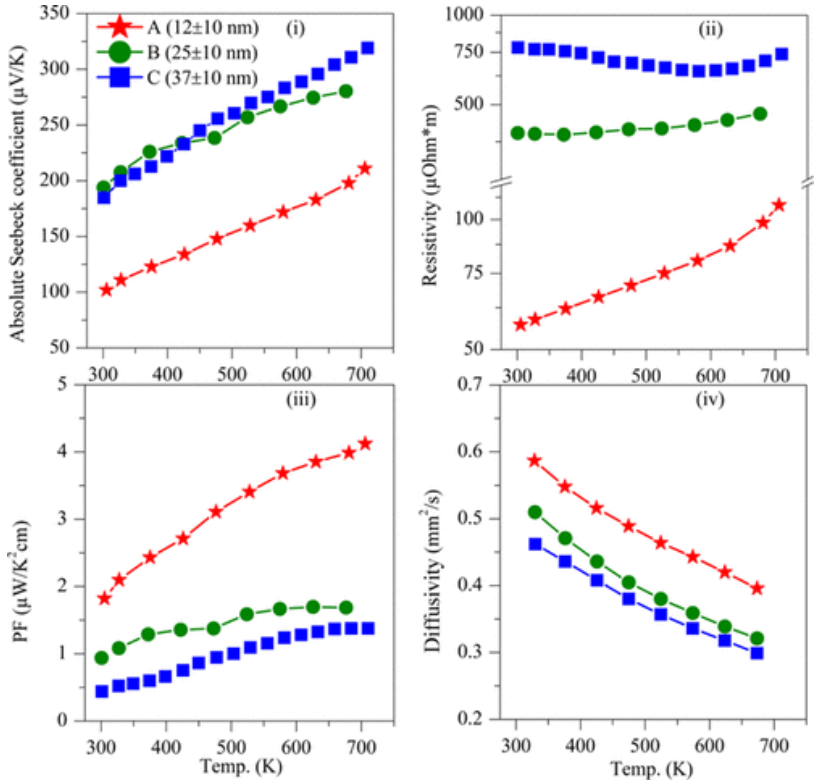

Figure 4.4. Temperature-dependent (i) absolute Seebeck coefficient, (ii) resistivity, (iii) *PF*, and (iv) diffusivity for sintered samples A, B, and C.

It is well known that undoped CTS is highly resistive with a nondegenerate semiconductor-like trend in temperature owing to its low carrier concentration.[105] However, samples A and B show a degenerate semiconductor-like nature, whereas sample C, with the largest S (~320 μV/K, above 650 K), shows a nondegenerate trend up to ~650 K. As expected, samples with a higher Seebeck coefficient have higher electrical resistivity and vice versa, but a trend of

decreasing electrical resistivity can also be observed with the decrease in the crystalline domain size. It is worth mentioning here that off-stoichiometry in CTS compounds can lead to similar results, although such deviations should have a Cu/Sn ratio >2. In fact, Deng et al. [100] show that an excess of Cu in $Cu_{2+x}Sn_{1-x}S_3$ ($x \geq 0.016$) changes the electrical resistivity from a nondegenerate to degenerate behavior. This suggests that the CTS phase, especially when sintered at low *T* (400 °C, sample A), is nonstoichiometric.

In general, a small grain size leads to a higher Seebeck coefficient due to the scattering of charge carriers by the grain boundary, otherwise known as energy filtering.[110] This, however, decreases the mobility and, in turn, increases the electrical resistivity. The lower grain size is also crucial in the suppression of thermal conductivity by scattering phonon waves effectively. The results shown here contrast with the energy filtering mechanism. The samples with smaller domains are more conductive, and we observe a trend of increasing resistivity with an increase in grain size. Carrier concentration measurements on these samples revealed that the higher conductivity of samples with small domains correlates with a higher carrier concentration, 8.6×10^{20} and 7.4×10^{19} cm^{-3} for samples A and B, respectively. These values are 1–2 orders of magnitude higher than the reported values for the CTS.[32] However, other Cu–Sn–S-based compounds with higher Cu/Sn ratios presented increasing carrier concentration with increasing Cu/Sn ratio, that is, 2.6×10^{21} and 5.6×10^{21} cm–3 for $Cu_7Sn_3S_{10}$[109] and $Cu_5Sn_2S_7$,[99] respectively. Sample A sintered at a low sintering temperature has a lower carrier mobility (1.2 cm^2/V s) than sample B (2.1 cm^2/V s), which is explained by the larger carrier concentration (increased probability of charge carrier collision) and lower grain size in sample A.

Due to the decreased electrical resistivity, sample A shows the highest *PF* value of ~4.5 μW/K^2 cm, above 650 K, which is 3-fold and 9-fold higher than cubic (disordered) CTS (*PF* ~1.5 μW/K^2 cm)[32] and monoclinic (ordered) CTS (*PF* ~0.47 μW/K^2 cm),[85] respectively. Samples B and C have comparatively lower *PF* values of ~1.5 and ~1.2 μW/K^2 cm, respectively. The thermal diffusivity measurements are shown in Figure 4.4 (iv). It is evident from the data that samples with smaller domains (more conductive) have a higher diffusivity. From the above considerations, it appears that the electrical properties are strongly dependent on the sintering temperature and grain size. Additional results following the same trend of the Seebeck coefficient and electrical resistivity with grain size support this statement (Figure 4.S7). As mentioned above, a slight stoichiometric deviation can occur in the small grains due to the incomplete reaction and crystallization at low temperature, leading to high carrier concentration and electrical conductivity. The fast kinetics of the reaction and crystallization during SPS may also lead to variation of compositions at the grain surfaces and boundaries, which could be highly conductive and possibly injecting additional charge carriers in the system.

To investigate this further, three ordered and two disordered CTS surfaces (shown in Figures 4.5 and 4.6, respectively) were studied. The first three images in Figure 4.5 show ordered CTS slabs with (001), (010), and (100) planes. The other two images show disordered structures consisting of a Cu-rich layer and a Sn-rich layer, just below the terminating sulphur layer. Please note that the overall chemistry of the CTS system was respected while making all the structures shown in Figures 4.5 and 4.6. For each structure in Figures 4.5 and 4.6, the corresponding DOS are shown with the structures. After minimization, large distortions were observed for the surface atoms of all the

structures. The reason is that surface atoms form incomplete bonds due to the change in the coordination number caused by the surface termination. The DOS on the VB side is higher than that on the CB side, showing p-type nature. However, no band gap was observed, suggesting a metallic character of all the studied structures. The localized states are visible near the Fermi level due to the dangling bonds on the surface. These dangling bonds provide additional charge carriers (holes), which increase the carrier concentration, leading to the degenerate semiconductor-like behavior observed in Figure 4.4. We are aware that the calculated structures are not an exact model of the grain boundary effects. Since the grains could terminate with any plane or orientation (favoured by the local environment), these calculations only make the hypothesis plausible that CTS grains should have dangling bonds, which would lead to localized states at the Fermi level and increased electrical conductivity. These results are in agreement with a recent report by Dahule et al.,[103] although limited to the monoclinic phase.

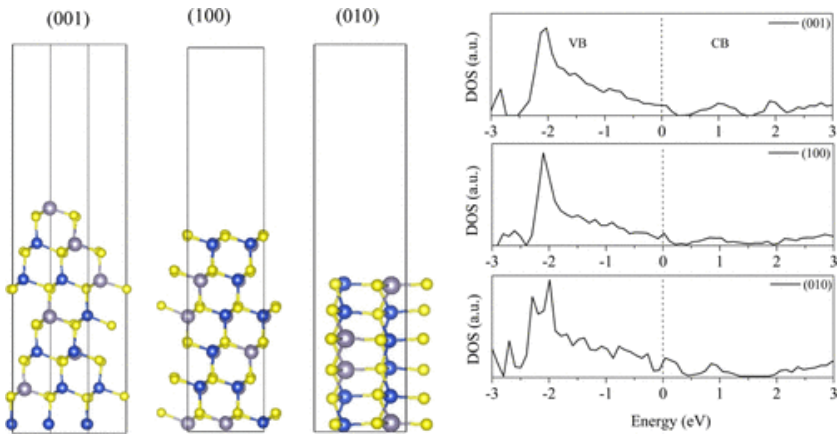

Figure 4.5. Monoclinic (ordered) CTS slabs with orientations (001), (100), and (010) and corresponding DOS plots. Here, the Fermi level is set to zero. Cu, Sn, and S atoms are represented by blue, gray, yellow colors, respectively.

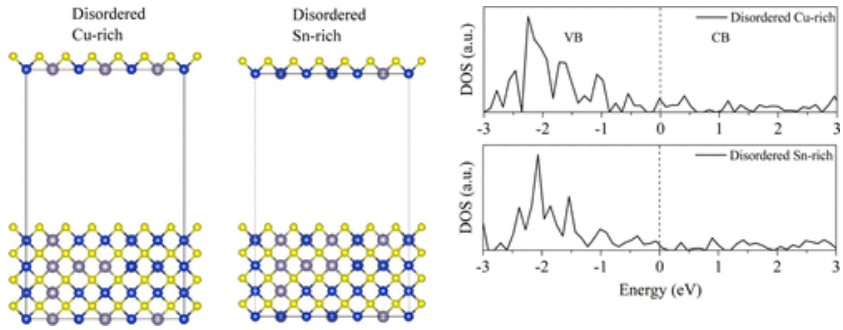

Figure 4.6. Structures and corresponding DOS for two disordered structures, where one has a Cu-rich and the other has a Sn-rich layer, just below the terminating sulfur layer. Here, the Fermi level is set to zero.

Table 2 reports the formation energy per unit atom for vacancy and off-stoichiometry in CTS, as obtained from DFT simulations. It is evident from the reported values that after the stoichiometric CTS, Cu-vacant and Cu-rich systems are energetically more viable, whereas Sn-vacant and Sn-rich systems seem less likely to form. The corresponding DOS plots are shown in Figure 4.S6. Thermodynamically, these conclusions could be generalized to the whole family of Cu−Sn−S systems. In other Cu−Sn−S systems, Cu-vacant and Cu-rich systems would be more likely to form than Sn-rich and Sn-poor phases. Moreover, in this family of materials, Cu vacancy, Cu excess, and Sn vacancy would enable p-type doping-like effects, whereas Sn excess showed n-type behavior.

Table 4.2. Energy of the System, Formation Energy, and Formation Energy per Unit Atom for Various CTS Systems

System	Configuration	Energy of the system (eV)	Formation energy (eV)	Formation energy / unit atom (eV/atom)
CTS	24-Cu, 12-Sn, and 36-S	–308.0450	–23.8016	–0.3306
Cu-vacant	23-Cu, 12-Sn, and 36-S	–303.7652	–23.2520	–0.3275
Cu-rich	25-Cu, 11-Sn, and 36-S	–307.5523	–23.4263	–0.3254
Sn-rich	23-Cu, 13-Sn, and 36-S	–306.7465	–22.3857	–0.3109
Sn-vacant	24-Cu, 11-Sn, and 36-S	–302.2878	–21.8920	–0.3083

The thermal conductivity and figure of merit are shown in Figure 4.7 (i,ii), respectively. Since we are considering the heat capacity well above the Debye temperature (θ_D ~213 K), the total thermal conductivity was calculated considering a constant value of C_p ~0.44 J/g K for all samples. The total thermal conductivity for all samples decreases with temperature due to an increased phonon–phonon interaction (Umklapp process or U-process). The electronic part of thermal conductivity (κ_e) was estimated according to the Wiedemann–Franz law (see equation 4.3), where the Lorenz number (L) was calculated using eq 4.[111]

$$L = 1.5 + e^{-(\frac{|S|}{116})} \ldots (4.4)$$

where L is in 10-8 WΩ/K^2 and S in μV/K.

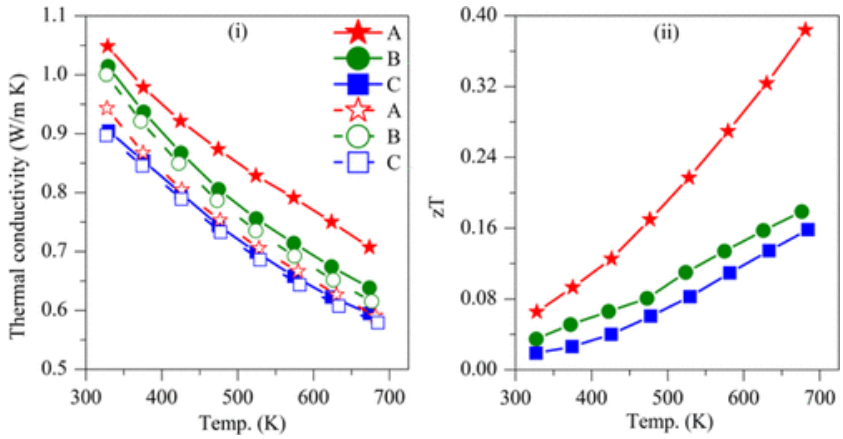

Figure 4.7. Temperature-dependent (i) total thermal conductivity (filled markers connected with the solid line) and lattice component of thermal conductivity (empty markers connected with the dashed line) and (ii) figure of merit.

It is evident from Figure 4.7 (i) that at higher temperatures, the lattice part of thermal conductivity is similar for all the samples, κ_l ~0.6 W/m K, above 673 K. This value is comparatively lower than the diamond-like $CuFeS_{2+x}$ system, where κ_l ~ 1.0 W/m K is reported at 650 K.[112] However, other Cu–Sn–S-based compounds such as Cu_3SnS_4 and Cu_7SnS_{10} show a similar κ_l around 650 K, which further decreases to κ_l ~0.4 W/m K at 750 K.[108,113] The electronic contribution of thermal conductivity is the highest for sample A, and it decreases for samples B and C. This agrees with the corresponding resistivity and carrier concentration measurements as samples A, B, and C have increasing resistivity (decreasing carrier concentration) in the same order. The figures of merit of samples A, B, and C are equal to 0.40, 0.17, and 0.14 at 673 K, respectively. Overall, the two-step production method can be used to produce high-density nanostructured pellets. The experimental results indicate that a similar zT is reported for $Cu_{2+x}Sn_{1-x}S_3$ systems with Sn substitution (x = 0.2) by Zn,[85] Ni,[50] In,[47] etc.

4.4 Conclusion:

We have studied the effects of crystalline domain size on the TE properties using experimental analyses and first-principles simulations. A CTS powder was produced from elemental powders (Cu, Sn, and S) by high-energy reactive ball milling, and subsequently, high-density pellets were produced using SPS. This method adds a distinct advantage by maintaining the nanostructure while reaching the required high density. Rietveld refinement of the XRD patterns revealed average domain sizes below 50 nm for samples sintered under different conditions. Low-temperature SPS sintering of mechanically alloyed powders allows to maintain structural disorder of the CTS phase while resulting in nanostructured ceramics. This leads to extremely low lattice thermal conductivity. On the other hand, the sample with the smallest average domain size also presents the lowest resistivity and Seebeck coefficient, resulting in the highest PF. Experimental evidence suggests that S and ρ correlate with the sintering temperature, which induces stoichiometric deviations and different grain sizes. First-principles (DFT) simulations of three ordered and two disordered surfaces revealed the presence of dangling bonds and localized states near the Fermi level. DOS at the Fermi level was continuous, that is, band gap was absent, suggesting that CTS grain boundary is conductive. Formation energies for stoichiometric CTS, Cu-vacant, Cu-rich, Sn-vacant, and Sn-rich CTS are in the increasing order, implying that stoichiometric CTS is energetically the most favourable, followed by Cu-vacant and Cu-rich systems. The Cu-vacant, Cu-rich, and Sn-vacant systems increase the p-type behavior and carrier concentration, thus explaining the observed low resistivity of the sintered components. The samples with average domain sizes of 12 ± 10, 25 ± 10, and 37 ± 10 nm displayed figures of merit zT of 0.40, 0.17, and 0.14, respectively, around 673 K. The results presented here for various CTS surfaces,

formation energies, and doping effects can be generalized to a broad family of Cu−Sn−S-based systems. Our synthesis method also provides an interesting route for many materials to synergistically tune their electrical and thermal properties.

Appendix

SEM-EDX data on 60-min milled CTS powder. Data collected on different parts of SEM grid.

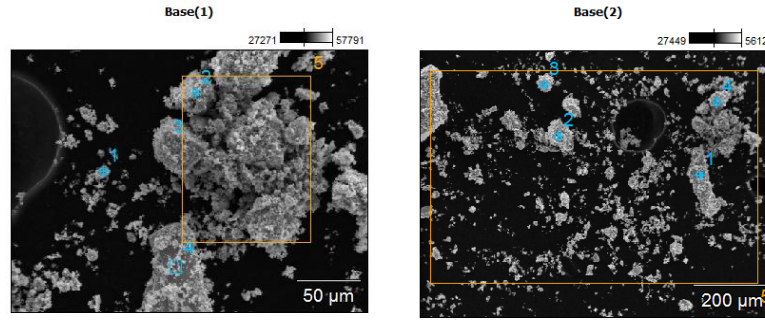

Atomic %	C (±1%)	O (±1%)	S (±1%)	Cu (±1%)	Sn (±1%)
pt1	36.6	11.1	22.9	21.9	7.5
pt2	8.1	8.9	24.7	45.6	12.8
pt3	6.1	8.4	39.6	30.6	15.3
pt4	10.1	19.1	35	2.5	33.3
pt5	14.8	12.3	30.1	30.9	11.9

Atomic %	C (±1%)	O (±1%)	S (±1%)	Cu (±1%)	Sn (±1%)
pt1	No Data collected				
pt2	9.6	07.7	26.5	41.7	14.5
pt3	17.4	09.4	09.8	57.2	06.2
pt4	28.0	13.8	13.2	37.9	07.1
pt5	58.7	26.3	06.6	05.6	02.8

Figure 4.S1. SEM Micrographs and corrosponsding EDX data collected on 60-min milled powder from the different parts of SEM grid. Corrosponding atomic % and errors are listed in table below.

Rietveld refinement was performed on XRD data collected on samples B and C.

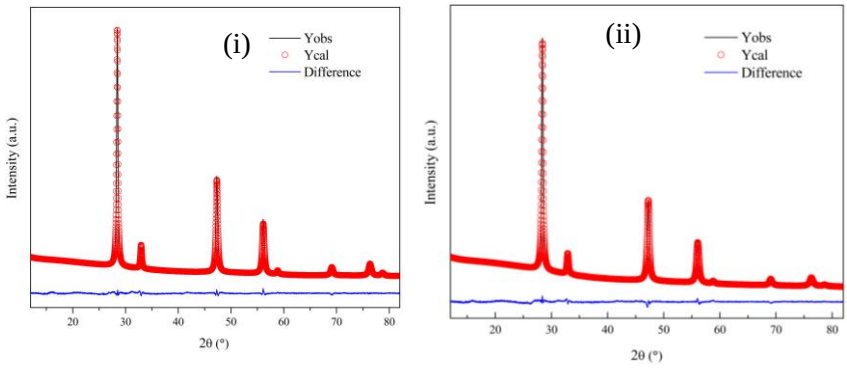

Figure 4.S2. Rietveld refinement data for samples (i) B and (ii) C, respectively.

EDX data for Figure 4.3 (i), 4.3(iii), and 4.3(iv), respectively.

Atomic %	Map	Spectrum 1	Spectrum 2	Spectrum 3
S	50,25	44,59	51,09	48,02
Cu	22,72	1,69	31,99	1,62
Sn	27,03	53,72	16,92	50,36
Total	100	100	100	100,01
	CTS	SnS	CTS	SnS
Ratio	Map	Spectrum 1	Spectrum 2	Spectrum 3
S/Sn	1,86	0,83	3,02	0,953
Cu/Sn	0,84		1,89	
Sn/Sn	1	1	1	1
	Sn-rich	SnS	CTS	SnS

Atomic %	Spetrum 1	Ratio	Spetrum 1
S	48,67	S/Sn	2,82
Cu	34,05	Cu/Sn	1,97
Sn	17,28	Sn/Sn	1
Total	100		
	CTS		CTS

Atomic %	Spetrum 1	Spetrum 2	Spetrum 3	Spetrum 4
	49,14	49,14	49,19	49,13
Cu	33,71	33,71	33,68	33,6
Sn	17,15	17,15	17,13	17,27
Total	100	100	100	100
	CTS	CTS	CTS	CTS
Ratio	Spetrum 1	Spetrum 2	Spetrum 3	Spetrum 4
S/Sn	2,86	2,87	2,84	2,84
Cu/Sn	1,96	1,96	1,94	1,94
Sn/Sn	1	1	1	1
	CTS	CTS	CTS	CTS

Table 4.S1. SEM-EDX data for Figure 4.3.

Comparative SEM-EDX data on unpolished and polished Sample A and B.

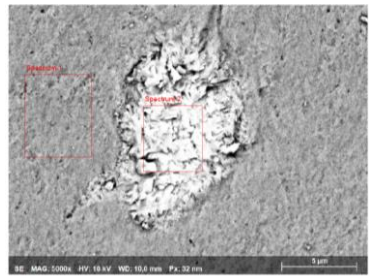

Atomic %	Spectrum 1	Spectrum 2	Ratio	Spectrum 1	Spectrum 2
S	51,33	49,9	S/Sn	2,89	1,02
Cu	30,91	1,03	Cu/Sn	1,74	
Sn	17,76	49,07	Sn/Sn	1	1
Total	100,01	100			
	CTS	SnS		CTS	SnS

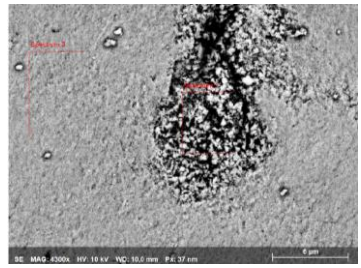

Atomic %	Spectrum 1	Spectrum 3	Ratio	Spectrum 1	Spectrum 3
S	51,75	50,19	S/Sn	3,03	2,87
Cu	31,19	32,32	Cu/Sn	1,83	1,85
Sn	17,06	17,49	Sn/Sn	1	1
Total	100	99,99			
	CTS	CTS		CTS	CTS

Figure S3. Morphological images and corresponding EDX data on unpolished Sample A.

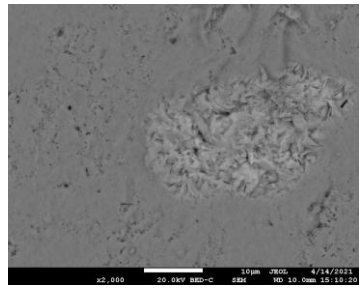

Atomic %	Spectrum 1	Spectrum 2	Ratio	Spectrum 1	Spectrum 2
S	47,77	48,32	S/Sn	2,77	2,75
Cu	35,03	34,13	Cu/Sn	2,04	1,94
Sn	17,20	17,54	Sn/Sn	1	1
Total	100	99.99			
	CTS	CTS		CTS	CTS

Figure S4. Morphological images and corresponding EDX data on unpolished Sample B.

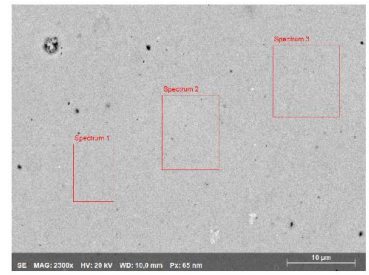

Atomic %	Spectrum 1	Spectrum 2	Spectrum 3	Ratio	Spectrum 1	Spectrum 2	Spectrum 3
S	48,61	48,75	48,67	S/Sn	2,838	2,81	2,81
Cu	34,26	33,89	34,03	Cu/Sn	2	1,95	1,96
Sn	17,13	17,37	17,3	Sn/Sn	1	1	1
Total	100	100,01	100				
	CTS	CTS	CTS		CTS	CTS	CTS

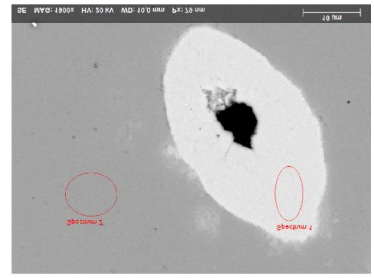

	Spectrum 1	Spectrum 2	Ratio	Spectrum 1	Spectrum 2
S	47,39	48,97	S/Sn	0,90	2,81
Cu	0	33,6	Cu/Sn		1,93
Sn	52,61	17,43	Sn/Sn	1	1
Total	100	100			
	SnS	CTS		SnS	CTS

Figure 4.S5. Morphological images and corresponding EDX data on polished Sample A.

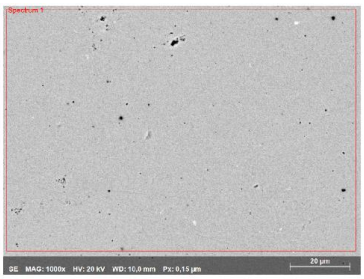

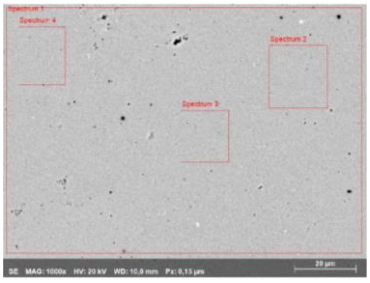

Atomic %	Spectrum 1	Ratio	Spectrum 1
S	49,15	S/Sn	2,85
Cu	33,61	Cu/Sn	1,95
Sn	17,24	Sn/Sn	1
Total	100		
	CTS		CTS

Atomic %	Spectrum 1	Spectrum 2	Spectrum 3
S	49,14	49,14	49,19
Cu	33,71	33,71	33,68
Sn	17,15	17,15	17,13
Total	100	100	100
	CTS	CTS `	CTS

Figure 4.S6. Morphological images and corresponding EDX data on polished Sample B.

Temperature dependent absolute Seebeck coefficient and resistivity for various CTS samples with increasing average domain size.

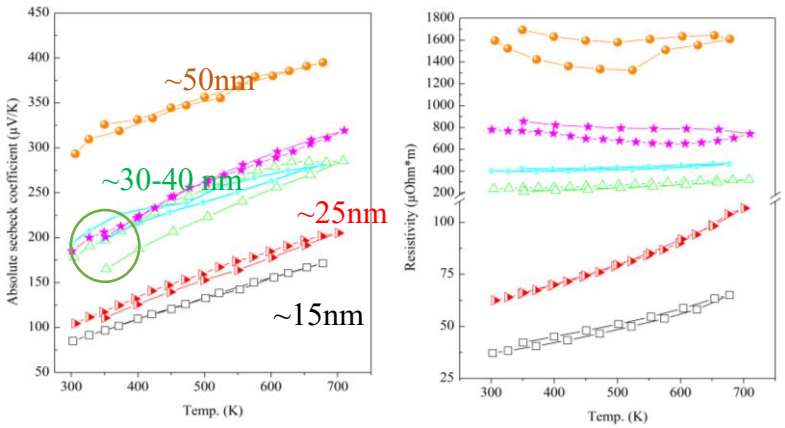

Figure 4.S7. Temperature dependent absolute Seebeck coefficient and resistivity data on many CTS samples with different average domain sizes.

The Density of States (DOS) for Stoichiometric, Cu-vacant, Cu-rich, Sn-vacant, and Sn-rich CTS systems.

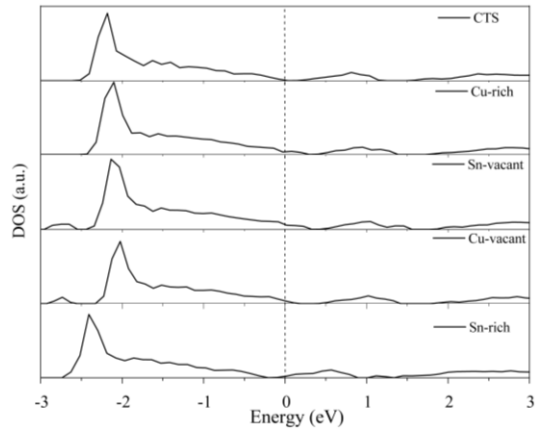

Figure 4.S8. DOS for Stoichiometric, Cu-vacant, Cu-rich, Sn-vacant, and Sn-rich CTS systems. Here the Fermi energy is set to zero. In the Cu-vacant and Sn-vacant systems, the vacancy is acting as acceptor states, it shifts the Fermi level inside the valence band. Alike, the Cu-vacant and Sn-vacant systems in the Cu-rich system, the Fermi energy shifts in the VB, reason being introduction of unfilled d-orbitals of Cu atom, in the place of Sn. However, in the case of the Sn-rich cell, the Fermi energy shifts towards the conduction band.

5. Enhanced Thermoelectric Performance of Nanostructured Cu_2SnS_3 via Ag Doping

This section is taken from Lohani, K.; Nautiyal, H.; Ataollahi, N.; Tamburini, U.A.; Fanciulli, C.; Scardi, P.* "Enhanced Thermoelectric Performance of Nanostructured Cu_2SnS_3 via Ag Doping. ACS Appl. Nano Mater. X (XX), XXXX-XXXXX. https://doi.org/10.1021/acsanm.3c00716."

*Correspondence: paolo.scardi@unitn.it

Abstract

The present work aims to investigate the effect of Ag doping on the thermoelectric properties of Cu_2SnS_3. Various $Cu_2Ag_{(x)}Sn_{(1-x)}S_3$ ($0.05 \leq x \leq 0.25$) samples were synthesised by mechanical alloying followed by spark plasma sintering, and their structural and transport properties were systematically investigated. The $x = 0.15$ sample presented a ~10-fold higher power factor than the undoped CTS. Although, the $x = 0.125$ sample had a lower power factor than the $x = 0.15$ sample, owing to its lower thermal conductivity, both the samples showed the highest zT ~ 0.8 at 723 K. This value is comparable to the best results available in the literature for earth-abundant and eco-friendly thermoelectric materials. Interestingly, the thermal conductivity of $Cu_2Ag_{(x)}Sn_{(1-x)}S_3$ samples increased with Ag substitution, which was further investigated using first principle and *ab initio* molecular dynamics calculations. It was observed that the incorporation of Ag into the system decreases the root mean squared displacement of the other cations and anions, reducing the scattering of phonons, thereby increasing the lattice thermal conductivity. Moreover, the calculations on the formation energy have revealed the reason for the structural transformation of

CTS and similar diamond-like structures towards high symmetry polymorphs by external doping. The increase in *zT* is directly related to the optimization of the band gap and the weighted mobility, which have been investigated experimentally and using the first principle method.

5.1 Introduction

Heat is a low-grade energy form and a common by-product in almost all power generation and transmission processes. Thermoelectric (TE) devices are solid-state, scalable, and noise-free, and they can convert waste heat into electrical energy. TE devices consist of several pairs of *p*- and *n*-type semiconducting legs connected electrically in series and thermally in parallel. Heat to electrical energy conversion of such a device is assessed by Carnot efficiency (η).[5]

$$\eta = \left(\frac{T_{hot}-T_{cold}}{T_{hot}}\right)\left[\frac{\sqrt{(1+zT_{avg})}-1}{\sqrt{(1+zT_{avg})}+\left(\frac{T_{cold}}{T_{hot}}\right)}\right] \ldots(5.1)$$

$$zT = \left(\frac{S^2}{\rho\kappa}\right)T \ldots (5.2)$$

where T_{hot}, T_{cold}, and zT_{avg} are hot-side temperature, cold-side temperature, and average TE figure of merit, respectively. The latter is characteristic of a given material, as defined in equation 5.2, where *S*, ρ, κ, and *T* are Seebeck coefficient, electrical resistivity, thermal conductivity, and absolute temperature, respectively. Thus, *p*- and *n*-type materials presenting a high figure of merit are essential to produce high-performing TE devices. However, various physical properties that determine the *zT* of materials show strong interdependence, limiting its enhancement. Several strategies to enhance the *zT* of materials are discussed in the literature, such as nanostructuring[104], alloying[105], band engineering,[88] energy-filtering[110], etc.

Cu_2SnS_3 is a non-toxic, eco-friendly, and low-cost thermoelectric material. Although the first lab synthesized and naturally discovered CTS had a triclinic (*P1*) structure,[40] authors have diffusely reported monoclinic (*Cc*) CTS synthesized by high-temperature solid-state reactions from a thermoelectric perspective. Frequently, a blend of cubic (*F-43m*) and tetragonal (*I-42m*) CTS polymorphs can be observed with monoclinic CTS. The monoclinic CTS polymorph shows low *zT* ~ 0.05 above 700 K, due to its low carrier concentration and high thermal conductivity. The external cation doping at the Sn site transforms the monoclinic polymorph into cubic (*F-43m*). It is worth mentioning that partially (SG: $I\bar{4}2m$) or fully (SG: *F-43m*) disordered CTS polymorphs can also be obtained by synthesis methods, e.g. colloidal method[114] and high-energy reactive ball milling.[105,115] Recently, Koskela et al.[116] have reported an orthorhombic ($Cmc2_1$) CTS polymorph. Polymorphism in these materials offers multiple possibilities of structural manipulation and band engineering to boost the TE performance. Moreover, Cu-Sn-S-based systems have low formation energy; therefore, they are suitable for large-scale and low-cost production. These systems are safe to use in the medium temperature range due to the high melting temperature (~1000 K). Recent work on CTS and similar chalcogenides-based in-plane TEGs shows promising power output per unit active planar area.[117]

Generally, crystalline materials arrange their atoms regularly and periodically in three dimensions, according to a characteristic long-range order. Various crystalline materials also present complex crystallographic structures also known as disordered materials, where long-range order is absent. The disordered materials are mainly characterized by structural disorder induced by partial occupancy of

cations in the unit cell and/or local deviation from the periodic arrangement. These materials can be utilized to achieve so-called Phonon-Glass-Electron-Crystal (PGEC) behavior. Disordered polymorphs of Cu_2SnS_3[32], Cu_2SnSe_3[118], $CuFeS_2$[119], $Cu_5Sn_2S_7$[120], $Cu_7Sn_3S_{10}$[109], Cu_2ZnSnS_4[121–123], and numerous other materials show remarkably suppressed thermal conductivity when compared with the corresponding ordered polymorphs. It has been verified by experimental and *ab-initio* methods that the above-discussed cubic materials also present higher Grüneisen parameters, which is a measure of anharmonicity, in comparison with the ordered phases.[32] Lattice distortions, irregular bond length, and soft bonds cause higher anharmonicity, originating from structural disorder. Moreover, the low electronegativity difference and high covalent character of CTS bonds and band tailing enhance the electronic transport properties.[32]

Ag is the most conductive metal. Ag-doping has been used to enhance (SnSe[124], Cu_2SnZnS_4[125], Cu_2SnSe_3[118], etc.) and reduce (Cu_2Se[126], Cu_2Te[126], SnTe[127], etc.) the carrier concentration, depending on whether the materials have high or low carrier density. In 1970, Ag-containing Cu_2Se-based materials were considered a potential candidate for radioisotope TEG.[128] At RT, Ag-doped Cu_2Se shows multiple phases. When sintered above 410 K, it transforms its crystallographic structure into the cubic phase.[128]

Sharma et al.[125] have studied TE properties of Ag nanoparticles blended in Cu_2ZnSnS_4 (CZTS) microspheres via microwave method followed by hot pressing. They observed that Ag nanoparticles were mainly a secondary phase in the materials, acting as a bridge between CZTS grains for electrical transport and as scattering centers for phonons. Overall, Ag mixed CZTS presents a maximum zT = 0.14 at 623 K.

Cheng et al.[129] investigated Ag substitution at the Cu site in a similar Cu_2SnSe_3 system, which resulted in a zT ~ 1 at 800 K. They extended the study by simultaneous In-doping at Sn site and introduction of Ag_2S, forming a $Cu_{1.85}Ag_{0.15}Sn_{0.91}In_{0.09}Se_3$ / 4% Ag_2S composite. The combined effect of band structure engineering (via doping) and microstructural engineering (via Ag_2S) enhanced its zT to 1.58 at 800K, which is two-fold higher than Cu_2SnSe_3. In addition, Mehmood et al.[130] reported a zT ~ 0.25 for $Cu_2ZnSnSe_4$ by Ag alloying.

The present work combines a two-step high-density thermoelectric sample preparation method (high-energy reactive ball-milling followed by Spark Plasma Sintering (SPS))[131] with Ag substitution at the Sn site in CTS. Various $Cu_2Ag_{(x)}Sn_{(1-x)}S_3$ ($0.05 \leq x \leq 0.25$) samples were prepared, and their TE properties systematically investigated. It is well known that the holes in CTS and similar systems (Cu_2SnZnS_4[70], $Cu_2SnZnSe_4$[132], Cu_2SnSe_3[133], etc.) are produced by the unfilled Cu *3d* orbital. The maximum contribution to the DOS in the valence band comes from the Cu *3d* orbital, followed by the S/Se *3p/4p* orbital, while the contribution of the Sn *5s* orbital is minimal. The Sn atoms contribute minimally to electronic transport. Thus, an effort has been made to improve the thermoelectric properties of CTS by means of Ag substitution at the Sn lattice site.

5.2 Experimental and computational methodology

5.2.1 Experimental Methods:

$Cu_2Ag_{(x)}Sn_{(1-x)}S_3$ (x = 0.05, 0.10, 0.125, 0.15, 0.20, and 0.25), powder samples were synthesized from elemental powders using high energy ball milling (Fritsch P4). Elemental powder of Cu, Ag, Sn, and S were fed in WC vials in stoichiometric ratio and milled for three hours, producing ~6 g powder sample (rotation and spinning speed of -1080

rpm and 300 rpm, respectively). Whole synthesis process was performed in highly controlled Ar environment (O_2 and H_2O < 10 ppm).

The as-milled powder was sintered at 400 ˚C for 10-15 min under 50 MPa pressure using SPS equipped with a WC die. A boron nitrate layer was applied while performing the sintering to avoid current passing through the sample and contamination from the die. The resulting samples had density of ~4.18 g/cm^3, which is >90% of theoretical density for CTS.

Structural, microstructural, and chemical information on the samples were collected by combining results from X-ray Diffraction (XRD), Scanning Electron Microscopy (SEM), and Energy-Dispersive X-ray spectroscopy (EDX) analysis. The XRD patterns were collected in Bragg–Brentano geometry using a Bruker D8 diffractometer equipped with a Co Kα (λ = 1.7889 Å) source. SEM-EDX measurements were performed using a Jeol IT300 scanning electron microscope. Rietveld refinement [67,134] was performed on XRD data using WPPM modeling[68,135] as implemented in TOPAS 6[69] software.

Thermoelectric properties were investigated by temperature-dependent (323 - 723 K) resistivity (ρ), Seebeck coefficient (S), and thermal diffusivity (D) measurements. Linseis Messgeraete GmbH's LSR-3 was used for Seebeck coefficient and resistivity measurements, whereas LFA-500 was used to measure the thermal diffusivity.

The Cp measurements were performed at 50 ˚C using a thermal analysis Q100 DSC instrument. The same instrument was used for heat flux measurements in a temperature span of 50 ˚C to 350 ˚C in both heating and cooling cycles. Archimedes' principle was employed for the density measurement.

A UV-VIS-NIR spectrophotometer with a 150 mm integrating sphere (PerkinElmer spectrophotometer, LAMBDA 750) was used to record the optical absorption spectra on several CTS samples. The absorption spectra were collected on ground samples weighing 0.10 g, which were sonicated for 4 h in 40 ml ethanol solution.

5.2.2 Computational Methods

The first-principles calculations were conducted using the Vienna Ab initio Simulation Package (VASP).[61,62] The Perdew-Burke-Ernzerhof (PBE) [26] under the generalized gradient approximation (GGA) was used for the Self-Consistent Field (SCF) calculations. The electron-ion interaction was described using the Projector-Augmented-Wave (PAW) method with the VASP recommended potentials.

The calculations were performed on a 72-atom supercell containing 24-Cu, 12-Sn and 36-S atoms (CTS). Three other supercells were also modelled with single, double, and triple Sn atoms replaced by Ag atoms, respectively, and represented as CTS (Cu_2SnS_3), CTS-1 ($Cu_2Ag_{0.083}Sn_{0.91}S_3$), CTS-2($Cu_2Ag_{0.16}Sn_{0.84}S_3$), and CTS-3($Cu_2Ag_{0.25}Sn_{0.75}S_3$).

The wavefunction obtained with the SCF calculations were then used to perform the Density of States (DOS) calculations with a Heyd-Scuseria-Ernzerhof (HSE06)[136] potential. The cut-off energy for the plane-wave-basis was set to 400 eV and the electronic convergence was set to 10^{-6} eV for DOS calculations. Brillion zone sampling was performed on a *k*-mesh of 4×4×4 centered at the Γ-point. Furthermore, the calculations of the formation energy were performed on the supercells described above.

Ab Initio Molecular Dynamics (AIMD) calculations were performed to investigate the temperature-dependent time evolution of the different Ag-doped CTS systems. The electron exchange-correlation function was approximated by the PBE. Again, all calculations were performed with an energy cut-off of 400 eV and a Gaussian charge smearing of 0.1 eV. The irreducible Brillouin zone was sampled on a single-point using a 1×1×1 Monkhorst Pack gamma-centred k-grid. A canonical (NVT) ensemble with a Nose-Hoover thermostat was used for AIMD calculations. In each case, the system was allowed to evolve over 10000 steps with a time step of 2 femtoseconds, corresponding to a total simulation time of 20 picoseconds. The AIMD simulations were performed at 450 K, 500 K, and 550 K. From the calculated trajectories of the AIMD simulations, the Vibrational Density of States (VDOS) was calculated by computing the Fourier transform of the velocity auto correlation function. The VDOS was also calculated with Density Functional Perturbation Theory (DFPT) using the Phonopy code.[29] For DFPT calculations, the electronic convergence was set to 10^{-8} eV. The VDOS was calculated by sampling the Brillion zone on a grid of 20 × 20 × 20 q-mesh.

5.3 Results and Discussion

XRD data collected on all the $Cu_2Ag_{(x)}Sn_{(1-x)}S_3$ (x = 0.05, 0.10, 0.125, 0.15, 0.20, and 0.25) samples are shown in Figure 5.1. Samples with different weight percentages of Ag showed cubic Sphalerite-like (*F-43m*) phase, characterized by (111), (200), (220), and (311) Bragg peaks at 2θ ~ 33.5°, 38.7°,55.8°, and 66.9°, respectively. We do not observe additional Bragg peaks for Ag in XRD patterns, implying Ag substitution with different weight fractions was successful, and $Cu_2Ag_{(x)}Sn_{(1-x)}S_3$ samples belong to the disordered cubic phase (lattice parameter shown in Figure 5.2 (b)). Moreover, with the increased

amount of Ag substitution, Bragg peaks show a shift towards higher 2θ or decreased interplanar spacing (See inset in Figure 5.1).

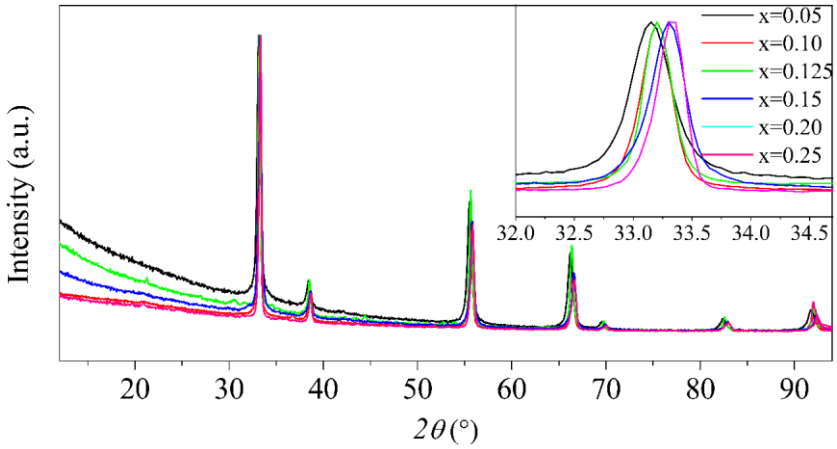

Figure 5.1. XRD data on $Cu_2Ag_{(x)}Sn_{(1-x)}S_3$ samples. The inset shows the highest intensity Bragg peak shift with increased Ag substitution.

The information on structure, lattice parameters, strain, and domain size were extracted using Rietveld refinement (shown in Figure 5.2 (a) and Figure 5.S1). Due to the smaller atomic radii of Ag as compared to Sn, the shrinking of lattice parameters with increased Ag substitution can be observed (shown in Figure 5.2 (b)). The lattice parameter decreases up to $Cu_2Ag_{(x)}Sn_{(1-x)}S_3$ (x = 0.20), and then saturates, possibly reaching the solubility limit of Ag in the CTS lattice. The average domain size of the samples is ~50 nm. And no significant microstrain was observed in the samples. Literature reports that the CTS samples prepared via widely used solid state reaction show significant grain growth, where the average crystallite size ranges from a few hundreds of nanometers to several microns.[52]

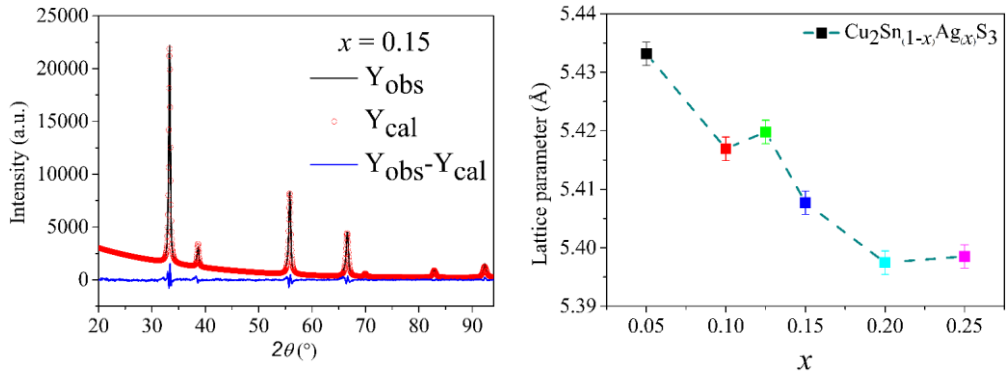

Figure 5.2 (a). Rietveld refinement performed on x = 0.15 sample, (b) change in lattice parameters with increased Ag substitution. (Rietveld refinement data on all the samples are shown in Figure S1 and Table S1-S3).

SEM Micrographs and SEM-EDX analysis on sample surfaces showed dense microstructure with almost no porosity. The grains of the samples are much smaller than the magnification of the microscope (shown in Figure 5.S2). Chemical maps were collected, Cu, Sn, and S showed a homogeneous chemical distribution for most samples. However, samples with $x \geq 0.20$ showed a non-homogeneous chemical distribution of Ag (Shown in Figure 5.3 and Figure 5.S3). Furthermore, Rietveld refinement revealed that the lattice parameters also do not decrease for x = 0.20 and 0.25 samples, implying the excess of Ag precipitates as a metallic phase in the doped matrix. A similar observation was made by Sharma et al.,[125] for Cu_2SnZnS_4 on adding Ag nanoparticles.

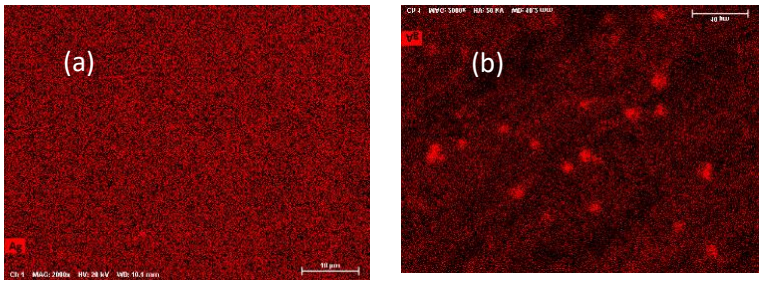

Figure 5.3. Chemical maps collected using SEM-EDX on $Cu_2Ag_{(x)}Sn_{(1-x)}S_3$ samples. Showing a homogeneous and non-homogeneous Ag substitution on (a) $x \leq 0.15$, and (b) $x \geq 0.20$ sample, respectively. (Elemental maps on all elements are shown in Figure S3.)

Temperature-dependent thermoelectric measurement on $Cu_2Ag_{(x)}Sn_{(1-x)}S_3$ ($0.05 \leq x \leq 0.25$) samples are shown in Figure 5.4. All the CTS samples show *p*-type, degenerate semiconductor-like behavior, confirmed by the positive value of the Seebeck coefficient and increasing resistivity in temperature. With the increased Ag substitution, samples show decreasing absolute Seebeck coefficient due to increased carrier concentration. Even with the lowest Ag (x = 0.05) substitution, CTS samples showed a degenerate or metal-like nature of resistivity, ranging from 170 to180 μΩ-m. For x = 0.05 - 0.15, the absolute Seebeck coefficient and resistivity also decreased with increasing Ag substitutions. Among various Ag doped samples x = 0.15 showed the lowest value of resistivity in measured temperature span, i.e. 4-8 μΩ-m, which is significantly lower than undoped disordered CTS samples (~5000-2000 μΩ-m).[32] Heavily doped CTS samples prepared via different synthesis routes have shown comparable values of resistivity/conductivity.[49,85,137] For x = 0.20 and 0.25 samples show anomalous values of S and ρ, likely caused by the interplay between carrier concentration and mobility, as these samples have some Ag present in the lattice and rest in bulk.

The unreacted metallic Ag grains in bulk would introduce free electrons into the system. However, we do not observe any sharp decrease in S

and simultaneous increase in ρ at elevated temperatures, an effect of bipolar conduction. In such cases, the thermopower (S) is a weighted average of Seebeck coefficients associated with both types of carriers. Opposite signs of both charge carriers diminish the thermopower of the material. The x = 0.25 and 0.20 samples respectively show S ~ 20 - 40 μV/K and S ~ 30 - 60 μV/K in the temperature range 300-723 K, which is one order of magnitude lower than undoped CTS[138] prepared by various synthesis and sintering techniques. It is worth mentioning here that with a small amount of external doping, x = 0.05, S was 100-200 μV/K in the same temperature span, which is comparable to the literature.[139]

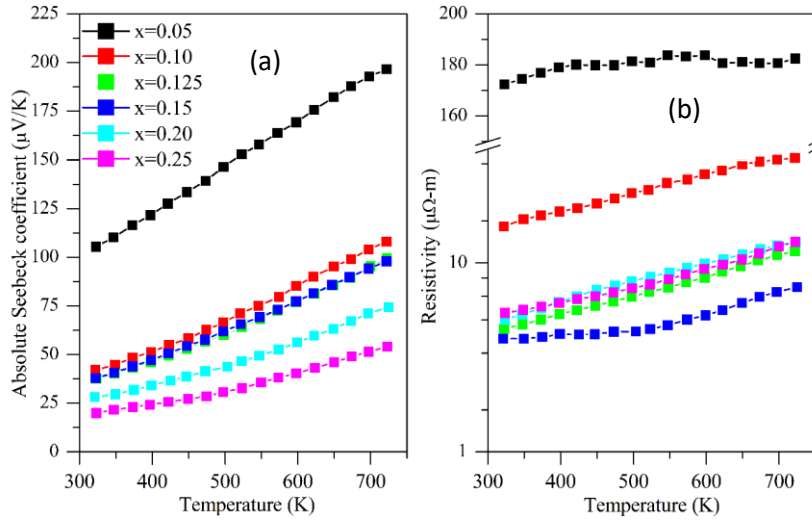

Figure 5.4. (a) Temperature-dependent Absolute Seebeck Coefficient (S), and (b) resistivity (ρ) measurements on $Cu_2Ag_{(x)}Sn_{(1-x)}S_3$ ($0.05 \leq x \leq 0.25$) samples.

In a recent work, Snyder et al.[140] proposed the calculation of the weighted mobility (μ_W) from the experimentally measured Seebeck coefficient and resistivity, under the assumption that the charge transport is dominated by a single band. In this context, we calculated the weighted mobility of $Cu_2Ag_{(x)}Sn_{(1-x)}S_3$ ($0.05 \leq x \leq 0.25$) samples. For

the calculation of the μ_W, the following formula from the aforementioned work is used,

$$\mu_W = \left(\frac{331}{\rho}\right)\left(\frac{T}{300}\right)^{-\frac{3}{2}}\left[\frac{exp\left(\frac{|S|}{86.3}-2\right)}{1+exp\left(-\frac{|S|}{17.3}+5\right)} + \frac{\frac{3}{\pi^2}\frac{|S|}{86.3}}{1+exp\left(\frac{|S|}{17.3}-5\right)}\right] \ldots (5.3)$$

Here μ_W, ρ, S, and T are expressed in the units of $cm^2V^{-1}s^{-1}$, mΩcm, μVK^{-1}, and K, respectively.

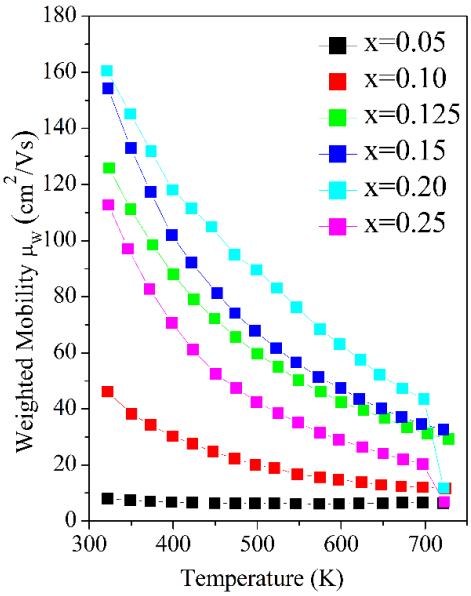

Figure 5.5. Variation of weighted mobility (μ_W) with temperature for various $Cu_2Ag_{(x)}Sn_{(1-x)}S_3$ ($0.05 \leq x \leq 0.25$) samples.

Due to the inherent $T^{-3/2}$ term in the weighted mobility formula, a decreasing trend with temperature was observed, indicating acoustic phonon scattering of charge carriers. The transport properties (S and ρ) show an optimization with increasing Ag content in the samples. The weighted mobility of samples has an increasing trend with Ag substitution ($x \leq 0.20$) contrary to the general view of Hall mobility, which decreases with carrier concentration. However, the heavily doped CTS sample $x = 0.25$ showed a drop in weighted mobility. This is in agreement with the XRD and SEM chemical maps showing the

threshold ($x \leq 0.20$) of Ag substitution in the CTS lattice. The corresponding effects can also be observed in the transport properties of heavily doped CTS samples (x= 0.20 and 0.25). The sample with the highest Ag precipitate in bulk (x=0.25) shows an intermediate value of weighted mobility, suggesting Ag excess in bulk is acting as scattering centres for charge carriers and decreasing the weighted mobility, in turn, increasing the resistivity of the sample (see figure 5.4 (b)).

The electronic DOS was calculated to validate the experimentally observed results. The experimental results showed that the increased Ag content in the prepared samples leads to a decrease both in the S and in the ρ value. This can be explained by considering that Cu, Sn, and S's oxidation state in CTS is +1, +4, and -2, respectively. Therefore, the non-isoelectronic replacement of Sn by an Ag atom would lead to additional holes in the system, enhancing the valence band edge, see Figure 5.6.

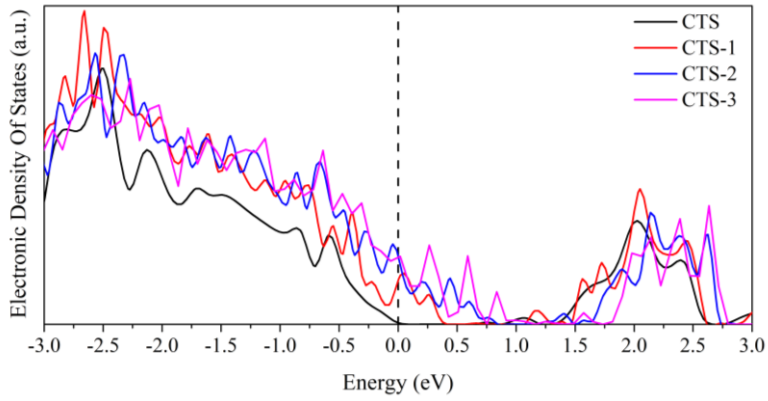

Figure 5.6. Calculated DOS on monoclinic CTS, and 1 Ag, 2 Ag, and 3 Ag atom substituted CTS systems, shown as CTS (Cu_2SnS_3), CTS-1 ($Cu_2Ag_{0.083}Sn_{0.91}S_3$), CTS-2($Cu_2Ag_{0.16}Sn_{0.84}S_3$), and CTS-3($Cu_2Ag_{0.25}Sn_{0.75}S_3$) respectively. Here, the dotted line represents the Fermi level, set at zero. The Atomic projected DOS for all calculated structures is shown in Figure 5.S4

The DOS of CTS and Ag substituted CTS systems is higher at the valence side than the conduction, confirming the *p*-type nature of all

calculated supercells. The Valence Band (VB) edge shifted toward higher energy with the increased Ag-content. The Fermi level lies deep inside the VB for Ag substituted systems, with a shift of the Fermi level inside the valence band increasing with the substitution. Thus, the increased substitution of Ag in the lattice would enable a more degenerate semiconductor-like nature in CTS and other similar systems, such as Cu_2SnZnS_4,[125] $CuFeS_2$,[141] Cu_2SnSe_3,[142] etc.

The optical absorption spectrums were collected on $Cu_2Ag_{(x)}Sn_{(1-x)}S_3$ (x = 0.05, 0.10, 0.125, 0.15, 0.20, and 0.25) samples (shown in Figure 5.S5). Figure 5.7 shows the estimated bandgap (E_g) by linear extrapolation in the Tauc plot, using the equation $\alpha h\nu = A(h\nu - E_g)^{1/2}$, where α, h, ν, A, and E_g are absorption coefficient, Planck constant, frequency, transmission constant, and bandgap, respectively. These measurements are qualitatively in agreement with the calculated DOS, confirming that by increasing Ag substitutions the bandgap decreases. The bandgap values for undoped ordered and disordered CTS polymorphs are ~0.99 and ~0.95 eV, respectively.[32] In the present work, the x = 0.05 sample showed a lower bandgap of ~0.85 eV, which further decreased with increased Ag substitution (shown in Figure 5.7).

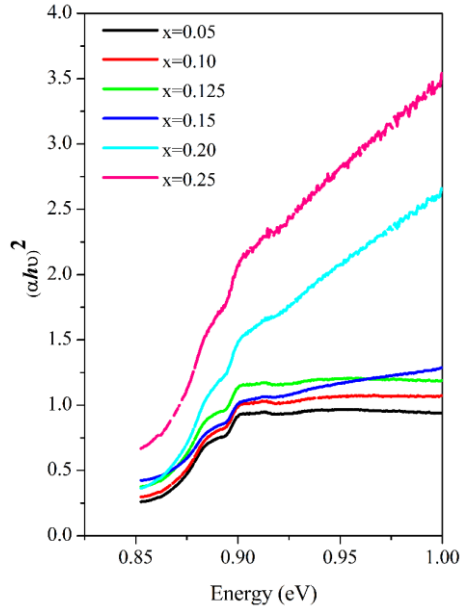

Figure 5.7. Bandgap measurements performed on various $Cu_2Ag_{(x)}Sn_{(1-x)}S_3$ ($0.05 \leq x \leq 0.25$) samples.

An essential aspect of external doping in the CTS system is the structural transformation from a monoclinic to a disordered cubic phase, which means a tendency toward higher symmetry. To understand this, additional DFT calculations were performed to calculate the formation energy of the three doped systems concerning the monoclinic system. Table 5.1 reports the formation energy calculated for the four systems. Formation energy calculations confirm that the monoclinic CTS structure is the most stable, with the lowest formation energy. The introduction of Ag at the Sn site increases the formation energy, making the Ag-doped systems less stable in monoclinic form. Therefore, external doping drives the system toward higher symmetry structures in CTS and various similar diamond-like materials.[32,51,52,59,85,143]

Table 5.1. The formation energy per unit atom of CTS and Ag-doped CTS systems.

System	Configuration	The energy of the system (eV)	Formation energy per unit atom (eV/atom)
CTS	Cu-24, Sn 12, S-36	-308.037	-24.117
CTS-1	Cu-24, Ag-1, Sn, 11, S-36	-305.925	-23.135
CTS-2	Cu-24, Ag-2, Sn, 10, S-36	-303.680	-22.020
CTS-3	Cu-24, Ag-3, Sn-9, S-36	-301.438	-20.908

The power factor (*PF* ~ 12.8 μw/K^{2}cm) for the $x = 0.15$ sample is high, compared to the literature for a similar system. It should be noted that it is ~10 and ~3 fold higher than, respectively, undoped disordered CTS[105] and CTS with the smallest domain size, i.e., 12 nm.[131] Similar Cu_3SnS_4,[108] $Cu_5Sn_2S_7$,[144] and $Cu_7Sn_3S_{10}$[109] systems also show comparable value of *PF* at the same temperature.

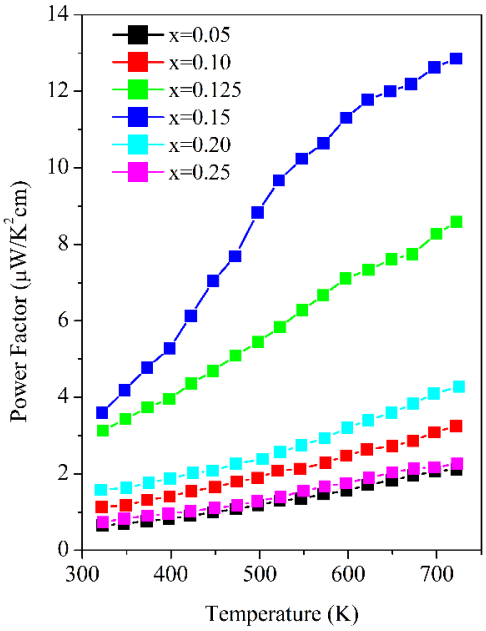

Figure 5.8. Temperature-dependent power factor (*PF*) calculated as $PF=S^2/\rho$ for $Cu_2Ag_{(x)}Sn_{(1-x)}S_3$ ($0.05 \leq x \leq 0.25$) samples.

The highest *PF* of $x = 0.15$ sample is supported by its moderate Seebeck coefficient and very low electrical resistivity, its resistivity is lowest among all $Cu_2Ag_{(x)}Sn_{(1-x)}S_3$ (x = 0.05, 0.10, 0.125, 0.15, 0.20, and 0.25) samples. Although the x = 0.25 sample also has lower electrical resistivity, the extremely suppressed Seebeck coefficient diminishes its power factor, making it the same as the lowest doped x = 0.05 sample, see Figure 5.8.

The total thermal conductivity was calculated as $\kappa = DC_pd$, where D, C_p, and d are diffusivity, specific heat capacity, and density, respectively. At 323 K, the *Cp* values for $Cu_2Ag_{(x)}Sn_{(1-x)}S_3$, ($0.05 \leq x \leq 0.25$) samples was in the range of 0.369 to 0.394 J/gK, (values for all the samples are reported in Table S4). The *Cp* for Ag substituted samples is lower than the reported value for undoped CTS ~0.44 J/gK.[51] This reduction is due to the substitution of heavier (Sn) atoms with comparatively lighter (Ag) atoms. Additionally, heat flux measurements in two successive heating and cooling cycles in temperature span 325 K to 625 K showed that the samples are thermally stable (see Figure 5.S6).

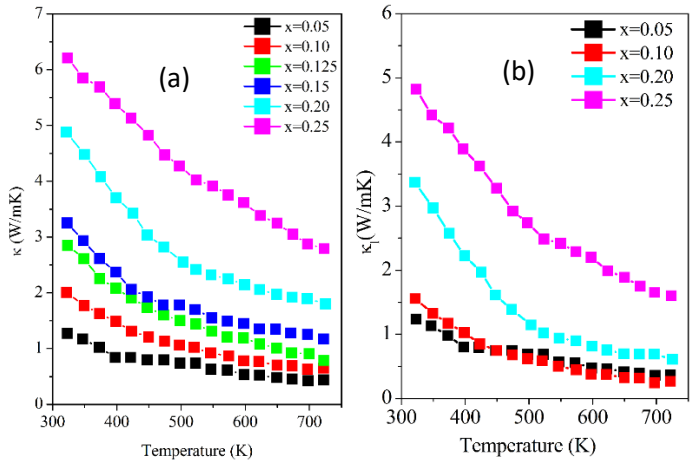

Figure 5.9. (a) Total thermal conductivity (κ), and (b) lattice thermal conductivity (κ_l) for $Cu_2Ag_{(x)}Sn_{(1-x)}S_3$ ($0.05 \leq x \leq 0.25$).

Ag substitution significantly reduced the electrical resistivity of CTS, resulting in a higher *PF*. Nevertheless, increased charge carrier density also increases the thermal conductivity of the samples. The total thermal conductivity of $Cu_2Ag_{(x)}Sn_{(1-x)}S_3$ (x = 0.05, 0.10, 0.125, 0.15, 0.20, and 0.25) samples grows with increasing Ag substitution (Figure 5.9). The decreasing trend of κ with temperature shows increased phonon-phonon or Umklapp scattering. However, the thermal conductivity appears to be governed by a complex mechanism. The x = 0.05 sample showed the lowest κ ~ 0.5 W/m-K, and the x = 0.10 and 0.125 samples showed a similar κ ~ 0.8 at 723K. The sample with the highest *PF* (x = 0.15) showed a further increase in κ ~ 1.2 W/m-K at the same temperature. The x = 0.25 sample showed the highest κ ~ 6-3 W/m-K, which is ~6 fold higher than the lowest Ag doped (x = 0.05) sample.

Total thermal conductivity (κ) consists of lattice (κ_l) electronic (κ_e) contributions. The lattice component of thermal conductivity ($\kappa_l = \kappa - \kappa_e$) is estimated via the Wiedemann Franz law ($\kappa_e = L_o \sigma T$), where L_o is Lorenz number. The Lorenz number is calculated via widely accepted method of fitting the Seebeck coefficient data to the reduced chemical potential. Besides, $L_o = 1.5 + exp\left[-\frac{|S|}{116}\right]$ (where L_o is in 10^{-8} WΩ/K^2 and S in μV/K)[111] has been proposed as a good approximation for single parabolic band scattering (shown in Figure 5.S7(a)). However, for materials with complex and multiple scattering mechanisms, this estimation could introduce large errors.

Samples with x = 0.125 and x = 0.15 have shown a complex optimization of S and ρ, resulting in a high *PF*. The κ_l computed via Wiedemann Franz law for these two samples, showed negative values above 425 K. Ballikaya et al.[126] have also observed difficulty in the determination of lattice thermal conductivity in Ag doped systems. These systems were highly conductive due to contribution of charge

carriers (holes) and mobile ions (Ag^+) in the conduction, and it is not clear which form of Wiedemann Franz law should be applied to determine κ_l. However, samples x = 0.05, 0.10, 0.20, and 0.25 show positive and increasing κ_l with increased Ag substitution. It is important to note Figure 5.9 only depicts the trend of lattice thermal conductivity with Ag substitution, not its absolute value.

The electronic contribution to the thermal conductivity is shown in Figure 5.S7 (b). The trend of κ_e with Ag doping is similar to that of electrical resistivity, owing to the linear relationship with conductivity. The κ_e values are not sufficiently high to explain the significant increase in total thermal conductivity. An interesting effect of Ag doping in the CTS system was the improvement of lattice thermal conductivity (κ_l), see Figure 5.9 (b). When external dopants are introduced into the system, they generally act as scattering centers for phonons that reduce the lattice thermal conductivity. The effect of Ag doping in the system to improve TE performance has resulted in atypical behavior of lattice thermal conductivity.

To gain insight into the atypical behavior, the temperature-dependent time evolution of the Ag doped systems was investigated. From the AIMD trajectories, the root mean square displacement (RMSD) was calculated for different cations and anions, see Figure 5.10. The RMSD values with error are given in Table 5.S5. A relatively large RMSD value generally means that the corresponding atom vibrates with a higher amplitude about its equilibrium position, due to the weak restoring forces on the vibrating atoms or soft bonds. The increase of Ag concentration resulted in a decrease in the RMSD of all cations and anions, except Ag. The increase in temperature leads to an increase in the RMSD value for all atoms, a typical temperature dependent behavior. From the results, it appears that the introduction of Ag into

the system suppresses the RMSD of other atoms and reduces the overall RMSD, see Figure 5.S8. The reduced RMSD of the cations/anions indicates a stronger interaction between the atoms, which reduces the scattering of the phonons and thus increases the κ_l with the Ag substitution. Similar results were obtained by Liu et al.[145] where the Ag doping induced abnormal lattice thermal conductivity in Cu_2Se with an increasing Ag concentration. Moreover, Cao et al.[146] also observed increase of lattice thermal conductivity in CTS via Fe^{3+} doping.

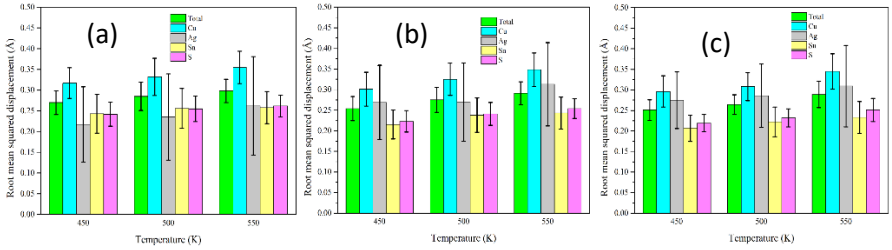

Figure 5.10. Temperature-dependent root mean square displacement (RMSD) for (a)1 Ag, (b) 2 Ag , and (c) 3 Ag atom substituted CTS systems.

To further support the argument, we looked at the VDOS calculated using two different methods, one using the DFPT and the other using the AIMD trajectories, shown in Figure 5.11 (a) and (c), respectively. Although the two methods used to calculate the VDOS were different, the results were consistent. We observed that with the introduction of Ag into the system, the magnitude of VDOS at low frequencies decreased (< 3 THz) and a small shift towards higher frequencies was observed, see magnified VDOS in Figure 5.11 (b) and (d). This would reduce the scattering of low frequency phonons, which are primarily responsible for the thermal transport. Apart from this, the VDOS calculated from the AIMD trajectories also showed broadening, as it was calculated at higher temperature i.e., 450 K.

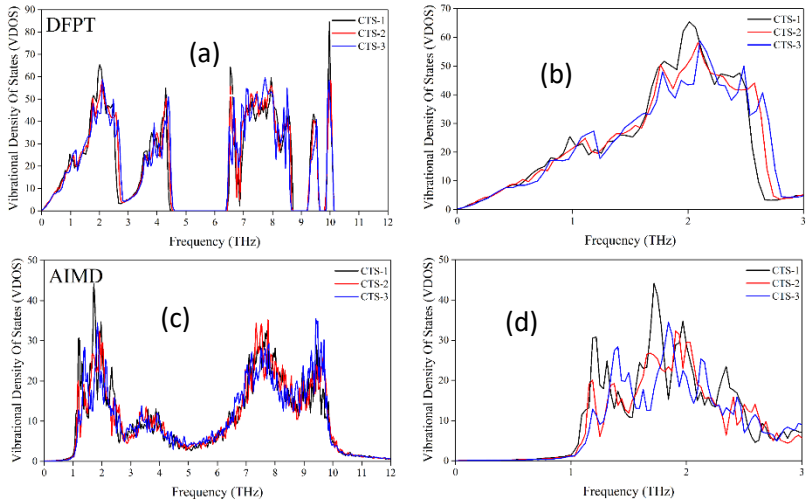

Figure 5.11. Vibrational Density of States (VDOS) calculated via (a) DFPT and (c) AIMD (at 450 K) for 1 Ag, 2 Ag, and 3 Ag atom substituted CTS systems. The adjecent Figures (b) and (d) show the magnified VDOS at low frequency span via DFPT and AIMD, respectively.

Overall, x = 0.15 and 0.125 samples show the highest $zT \sim 0.8$ at 723 K, see figure Although, x = 0.125 has a slightly lower PF ~ 8 μw/K^{2}cm than x = 0.15 (PF ~ 12.8 μw/K^{2}cm) sample, the lower thermal conductivity of x = 0.125 samples increases its zT. The highest zT, of x = 0.15 and x = 0.125 samples was followed by second highest zT ~ 0.35 for the x = 0.05 and x = 0.10 samples. Another sample, x = 0.20, showed zT ~ 0.15 at 723 K. The sample containing the highest amount of Ag (x = 0.25) deteriorates the zT ~ 0.05, due to its high thermal conductivity and low Seebeck Coefficient. Interestingly, the samples with intermediated weighted mobility and bandgap (x = 0.15) show higher PF and zT, indicating an optimization of charge and heat transport.

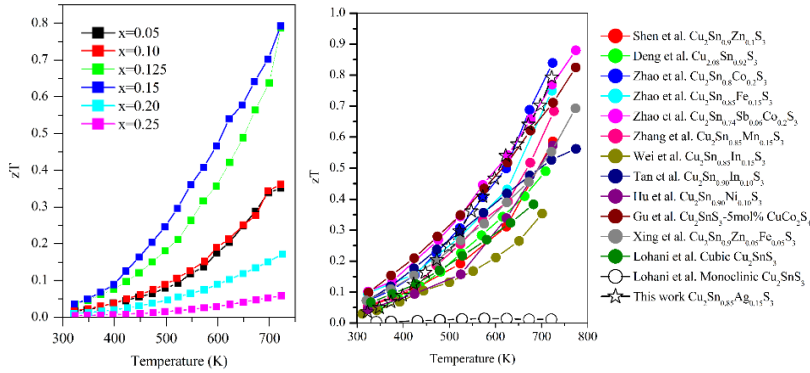

Figure 5.12. (a) Thermoelectric figure of merit for $Cu_2Ag_{(x)}Sn_{(1-x)}S_3$, ($0.05 \leq x \leq 0.25$) samples, and (b) a comparison between various investigation performed on CTS systems in the literature.

Figure 5.12 (b) shows a comparison of various investigations performed on CTS systems. Our past works showed that pristine disordered (cubic) CTS polymorph has a higher thermoelectric figure of merit than ordered (monoclinic).[32,131] Initially, researchers tried to optimize the thermoelectric properties of CTS via various single element doping, such as Zn,[85] Cu,[139] Co,[52] Fe,[51] Mn,[49] In,[147] and Ni[50]. Subsequently, simultaneous doping of two elements was tested in CTS, e.g. (Co-Sb[148] and Zn-Fe[149]). Recently, researchers have tried to increase the thermoelectric figure of merit of CTS via twin boundary engineering[114] and 3D modulation doping.[150] However, in the present work, $Cu_2Ag_{(x)}Sn_{(1-x)}S_3$ (x = 0.15) sample prepared via two-step method (mechanical alloying followed by SPS) presented one of the highest zT reported for CTS. Ag doping in CTS yields ~16 times higher zT than pristine monoclinic CTS reported in the literature. Although, Co doping[52], simultaneous Co-Sb[148], and modulation doping via $CuCo_2S_4$[150] showed slightly higher zT than Ag doped CTS, Ag is a non-toxic material. Additionally, the two-step method presented in this work is less time and resource consuming, consequently, cost-effective.

5.4 Conclusion:

Herein, various Ag substituted disordered $Cu_2Ag_{(x)}Sn_{(1-x)}S_3$ ($0.05 \leq x \leq 0.25$) polymorph samples were stabilized by a two-step synthesis method. The experimental and computational methods were employed to study their thermoelectric properties. Rietveld refinement of XRD patterns and SEM-EDX chemical maps confirmed successful Ag substitution at Sn site up to $x \leq 0.15$. For samples $x \geq 0.20$, some Ag substituted Sn in the lattice; the rest was diffusely distributed in bulk as metallic Ag. The $Cu_2Ag_{(x)}Sn_{(1-x)}S_3$, $x = 0.15$ sample presented ~10-fold higher *PF* (~ 12.8 µw/K^{2}cm) than reported for undoped cubic CTS (*PF* ~ 1.1 µw/K^{2}cm). However, due to the interplay between κ and *PF*, $x = 0.125$ and $x = 0.15$ showed the highest $zT \sim 0.8$, at 723 K. First principle DFT simulations revealed suppression of bandgap with increased Ag substitution at the Sn site. The optical absorption spectra measurements on various $Cu_2Ag_{(x)}Sn_{(1-x)}S_3$ confirm the DFT results. The lattice thermal conductivity depicted an unconventional behavior i.e, enhancement with Ag substitution. AIMD and DFPT were employed to shed light on the atypical behavior. It was observed that the introduction of Ag in the system was suppressing the RMSD of other atoms. Due to reduction of RMSD, a reduction in the scattering of the phonons would occur, thus, increasing the κ_l. The results were also supported by VDOS calculations using AIMD and DFPT. The two-step sample preparation method combined with doping is relatively inexpensive and sustainable, as it does not require thermal treatment at very high temperatures. A high $zT \sim 0.8$ was achieved by optimizing various TE parameters (S, ρ, μ_W, κ, and Eg).

Appendix

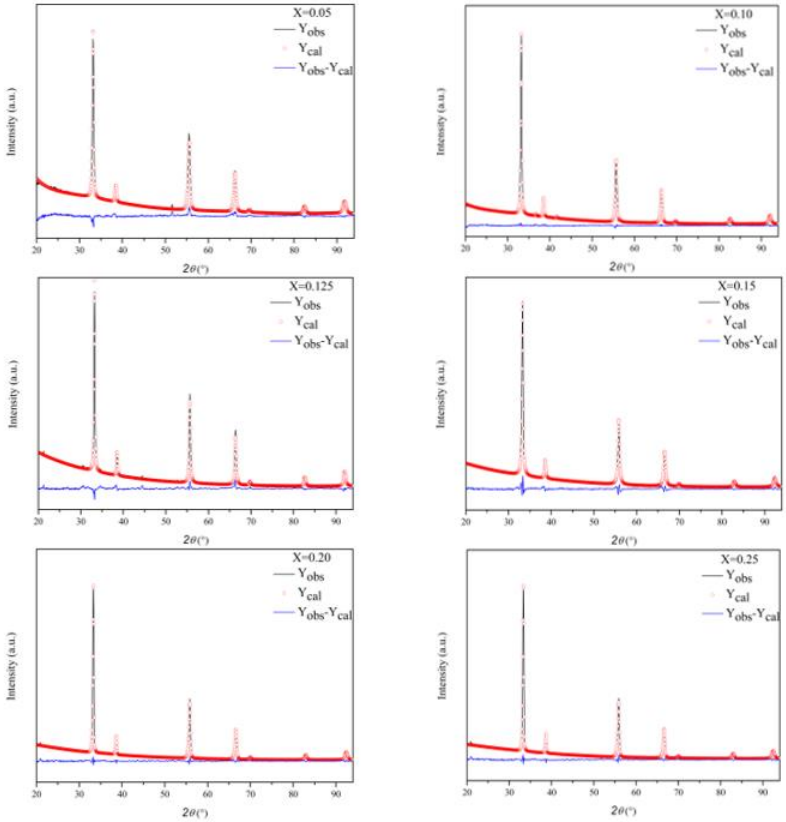

Figure 5.S1. Rietveld refinement data on $Cu_2Ag_{(x)}Sn_{(1-x)}S_3$ (x= 0.05, 0.10, 0.125, 0.15, 0.20, and 0.25) samples.

Table S1: Structural data on Cu_2SnS_3 (space group *F-43m* (216)).

	x	*y*	*Z*	Occupancy	Site	B_{iso}
Cu	0	0	0	2/3	4*a*	1.0
Sn	0	0	0	1/3	4*a*	1.0
S	0.25	0.25	0.25	1.0	4*c*	1.0

For the Rietveld refinement of $Cu_2Sn_{(1-x)}Ag_{(x)}S_3$ samples. The Ag was introduced at Sn site, and the occupancy for Cu and S was kept same as table S1. The variation of various parameters is sown in table S2.

Table S2: Initial occupancy of Cu, Sn and Ag at 4*a* site and lattice parameter (a=b=c) used for the Rietveld refinement of various $Cu_2Sn_{(1-x)}Ag_{(x)}S_3$ samples.

x	Occupancy				(a=b=c) Å
	Cu	Sn	Ag	S	
0.05	0.6667	0.3135	0.0165	1.0	5.43
0.10	0.6667	0.2970	0.0334	1.0	5.43
0.125	0.6667	0.2885	0.04125	1.0	5.43
0.15	0.6667	0.2805	0.0465	1.0	5.43
0.20	0.6667	0.264	0.0667	1.0	5.43
0.25	0.6667	0.2475	0.0825	1.0	5.43

Table 5.S3: After Rietveld refinement final occupancy, Debye Waller factor (B_{iso}), and the goodness of fit (GoF) for various $Cu_2Sn_{(1-x)}Ag_{(x)}S_3$ samples.

x	Occupancy				a=b=c Å	B_{iso}				GoF
	Cu	Sn	Ag	S		Cu	Sn	Ag	S	
0.05	0.6378	0.3141	0.0094	1.15	5.4334(6)	1.5	1.6	1.8	2.1	1.72
0.10	0.6537	0.2920	0.0280	1.14	5.4169(1)	1.2	1.1	2.8	3.1	1.63
0.125	0.6592	0.2899	0.0384	1.04	5.4198(6)	1.4	1.2	2.1	2.4	2.30
0.15	0.6499	0.2737	0.0402	1.17	5.4077(5)	1.8	1.2	2.7	3.2	1.81
0.20	0.6544	0.2587	0.0607	1.11	5.3974(1)	1.7	1.0	1.3	2.5	1.54
0.25	0.6641	0.2440	0.0769	1.06	5.3985(4)	0.9	1.1	1.2	1.6	1.55

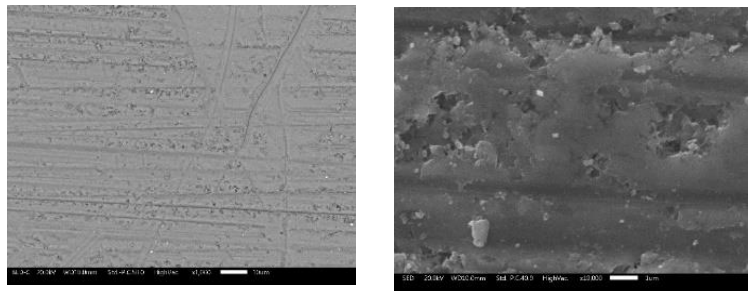

Figure 5.S2. Morphological image on $Cu_2Ag_{(x)}Sn_{(1-x)}S_3$ samples in different magnifications, showing dense microstructure with almost no porosity. Moreover, the grains of the samples are much smaller than the microscope's magnification.

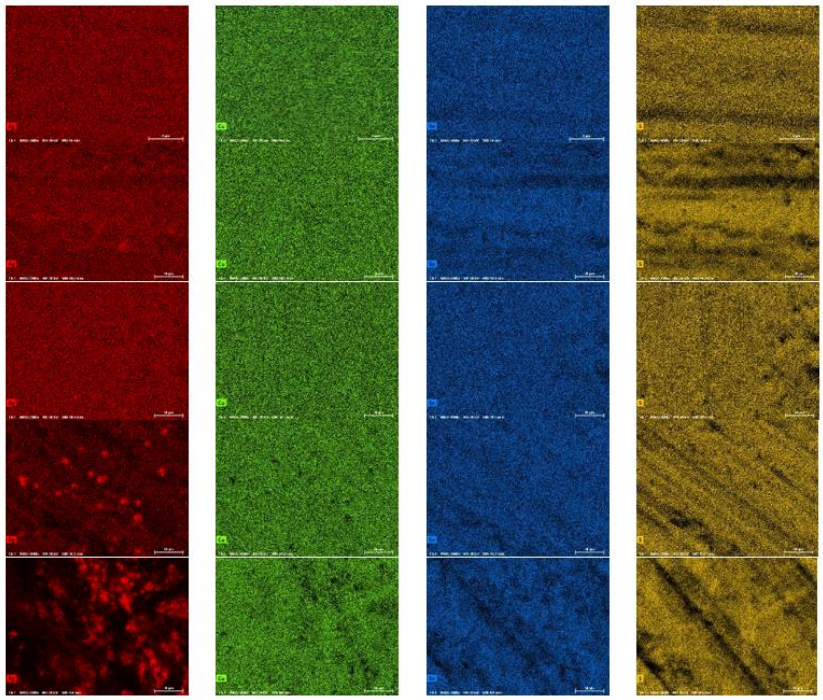

Figure 5.S3. Chemical maps collected on $Cu_2Ag_{(x)}Sn_{(1-x)}S_3$ samples (x= 0.05, 0.10, 0.15, 0.20, and 0.25), respectively. Chemical maps for Cu (Green), Sn (Blue), and S (Yellow) are homogeneous for all the samples. However, $x \leq 0.20$ samples show a non-homogeneous Ag (Red) distribution.

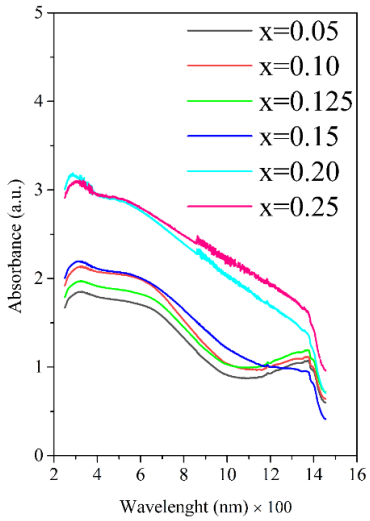

Figure 5.S4. Optical absorption spectra collected on $Cu_2Ag_{(x)}Sn_{(1-x)}S_3$ (x= 0.05, 0.10, 0.125, 0.15, 0.20, and 0.25) samples.

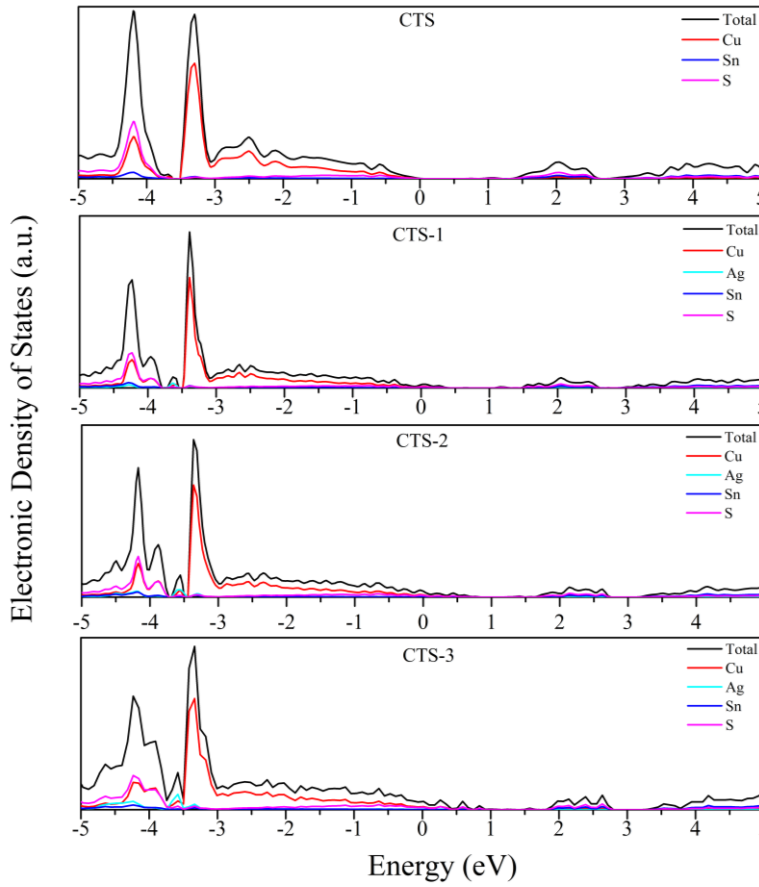

Figure S5. Atomic projected Density of States (DOS) plot for monoclinic CTS, and 1 Ag atom and 2 Ag atom substituted CTS systems, shown as CTS (Cu_2SnS_3), CTS-1 ($Cu_2Ag_{0.083}Sn_{0.91}S_3$), CTS-2($Cu_2Ag_{0.16}Sn_{0.84}S_3$), and CTS-3($Cu_2Ag_{0.25}Sn_{0.75}S_3$), respectively. Here, the Fermi level is set at zero.

Table 5.S4. Specific heat capacity values for $Cu_2Ag_{(x)}Sn_{(1-x)}S_3$ at 50 ºC.

$Cu_2Ag_{(x)}Sn_{(1-x)}S_3$	Temperature (ºC)	Cp (J/gºC)
x=0.05	50	0.387 ± 0.01
x=0.10	50	0.364 ± 0.01
x=0.125	50	0.369 ± 0.01
x=0.15	50	0.394 ± 0.01
x=0.20	50	0.378 ± 0.01
x=0.25	50	0.394 ± 0.01

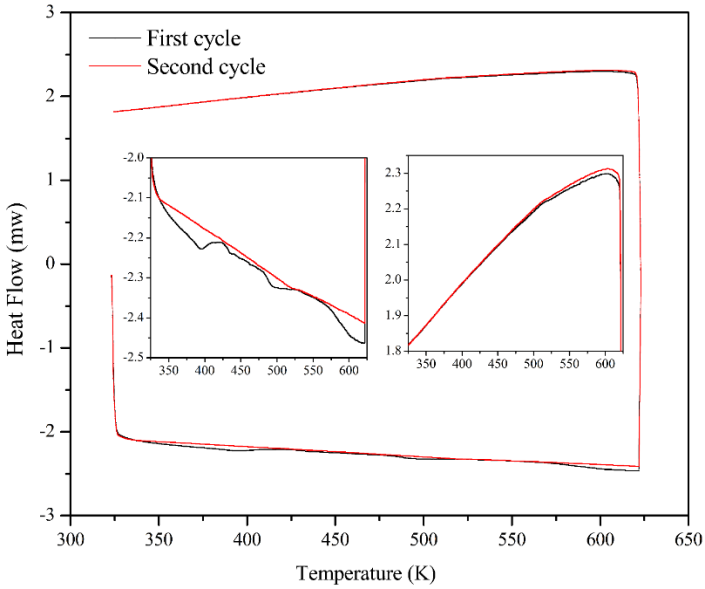

Figure 5.S6. Two temperature-dependent heat flow measurement cycles were performed on $Cu_2Ag_{(x)}Sn_{(1-x)}S_3$, $x = 0.15$ sample. Two insets show magnified heating and cooling cycles.

The heat flux measurements were carried out on x = 0.15 sample in two successive heating and cooling cycles in temperature span 325 K to 625 K. In the first cycle, while heating, an endothermic peak from ~350 K to ~425 K is associate to the release of water, which could be present in the samples due to humidity. Other than this, four features are evident in the first cycle of heat flux line and 435 K, 460 K, 500 K, and 600K, respectively. The enthalpy associated with first two peaks is very small ~0.0167 J/g and ~0.0024 J/g. The enthalpy associated with the third peak around 500 K has one order of magnitude higher (~ 0.1511 J/g) than peaks at 435 K and 460 K. The last peak in heat flux measurement is around 600 K. All these peaks are very small and possibly related to release of S and or oxidization of the sample. Moreover, these peaks completely disappeared in second cycle. Thus, confirming the thermal stability of Cu2Ag(x)Sn(1-x)S3, x = 0.15 sample.

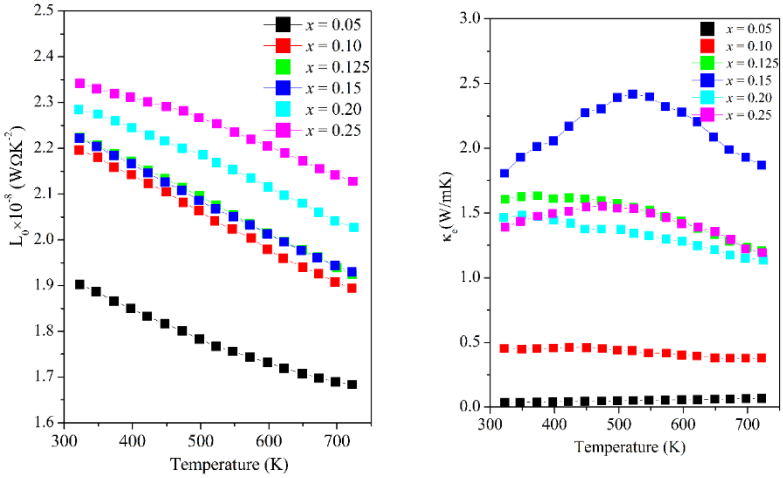

Figure 5.S7. (a) Calculated Lorenz number (L_o), and (b) electronic contribution to the thermal conductivity (κ_e).

Table S5: AIMD temperature-dependent RMSD values and error for simulated CTS-1 ($Cu_2Ag_{0.083}Sn_{0.91}S_3$), CTS-2($Cu_2Ag_{0.16}Sn_{0.84}S_3$), and CTS-3($Cu_2Ag_{0.25}Sn_{0.75}S_3$) supercells, respectively

CTS-1

Temperature	Total	Error	Cu	Error	Ag	Error	Sn	Error	S	Error
450 K	0.27	0.029	0.317	0.037	0.217	0.091	0.243	0.047	0.242	0.029
550 K	0.285	0.034	0.332	0.045	0.235	0.104	0.256	0.048	0.255	0.031
650 K	0.298	0.028	0.355	0.039	0.262	0.119	0.258	0.039	0.262	0.026

CTS-2

Temperature	Total	Error	Cu	Error	Ag	Error	Sn	Error	S	Error
450 K	0.254	0.029	0.301	0.041	0.269	0.09	0.215	0.035	0.223	0.026
550 K	0.275	0.03	0.325	0.039	0.27	0.095	0.238	0.042	0.241	0.028
650 K	0.291	0.028	0.348	0.041	0.313	0.101	0.243	0.039	0.254	0.024

CTS-3

Temperature	Total	Error	Cu	Error	Ag	Error	Sn	Error	S	Error
450 K	0.251	0.025	0.296	0.038	0.275	0.069	0.207	0.032	0.219	0.021
550 K	0.264	0.024	0.308	0.034	0.286	0.077	0.222	0.036	0.232	0.022
650 K	0.289	0.032	0.345	0.043	0.309	0.099	0.233	0.039	0.251	0.028

6. Mechanochemical Synthesis of Sustainable Ternary and Quaternary Nanostructured Cu_2SnS_3, Cu_2ZnSnS_4, and $Cu_2ZnSnSe_4$ Chalcogenides for Thermoelectric Applications

This section is taken from[115]: Nautiyal, H., Lohani L., Mukherjee, B., Isotta, I., Malagutti, M.A., Ataollahi, N., Pallecchi, I., Putti, M., Misture, S.T., Rebuffi, L., and Scardi, P.* "Mechanochemical Synthesis of Sustainable Ternary and Quaternary Nanostructured Cu2SnS3, Cu2ZnSnS4, and Cu2ZnSnSe4 Chalcogenides for Thermoelectric Applications. Nanomaterials 2023, 13 (2), 366. https://doi.org/10.3390/nano13020366."

* Correspondence: paolo.scardi@unitn.it

Abstract

Copper-based chalcogenides have emerged as promising thermoelectric materials due to their high thermoelectric performance, tunable transport properties, earth abundance and low toxicity. We have presented an overview of experimental results and first-principal calculations investigating the thermoelectric properties of various polymorphs of Cu_2SnS_3 (CTS), Cu_2ZnSnS_4 (CZTS), and $Cu_2ZnSnSe_4$ (CZTSe) synthesized by high-energy reactive mechanical alloying (ball milling). Of particular interest are the disordered polymorphs of these materials, which exhibit phonon-glass–electron-crystal behavior—a decoupling of electron and phonon transport properties. The interplay of cationic disorder and nano structuring leads to ultra-low thermal conductivities while enhancing electronic transport. These beneficial transport properties are the consequence of a plethora of features, including trap states, anharmonicity, rattling, and conductive surface

states, both topologically trivial and non-trivial. Based on experimental results and computational methods, this report aims to elucidate the details of the electronic and lattice transport properties, thereby confirming that the higher thermoelectric (TE) performance of disordered polymorphs is essentially due to their complex crystallographic structures. In addition, we have presented synchrotron X-ray diffraction (SR-XRD) measurements and ab initio molecular dynamics (AIMD) simulations of the root-mean-square displacement (RMSD) in these materials, confirming anharmonicity and bond inhomogeneity for disordered polymorphs.

6.1 Introduction

The depletion of fossil fuels and their harmful effects on the environment has encouraged the scientific community to explore the field of renewable energy. In particular, technologies enabling the harvesting of dispersed sources of energy, such as photovoltaics, thermoelectrics, piezoelectrics and so on, have attracted great interest.[34] Among them, the thermoelectric (TE) technology has been proposed for waste heat recovery, off-grid power generation, as well as refrigerant-free cooling and thermal regulation. Compared to conventional power generation methods, TE materials can directly harness heat, a low-grade form of energy, and convert it into electricity, a high-grade form of energy. The solid-state nature, absence of noise and moving parts, long life span, and portable nature are some advantages of TE generators.[96] Recently, interconnected sensors for various applications, including the Internet of Things, and hybrid thermoelectric-photovoltaic devices have attracted the TE research community and industry.[151]

In terms of performance, the maximum energy conversion efficiency of a TE material is determined by the dimensionless figure of merit (zT) proposed by Ioffe in 1957,[4] which is defined as

$$zT = \frac{S^2\sigma}{\kappa}T = \frac{S^2\sigma}{(\kappa_l+\kappa_e)}T \quad \text{... (6.1)}$$

where S is the Seebeck coefficient (thermopower), σ is the electrical conductivity, κ is the thermal conductivity, and T is the absolute temperature. The power factor $S^2\sigma$ is associated with electrical transport. The thermal conductivity comprises two parts, the lattice part κ_l and the electronic part κ_e . To achieve a high zT, a large S is required to ensure a high output voltage, a high σ to reduce Joule heat losses, and a low κ to maintain the temperature gradient between the hot and cold sides. However, these three transport parameters, S, σ, and κ, are highly interdependent and depend on the band structure, carrier concentration, microstructure, and many other factors. The following three equations show the linkage of the transport parameters,

$$S = \frac{8\pi^2 k_B^2}{3eh^2} m^* \left(\frac{\pi}{3n}\right)^{2/3} T \quad \text{… (6.2)}$$

$$\sigma = ne\mu \quad \text{…(6.3)}$$

$$\kappa_e = L\sigma T \quad \text{…(6.4)}$$

here k_B, h, m^*, n, μ, e, and L represent Boltzmann constant, Planck constant, effective mass of charge carriers, carrier concentration, carrier mobility, the charge of an electron, and the Lorenz number, respectively.[33]

Equation 6.1 shows that κ_l is the only independent variable in transport properties. Therefore, reducing it is one of the most effective ways to increase zT. There are several strategies to decrease the lattice thermal

conductivity, such as introducing rattling atoms,[152] nano structuring, lattice anharmonicity that can be induced by layered structures,[153] or lone-pairs,[154] and introduction of disorder in the crystal structure. [54]

An optimal range for carrier concentration (10^{18}-10^{20} cm^{-3}) and low thermal conductivity are desired for high-performing TE materials.[95] To this end, state-of-the-art TE materials employ heavy-mass elements, such as Pb, Hg, Cd, Te, Sb, Bi, etc.,[155–157] materials which are often rare and/or toxic. For the sake of scalable commercial application, intensive efforts are required to explore non-toxic, earth-abundant, environment-friendly, sustainable, and economically viable materials. Cu-based sulphides/selenides have recently attracted much attention in TE research, in part because of their earth abundance. Devices employing these materials showed power output per unit cost comparable to high-performance thermoelectric devices, underlining the relevance of obtaining a thorough understanding of the transport mechanism in these materials.[117,158] Mechanochemical syntheses via high-energy reactive milling offer the unique advantage of producing various disordered polymorphs of these compounds. This single-step and solvent-free method can alloy materials with different melting points, such as transition metals and chalcogenides, due to the highly entropic environment of the milling.[159–162] Such an environment also favours the disordering of these Cu-alloys. Recently, we have synthesized and stabilized various polymorphs of Cu_2SnS_3 (CTS),[54] Cu_2ZnSnS_4 (CZTS),[163] and $Cu_2ZnSnSe_4$ (CZTSe)[132] through this bottom-up ball-milling technique.

The constituting elements of ternary CTS are earth abundance and eco-friendly making it suitable for sustainable and large-scale use. Researchers have investigated CTS polymorphs for a number of

applications, such as, optoelectronics,[164] sensors,[165] absorber layer of solar cell,[166] TE,[147] etc. The complex crystallographic structure of CTS allows to synergistically tune the electronic and thermal transport properties, resulting in a high thermoelectric figure of merit. Heavily In[147] and Zn[48] doped CTS systems were among the first CTS systems investigated for TE application in the last decade. Subsequently, several other cationic substitutions were investigated with the aim of improving the TE performance by tuning the carrier concentration and introducing structural disorder such as Co,[52] Cu,[167] Ni ,[50] Fe, [51] and Mn.[49] Recently, Wei et al.[114] showed effective suppression of thermal conductivity of CTS by manipulating the phase composition and twin boundary engineering. Zhao et al. achieved the highest $zT \sim 0.9$ above 700 K by simultaneous doping with cobalt and antimony.[148] Moreover, 3D modulation doping has also been studied in nanocomposites CTS, which have an ultra-low thermal conductivity and high zT.[168] The disordered cubic phase of CTS/CTSe was also synthesised without external doping.[32,54,59,169]

The quaternary chalcogenides CZTS and CZTSe have also been investigated for application in other fields of energy materials. In particular owing to their structural similarity with $Cu_2InGaSe_4$ (CIGS), they have been extensively studied as a sustainable replacement for the absorber layer in thin-film solar cells due to an optimal, direct band gaps and high absorption coefficients.[123,170] CZTS has also been explored as a hole transport layer in perovskites solar cells.[171] In addition, both CZTS and CZTSe have received attention for thermoelectric application.[172] When the carrier density is optimized, they have shown potentially outstanding mid-to-high temperature performance, in part due to their complex structure and intrinsically low thermal conductivity. This was achieved through Cu-rich [172–175] or Sn deficient

[176,177] stoichiometries. These strategies rely on the conversion of the insulating ZnS_4/Se_4 and SnS_4/Se_4 pathways into conducting pathways by the substitution of Zn and Sn for Cu in the CZTS/Se compounds [172]. The vacancy cluster-induced localized disorder on the domains reported for CZTSe by Li *et al.*[177] also improved the TE performance for this system, an effect which proved to be superior to the enhancement due to phonon-glass electron-crystal from nanostructuring. The extrinsic doping with Na,[178] Ag,[130] Ni,[179] and Ga[180] also have shown significant improvement in the performance of these materials. In addition, the disorder in these systems introduced by temperature,[70,71] chemistry,[177] or synthesis method [122,132,143] revealed to be critical to their improvement as TE materials.

In the present work, we summarize recent advances in disordered CTS, CZTS and CZTSe materials and discuss the effects of cation disorder on the TE properties. The rest of this article is structured as follows. First, we examine the various crystallographic structures of these compounds. Subsequently, we discuss the intrinsic disorder present in these systems, as reflected in the root-mean-square displacement (RSMD), through a combination of ab initio molecular dynamics (AIMD) and in situ SR-XRD. This is followed by a discussion of the rich and diverse phenomenology behind the electron and phonon transport mechanisms in these disordered materials, and how they affect the key thermoelectric properties. Finally, we conclude with a brief description of the atypically inverse dependence of the electrical conductivity on the sample grain size in both CZTS and CTS, and the different origins of this behavior in the two compounds.

6.2 Experimental and computational methodology

Synchrotron

High-resolution synchrotron radiation X-ray diffraction (SRXRD) measurements were performed at the 11bm beamline of the Argonne National Laboratory. Data were collected at 300K, 200K, 100K using a blower for cooling and at a wavelength of 0.45820 Å, in the 2θ range 0-50°. In the temperature range 90K-10K, data were collected every 20K using a Helium cryostat for cooling, a wavelength of 0.44262 Å and a 2θ range of 0-46°. LaB_6 standard patterns were collected to model the instrumental profile. Specimens were loaded in an Ar filled glovebox in 0.3 mm-diameter (for CZTSe) and 0.5 mm-diameter (for CZTS) Kapton or glass capillaries and diluted with 70%vol borosilicate glass powder. This was done to reach linear absorption coefficients μR < 0.3 and keep systematic deviations in intensity between low and high angles below <1%, thus yielding greater confidence in the estimation of Debye-Waller coefficients.

In a similar manner, temperature-dependent SXRD measurements were performed on ordered and disordered CTS samples from 50° C to 500° C with the step of 50°C at MS-Xo4SA: Materials Science beamline, Swiss Light Source, Paul Scherrer Institut. SXRD data was collected using **MYTHEN II** detector in 2θ range 0-60°, while the beam wavelength was 0.56300 Å.

Rietveld refinements of XRD data were performed with the software TOPAS version 6.[69] For cubic and tetragonal CZTS, and monoclinic and cubic CTS, refinements were based on structure models described in previous work from some of the authors.[181] Cubic CZTSe has been modelled as a zinc-blende *F-43m* structure, with full cation disorder on the cation site, keeping an occupancy ratio of 0.5:0.25:0.25 for Cu:Zn:Sn. Tetragonal CZTSe has been modelled with a *I-42m* disordered kesterite structure (see[181] for details). Crystallite size analysis was carried out with the support of macros based on whole

powder pattern modelling(WPPM) [182,183]. Microstrain was estimated with built-in TOPAS macros. For the estimate of Debye-Waller coefficients, a unique B_{iso} has been used for all the cation sites of the tetragonal samples, to allow a comparison with the single cation B_{iso} of the disordered cubic samples.

Raman spectroscopy

Raman spectra were collected with a WiTec spectrometer model alpha 300 RA, using a grating of 1800 g/mm, and with a spectral center at 700 1/cm. A 488 nm laser was employed with a power of 0.5 mW. The measurements were performed with an integration time of 40 s and with 100 accumulations.

TE measurement: The Seebeck coefficient and resitivity were simultaneously measured in four contact set-up using LSR-3 Linseis Messgeraete GmbH. The thermal diffusivity (D) was measured using LFA-500 from Linseis Messgeraete GmbH.

Low temperature mobility measurements

Resistivity (ρ), magneto resistivity (ρ(H)- ρ(H=0)/ ρ(H=0), and Hall effect data were measured in a PPMS (Physical Properties Measurement System) by Quantum Design, at temperatures from room temperature down to 10 K and in magnetic fields up to 9 T. More specifically, resistivity was measured using a standard four probe method, and the Hall resistance RH was determined by measuring the transverse resistivity at selected fixed temperatures, sweeping the field from −9 T to 9 T. From ρ and RH, the concentration and mobility of charge carriers were extracted in a single band picture.

Computational

The ab initio molecular dynamics simulations were performed using the Vienna ab initio simulation package (VASP) [61,62] A 192-atom and 216-atom supercell were used to represent the ordered and disordered cubic polymorphs of CTS respectively. While a 64-atom supercell was used to represent both the ordered tetragonal and disordered cubic polymorphs of CZTSe. The disordered structures were modelled by randomly assigning the cation site. The electron-exchange-correlation function was approximated by the PBE.[26] All calculations were performed with an energy cut-off of 400 eV and with a Gaussian charge smearing of 0.1 eV. The irreducible Brillouin zone was sampled on a single point 1×1×1 Monkhorst Pack gamma-centred k-mesh. Molecular dynamics simulations were performed in a canonical (NVT) ensemble with a Nose-Hoover. In each case, the system was allowed to evolve with a time step of 2 femtoseconds, for 5000 steps, corresponding to a total simulation time of 10 picoseconds. All the structures were relaxed until the force on each atom was <0.01 eV $Å^{-1}$, using a Gaussian smearing of 0.01. The electronic convergence was set to 10^{-6} eV. For the density of states calculation, the hybrid HSE-06[184] exchange-correlation functional was used with a denser k-mesh of 6×6×6 for disordered cases while 8×6×8 for monoclinic case. The phonon dispersion curves are obtained using the density functional perturbation theory. PHONOPY code[29] was used to diagonalize the dynamical matrix to calculate the interatomic force constants from which the phonon dispersion curves were calculated.

6.3 Results

6.3.1 Structure and Nature of Disorder

Various preparation methods, such as solid-state reaction [50], hot-injection,[185] ball-milling [70,71] have been proposed in the literature for the synthesis of Cu-based chalcogenides,[186,187] They have a low formation

energy, which makes them suitable to be prepared via high-energy reactive milling in a highly controlled atmosphere,[138] Usually, the disordered phases of CTS are prepared by high-temperature solid-state reactions with acceptor doping,[48,114] while the disordered cubic phases of CZTS and CZTSe coexist in small phase fractions with their ordered phase. In our previous work, the disordered phases of all three compounds were stabilized by high-energy reactive milling.[32,54,70,122,169] This is only possible because of the highly entropic environment promoted by ball-milling, which is known to form unique metastable phases. The modern understanding of the mechanochemical reaction is based on the transfer of electrons and exchange of ions[159] in the interfacial component of the milled material during the process of phase nucleation. Due to this phase formation process, a more "kinetic" state of matter is achieved when compared to other solvent-dependent bottom-up approaches.[162,188] This characteristic of mechanochemistry promotes the formation of metastable phases and, for the systems studied here, the structural disorder attained is so high that the crystal structure is better described by a cubic symmetry. The preparation of the samples by ball-milling also offers the unique advantage of preserving the nanostructure, maintaining a high density of crystalline defects, and an inhomogeneous distribution of finely dispersed crystalline grains. Apart from this, mechanochemistry is in line with the 12 principles of green chemistry,[189] especially in terms of limited solvent use, lower energy consumption, and suitability for low-cost large-scale production.[143]

Regarding the Cu-based alloys, CTS has three widely reported structures – the ordered monoclinic (*Cc*), tetragonal ($I\bar{4}2m$) and the disordered cubic ($F\bar{4}3m$). Recently, an orthorhombic ($CmC2_1$) CTS polymorph was produced [116]. CZTS and CZTSe on the other hand, have

three polymorphs: an ordered tetragonal ($I\bar{4}$), a disordered tetragonal ($I\bar{4}2m$) with Cu-Zn disorder, and a disordered cubic ($F\bar{4}3m$) with a full-cation disorder. The schematic diagram of the structures, all based on a diamond-like tetrahedral coordination, is presented in Table 1. The disordered cubic polymorphs are a variant of the zincblende (ZnS) structure, which consists of tetrahedral S-cages (Wyckoff position 4*c*) with a cation (Zn) positioned in the centre (4*a*). In disordered CTS, the Zn cation is randomly replaced by Cu and Sn, leading to a partial cation occupation of 2/3 and 1/3 for Cu and Sn, respectively. In the case of the disordered cubic CZTS and CZTSe, the Zn cation is replaced by Cu, Zn and Sn in partial occupation of 1/2, 1/4, and 1/4, respectively.

CZTS and CZTSe show a reversible temperature-dependent phase transition, also observed in analogous quaternary chalcogenides [190]. In the ordered form, they crystallise in the Kesterite structure with the tetragonal space group *I-4*, consisting of alternating Cu-Zn and Cu-Sn layers sandwiched between the anion (S/Se) layers. At relatively low temperatures, CZTS/Se shows a structure transition from *I-4* to a partially disordered tetragonal structure with space group *I-42m*. In this, due to the large chemical and size mismatch between Cu and Sn, an appreciable disorder is only possible on the Cu–Zn sublattice, while the Cu-Sn layer remains ordered. Nevertheless, the structural complexity of these quaternary chalcogenides frequently causes the occurrence of various types of structural defects even close to room temperature. The most common one is the Cu_{Zn} substitutional, which is believed, along with Cu vacancies, to be the cause of the *p*-type nature of Kesterite and has the lowest formation energy among the possible defects [191–193].

Table 6.1. Structural information for the different polymorphs of CTS, CZTS, and CZTSe. The structures have been produced using VESTA software. [194]

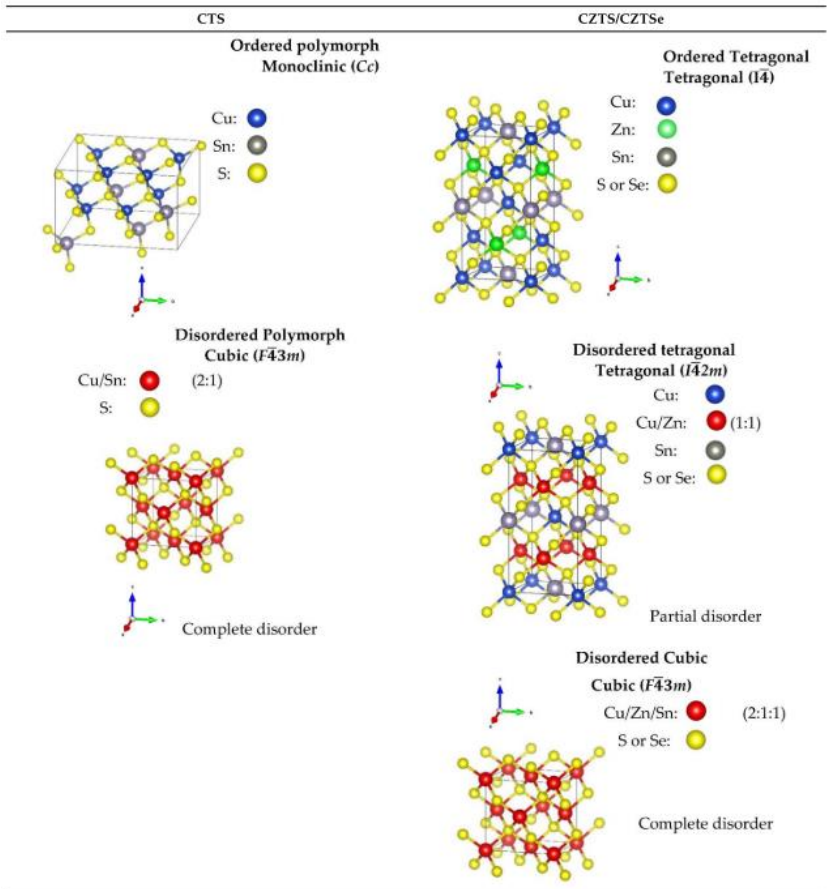

The difference between monoclinic and cubic polymorphs of CTS is quite evident from the structural data. It has been shown by the combination of XRD, SAED (see supplementary file Figure 6.S2) and Raman spectroscopy. [54] The cubic CTS did not show critical low-angle reflections in XRD and SAED patterns. Moreover, two distinctive Raman modes were observed (at 283 cm^{-1} and 337 cm^{-1}) for disordered cubic CTS.[54] Regarding the CZTS/Se system, the difference between disordered cubic CZTS/Se (*F-43m*) and disordered tetragonal CZTS/Se (*I-42m*) are the superstructure reflections visible through the low-angle Bragg-peaks in XRD and the observed new rings in the SAED patterns

[45–47]. These transitions were also observed in DSC measurements for CZTS/Se.[122,132] The SR-XRD for the monoclinic and cubic CTS at 350˚ C is shown in Figure 6.1. The SR-XRD result for the different temperature is shown in the Appendix (Figure 6.S1). Table 6.2 reports the structural parameters and band gap of various polymorphs.

Figure 6.1. SR-XRD measurements on monoclinic (a), and cubic (b) Cu_2SnS_3 polymorphs collected at 350˚ C. The zoomed images show the superstructure Bragg peaks (2θ< 10˚) for monoclinic CTS phase representing (110), (11-1), and (021)

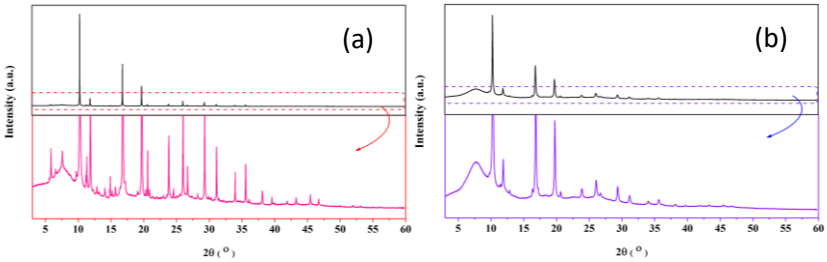

reflections. These superstructure Bragg peaks are absent for the cubic CTS phase. The broad peak with diffused background at low 2-theta is due to the use of borosilicate glass for the dilution of samples.

Table 6.2. Structural information and band gap values for the different polymorphs of CTS, CZTS, and CZTSe.

	CTS	**CZTS**	**CZTSe** [132]
Lattice parameters	*Ordered* a = 6.660(1) Å b = 11.536(2) Å c = 6.660(1) Å *Disordered* a = 5.4316(1) Å	*Tetragonal* [181] a = 5.4345(1) Å b = 5.4345(1) Å c = 10.8380(1) Å *Disordered cubic* [181] a = 5.4150(1) Å	*Tetragonal* a = 5.69706(3) Å b = 5.69706(3) Å c = 11.3472(1) Å *Disordered cubic* a = 5.68719(9) Å
Band gap	*Ordered* [32] 0.99 eV *Disordered* [32] 0.95 eV	*Tetragonal* [122] 1.56 eV *Disordered cubic* [122] 1.53 eV	*Tetragonal* [196–198] *0.9-1.5 eV*

Role of Disorder:

The combination of molecular dynamics simulations and XRD measurements with WPPM modelling [68,183] has been demonstrated to be a simple yet effective measure of atomistic disorder [181], with a remarkable agreement between theory and experiment. To observe the effect of structural disorder on the RMSD, the temperature evolution of the ordered and disordered CTS, CZTS [181], and CZTSe was investigated by temperature-dependent XRD and AIMD simulations. The disordered CTS presented a higher value of the Grüneisen parameter (a measure of anharmonicity) when investigated by nuclear inelastic scattering, results which were verified by calculating the mode Grüneisen parameter in the quasi-harmonic approximation using DFT [32]. As such, the evolution of RMSD value was expected to be higher in the case of disordered CTS/CZTS/Se as compared with the ordered

counterpart. XRD patterns for CTS were collected in the temperature range from 323 K to 773 K with a step size of 50 K. While for CZTSe were collected from 25 K to 300 K. In Rietveld refinements, the value of isotropic Debye-Waller coefficient (B_{iso}) for all the cation positions was assumed to be the same. From the B_{iso}, the RMSD was calculated using the following relation, where $\langle u^2 \rangle$ is the mean squared displacement (MSD):

$$B_{iso} = \frac{8\pi^2}{3}\langle u^2 \rangle \ldots (6.5)$$

Figure 6.2 shows the results of RMSD calculated from the temperature dependent XRD and AIMD simulations. As expected, the value of RMSD increased with temperature for all the polymorphs, implying that the amplitude of the atomic vibrations increases with temperature. The RMSD value for the disordered polymorph was higher than the ordered phase, pointing to an increased static disorder. This corresponds to the static (temperature-independent) distortion in the crystalline lattice due to cation disorder and is connected to higher anharmonicity and bonding inhomogeneity in the disordered phase, which is then directly responsible for the ultra-low thermal conductivity. For CZTS/Se, the RMSD values calculated using AIMD simulations agree well with the experimental results.

For CTS, the RMSD values calculated from the experiment and the AIMD simulation are in qualitative agreement. A slight deviation was observed in the absolute RMSD value was observed. The reason for this discrepancy could be due to the clustering effect observed in the CTS systems.[56] The clustering effect in CTS structures restricts the formation of S−Cu_4, S−$CuSn_3$, and S− Sn_4 motifs. In ordered CTS, a regular distribution of S−Cu_2Sn_2 and S−Cu_3Sn motifs was observed, while in disorder CTS, S−Cu_2Sn_2 motifs form nanometre-scale clusters.

This consideration of clustering was not considered in the modelling of the system, due to the limitation of plain wave density functional theory in handling systems of the nanometre range.

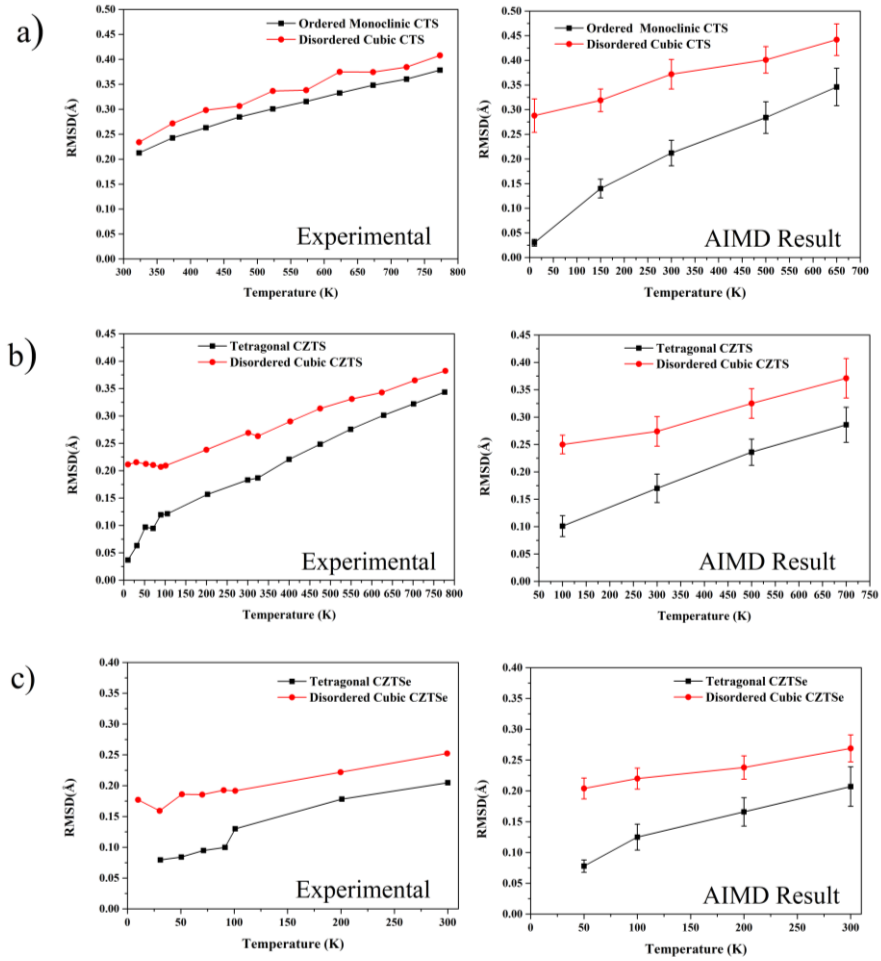

Figure 6.2. Temperature variation of RMSD calculated from SXRD and AIMD simulation for CTS (a), CZTS (b), and CZTSe (c)

Overall, the emerging key result is that the disordered compounds present an additional temperature-independent contribution to the RMSD. Indeed, the highly varying coordination environment and bonding inhomogeneity in these phases likely lead to non-uniform distortions in the coordination tetrahedra. This, by bulk-averaging techniques like XRD, is collectively observed as an increase in the RMSD. This interpretation is also supported by the significant broadening of Raman peaks for the disordered compared to the ordered compounds, illustrated for CZTS and CTS in Figure 6.3. As visible, the disordered phases show peaks approximately at the same locations, but significantly broader. This likely reflects the larger distribution of vibrational frequencies associated with specific phonon modes, due to the contribution of highly inhomogeneous bonds and non-uniform coordination environments. A similar broadening was also observed by other studies on mechanically alloyed CZTS in the literature.[199]

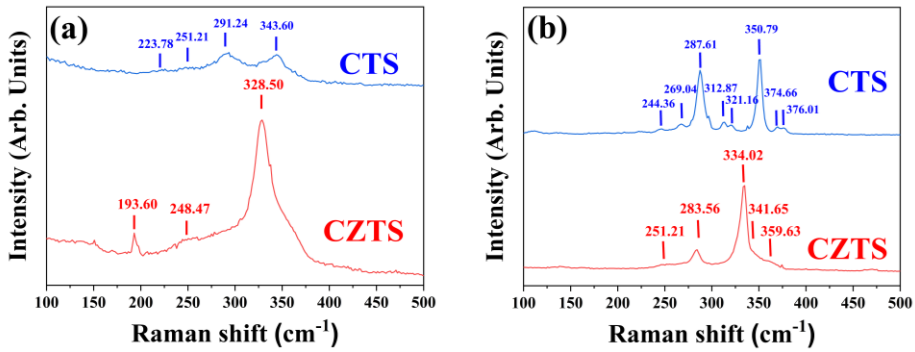

Figure 6.3. Raman spectra collected with a 488 nm laser on as-milled (a) and thermally treated (b) samples of CTS and CZTS. The samples in (a), in the disordered cubic phase, display significantly broader peaks than the ordered (monoclinic CTS and tetragonal CZTS) phases in (b). This is believed originating from cation disorder itself, likely causing variable coordination environments and inhomogeneous bonds, leading to a spread in vibrational modes.

6.3.2 Electronic properties:

Seebeck coefficient, resistivity, and power factor

All polymorphs of CTS, CZTS and CZTSe exhibit a positive absolute Seebeck coefficient, due to their p-type nature (shown in Figure 6.4). Both the ordered and disordered polymorphs of CTS are stable up to 723 K. The tetragonally ordered CZTS/Se samples were also studied up to 723 K and showed a reversible phase transition to the tetragonally disordered phase above 500 K and 400 K, respectively. However, the cubic/disordered polymorphs of CZTS and CZTSe from mechanical alloying were stable up to ~500K and 600K, respectively.

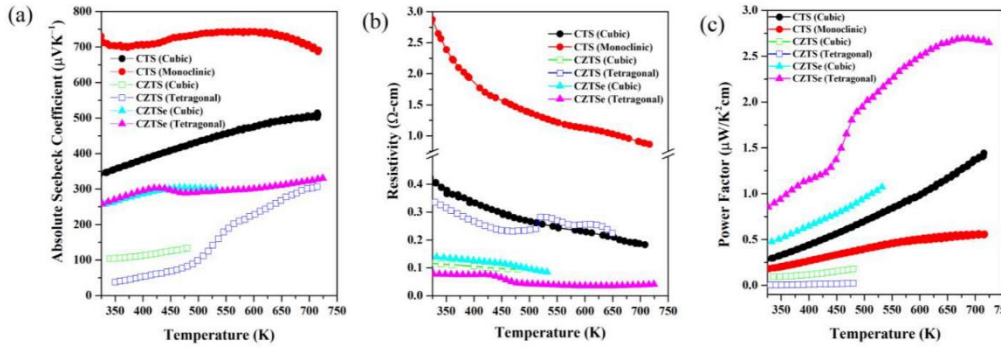

Figure 6.4. Temperature-dependent Seebeck coefficient (a), electrical resistivity (b), and power factor (c) curves for CTS, CZTS, and CZTSe polymorphs retrieved from[32,71,122,132]

As all the samples discussed were undoped, they exhibited a non-degenerate nature of the electrical resistivity. Monoclinic CTS presents the highest Seebeck coefficient (S~ 700-750 μV/K) and a non-linear trend in temperature. It has been reported that this trend is caused by bipolar contributions to charge carriers [48]. Interestingly, tetragonal CZTS exhibits a sharp increase in the Seebeck coefficient due to the order-disorder transition, while the same transition causes a slight decrease in the Seebeck coefficient for CZTSe. The origin of this

behaviour is explained in the following section. It is important to note that CZTSe samples are generally more conductive than CTS and CZTS, with tetragonal CZTSe having the lowest resistivity (< 0.1 Ω-cm) among these samples. This is due to the Cu-Se conduction network, which should be more conductive than the Cu-S conduction network.

In contrast with ordered CTS, disordered CTS shows a linearly increasing See-beck coefficient. Furthermore, disordered CTS presents a lower Seebeck coefficient and resistivity than monoclinic/ordered CTS. In terms of overall power factor, CZTSe samples perform better than CZTS and CTS. When comparing polymorphs of the same composition, it can be generalised that the disordered ones (i.e., disordered cubic for CTS and CZTS and disordered tetragonal CZTSe) have better performance than their ordered counterparts.

The role of electronic structure

As discussed, the tetragonal order-disorder transition in CZTS/CZTSe manifests in a variation of the Seebeck value, which sharply increases for CZTS, and moderately decreases for CZTSe at the transition temperatures of ~500 K and ~450 K, respectively. This behaviour is associated with two different mechanisms, as shown by first-principles calculations [71,132]. In both cases, the disorder contributes to a flattening of the bands (increasing the Seebeck coefficient) and suppression of the band gap (decreasing the resistivity). However, in the case of the sulphide, the Cu-Zn disorder generally leads to a convergence in the energy of the three valence bands at the Gamma point, whereas in the case of the selenide it leads to a divergence of the same bands. This opposite behaviour is the result of two competing effects: homogenisation of the charge density and crystal field splitting. In CZTS, the Cu-Zn disorder leads to a homogenisation of the local bonding environment around each ion since the electronic

configurations of Cu and Zn differ by only a single electron. In contrast, the presence of the heavier Se ions in CZTSe leads to a stronger crystal field splitting, causing the energy levels to diverge. Despite this variation in mechanism, both disordered tetragonal polymorphs show an improved power factor compared to their ordered counterparts. The conduction and valence bands are derived from anion-*p* and Cu-*d* electrons. For the cubic polymorphs of CZTS and CZTSe, the bulk band structures are significantly flattened compared to the ordered polymorphs, corresponding to a reduced charge carrier mobility, in turn resulting in an increased Seebeck coefficient. In addition, the band extrema of the two quaternary chalcogenides show deviations from the standard parabolic nature, in the form of anti-crossing or "camel's-back" features (see Figure 6.10(a)). These features are accompanied by band inversion - a localised reversal of orbital contributions - with Cu-*d* orbitals dominating the conducting band minimum (CBM) and anion-*p* orbitals dominating the valence band maximum (VBM). Band inversion is associated with topological insulators, and in this respect, disordered cubic CZTS is of particular importance, as these topological features are not present in either the ordered or disordered tetragonal forms. This indicates a topologically non-trivial behaviour caused by the complete disorder of the cations, and as such, it has been predicted to be the first topological Anderson insulator in a real material system[200]. In CZTSe, on the other hand, all polymorphs show band inversion in the bulk band structure and have been theoretically predicted to be topological insulators.

The electronic density of states of the different polymorphs of the three compounds shown in Figure 6.5 shows strong similarities. In the VBM of CTS, the main contribution to DOS is made by Cu 3d and S 3p orbitals, while the CBM consists of Sn 5s and S 3p orbitals. In CZTS,

the states in the VBM are dominated by Cu 3d electrons, while the states in the CBM consist mainly of S 3p orbitals. In the case of CZTSe, the valence band in each polymorph is strongly hybridised between contributions from Cu 3d and Se 4p orbitals, while the conduction band is dominated mainly by Se 4p orbitals. The structural disorder leads to fluctuations in the potential energy landscape of the lattice, allowing energy levels within the forbidden gap, which are responsible for the band tailing and reduced band gap. In the case of CZTS and CTS, these states are highly localized and located near the valence band, can be observed from the inverse participation ratio (IPR) plot in Figure 6.5. These states trap electrons from the VB, leading to an increase in the number of holes without a corresponding increase in the number of electrons in the conduction band. This leads to an increase in the p-type charge carrier concentration, as measured experimentally. The Figure 6.6 shows a schematic diagram of the effects of highly localized intermediate gap states near the valence band. These localized trap states lead to a significantly higher power factor for disordered cubic CZTS and CTS. However, in the case of CZTSe, these states are distributed over the en-tire gap and are less localised. Therefore, the cubic polymorph shows a conventional behaviour with a lower conductivity and a higher Seebeck coefficient, with an overall lower PF comparable to the tetragonal phase.

The electronic structure calculations presented in the previous works were limited to the use of the Perdew-Burke-Ernzerhof (PBE)[26] exchange-correlation functional due to the limited computational resources and time constraints. In this work, the electronic structure calculations were performed using the hybrid Heyd-Scuseria-Ernzerhof (HSE)[184] exchange-correlation functional, which provides a better description of the band gap. These results confirm that band tailing and

mid-gap states are an intrinsic part of the electronic density of states for the disordered structures.

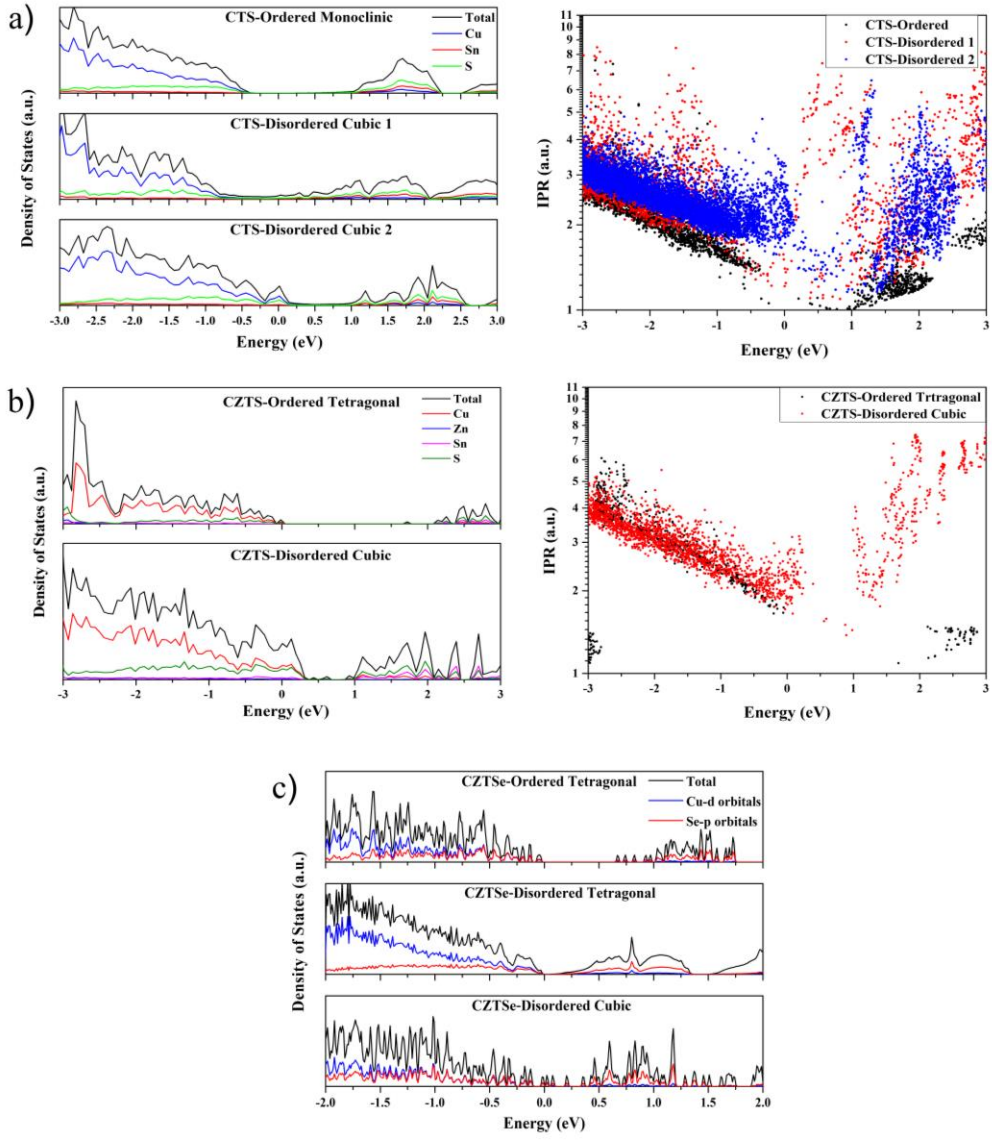

Figure 6.5. The total and atomic projected electronic density of states for CTS ordered monoclinic, CTS Disordered Cubic 1 (Cu-21, Sn-11, S-32), and CTS Disordered Cubic 2 (Cu-22, Sn-10, S-32) (a), CZTS (b), and CZTSe (c) polymorphs. Here, the Fermi level is set to zero. The IPR for the CTS and CZTS shows localized states near the Fermi level.

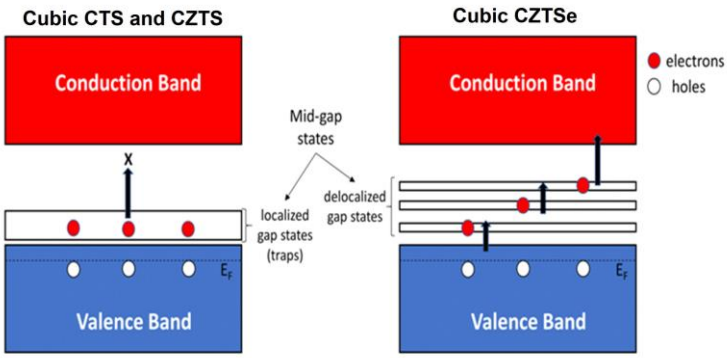

Figure 6.6. A schematic diagram showing the effect of mid-gap states: In cubic CTS/CZTS, the localized nature of these states acts to unilaterally enhance hole concentration at finite temperature by 'trapping' electrons. For cubic CZTSe instead, these states are delocalized within the gap, and therefore do not act as traps.

6.3.3 Thermal conductivity:

The most dramatic improvement in the TE properties of these disordered cubic chalcogenides is due to a significant reduction in thermal conductivity. Figure 6.7(a) shows the variation of thermal conductivity of all polymorphs. The thermal conductivity for CTS and tetragonal phases of CZTS/Se follows a T^{-1} trend, indicating that the thermal conduction is dominated by Umklapp scattering. In the case of cubic CZTS/Se, the low values of thermal conductivity remained almost constant over a wide range of temperatures. This suggests an additional, temperature-independent contribution to the low thermal conductivity. The trend in thermal conductivity clearly shows the effects of structural disorder. It is worth noting that all the samples discussed have a lower density (~20 - 25 %) than the theoretical one, which is due to the preparation method where manual cold pressing was used. However, the comparison between the above samples is fair as they have similar densities and the same preparation method. It should be noted here that the literature increasingly recommends the use of

low-density materials for TE applications to reduce the cost and quantity of materials used.[201,202] However, the effect of low density appears to be less pronounced for electronic transport [138]. The ultra-low thermal conductivity of CTS samples was pertinent even after employing spark plasma sintering[169]

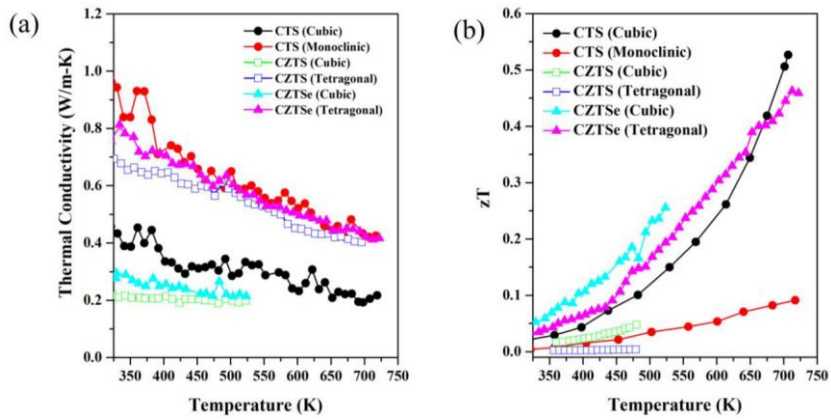

Figure 6.7. Temperature-dependent thermal conductivity (a) and zT (b) for CTS, CZTS, and CZTSe polymorphs data retrieved from [20,34,51,52]

Regardless of the three different materials discussed in this article, the disordered cubic polymorphs have the lowest thermal conductivity, featuring values less than half that of their monoclinic and tetragonal counterparts. These samples showed a non-degenerate trend of resistivity as a function of temperature, with high values of resistivity. This suggests that the electronic contribution to κ is minimal and that the lattice thermal conductivity dominates κ.

The first-principle calculations show that all three cubic compounds have similarities in their phonon dispersion, with a lower slope of the acoustic modes (lower group velocity) compared to their ordered counterparts and low-lying optical modes (Figure 6.8). These low-lying optical modes interact with the heat-carrying acoustic modes and lead to the dissipation of thermal energy. The possibility of this dissipative

scattering is enhanced by the dense band of optical modes present (due to disorder) in all disordered polymorphs above 1.25 THz, which provides multiple channels for scattering. In cubic CZTS, these low-lying modes are directly associated with the rattling of certain Sn ions, which are characteristic features of this compound. Due to the retention of the lone Sn *s2* pair in cubic CZTS, certain Sn ions form electron-poor bonds with the coordinating S ions (see Figure 6.9(a)). These weakly bound Sn ions contribute to low-frequency vibrational modes in the DOS vibration and are additionally responsible for the nature of the electronic states within the band gap, which fundamentally affects the electrical transport properties as described above. Interestingly, these rattling ions are not present in CZTSe and CTS. In particular, the electron localization function showed an inhomogeneity in bonding for cubic CTS (see Figure 6.9(b)), leading to a higher anharmonicity, which was confirmed by the calculation of the mode Grüneisen parameter by DFT and Nuclear inelastic scattering (NIS) measurements. The strong anharmonicity leads to an overall ultra-low thermal conductivity.[32]

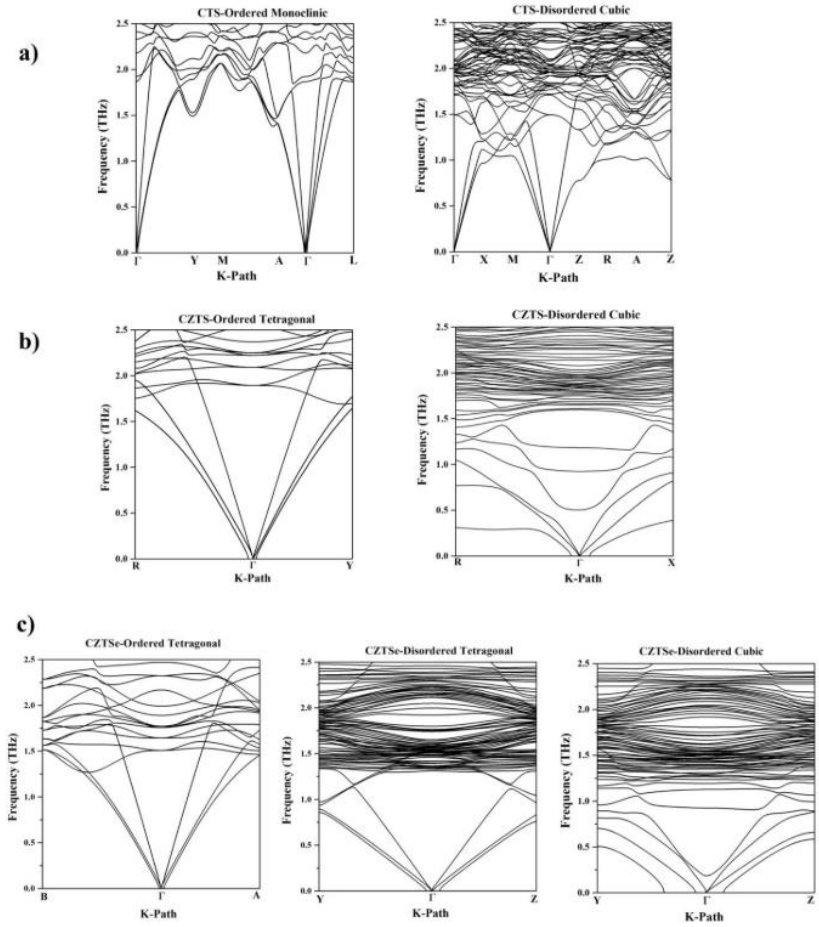

Figure 6.8. Phonon dispersion curve for CTS (a), CZTS (b), and CZTSe (c) polymorphs. The effect of structural disorder on the phonon dispersion curve manifests itself in the form of a gentle slope of the acoustic branches and the low-lying optical modes.

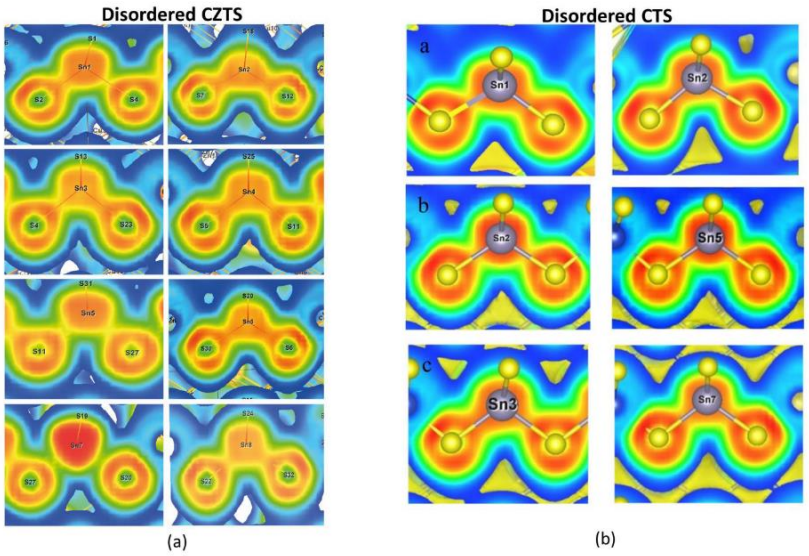

Figure 6.9. The calculated electron localization function mapped on to the Sn-S bonds in (a) disordered CZTS and (b) disordered CTS. The ELF distribution for certain Sn ions shows a strong bonding inhomogeneity in both systems, with only CZTS showing lone-pair localization in a fraction of ions (for example see Sn7 in the panel in the bottom left corner of the figure). These images are taken from [32,122]

The disordered cubic polymorphs have a higher *zT* than the monoclinic or tetragonal ones. The inherently low thermal conductivity of high symmetric cubic polymorphs suggests a phonon-glass electron crystal behaviour, as the remarkable kappa suppression does not negatively affect the electronic conductivity. Similar effects are also reported for CTS samples prepared by different preparation techniques such as open die pressing(ODP) and traditional sintering, resulting in samples with different proportions of porosity.[138]

From near room temperature to intermediate temperatures, CZTSe polymorphs appear to have the best performance among these samples. Cubic CZTSe, which is stable up to 500 K, shows the best performance over the entire measured temperature range, exhibiting a *zT*~0.25 at 500 K. Interestingly, cubic CTS performs better than all other samples at the highest measured temperature of ~723 K, resulting in a *zT*~0.5. This

performance is followed by tetragonal CZTSe, which has a zT~0.45 at 723 K. Similarly, cubic CZTS performs better than its tetragonal polymorph, which exhibits a zT~0.05 at 500 K. The main reason for the low performance of monoclinic CTS and tetragonal CZTS is their higher electrical resistivity and thermal conductivity compared to their disordered phase. Although the overall thermoelectric figure of merit of these materials is moderate, it is worth noting that disorder causes a significant enhancement of zT, leading to the highest performance for undoped compositions. This indicates a clear direction for optimization of this family of compounds. Here, we put forward, that the low-density doped samples of these sustainable materials could be interesting study cases for thermoelectric performance analysis, thanks to their highly suppressed thermal conductivity and relatively high electrical conductivity.

6.3.4 Effect of grain size:

The synthesis route of high-energy reactive ball-milling helps to stabilise the disordered phases at low temperatures through nano structuring. The use of different sintering conditions leads to a variation in the average grain size of the nanoparticles. Larger grains have fewer grain boundaries and thus less electron scattering, which usually leads to higher electrical conductivity. Interestingly, disordered cubic CZTS and CTS show the opposite trend, where samples with smaller grain sizes possess higher electrical conductivity. This trend is in contrast to the mechanism of grain boundary scattering normally observed in TE materials.[203] In fact, the evidence points to beneficial surface effects in these compounds. Interestingly, the reason for this trend is quite different for the two compounds - the small-grained samples (below 50 nm)[169] from CTS show an increase in carrier concentration compared

to the larger-grained samples, while CZTS shows an increase in carrier mobility.

The topological properties of cubic CZTS should favour large surface mobility. This should partially compensate for the low bulk mobility observed instead in the band structure, which is related to bulk cation disorder. To highlight the contribution of the surface to mobility, one can look at the behaviour of samples where surface states should be increasingly dominant (e.g. the trend of mobility with progressively smaller grain size, see ref.[200]). Alternatively, measurements at low temperature or in the presence of a magnetic field should highlight the contribution of surface states. Indeed, the positive contribution to magnetoresistance at low temperature is greater in the cubic polymorph than in the tetragonal phase (see Supplementary Figure 6.S3), indicating greater carrier mobility in the former sample. The mobility measurements below room temperature show an order of magnitude higher upper limit for the cubic phase compared to the tetragonal phase (see Supplementary Figure 6.S4). The greater mobility of the cubic polymorph below room temperature (where elastic scattering due to disorder should dominate over inelastic scattering) is experimental evidence in favour of the topological surface states hosted in cubic CZTS due to the theoretically predicted topological Anderson insulator (TAI) behaviour.[200] These topologically protected, quasi-gapless states, immune to backscattering, are then responsible for the transport of charge carriers with higher mobility, leading to increased electrical conductivity.

For CTS, the improvement in charge carrier concentration is attributed to the stoichiometry of the grain surface, which forms incomplete bonds due to the change in coordination number caused by surface termination. Due to the dangling bonds on the surface, localised states

near the Fermi level are present. These dangling bonds provide additional charge carriers (holes), which increase the charge carrier concentration and lead to degenerate semiconductor-like behaviour.[169] Similar results have been obtained for the disordered CTSe system.[204]

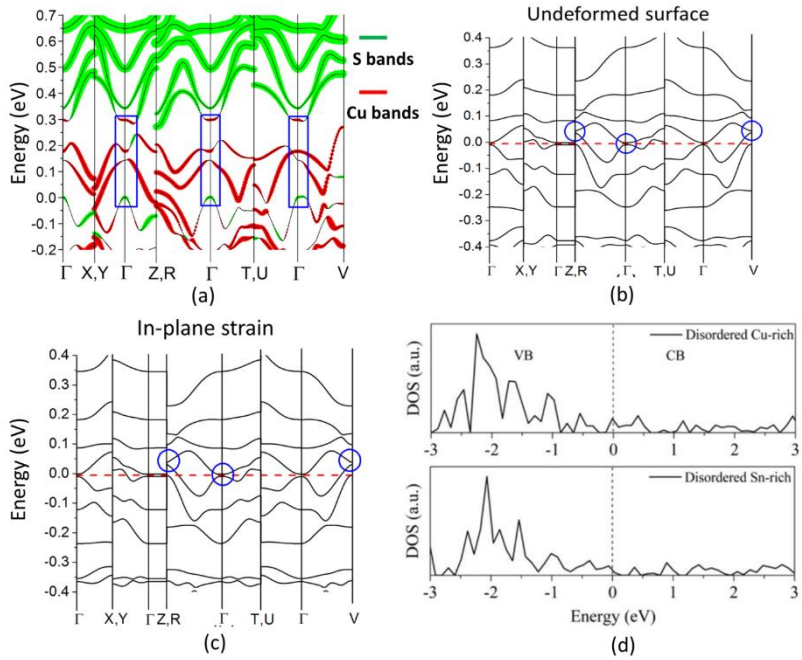

Figure 6.10. (a) Bulk band inversion and (b) topological surface states in pristine form and (c) under in- plane strain for disordered cubic CZTS; (d) surface DOS for disordered cubic CTS showing metal-like surface states. These band structure and density of states plots are taken from [56,74]

6.4 Conclusion

Herein, we have presented a comparative study of the TE properties for various disordered polymorphs of the low-toxicity, earth abundant chalcogenides CTS, CZTS, and CZTSe, synthesized via high-energy reactive milling. The low-cost synthesis route is crucial in stabilizing the polymorph with cubic structures and complete cation dis-order. The CTS system exhibits a monoclinic and a disordered cubic arrangement,

while CZTS and CZTSe shows tetragonal, disordered tetragonal, and disordered cubic structures. The effect of disorder was quantified by calculating the RMSD for ordered and disordered phases using AIMD simulations and comparing the results with temperature dependent XRD. This structural disorder promotes the optimization of the electrical and thermal transport properties through various mechanisms. The ternary disordered CTS presents a better electrical conductivity than the ordered CTS due to the reduction of band gap and band tails, while the large anharmonicity and inhomogeneous bonds lead to extremely low thermal conductivity. The quaternary systems of CZTS and CZTSe show a temperature-activated phase transformation for the tetragonal phase from an ordered tetragonal to a partially disordered tetragonal arrangement. Moreover, CZTS and CZTSe can be stabilized at low temperatures in a novel disordered cubic phase with full cation disorder. This disorder manifests itself in the form of simultaneous enhancement of the Seebeck coefficient and electrical conductivity in CZTS due to band engineering. In addition, disordered cubic CZTS has been predicted to be a topological Anderson insulator, with topologically protected surface states, a prediction supported by the experimental measurements of high mobility at very low temperatures. Furthermore, because of the bonding inhomogeneity, the disordered cubic phases of the two quaternary compounds also showed ultra-low thermal conductivity, due to anharmonicity, as well as low phonon group velocity and low-lying optical modes. The RMSD showed a higher value for disordered phases, confirming a higher degree of anharmonicity in the cubic disordered phases, which is responsible for ultra-low thermal conductivity. Finally, both CTS and CZTS show the presence of beneficial surface states, making these materials highly suitable for nano structuring. The combination of these diverse and intriguing transport mechanisms and the high chemical tunability of the

complex structures leads to competitive thermoelectric performance and makes this class of materials a promising candidate for the fabrication of high-performance, sustainable thermoelectric devices.

Appendix

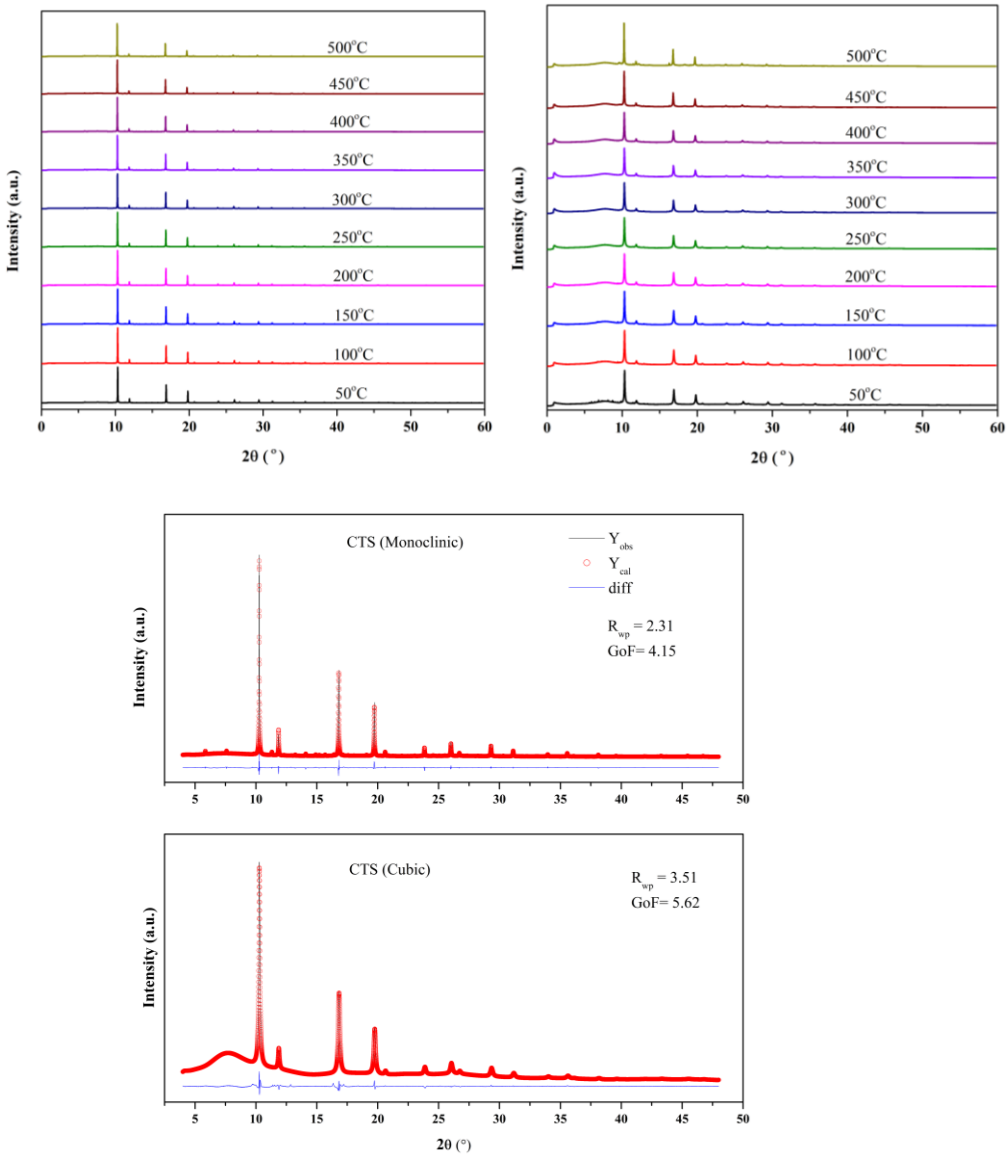

Figure 6.S1. Temperature dependent SXRD measurement on CTS Ordered (a) and disordered cubic (b) Rietveld refinement performed on ordered and disordered CTS XRD data collected at 350˚C, where $Y_{obs,}$ Y_{cal}, and diff are collected, calculated and difference, respectively. The value of R_{wp} and GoF for other patterns were similar to the values observed here.

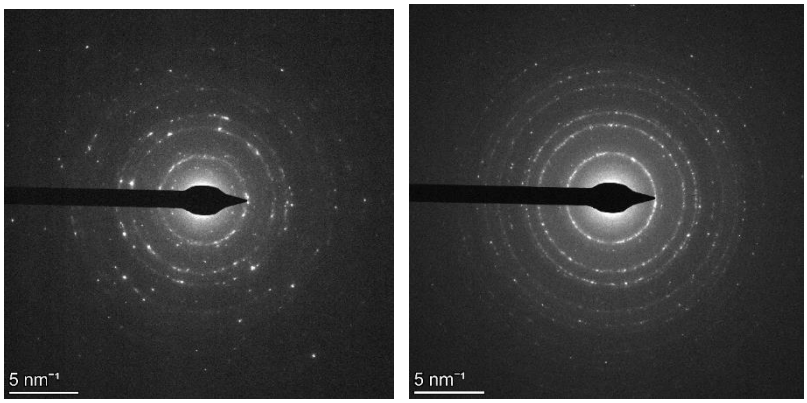

Figure 6.S2. SAED patterns for of (a)Monoclinic CTS and (b)Disordered Cubic CTS. It is evident from SAED the inner Debye-Scherrer rings are missing for Disordered Cubic CTS representing, (11-1), (021).

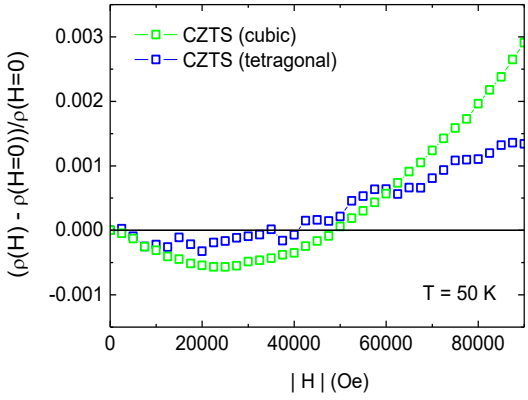

Figure 6.S3. Magnetoresistivity (ρ(H)-ρ(H=0))/ρ(H=0) of (a)Tetragonal CZTS and (b)Disordered Cubic CZTS, measured at T=50K

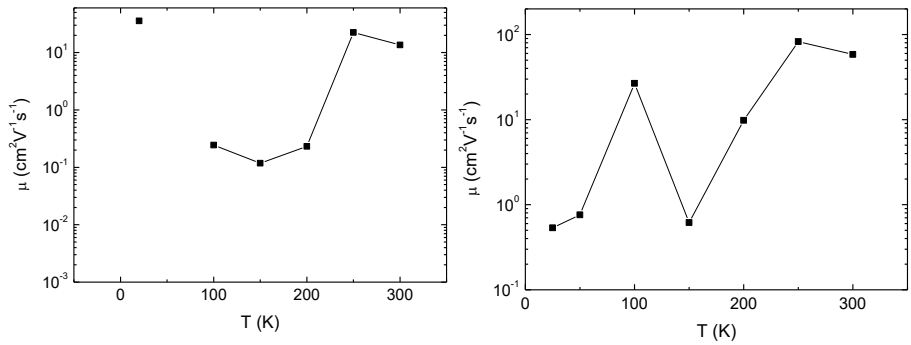

Figure 6.S4. Temperature-dependent mobility measurement of (a)Tetragonal CZTS and (b)Disordered Cubic CZTS

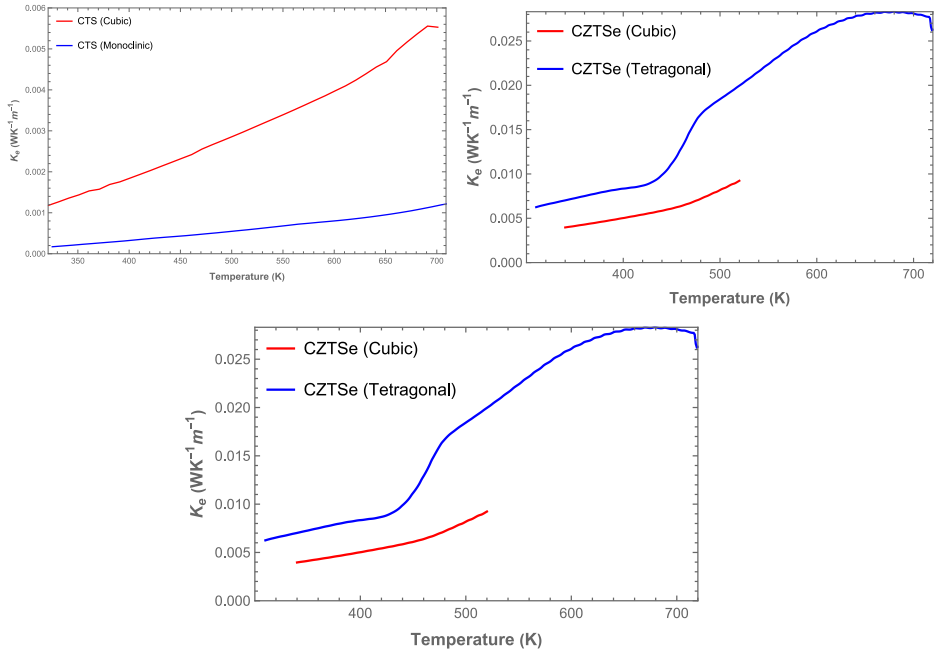

Figure 6.S5. Temperature-dependent electronic part of the thermal conductivity according to the Wiedemann-Franz law: κ_e=L σ T and L = 1.5 + exp[-|S|/116], where L in 10^{-8} WΩK^{-2} and S in μV/K of (a) CTS, (b)CZTS and (c) CZTSe

7. First principles study of SnX_2 (X = S, Se) and Janus SnSSe monolayer for thermoelectric applications

This section is taken from[205]: Nautiyal, H.,* and Scardi, P.* "First Principles Study of SnX_2(X = S, Se) and Janus SnSSe Monolayer for Thermoelectric Applications. Nanotechnology 2022, 33 (32). https://doi.org/10.1088/1361-6528/ac6c37."

* Correspondence: paolo.scardi@unitn.it

himanshu.nautiyal@unitn.it

Abstract

Tin-based chalcogenides are of increasing interest for thermoelectric applications owing to their low-cost, earth-abundant, and environmentally friendly nature. This is especially true for 2D materials, in which breaking of the structural symmetry plays a crucial role in tuning the electronic properties. 2D materials present a unique opportunity to manipulate the electronic and thermal properties by transforming a monolayer into a Janus monolayer. In the present work, we have investigated the thermoelectric properties of hexagonal SnS_2, $SnSe_2$ monolayer, and Janus SnSSe monolayer. Density functional theoretical calculations points out the hexagonal Janus SnSSe monolayer as a potential high-performing thermoelectric material. Results for the Janus SnSSe monolayer show an ultra-low thermal conductivity originating from the low group velocity of the low-lying optical modes, leading to superior zT values of 0.5 and 3 at 300 K and 700 K for the p-type doping, respectively.

7.1 Introduction

The thermoelectric (TE) conversion is an environment friendly option for generating electricity from waste heat.[206] The energy conversion efficiency of a TE material is characterised by the figure of merit

$$zT = \frac{S^2\sigma}{\kappa_e+\kappa_L}(T) \ldots (7.1)$$

where S, σ, T, κ_e and κ_L are the Seebeck coefficient, electrical conductivity, temperature, thermal conductivity of electrons and phonons, respectively. $S^2\sigma$ is collectively referred to as Power Factor (PF). The high-performing TE materials require a high-PF and low thermal conductivity. However, simultaneously optimizing the above parameters is difficult due to their complex interrelationships. According to the Wiedemann-Franz law and Mott's formula,[207] increasing electrical conductivity also increases the thermal conductivity of electrons, and reduces the Seebeck coefficient, which makes it challenging to control κ_e, σ, and S independently. As a result, to improve the TE performance of a material a trade-off between the κ_e, σ, and S should be achieved.[33,34]

Two-dimensional (2D) materials exhibit a wide range of unique electrical, optical, mechanical, and thermal properties making them promising candidates for advanced energy applications.[208,209] The recent discovery of Graphene and its remarkable properties have created great excitement in the research community.[210,211] Layered metal dichalcogenides are an emerging class of 2D materials that go beyond graphene.[212] Tin disulphide (SnS_2) and tin diselenide ($SnSe_2$) are among such layered *s-p* metal chalcogenide semiconductors. They have a layered structure, which exhibit a rich polymorphism resulting from the different stacking sequences. These single and multilayer layer materials have wide range of applications e.g., phase change

memory,[213] water splitting,[214] field effect transistors,[215] gas sensing[216], thermoelectricity,[217] and high-speed photodetection[218]. The weakly bonded layered structure of these compounds allows the use of conventional exfoliation techniques to isolate single or few layers.[219,220] The SnS_2 and $SnSe_2$ monolayers have been extensively investigated by means of computational methods. Xiang et al.[221] have explored the magnetic properties of strained SnS_2 and $SnSe_2$ monolayers, while Gonzalez et al.[222] have investigated their layer dependent properties.

The new derivatives of two-dimensional (2D) materials, Janus 2D materials (*word derived from the ancient Roman mythology where Janus is depicted as a mythical god with two faces*), have attracted considerable research attention due to their distinct properties. Breaking the structural symmetry allows for a fine tuning of the electronic properties of traditional 2D materials.[223] Therefore, by converting a monolayer structure into a Janus monolayer the electronic, thermal and mechanical behaviours can be manipulated. 2D Janus type monolayers are extensively discussed in the literature.[224–227] Shi et al.[228] have studied mechanical and electronic properties of different metal dichalcogenide Janus monolayers. Recently Nguyen et al.[229] have studied the Janus SnSSe monolayer under strain for optical properties. Furthermore, Lu et al.[223] and Zheng et al.[230] have recently successfully synthesized Janus MoSSe monolayer, paving the path for the synthesis of other Janus-like metal dichalcogenide structures. Tin-based chalcogenides are earth-abundant, sustainable and show interesting thermoelectric properties. A recent experimental study showed zT=3.1 at 783 K, for the layered polycrystalline SnSe.[231] Inspired by the high TE performance of SnSe, the present work aims to investigate the thermoelectric properties of SnS_2, $SnSe_2$, and Janus SnSSe monolayers using first principles calculations.

7.2 Computational Method

The first principles calculations of the monolayers were performed using DFT with Projector-Augmented Wave (PAW) pseudopotential as implemented in the Vienna Ab Initio Simulation Package (VASP).[61,62] Electron exchange and correlation effects were described using the Generalised Gradient Approximation (GGA) by Perdew-Burke-Ernzerhof (PBE) functional using the potential recommended by VASP.[26]

The energy cut-off for the plane-wave basis was set to 400 eV on the 5×5×1 Monkhorst-Pack[232] *k*-point grid for relaxation. During relaxation, the cell shape was allowed to change, but the cell volume was kept constant. The Gaussian smearing with a width of 0.01 eV was used. The convergence set to 10^{-6} eV for the iterations of the electronic self-consistent field. The atom positions were optimised until the maximum Hellman-Feynman force on each atom was less than 10^{-3} $eVÅ^{-1}$. A vacuum of 20 Å was chosen to avoid interactions between the periodic copies.

The stiffness tensor was calculated using the Density Functional Perturbation Theory (DFPT). The dynamic stability of the monolayers was examined by calculating the phonon dispersion curves using the finite displacement method. Supercells of 5×5×1 were created to extract the force constants and the force constants were extracted using the Phonopy code.[29] To calculate the lattice thermal conductivity, we also need third order force constants for that supercells of 3×3×1 were created . Both the second and third order Interatomic Force Constants (IFCs) were calculated using the finite displacement method. Phono3py[31] is used to obtain the lattice thermal conductivity (κ_L) by solving the phonon Boltzmann transport equation in the Single-Mode

Relaxation Time Approximation (SMRTA). The lattice thermal conductivities for the monolayers were calculated with dense 81×81×1 q-mesh.

For the DFPT, Phonon, and lattice thermal conductivity calculations the electronic convergence was changed to 10^{-8} eV. The TE properties were calculated using the BoltzTrap2 code.[28] For the calculation of the transport properties, the Brillouin zone was sampled on a *k*-mesh of 21×21×1 by tetrahedron method with Blöch corrections.[64]

7.3 Results and Discussion

The bulk SnS_2/$SnSe_2$ crystallises in various polymorphs. However, the layered hexagonal structure is a stable one which arranges its atoms in the $P\bar{3}m1$ space group. To create the studied SnS_2 and $SnSe_2$ monolayers, a vacuum of 20 Å was applied along the *z*-direction, in the stable structure. The two monolayers also belongs to $P\bar{3}m1$ space group.[222] The studied Janus monolayer can be constructed from the SnS_2/$SnSe_2$ monolayer by replacing the S/Se layer with a Se/S layer. Since the Janus monolayer loses mirror symmetry with respect to the central Sn atoms its space group transforms to *P3m1*. The structures of the relaxed monolayers are shown in Figure 7.1. Table 7.1 reports the structural information of the monolayers, which is in agreement with the literature.[229,233] Table 7.2 reports the elastic constant calculated by DFPT, using PBE and PBEsol[234] potential. The calculated elastic tensors of the three monolayers are much smaller than graphene (354.6 N/m), MoS_2 (134.3 N/m), and WS_2 (146.5 N/m).[235]

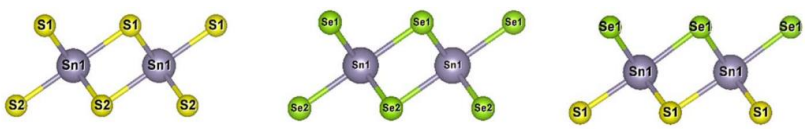

Figure 7.1. Crystal structure of the SnS_2, $SnSe_2$, and the Janus SnSSe monolayer. The atomic structure produced using VESTA software.[194]

Table 7.1. Bond angle, bond length, and lattice parameter of the three monolayers.

System	Bond Angle (˚)	Bond Length (Å)	Lattice Parameter (a=b) (Å)
S-Sn-S	89.022˚	Sn-S= 2.5981	3.7055
Se-Sn-Se	90.174˚	Sn-Se=2.7473	3.8794
Se-Sn-S	89.527˚	Sn-S= 2.6292 and Sn-Se= 2.7191	3.7947

Table 7.2. Elastic constant calculated with PBE and PBEsol potential of the three monolayers.

System	Elastic constant C_{2D} (N/m)	
	PBE potential	PBEsol potential
SnS_2	60.64	59.20
$SnSe_2$	50.07	48.85
SnSSe	52.80	51.49

7.3.1 Electronic properties

To understand the TE properties of a material a detailed understanding of the electronic structure is required. Therefore, the electronic structure calculations were performed, to obtain the band structure along high symmetry path, and the electronic Density of States (DOS) are shown in Figure 7.2. An indirect band gap nature was observed for all three monolayers. The obtained band gap values are 1.5811, 0.7964, and 0.9823 eV for SnS_2, $SnSe_2$, and SnSSe monolayers, respectively, using PBE potential. The results agree with the previous studies.[229]

The difference in the magnitude of the indirect bandgap is a clear feature of the band structures. The band structures of all monolayers exhibited band degeneracy at Γ-point. In the SnS_2 and $SnSe_2$ monolayers the Valence Band Maximum (VBM) appears along the Γ-M direction, and the Conduction Band Minimum (CBM) appears at the M-point. In contrast, for the Janus SnSSe, the VBM occurs at the Γ-point, and the CBM at the M-point.

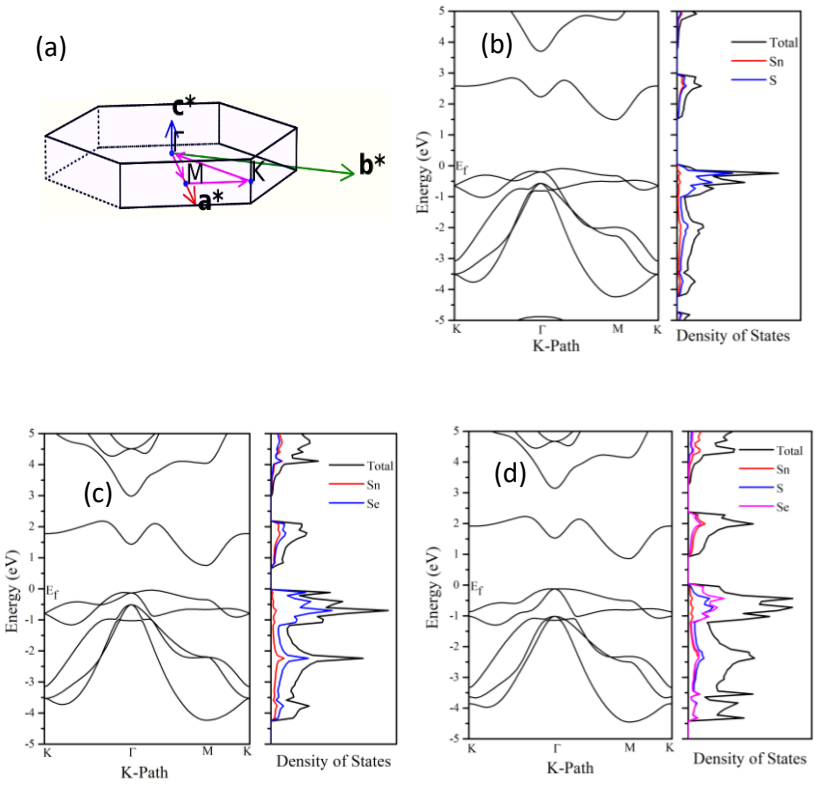

Figure 7.2. Calculated band structures along high-symmetry (a) path and electronic density of states for (b) SnS_2, (c) $SnSe_2$, and (d) SnSSe.

The difference in the magnitude of the indirect bandgap is a clear feature of the band structures. The band structures of all monolayers exhibited band degeneracy at Γ-point. In the SnS_2 and $SnSe_2$ monolayers the Valence Band Maximum (VBM) appears along the Γ-M direction, and the Conduction Band Minimum (CBM) appears at the M-point. In contrast, for the Janus SnSSe, the VBM occurs at the Γ-point, and the CBM at the M-point.

The electron states near the Fermi level have an important influence on the transport properties, we have calculated the atomic Projected Density of States (PDOS). From the PDOS, we find that the VBM of SnS_2 is mainly dominated by Sn *5p* and S *3p*, while the CBM consists

of Sn *5s* and S *3p*. In $SnSe_2$ VBM is composed of Sn *5p* and Se *4p*, while the CBM is composed of Sn *5s* and Se *4p* orbitals. For SnSSe, the VBM is composed of Sn *5p*, S *3p*, Se *4p*, and the CBM is composed of Sn *5s*, S *3p*, Se *4p* orbitals. In the case of SnSSe, the Se *4p* orbital contributes more than the S *3p* orbital at the valence band edge, while the contribution of S and Se at the conduction band edge is similar (the orbital projected density of states is shown in the supplementary Figure 7.S1).

The flatter dispersion of bands near E_f indicates strong localization of charge carriers with large effective mass. (Figure 7.2) This localization gives rise to a steep electronic DOS which is one of the requirements for high performing TE materials, from the Mott equation[207]:

$$S = \frac{\pi^2 k_B^2 T}{3e}\left\{\frac{d(ln(\sigma(E))}{dE}\right\}_{E_f} = \frac{\pi^2 k_B^2 T}{3e}\left\{\frac{1}{n}\frac{d[n(E)]}{dE} + \frac{1}{\mu}\frac{d[\mu(E)]}{dE}\right\}_{E_f} \ldots (7.2)$$

Therefore, increasing $\frac{dn(E)}{dE}$ could be a viable approach to enhance the Seebeck coefficient by increasing the slope of the density of states, a strategy also known as band engineering.

A known problem with the PBE potential is underestimation of the band gap due to the delocalisation of electrons.[236] Therefore, the hybrid Heyd-Scuseria-Ernzerhof (HSE)[184] potential with 25% exact Hartree-Fock exchange was also used to calculate the band structure (Figure 7.S2). Overall, the HSE functional increased the band gap, while the main features of the band dispersions resemble those obtained with the PBE potential. The band gap values obtained with the different potentials are summarised in Table 7.3.

Table 7.3. Band gap calculated for the three monolayers using different potentials.

System	SnS_2			$SnSe_2$			SnSSe		
Potential	PBE	PBE+ SOC	HSE	PBE	PBE+ SOC	HSE	PBE	PBE+SOC	HSE
Band gap (eV)	1.5811	1.4544	2.4420	0.7964	0.6806	1.450	0.9823	0.7794	1.6958

Due to the presence of the heavy Sn atom, the effect of Spin-Orbit Coupling (SOC) was also investigated on band structure (Figure 7.3). The band gap decreases with the introduction of SOC. In addition, spin-orbit splitting of the degenerate bands located at Γ-point was observed. The $SnSe_2$ and SnSSe monolayers presented a stronger spin-orbit splitting compared to SnS_2. In Table 7.4. the spin-orbit splitting values are listed.

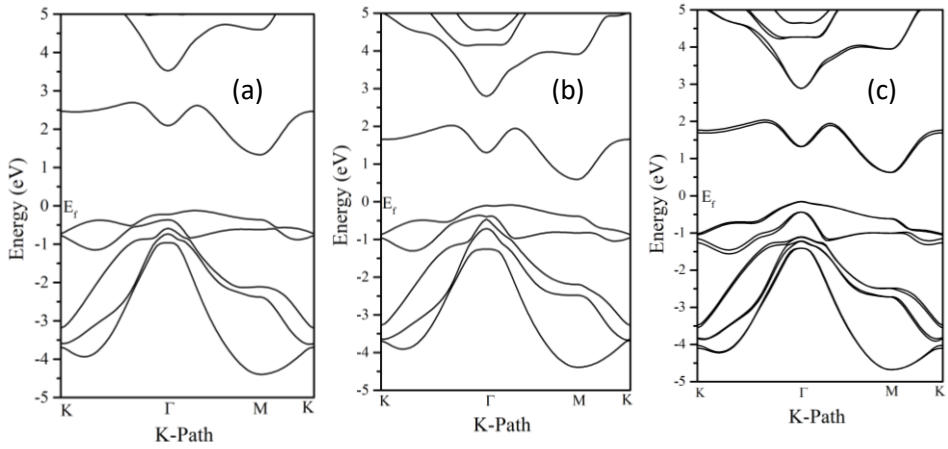

Figure 7.3. Band structures of (a) SnS_2, (b) $SnSe_2$ and (c) SnSSe monolayers with SOC.

Table 7.4. Spin-orbit splitting for the three monolayers at Γ-point.

Structure	Spin-orbit splitting of bands at Γ-point (eV)
SnS_2	0.14
$SnSe_2$	0.28
SnSSe	0.26

Apart from the indirect bandgap nature of all monolayers, the Janus monolayer showed a shift in the VBM towards the Γ-point, which was a common feature in the band structures calculated using different potentials. The indirect bandgap of the Janus monolayer was intact, even though structural symmetry was broken. Moreover, the band population near the Γ-point was much smaller for the Janus monolayer. These features would lead to a variation in charge trasport in the Janus monolayer.

7.3.2 Vibrational and Thermal properties

To study the dynamical stability of monolayers, phonon dispersion curves were calculated (Figure 7.4). All monolayers were dynamically stable as no negative phonon modes were present in phonon dispersion curves, which agrees with Nguyen et al.[229] Since, the investigated monolayers had three atoms in the primitive unit cell, the phonon dispersion curves show nine phonon branches, of which three were acoustic, and the rest were optical. Moreover, the trend of light and heavy atoms vibrating at high and low frequencies, respectively, can be observed. In SnS_2 monolayer low frequency modes were dominated by Sn atoms and higher frequency modes were dominated by the lighter S atoms. For $SnSe_2$ monolayer in the low frequency modes Sn and Se contributed equally, while the higher frequency modes were dominated by Se atoms. In the Janus monolayer low frequency modes were

dominated by Se and Sn atoms. The highest frequency of vibration in SnS_2, $SnSe_2$ and SnSSe was 10.14, 7.25, and 9.30 THz, respectively. Differently, the SnS_2 monolayer presented an acoustic-optical gap around 5 THz. However, no phonon gap was observed for $SnSe_2$ and SnSSe monolayers.

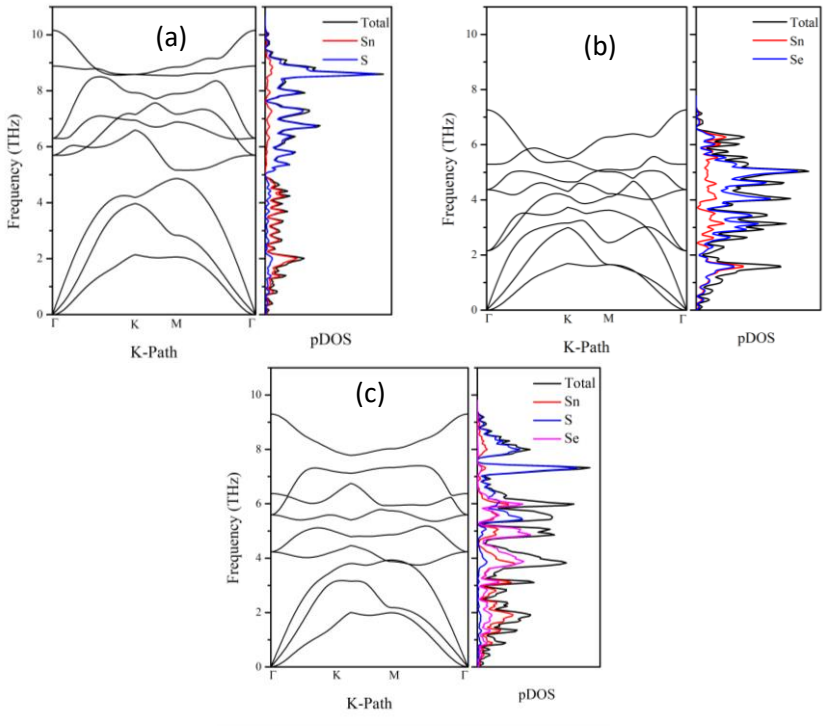

Figure 7.4. Phonon dispersions and atomic projected phonon density of states of (a) SnS_2, (b) $SnSe_2$, and (c) SnSSe.

The lattice thermal conductivity (κ_L) calculations were performed based on the harmonic and anharmonic IFCs, using the Phono3py code with SMRTA. Figure 7.5 shows the temperature-dependent lattice thermal conductivities of monolayers. Due to enhancement in phonon–phonon scattering (Umklapp scattering), a gradual decrease in κ_L with temperature can be observed. The lattice thermal conductivity spans from 3.73-1.55, 2.61-1.10, and 0.61-0.26 W/m-K, in the temperature

range from 300 to 700 K, for SnS_2, $SnSe_2$, and SnSSe monolayers, respectively. The value of lattice thermal conductivity of SnS_2 and $SnSe_2$ is in agreement with the results obtained by Shafique et al.[233] Interestingly, the SnSSe monolayer presented an ultra-low lattice thermal conductivity, a desirable property for high-performance TE materials.[231] However, the κ_L obtained for Janus SnSSe monolayer was much higher compared to Janus WSTe monolayer (around 0.07 W/m-K at 300 K).[237]

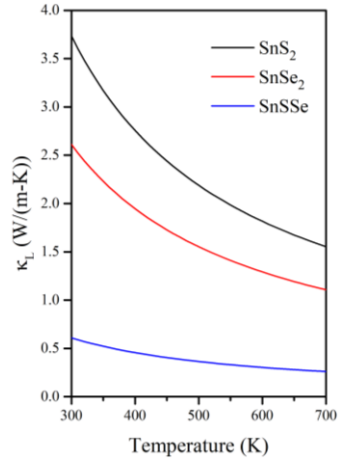

Figure 7.5. Calculated lattice thermal conductivities of SnS_2, $SnSe_2$, and SnSSe using SMRTA as implemented in the Phono3py code.

To understand the reason behind the ultra-low lattice thermal conductivity of the Janus monolayer, the phonon despersion curve were investigated again. The lattice thermal conductivity [238] is given by $\kappa_L = \frac{1}{3} C_v v_{ave} l$, where C_v denotes heat capacity per unit volume, v_{ave} is average speed of lattice vibration, l is phonon mean free path. The slope of phonon branches in the phonon despersion curves gives the group velocity of phonons($v_g = \frac{d\omega}{dq}$). From the phonon dispersion curves, the slope of the longitudinal acoustic branch in the SnS_2 and $SnSe_2$ monolayer was alike (Figure 7.4). At the same time, there is a

significant difference for the transverse acoustic branches (Figure 7.6 blue and orange colour). Although, the slope of the longitudinal acoustic branch is lower in the Janus monolayer and is consistent with the observed result of a lower κ_L, the difference is insufficient to justify the ultralow values of κ_L. To observe the phonon group velocity of each mode, we have calculated the mode level phonon group velocity. The acoustic phonon group velocities of SnS_2, $SnSe_2$, and SnSSe are 50.8 THz-Å, 51.4 THz-Å and 44.5 THz-Å, respectively (Figure 7.6). Thus, it is difficult to explain the ultra-low κ_L of the Janus monolayer only based on a difference in acoustic phonons group velocity, as discussed earlier. Apart from this, the mode level phonon group velocity plots show the presence of a phonon gap for SnS_2, which was missing for $SnSe_2$ and SnSSe. However, a closer look at the mode level group velocity plot shows a significant variation in group velocity of optical phonons for all studied monolayers. The group velocity of the low-lying optical phonons interacting with acoustic phonons in $SnSe_2$ is much higher compared to the SnSSe monolayer (see Figure 7.6).

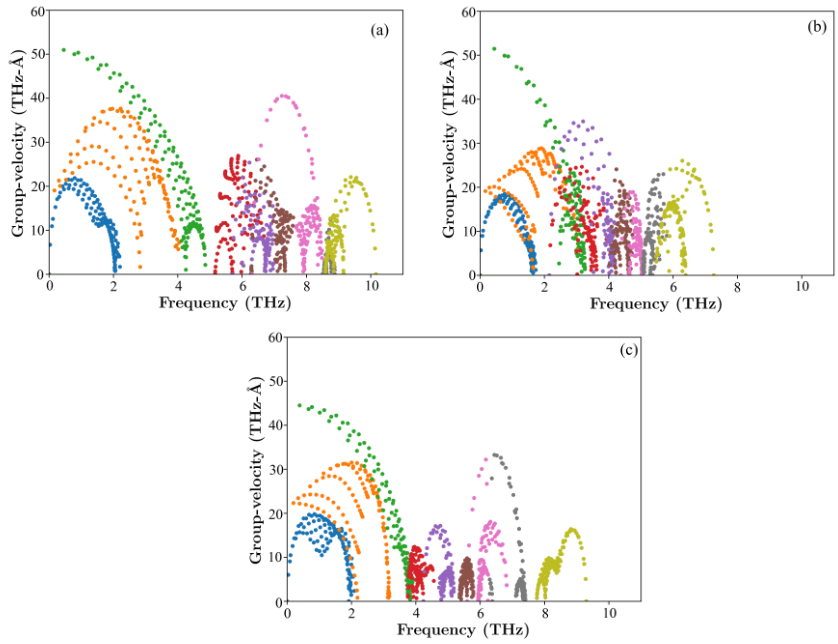

Figure 7.6. Calculated phonon group velocities of (a) SnS_2, (b) $SnSe_2$, and (c) SnSSe. The blue, orange, and green colours represents the group velocity of the two tranverse acoustic branches and one longitudnal acoustic branch, respectivily. The rest are the group velocity of optical branches. It can be observed in Fig. 6(c) that the red colour optical phonons in case of SnSSe have a low group velocity of 15 THz-Å while in case of $SnSe_2$ (b) it is around 28 THz-Å.

Other than the phonon group velocity, the phonon lifetime is an essential parameter to study the phonon transport. A lower phonon lifetime corresponds to an intense phonon scattering and a low lattice thermal conductivity. Therefore, the frequency-dependent phonon lifetimes were calculated at 300 K for SnS_2, $SnSe_2$, and SnSSe, and are shown in Figure 7.7

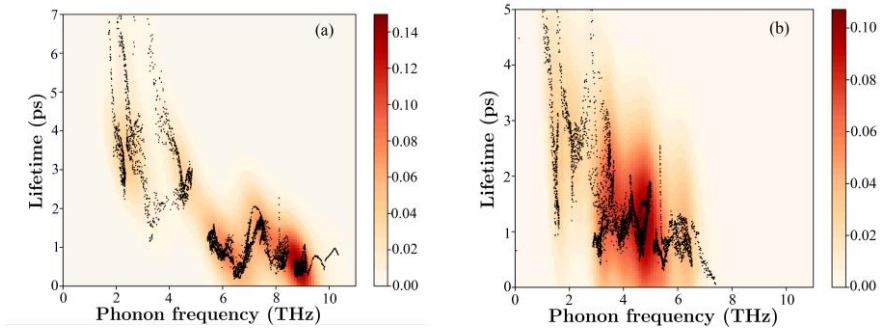

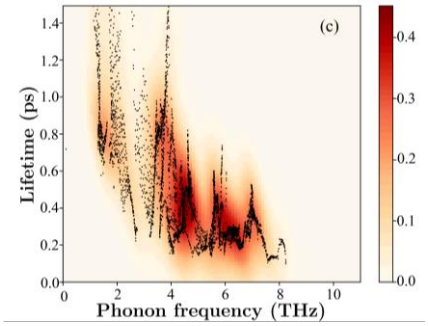

Figure 7.7. Phonon lifetimes of (a) SnS_2, (b) $SnSe_2$ and (c) SnSSe calculated at 300 K. The color in the figure represents the phonon density. Bright colour represents the higher phonon density.

These results show that the SnS_2 and $SnSe_2$ monolayers have significantly higher phonon lifetime than the Janus monolayer. It is worth mentioning, in the low-frequency range (<2 THz), the phonon lifetimes of the monolayers show a broad distribution with a maximum value of approximately 7 ps, 5 ps, and 1.4 ps for SnS_2, $SnSe_2$, and SnSSe, respectively. A significant difference in the phonon lifetimes of SnS_2 and $SnSe_2$ monolayers occurs at intermediate frequency phonons, (4-6 THz) due to phonon gap present in the SnS_2 monolayer. The phonon lifetime around the 4Thz frequency for the Janus layer (1.4 ps), where the optical phonons with small group velocity are present, is much smaller than that of the corresponding SnS_2 (6 ps) and $SnSe_2$ (4.5 ps) monolayers. The calculated lower phonon lifetime explains the reason for the Janus monolayer's ultralow lattice thermal conductivity. In the Janus monolayer, the low-velocity optical phonons act as heat traps[239] and are responsible for a remarkable phonon-phonon interaction between the acoustic and low-lying optical modes that more effectively scatters the heat-transmitting phonon waves and reduces the phonon lifetime in an unprecedented manner.

7.3.3 Thermoelectric properties

The transport properties of a material show a strong dependence on the carrier concentration. Therefore, the TE parameters were calculated as a function of carrier concentration considering the Constant Relaxation Time Approximation (CRTA), where $\tau = 10^{-14}$ *s*; the obtained results are shown in the supplementary (Figure 7.S3 to 7.S8). The |*S*| decreases with the carrier concentration (Pisarenko plot), whereas σ increased with carrier concentration. A maximum *PF* was obtained at the intermediate carrier concentration due to the inverse relationship between *S* and σ. The carrier concentration at which the *PF* was maximised was used to calculate the TE properties as a function of temperature for each monolayer.

Figures 7.8 and 7.9 reports the variation of the Seebeck coefficient and electrical conductivity as a function of temperature for *p*-and *n*-type doping, respectively. As expected, we obtained a positive Seebeck coefficient for *p*-type doping and a negative Seebeck coefficient for *n*-type doping. Due to the wide bandgap of the monolayers, the bipolar conduction ceases, and |*S*| increases with the temperature. The calculated Seebeck coefficient of SnS_2, $SnSe_2$, and SnSSe are 219, 213, and 243 μVK^{-1} for *p*-type doping and -132, -129, and -129 μVK^{-1} for *n*-type doping at 300 K, respectively. The SnSSe monolayer presented a higher Seebeck coefficient than SnS_2 and $SnSe_2$ in *p*-type doping. The electrical conductivity of SnSSe also showed an increasing trend with temperature, while a decreasing trend was observed for SnS_2 and $SnSe_2$. The possible reason for this trend in the Seebeck coefficient and electrical conductivity for *p*-type doping could be the shift of the VBM towards the Γ-point and the lower band population near the Fermi energy in the valence band side for the Janus monolayer (Figure 7.2(c)). In the case of *n*-type doping, the Seebeck value of $SnSe_2$ and SnSSe

were coincident. The electrical conductivity for the *n*-type doping side decreased with temperature.

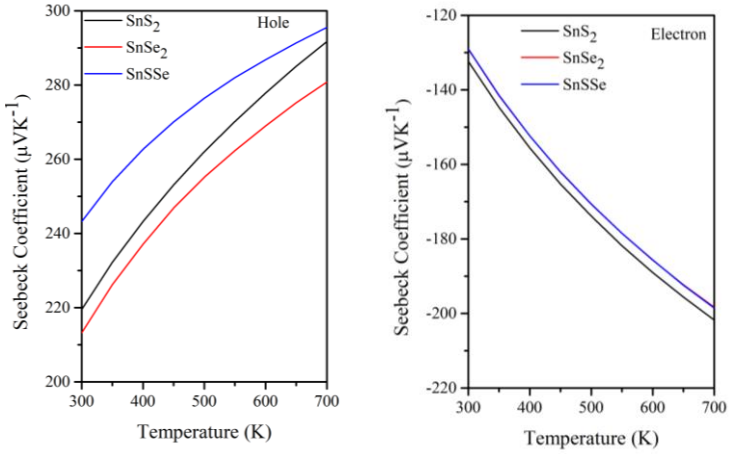

Figure 7.8. The Seebeck coefficient for *p*-and *n*-type doping in SnS_2, $SnSe_2$ and SnSSe calculated in a temperature range from 300 to 700 K.

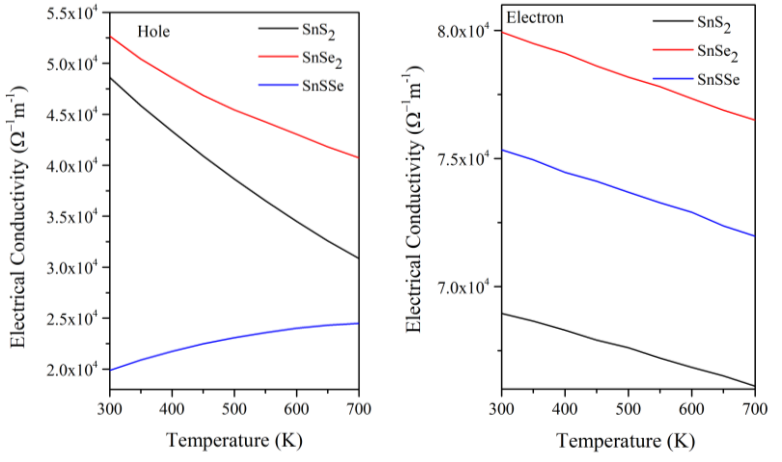

Figure 7.9. The electrical conductivity for *p*-and *n*-type doping in SnS_2, $SnSe_2$ and SnSSe calculated in a temperature range from 300 to 700 K

In Figure 7.10, the variation of total thermal conductivity with temperature is plotted for both *p*-and *n*-type doping. The lattice part calculated by Phono3py, and the electronic part calculated by the Boltztrap2 code were added to obtain the total thermal

conductivity. The contribution of κ_e to the total thermal conductivity is minimal in the case of *p*-type doping. For the of *n*-type doping, in the Janus monolayers κ remains almost constant and increases slightly in the higher temperature range. This result can be understood from the values of the electrical conductivity of the SnSSe monolayer for the *n*-type doping, which is much higher compared to the *p*-type doping. The Wiedemann-Franz law, $\kappa_e = L\sigma T$, states that the electronic thermal conductivity is directly proportional to the electrical conductivity and the temperature, with L as the Lorenz number. Since κ_L is ultra-low for the Janus monolayer, κ_e dominates due to the higher electrical conductivity of the electrons, and overall, a constant thermal conductivity results for the Janus monolayer with *n*-type doping.

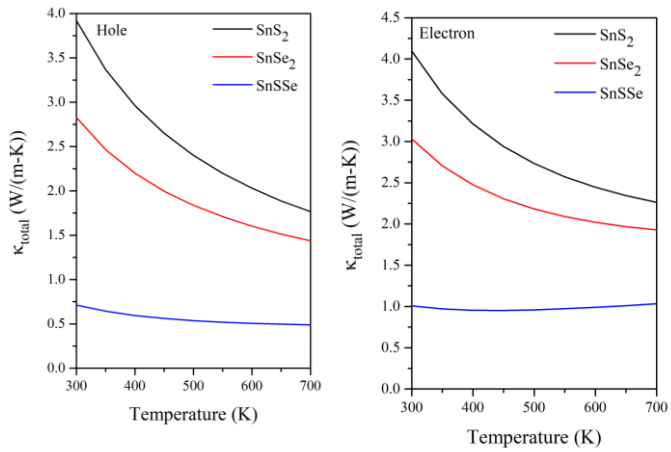

Figure 7.10. The total thermal conductivity for *p*-and *n*-type doping in SnS_2, $SnSe_2$ and SnSSe calculated in a temperature range from 300 to 700 K.

The *PF* obtained from the calculated Seebeck coefficient, and the electrical conductivity is shown in Figure 7.11. The $SnSe_2$ monolayer showed a higher *PF* than SnS_2 and SnSSe monolayer in both *p*-and *n*-type doping. A maximum *PF* of 2.6×10^{-3}, 3.2×10^{-3}, and 2.1×10^{-3}

W/mK^2 was obtained for SnS_2, $SnSe_2$, and SnSSe at 700 K, respectively with *p*-type doping. A maximum *PF* of 2.7×10^{-3}, 3.0×10^{-3}, and 2.8×10^{-3} W/mK^2 was achieved for SnS_2, $SnSe_2$, and SnSSe at 700 K, respectively, with *n*-type doping.

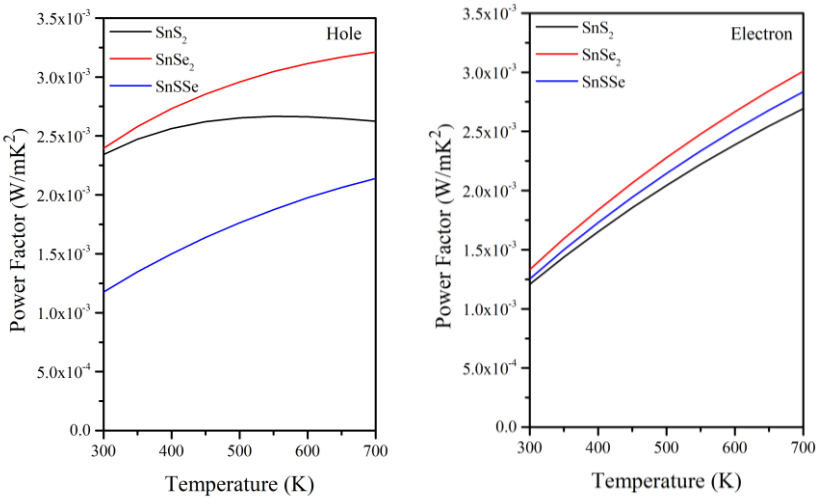

Figure 7.11. The Power factor for *p*-and *n*-type doping in SnS_2, $SnSe_2$ and SnSSe calculated in a temperature range of 300 to 700 K.

Since *zT* is a measure of the TE performance of a material, Figure 7.12 shows the *zT* calculated from the transport properties. The *zT* increased with temperature due to an increase in *PF* and decrease in lattice thermal conductivity. The SnS_2 and $SnSe_2$ monolayer have lower *zT* values in the whole temperature range because both these materials have higher thermal conductivity than the Janus monolayer. Although the *PF* was higher in $SnSe_2$, due to the lower thermal conductivity, the Janus monolayer presented the highest *zT* of 3 at 700 K in the p-type doping, while a *zT* of 1.9 was obtained for the n-type doping. The *zT* for $SnSe_2$ was 1.5 and 1.0 at 700 K for *p*-and *n*-type doping, respectively. The lowest *zT* was obtained for SnS_2 with 1.0 and 0.8 at 700 K for *p*-and *n*-type doping, respectively. Patel et al.[237] have reported a *zT* spanning from 0.74-2.56 and 0.013-0.355 for Janus

monolayer of WSTe, and WSSe in the temperature range from 300 K and 1200 K. Deng et al.[240] calculated a *zT* of 1.64 for armchair MoSSe at 300 K. Vu et al. have reported *zT* of In_2SeTe for *p*-type is 0.330 at 300 K.[227] Khosa et al.[226] have calculated a *zT* of 1.38 for *n*-type Janus Al_2SeTe monolayer at room temperature. More recently, Tao et al.[241] have predicted a zT of 5.05 at 500 K for anisotropic $PtTe_2$ along the *x*-direction due to the low thermal conductivity (1.77 W/(m-K)). In conclusion, the present results show that asymmetric SnSSe Janus monolayer is a potential candidate for high performing TE applications.

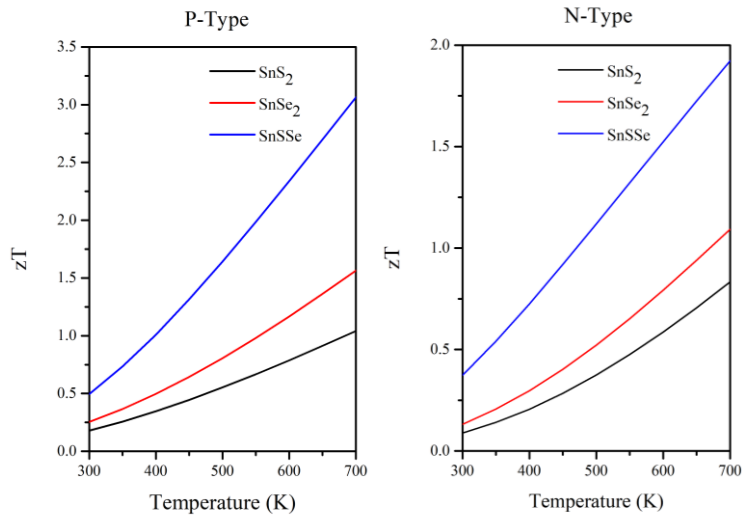

Figure 7.12 The TE figure of merit for *p*-and *n*-type doping in SnS_2, $SnSe_2$ and SnSSe calculated in a temperature range from 300 to 700 K.

7.4 Conclusion

In the present work, we have studied the structural, electronic, vibrational, and TE properties of the 2D monolayers using the first-principles calculations. A Janus SnSSe monolayer was created, and its transport properties were studied comparing the results with the SnS_2 and $SnSe_2$ monolayers. The band structure showed an indirect band gap,

with band gap values estimated as 2.44, 1.45 and 1.69 eV, for SnS_2, $SnSe_2$, and SnSSe, respectively, using the HSE06 potential. The Seebeck coefficient (*S*) values are 219, 213, and 243 μVK^{-1} for SnS_2, $SnSe_2$, and SnSSe, respectively, at 300 K with hole doping. Interestingly, the lattice thermal conductivity of the Janus structure was significantly reduced due to the low-lying optical modes having small group velocity. This reduction leads to a significant improvement in the *zT* values for the Janus monolayer. The Janus SnSSe monolayer shows superior *zT* =0.5-3, in temperature range 300 to 700 K for *p*-type doping, which is greater than most 2D materials. The Janus SnSSe monolayer can be proposed for TE applications for waste heat power generation. Further study will be required to calculate the transport properties of multi-layer Janus SnSSe.

Appendix

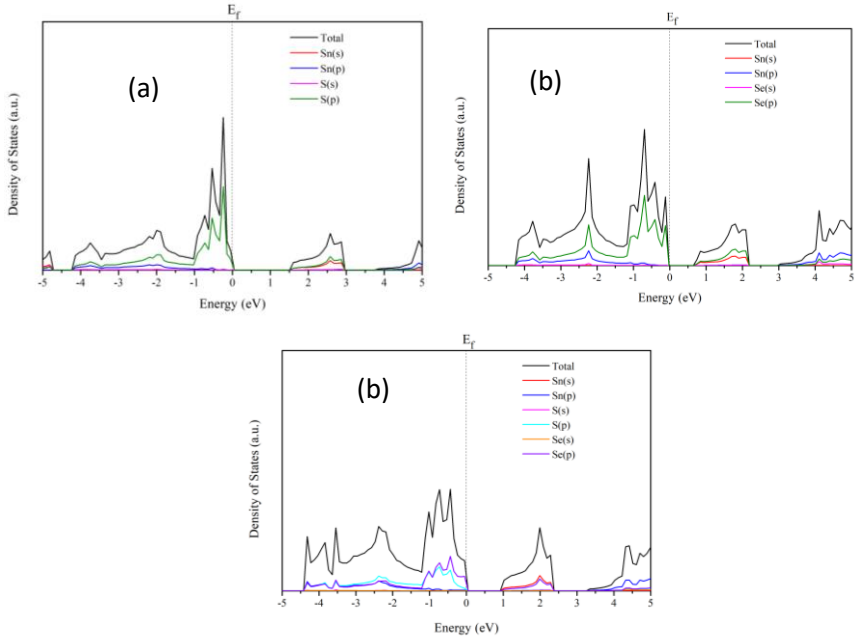

Figure 7.S1. Orbital projected density of states of three monolayers (a)SnS2, (b) SnSe2 and (c) SnSSe.

The bandstructure calculated with HSE potential with 25% of exact Hatree-Fock exchange.

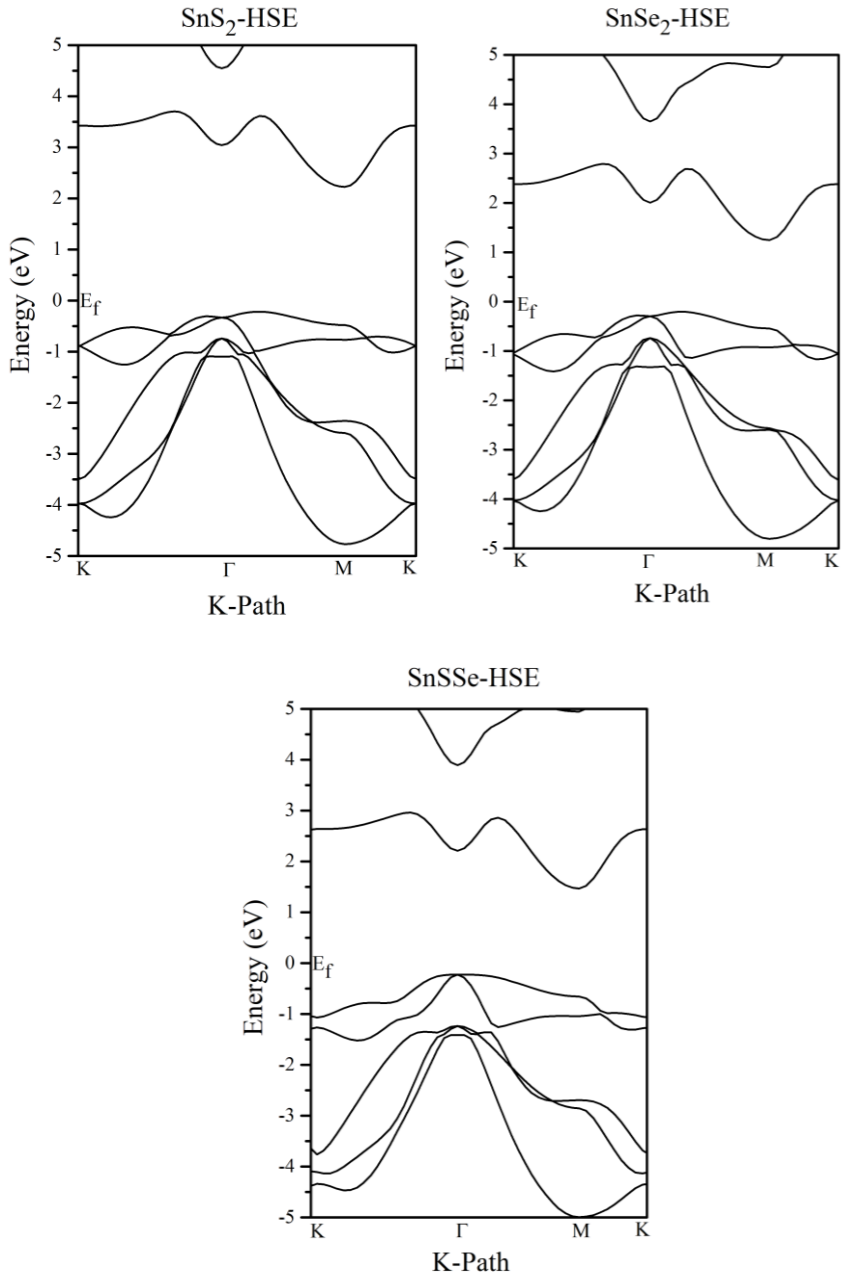

Figure 7.S2. Bands structures of the three monolayers using the HSE potential.

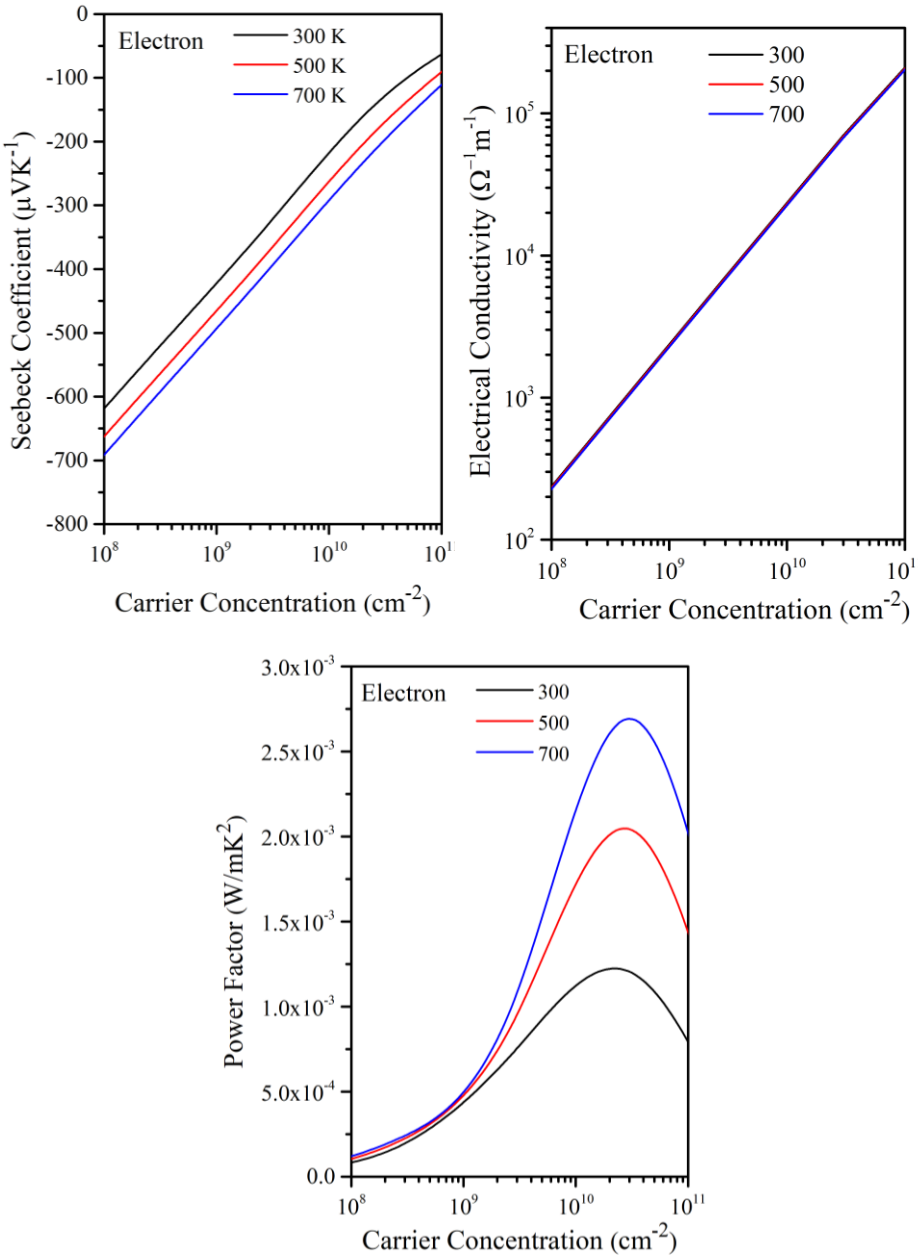

Figure 7.S3. Transport properties as a function of carrier concentration for SnS_2 electron doping.

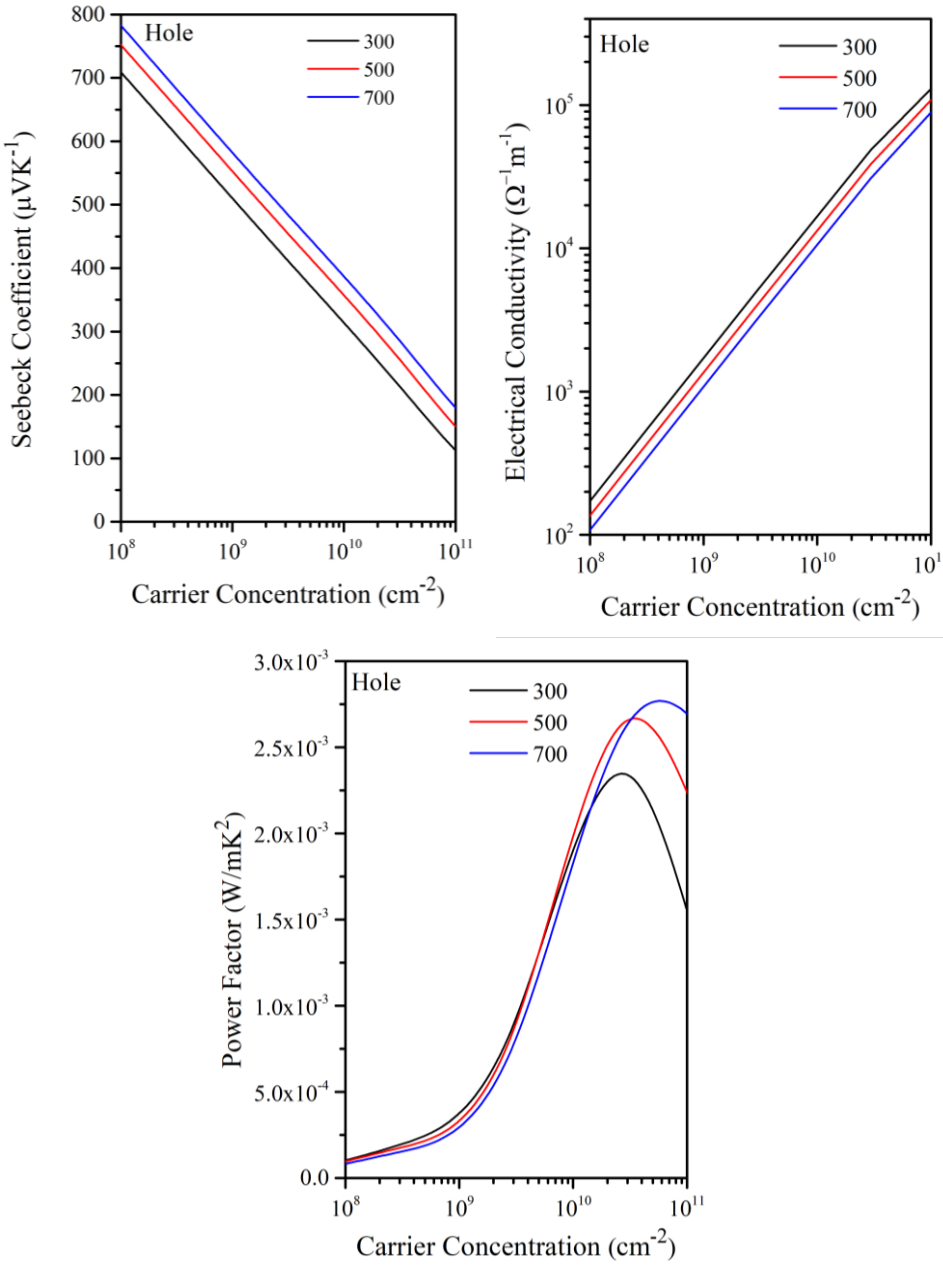

Figure 7.S4. Transport properties as a function of carrier concentration for SnS_2 hole doping.

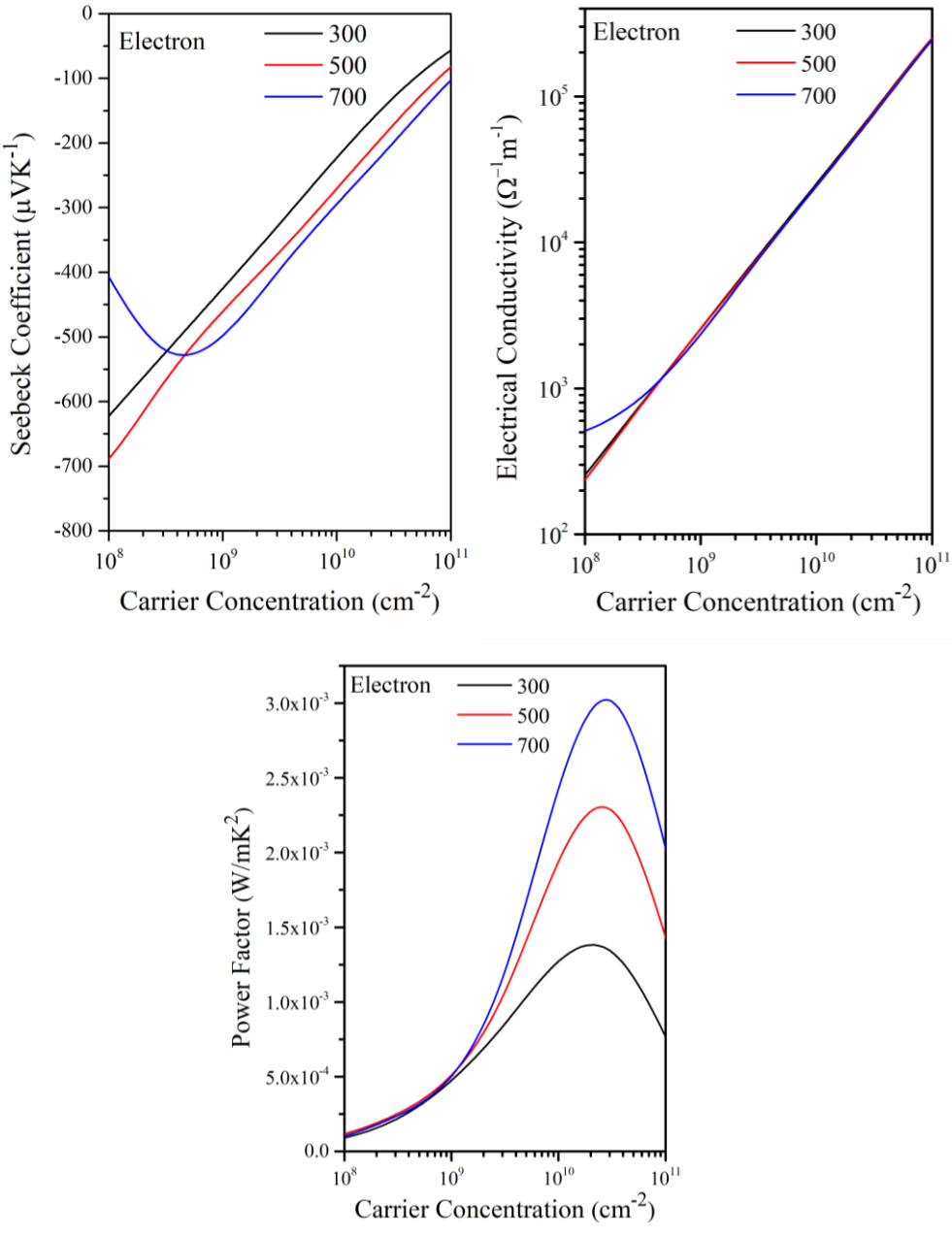

Figure 7.S5. Transport properties as a function of carrier concentration for $SnSe_2$ electron doping.

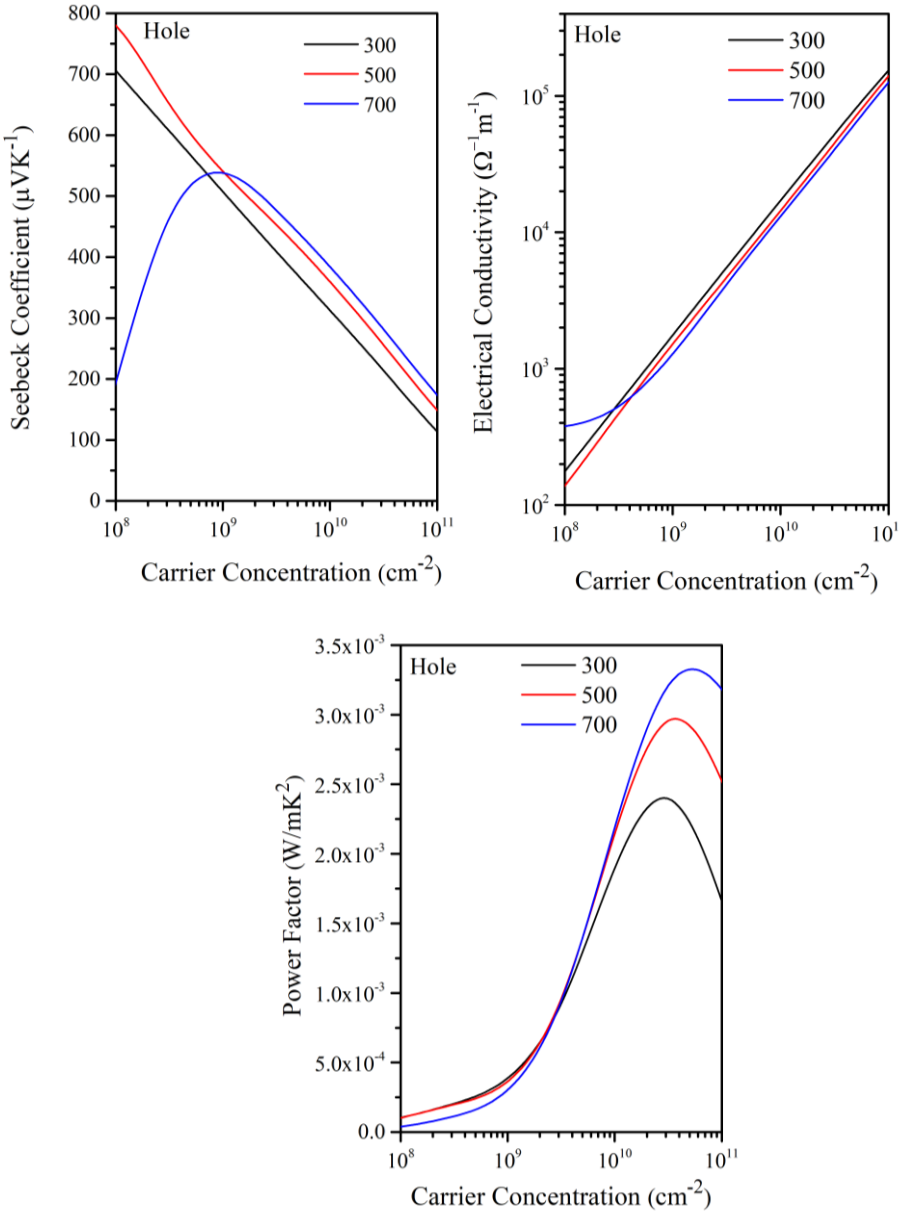

Figure 7.S6. Transport properties as a function of carrier concentration for $SnSe_2$ hole doping.

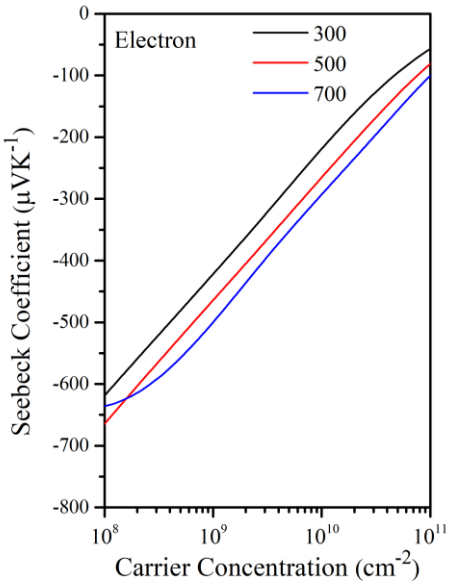

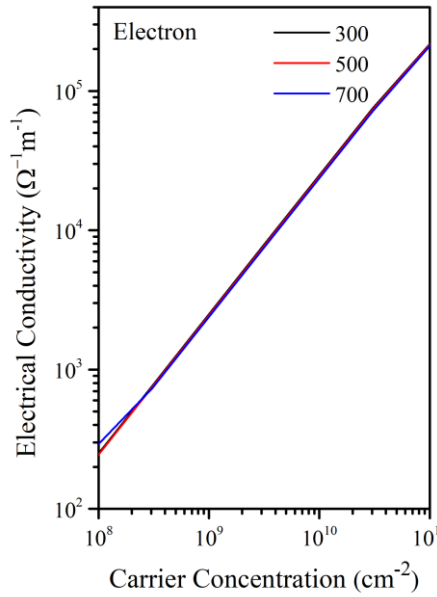

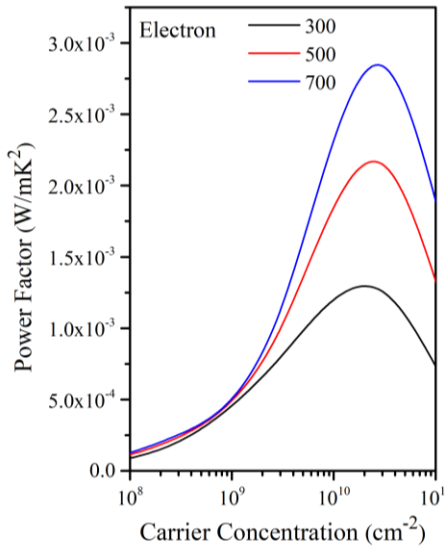

Figure 7.S7. Transport properties as a function of carrier concentration for SnSSe electron doping.

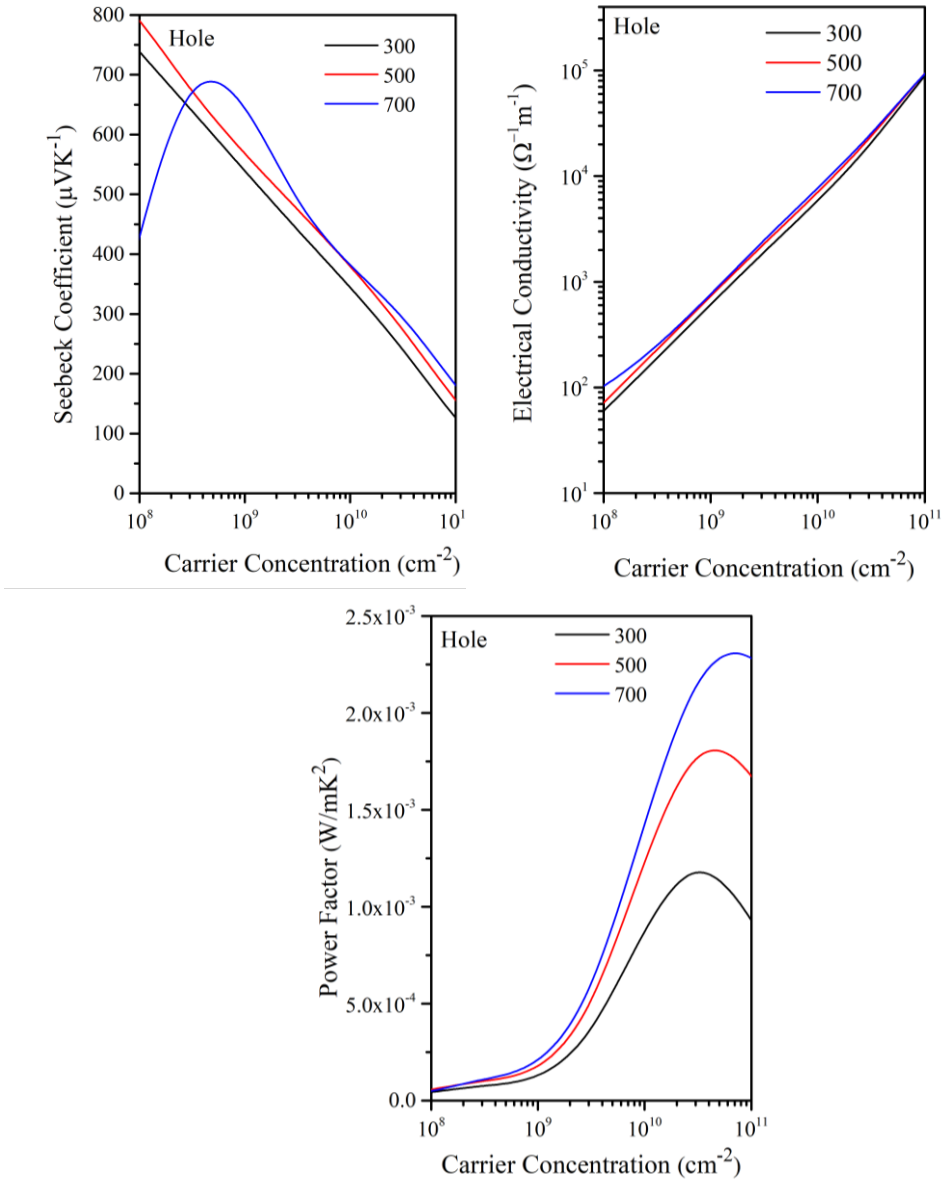

Figure 7.S8. Transport properties as a function of carrier concentration for SnSSe hole doping.

8. Conclusion

This thesis work presents first-principle analysis on chalcogenides, as promising candidates for the TE applications. Through DFT, DFTP, and AIMD simulations in-depth study was perfumed on the electronic and vibrational properties of binary, ternary, and quaternary chalcogenides.

Chapter 1 provides a brief introduction, overview, and literature survey on thermoelectric materials.

Chapter 2 presents details theory and methodology of computational techniques followed in this thesis work.

Chapter 3, studies CTS, which is an eco-friendly, earth abundant, non-toxic, and potentially high performing TE materials. The ordered monoclinic and two disordered cubic cells of CTS were modelled, slightly changing the partial occupation of Cu and Sn due to stoichiometric constraints. *Ab initio* DFT and DFPT calculations were performed to understand the fundamental principles behind the higher thermoelectric performance of the disordered phase. The electronic properties were analysed via density of states (DOS), band structures and Electron Localization Function (ELF) plots, while the vibrational properties were investigated using phonon dispersion curves, phonon density of states, group velocity and mode-Grüneisen parameter. The results showed that the disordered phase has a smaller band gap, more available states near the Fermi energy and low-lying optical modes that support acoustic-optical phonon scattering. The anharmonicity in the disordered structures depended on the concentration of Sn atoms, shown by the ELF plots and the mode Grüneisen parameter. These computational results were in agreement with experimental work, especially with respect to the vibrational properties and the mode

Grüneisen parameter, which were investigated by combining nuclear inelastic scattering (NIS) experiment and high-resolution XRD experiment performed at PETRA III synchrotron source.

The experimental results on CTS pointed that CTS samples with lower grain size showed a higher electrical conductivity and high zT in comparison to the relatively larger grains. To understand this effect the behaviour of surfaces was investigated in Chapter 4.

Therefore, the surfaces of three ordered CTS polymorph and two disordered CTS polymorph were calculated via first-principles methods. The different possible atomic arrangements at grain boundary showed that the surface of CTS is conducting due to the presence of dangling bonds. These atomic arrangements also reduced the bandgap of CTS surface close to zero. Additionally, calculations on the formation energy showed that stoichiometric CTS, Cu-vacant and Cu-rich systems are energetically favourable, while Sn-vacant and Sn-rich systems are less likely.

Various studies on CTS revealed that in the electronic transport the contribution on Sn in minimal. Thus, an effort was made to replace Sn with Ag in three different concentrations to enhance the overall TE performance of CTS in Chapter 5. The DOS showed that the valence band edge shifted to higher energy with increasing Ag content. Interestingly, the thermal conductivity of the $Cu_2Ag_{(x)}Sn_{(1-x)}S_3$ samples increased with Ag substitution. The AIMD simulation revealed that the incorporation of Ag into the system decreases the root mean squared displacement of the other cations and anions, which reduces the scattering of phonons and thereby increases the lattice thermal conductivity.

The chapter 6 deals with the TE properties of different disordered polymorphs of CTS, CZTS and CZTSe synthesised by high-energy reactive milling. AIMD simulations were used to quantify the effects of disorder, and the results were compared with temperature-dependent synchrotron XRD measurements. Structural disorder was found to promote the optimisation of the electrical and thermal transport properties through several mechanisms. The disordered cubic CTS had better electrical conductivity than the ordered CTS due to the reduction in band gap and band tails, while the large anharmonicity and inhomogeneous bonds resulted in extremely low thermal conductivity. The quaternary systems of CZTS and CZTSe showed a temperature-activated phase transformation for the tetragonal phase from an ordered tetragonal to a partially disordered tetragonal arrangement. Moreover, CZTS and CZTSe can be stabilised at low temperatures in a novel disordered cubic phase with complete cation disorder. The disordered cubic phases of the two quaternary compounds exhibit extremely low thermal conductivity due to anharmonicity and low phonon group velocity. Differently from the ordered tetragonal phase, the disordered cubic CZTS was predicted to be a topological Anderson insulator with topologically protected surface states, a prediction supported by the experimental measurements of high mobility at very low temperatures.

In the final study, the thermoelectric properties of hexagonal SnS_2, $SnSe_2$ monolayer and Janus SnSSe monolayer were investigated. A Janus SnSSe monolayer was modelled and its electronic and thermal transport properties were compared with SnS_2 and $SnSe_2$ monolayers. The band structure showed an indirect band gap. The calculations were performed with HSE06 potential and the band gap values of 2.44, 1.45 and 1.69 eV were obtained for SnS_2, $SnSe_2$ and Janus SnSSe monolayer, respectively. When doped with holes, the values of Seebeck coefficient

(S) at 300 K were 219, 213 and 243 μVK^{-1} for SnS_2, $SnSe_2$ and SnSSe, respectively.

Interestingly, the Janus structure exhibited significantly reduced lattice thermal conductivity due to the low-lying optical modes with small group velocity. This reduction led to a significant improvement in the *zT* values for the Janus monolayer. In particular, the Janus SnSSe monolayer showed excellent zT of 0.5-3 in the temperature span of 300-700 K for the p-type doping, making it a promising option for thermoelectric applications.

In this thesis first-principle methods were used to investigate the transport properties of different binary, ternary, and quaternary chalcogenides and explore their potential as a viable option for thermoelectric applications. The research presented here forms the basis for future studies in the field of thermoelectric materials and offers promising prospects for the development of high-performance thermoelectric materials and devices.

To gain a deeper understanding of the transport properties of materials, future research could focus on exploring different scattering mechanisms. This could include the study of acoustic deformation potential scattering, ionised impurity scattering, polar optical phonon scattering and piezoelectric scattering. In addition, studying the effects of spin-orbit coupling on electronic properties could reveal intriguing transport properties that could have applications in a range of fields.

9. Bibliography

(1) Timperley, J. Why Fossil Fuel Subsidies Are so Hard to Kill. *Nature* **2021**, *598* (7881), 403–405. https://doi.org/10.1038/d41586-021-02847-2.

(2) Forman, C.; Muritala, I. K.; Pardemann, R.; Meyer, B. Estimating the Global Waste Heat Potential. *Renew. Sustain. Energy Rev.* **2016**, *57*, 1568–1579. https://doi.org/10.1016/j.rser.2015.12.192.

(3) Bian, Q. Waste Heat: The Dominating Root Cause of Current Global Warming. *Environ. Syst. Res.* **2020**, *9* (1). https://doi.org/10.1186/s40068-020-00169-2.

(4) Ioffe, A. F. Semiconductor Thermoelectrics and Thermoelectric Cooling. *Infosearch Ltd. London* **1957**.

(5) Goldsmid, H. J. *Introduction to Thermoelectricity*; Springer Series in Materials Science; Springer Berlin Heidelberg: Berlin, Heidelberg, 2010; Vol. 121. https://doi.org/10.1007/978-3-642-00716-3.

(6) Witting, I. T.; Chasapis, T. C.; Ricci, F.; Peters, M.; Heinz, N. A.; Hautier, G.; Snyder, G. J. The Thermoelectric Properties of Bismuth Telluride. *Adv. Electron. Mater.* **2019**, *5* (6), 1800904. https://doi.org/https://doi.org/10.1002/aelm.201800904.

(7) Zhou, Y. Progress and Trend of PbTe Based Thermoelectric Materials. *J. Phys. Conf. Ser.* **2022**, *2194* (1). https://doi.org/10.1088/1742-6596/2194/1/012006.

(8) Raag, V.; Berlin, R. E. A Silicon-Germanium Solar Thermoelectric Generator. *Energy Convers.* **1968**, *8* (4), 161–168. https://doi.org/10.1016/0013-7480(68)90033-8.

(9) Dolyniuk, J. A.; Owens-Baird, B.; Wang, J.; Zaikina, J. V.; Kovnir, K. Clathrate Thermoelectrics. *Mater. Sci. Eng. R Reports* **2016**, *108*, 1–46. https://doi.org/10.1016/j.mser.2016.08.001.

(10) Zhu, T.; Fu, C.; Xie, H.; Liu, Y.; Zhao, X. High Efficiency Half-Heusler Thermoelectric Materials for Energy Harvesting. *Adv. Energy Mater.* **2015**, *5* (19), 1500588. https://doi.org/https://doi.org/10.1002/aenm.201500588.

(11) Huang, L.; Zhang, Q.; Yuan, B.; Lai, X.; Yan, X.; Ren, Z. Recent Progress in Half-Heusler Thermoelectric Materials. *Mater. Res. Bull.* **2016**, *76*, 107–112. https://doi.org/10.1016/j.materresbull.2015.11.032.

(12) Rull-Bravo, M.; Moure, A.; Fernández, J. F.; Martín-González, M. Skutterudites as Thermoelectric Materials: Revisited. *RSC Adv.* **2015**, *5* (52), 41653–41667. https://doi.org/10.1039/C5RA03942H.

(13) Koumoto, K.; Wang, Y.; Zhang, R.; Kosuga, A.; Funahashi, R. Oxide Thermoelectric Materials: A Nanostructuring Approach. *Annu. Rev. Mater. Res.* **2010**, *40* (1), 363–394. https://doi.org/10.1146/annurev-matsci-070909-104521.

(14) Yin, Y.; Tudu, B.; Tiwari, A. Recent Advances in Oxide Thermoelectric Materials and Modules. *Vacuum* **2017**, *146*, 356–374.

https://doi.org/10.1016/j.vacuum.2017.04.015.

(15) Qiu, P.; Shi, X.; Chen, L. Cu-Based Thermoelectric Materials. *Energy Storage Mater.* **2016**, *3*, 85–97. https://doi.org/10.1016/j.ensm.2016.01.009.

(16) Slack, G. A. New Materials and Performance Limits for Thermoelectric Cooling. In *CRC Handbook of Thermoelectrics*; 1995.

(17) Yang, J.; Caillat, T. Thermoelectric Materials for Space and Automotive Power Generation. *MRS Bull.* **2006**, *31* (March), 224–229.

(18) Zheng, X. F.; Liu, C. X.; Yan, Y. Y.; Wang, Q. A Review of Thermoelectrics Research - Recent Developments and Potentials for Sustainable and Renewable Energy Applications. *Renew. Sustain. Energy Rev.* **2014**, *32*, 486–503. https://doi.org/10.1016/j.rser.2013.12.053.

(19) Güler, N. F.; Ahiska, R. Design and Testing of a Microprocessor-Controlled Portable Thermoelectric Medical Cooling Kit. *Appl. Therm. Eng.* **2002**, *22* (11), 1271–1276. https://doi.org/10.1016/S1359-4311(02)00039-X.

(20) Vullers, R. J. M.; van Schaijk, R.; Doms, I.; Van Hoof, C.; Mertens, R. Micropower Energy Harvesting. *Solid. State. Electron.* **2009**, *53* (7), 684–693. https://doi.org/10.1016/j.sse.2008.12.011.

(21) Nozariasbmarz, A.; Collins, H.; Dsouza, K.; Polash, M. H.; Hosseini, M.; Hyland, M.; Liu, J.; Malhotra, A.; Ortiz, F. M.; Mohaddes, F.; Ramesh, V. P.; Sargolzaeiaval, Y.; Snouwaert, N.; Özturk, M. C.; Vashaee, D. Review of Wearable Thermoelectric Energy Harvesting: From Body Temperature to Electronic Systems. *Appl. Energy* **2020**, *258* (April 2019), 114069. https://doi.org/10.1016/j.apenergy.2019.114069.

(22) Hohenberg, P.; Kohn, W. Inhomogeneous Electron Gas. *Phys. Rev.* **1964**, *136* (3B), B864–B871. https://doi.org/10.1103/PhysRev.136.B864.

(23) Kohn, W.; Sham, L. J. Self-Consistent Equations Including Exchange and Correlation Effects. *Phys. Rev.* **1965**, *140* (4A), A1133–A1138. https://doi.org/10.1103/PhysRev.140.A1133.

(24) Martin, R. M. *Electronic Structure: Basic Theory and Practical Methods*; Cambridge University Press, 2004. https://doi.org/10.1017/CBO9780511805769.

(25) Perdew, J. P.; Zunger, A. Self-Interaction Correction to Density-Functional Approximations for Many-Electron Systems. *Phys. Rev. B* **1981**, *23* (10), 5048–5079. https://doi.org/10.1103/PhysRevB.23.5048.

(26) Perdew, J. P.; Burke, K.; Ernzerhof, M. Generalized Gradient Approximation Made Simple. *Phys. Rev. Lett.* **1996**, *77* (18), 3865–3868. https://doi.org/10.1103/PhysRevLett.77.3865.

(27) Becke, A. D. A New Mixing of Hartree-Fock and Local Density-Functional Theories. *J. Chem. Phys.* **1993**, *98* (2), 1372–1377. https://doi.org/10.1063/1.464304.

(28) Madsen, G. K. H.; Carrete, J.; Verstraete, M. J. BoltzTraP2, a Program for Interpolating Band Structures and Calculating Semi-Classical Transport Coefficients. *Comput. Phys. Commun.* **2018**, *231*, 140–145. https://doi.org/10.1016/j.cpc.2018.05.010.

(29) Togo, A.; Tanaka, I. First Principles Phonon Calculations in Materials Science. *Scr. Mater.* **2015**, *108*, 1–5. https://doi.org/10.1016/j.scriptamat.2015.07.021.

(30) Baroni, S.; de Gironcoli, S.; Dal Corso, A.; Giannozzi, P. Phonons and Related Crystal Properties from Density-Functional Perturbation Theory. *Rev. Mod. Phys.* **2001**, *73* (2), 515–562. https://doi.org/10.1103/RevModPhys.73.515.

(31) Togo, A.; Chaput, L.; Tanaka, I. Distributions of Phonon Lifetimes in Brillouin Zones. *Phys. Rev. B - Condens. Matter Mater. Phys.* **2015**, *91* (9). https://doi.org/10.1103/PhysRevB.91.094306.

(32) Lohani, K.; Nautiyal, H.; Ataollahi, N.; Fanciulli, C.; Sergueev, I.; Etter, M.; Scardi, P. Experimental and Ab Initio Study of Cu 2 SnS 3 (CTS) Polymorphs for Thermoelectric Applications. *J. Phys. Chem. C* **2021**, *125* (1), 178–188. https://doi.org/10.1021/acs.jpcc.0c09139.

(33) Snyder, G. J.; Toberer, E. S. Complex Thermoelectric Materials. *Nat. Mater.* **2008**, *7* (2), 105–114. https://doi.org/10.1038/nmat2090.

(34) Mao, J.; Liu, Z.; Zhou, J.; Zhu, H.; Zhang, Q.; Chen, G.; Ren, Z. Advances in Thermoelectrics. *Adv. Phys.* **2018**, *67* (2), 69–147. https://doi.org/10.1080/00018732.2018.1551715.

(35) Sootsman, J. R.; Chung, D. Y.; Kanatzidis, M. G. New and Old Concepts in Thermoelectric Materials. *Angew. Chemie - Int. Ed.* **2009**, *48* (46), 8616–8639. https://doi.org/10.1002/anie.200900598.

(36) Han, C.; Sun, Q.; Li, Z.; Dou, S. X. Thermoelectric Enhancement of Different Kinds of Metal Chalcogenides. *Adv. Energy Mater.* **2016**, *6* (15). https://doi.org/10.1002/aenm.201600498.

(37) Mao, J.; Liu, Z.; Ren, Z. Size Effect in Thermoelectric Materials. *npj Quantum Mater.* **2016**, *1* (August), 1–9. https://doi.org/10.1038/npjquantmats.2016.28.

(38) Mehta, R. J.; Zhang, Y.; Karthik, C.; Singh, B.; Siegel, R. W.; Borca-Tasciuc, T.; Ramanath, G. A New Class of Doped Nanobulk High-Figure-of-Merit Thermoelectrics by Scalable Bottom-up Assembly. *Nat. Mater.* **2012**, *11* (3), 233–240. https://doi.org/10.1038/nmat3213.

(39) Ibáñez, M.; Luo, Z.; Genç, A.; Piveteau, L.; Ortega, S.; Cadavid, D.; Dobrozhan, O.; Liu, Y.; Nachtegaal, M.; Zebarjadi, M.; Arbiol, J.; Kovalenko, M. V.; Cabot, A. High-Performance Thermoelectric Nanocomposites from Nanocrystal Building Blocks. *Nat. Commun.* **2016**, *7* (May 2015), 1–7. https://doi.org/10.1038/ncomms10766.

(40) Kovalenker, V. A. Mohite, Cu2SnS3, a New Sulfide of Tin and Copper. *Int. Geol. Rev.* **1983**, *25* (1), 117–120. https://doi.org/10.1080/00206818309466683.

(41) Fernandes, P. A.; Salomé, P. M. P.; Cunha, A. F. D. A Study of Ternary Cu2SnS3 and Cu3SnS 4 Thin Films Prepared by Sulfurizing Stacked Metal Precursors. *J. Phys. D. Appl. Phys.* **2010**, *43* (21). https://doi.org/10.1088/0022-3727/43/21/215403.

(42) Fernandes, P. A.; Salomé, P. M. P.; Da Cunha, A. F. CuxSnSx+1 (x = 2, 3) Thin Films Grown by Sulfurization of Metallic Precursors Deposited by Dc Magnetron Sputtering. *Phys. Status Solidi Curr. Top. Solid State Phys.* **2010**,

7 (3–4), 901–904. https://doi.org/10.1002/pssc.200982746.

(43) Pallavolu, M. R.; Minnam Reddy, V. R.; Pejjai, B.; Jeong, D. seob; Park, C. Effect of Sulfurization Temperature on the Phase Purity of Cu 2 SnS 3 Thin Films Deposited via High Vacuum Sulfurization. *Appl. Surf. Sci.* **2018**, *462* (August), 641–648. https://doi.org/10.1016/j.apsusc.2018.08.112.

(44) Chen, Q.; Maeda, T.; Wada, T. Optical Properties and Electronic Structures of Cu 2 SnS 3 , Cu 2 GeS 3 , and Their Solid Solution. *Jpn. J. Appl. Phys* **2018**, *57*. https://doi.org/https://iopscience.iop.org/article/10.7567/JJAP.57.08RC20.

(45) Raadik, T.; Grossberg, M.; Krustok, J.; Kauk-Kuusik, M.; Crovetto, A.; Bolt Ettlinger, R.; Hansen, O.; Schou, J. Temperature Dependent Photoreflectance Study of Cu2SnS3 Thin Films Produced by Pulsed Laser Deposition. *Appl. Phys. Lett.* **2017**, *110* (26), 3–7. https://doi.org/10.1063/1.4990657.

(46) Xi, L.; Zhang, Y. B.; Shi, X. Y.; Yang, J.; Shi, X.; Chen, L. D.; Zhang, W.; Yang, J.; Singh, D. J. Chemical Bonding, Conductive Network, and Thermoelectric Performance of the Ternary Semiconductors Cu 2SnX 3 (X= Se, S) from First Principles. *Phys. Rev. B - Condens. Matter Mater. Phys.* **2012**, *86* (15), 1–14. https://doi.org/10.1103/PhysRevB.86.155201.

(47) Tan, Q.; Sun, W.; Li, Z.; Li, J. F. Enhanced Thermoelectric Properties of Earth-Abundant Cu2SnS3 via In Doping Effect. *J. Alloys Compd.* **2016**, *672*, 558–563. https://doi.org/10.1016/j.jallcom.2016.02.185.

(48) Shen, Y.; Li, C.; Huang, R.; Tian, R.; Ye, Y.; Pan, L.; Koumoto, K.; Zhang, R.; Wan, C.; Wang, Y. Eco-Friendly p-Type Cu2SnS3 Thermoelectric Material: Crystal Structure and Transport Properties. *Sci. Rep.* **2016**, *6* (September), 2–9. https://doi.org/10.1038/srep32501.

(49) Zhang, Z.; Zhao, H.; Wang, Y.; Hu, X.; Lyu, Y.; Cheng, C.; Pan, L.; Lu, C. Role of Crystal Transformation on the Enhanced Thermoelectric Performance in Mn-Doped Cu2SnS3. *J. Alloys Compd.* **2019**, *780*, 618–625. https://doi.org/10.1016/j.jallcom.2018.11.329.

(50) Xu, X.; Zhao, H.; Hu, X.; Pan, L.; Chen, C.; Li, D.; Wang, Y. Synergistic Role of Ni-Doping in Electrical and Phonon Transport Properties of Cu2Sn1-XNixS3. *J. Alloys Compd.* **2017**, *728*, 701–708. https://doi.org/10.1016/j.jallcom.2017.08.227.

(51) Zhao, L.; Chen, C.; Pan, L.; Hu, X.; Lu, C.; Wang, Y. Magnetic Iron Doping in Cu2SnS3 Ceramics for Enhanced Thermoelectric Transport Properties. *J. Appl. Phys.* **2019**, *125* (9). https://doi.org/10.1063/1.5065074.

(52) Zhao, H.; Xu, X.; Li, C.; Tian, R.; Zhang, R.; Huang, R.; Lyu, Y.; Li, D.; Hu, X.; Pan, L.; Wang, Y. Cobalt-Doping in Cu2SnS3: Enhanced Thermoelectric Performance by Synergy of Phase Transition and Band Structure Modification. *J. Mater. Chem. A* **2017**, *5* (44), 23267–23275. https://doi.org/10.1039/c7ta07140j.

(53) Oliva, F.; Arqués, L.; Acebo, L.; Guc, M.; Sánchez, Y.; Alcobé, X.; Pérez-Rodríguez, A.; Saucedo, E.; Izquierdo-Roca, V. Characterization of Cu2SnS3 Polymorphism and Its Impact on Optoelectronic Properties. *J. Mater. Chem. A* **2017**, *5* (45), 23863–23871. https://doi.org/10.1039/C7TA08705E.

(54) Lohani, K.; Isotta, E.; Ataollahi, N.; Fanciulli, C.; Chiappini, A.; Scardi, P. Ultra-Low Thermal Conductivity and Improved Thermoelectric Performance in Disordered Nanostructured Copper Tin Sulphide (Cu2SnS3, CTS). *J. Alloys Compd.* **2020**, *830*, 154604. https://doi.org/10.1016/j.jallcom.2020.154604.

(55) Baranowski, L. L.; McLaughlin, K.; Zawadzki, P.; Lany, S.; Norman, A.; Hempel, H.; Eichberger, R.; Unold, T.; Toberer, E. S.; Zakutayev, A. Effects of Disorder on Carrier Transport in ${\mathrm{Cu}}_{2}{\mathrm{SnS}}_{3}$. *Phys. Rev. Appl.* **2015**, *4* (4), 44017. https://doi.org/10.1103/PhysRevApplied.4.044017.

(56) Zawadzki, P.; Zakutayev, A.; Lany, S. Entropy-Driven Clustering in Tetrahedrally Bonded Multinary Materials. *Phys. Rev. Appl.* **2015**, *3* (3), 1–7. https://doi.org/10.1103/PhysRevApplied.3.034007.

(57) Zhai, Y. T.; Chen, S.; Yang, J. H.; Xiang, H. J.; Gong, X. G.; Walsh, A.; Kang, J.; Wei, S. H. Structural Diversity and Electronic Properties of Cu2SnX 3 (X=S, Se): A First-Principles Investigation. *Phys. Rev. B - Condens. Matter Mater. Phys.* **2011**, *84* (7), 1–6. https://doi.org/10.1103/PhysRevB.84.075213.

(58) Crovetto, A.; Chen, R.; Ettlinger, R. B.; Cazzaniga, A. C.; Schou, J.; Persson, C.; Hansen, O. Dielectric Function and Double Absorption Onset of Monoclinic Cu2SnS3: Origin of Experimental Features Explained by First-Principles Calculations. *Sol. Energy Mater. Sol. Cells* **2016**, *154*, 121–129. https://doi.org/10.1016/j.solmat.2016.04.028.

(59) Siyar, M.; Cho, J. Y.; Youn, Y.; Han, S.; Kim, M.; Bae, S. H.; Park, C. Effect of Annealing Temperature on the Phase Transition, Band Gap and Thermoelectric Properties of Cu2SnSe3. *J. Mater. Chem. C* **2018**, *6* (7), 1780–1788. https://doi.org/10.1039/c7tc05180h.

(60) Lohani, K.; Isotta, E.; Ataollahi, N.; Fanciulli, C.; Chiappini, A.; Scardi, P. Ultra-Low Thermal Conductivity and Improved Thermoelectric Performance in Disordered Nanostructured Copper Tin Sulphide (Cu2SnS3, CTS). *J. Alloys Compd.* **2020**, *830*. https://doi.org/10.1016/j.jallcom.2020.154604.

(61) Kresse, G.; Furthmüller, J. Efficient Iterative Schemes for Ab Initio Total-Energy Calculations Using a Plane-Wave Basis Set. *Phys. Rev. B - Condens. Matter Mater. Phys.* **1996**, *54* (16), 11169–11186. https://doi.org/10.1103/PhysRevB.54.11169.

(62) Kresse, G.; Furthmüller, J. Efficiency of Ab-Initio Total Energy Calculations for Metals and Semiconductors Using a Plane-Wave Basis Set. *Comput. Mater. Sci.* **1996**, *6* (1), 15–50. https://doi.org/10.1016/0927-0256(96)00008-0.

(63) Pack, J. D.; Monkhorst, H. J. "Special Points for Brillouin-Zone Integrations"---a Reply. *Phys. Rev. B* **1977**, *16* (4), 1748–1749. https://doi.org/10.1103/PhysRevB.16.1748.

(64) Peter E. Blöchl, O. Jepsen, O. K. A. Improved Tetrahedron. **1994**, *49* (23). https://doi.org/10.1103/PhysRevB.49.16223.

(65) Hinuma, Y.; Pizzi, G.; Kumagai, Y.; Oba, F.; Tanaka, I. Band Structure Diagram Paths Based on Crystallography. *Comput. Mater. Sci.* **2017**, *128*, 140–184. https://doi.org/10.1016/j.commatsci.2016.10.015.

(66) Perdew, J. P.; Zunger, A. Self-Interaction Correction to Density-Functional Approximations for Many-Electron Systems. *Phys. Rev. B* **1981**, *23* (10), 5048–5079. https://doi.org/10.1103/PhysRevB.23.5048.

(67) McCusker, L. B.; Von Dreele, R. B.; Cox, D. E.; Louër, D.; Scardi, P. Rietveld Refinement Guidelines. *J. Appl. Crystallogr.* **1999**, *32* (1), 36–50. https://doi.org/10.1107/S0021889898009856.

(68) Scardi, P.; Azanza Ricardo, C. L.; Perez-Demydenko, C.; Coelho, A. A. Whole Powder Pattern Modelling Macros for TOPAS. *J. Appl. Crystallogr.* **2018**, *51* (6), 1752–1765. https://doi.org/10.1107/S160057671801289X.

(69) Coelho, A. A. TOPAS and TOPAS-Academic: An Optimization Program Integrating Computer Algebra and Crystallographic Objects Written in C++. *J. Appl. Crystallogr.* **2018**, *51* (1), 210–218. https://doi.org/10.1107/S1600576718000183.

(70) Isotta, E.; Fanciulli, C.; Pugno, N. M.; Scardi, P. Effect of the Order-Disorder Transition on the Seebeck Coefficient of Nanostructured Thermoelectric Cu2ZnSnS4. *Nanomaterials* **2019**, \ (762), 1–11. https://doi.org/10.3390 / nano9050762.

(71) Isotta, E.; Mukherjee, B.; Fanciulli, C.; Pugno, N. M.; Scardi, P. Order-Disorder Transition in Kesterite Cu2ZnSnS4: Thermopower Enhancement via Electronic Band Structure Modification. *J. Phys. Chem. C* **2020**, *124* (13), 7091–7096. https://doi.org/10.1021/acs.jpcc.0c00886.

(72) Tiwari, D.; Koehler, T.; Klenk, R.; Fermin, D. J. Solution Processed Single-Phase Cu 2 SnS 3 Films: Structure and Photovoltaic Performance . *Sustain. Energy Fuels* **2017**, *1* (4), 899–906. https://doi.org/10.1039/c7se00150a.

(73) Shigemi, A.; Maeda, T.; Wada, T. First-Principles Calculation of Cu2SnS3 and Related Compounds. *Phys. Status Solidi Basic Res.* **2015**, *252* (6), 1230–1234. https://doi.org/10.1002/pssb.201400346.

(74) Gajaria, T. K.; Dabhi, S. D.; Jha, P. K. Ab Initio Energetics and Thermoelectric Profiles of Gallium Pnictide Polytypes. *Sci. Rep.* **2019**, *9* (1), 1–20. https://doi.org/10.1038/s41598-019-41982-9.

(75) Lin, S.; Li, W.; Li, S.; Zhang, X.; Chen, Z.; Xu, Y.; Chen, Y.; Pei, Y. High Thermoelectric Performance of Ag9GaSe6 Enabled by Low Cutoff Frequency of Acoustic Phonons. *Joule* **2017**, *1* (4), 816–830. https://doi.org/10.1016/j.joule.2017.09.006.

(76) Zhao, L.-D.; Kanatzidis, M. G. Ultralow Thermal Conductivity and High Thermoelectric Figure of Merit in SnSe Crystals. *Nature* **2014**, *508* (7496), 373–377. https://doi.org/10.1038/nature13184.

(77) Toberer, E. S.; Baranowski, L. L.; Dames, C. Advances in Thermal Conductivity. *Annu. Rev. Mater. Res.* **2012**, *42* (April 2015), 179–209. https://doi.org/10.1146/annurev-matsci-070511-155040.

(78) Zhang, S.; Xu, B.; Lin, Y.; Nan, C.; Liu, W. First-Principles Study of the Layered Thermoelectric Material TiNBr. *RSC Adv.* **2019**, *9* (23), 12886–12894. https://doi.org/10.1039/c9ra00247b.

(79) Zhang, R.; Wen, X.; Xu, F.; Zhang, Q.; Sun, L. A Density Functional Theory

Study of the Cu 2 ZnSnS 4 Monolayer as a Photo-Electrointegrated Catalyst for Water Splitting and Hydrogen Evolution . *J. Phys. Chem. C* **2020**, *124* (22), 11922–11929. https://doi.org/10.1021/acs.jpcc.0c02103.

(80) Grin, Y. Inhomogeneity and Anisotropy of Chemical Bonding and Thermoelectric Properties of Materials. *J. Solid State Chem.* **2019**, *274* (November 2018), 329–336. https://doi.org/10.1016/j.jssc.2018.12.055.

(81) Bessas, D.; Sergueev, I.; Wille, H.-C.; Per\sson, J.; Ebling, D.; Hermann, R. P. Lattice Dynamics in Bi${}_{2}$Te${}_{3}$ and Sb${}_{2}$Te${}_{3}$: Te and Sb Density of Phonon States. *Phys. Rev. B* **2012**, *86* (22), 224301. https://doi.org/10.1103/PhysRevB.86.224301.

(82) Sergueev, I.; Hermann, R. P.; Bessas, D.; Pelzer, U.; Angst, M.; Schweika, W.; McGuire, M. A.; Sefat, A. S.; Sales, B. C.; Mandrus, D.; Rüffer, R. Effect of Pressure, Temperature, Fluorine Doping, and Rare Earth Elements on the Phonon Density of States of LFeAsO Studied by Nuclear Inelastic Scattering. *Phys. Rev. B* **2013**, *87* (6), 64302. https://doi.org/10.1103/PhysRevB.87.064302.

(83) Sergueev, I.; Glazyrin, K.; Kantor, I.; McGuire, M. A.; Chumakov, A. I.; Klobes, B.; Sales, B. C.; Hermann, R. P. Quenching Rattling Modes in Skutterudites with Pressure. *Phys. Rev. B* **2015**, *91* (22), 224304. https://doi.org/10.1103/PhysRevB.91.224304.

(84) Zhai, Y.-T.; Chen, S.; Yang, J.-H.; Xiang, H.-J.; Gong, X.-G.; Walsh, A.; Kang, J.; Wei, S.-H. Structural Diversity and Electronic Properties of Cu2SnX3 (X=S, Se): A First-Principles Investigation. *Phys. Rev. B* **2011**, *84* (7), 075213. https://doi.org/10.1103/PhysRevB.84.075213.

(85) Shen, Y.; Li, C.; Huang, R.; Tian, R.; Ye, Y.; Pan, L.; Koumoto, K.; Zhang, R.; Wan, C.; Wang, Y. Eco-Friendly p-Type Cu2SnS3 Thermoelectric Material: Crystal Structure and Transport Properties. *Sci. Rep.* **2016**, *6* (1), 32501. https://doi.org/10.1038/srep32501.

(86) Filik, J.; Ashton, A. W.; Chang, P. C. Y.; Chater, P. A.; Day, S. J.; Drakopoulos, M.; Gerring, M. W.; Hart, M. L.; Magdysyuk, O. V.; Michalik, S.; Smith, A.; Tang, C. C.; Terrill, N. J.; Wharmby, M. T.; Wilhelm, H. Processing Two-Dimensional X-Ray Diffraction and Small-Angle Scattering Data in DAWN 2. *J. Appl. Crystallogr.* **2017**, *50* (3), 959–966. https://doi.org/10.1107/S1600576717004708.

(87) Jaldurgam, F. F.; Ahmad, Z.; Touati, F. Low-Toxic, Earth-Abundant Nanostructured Materials for Thermoelectric Applications. *Nanomaterials* **2021**, *11* (4), 895. https://doi.org/10.3390/nano11040895.

(88) Wei, T. R.; Qin, Y.; Deng, T.; Song, Q.; Jiang, B.; Liu, R.; Qiu, P.; Shi, X.; Chen, L. Copper Chalcogenide Thermoelectric Materials. *Sci. China Mater.* **2019**, *62* (1), 8–24. https://doi.org/10.1007/s40843-018-9314-5.

(89) Suekuni, K.; Kim, F. S.; Nishiate, H.; Ohta, M.; Tanaka, H. I.; Takabatake, T. High-Performance Thermoelectric Minerals: Colusites Cu 26 V 2 M 6 S 32 (M = Ge, Sn). *Appl. Phys. Lett.* **2014**, *105* (13), 132107. https://doi.org/10.1063/1.4896998.

(90) Guélou, G.; Lemoine, P.; Raveau, B.; Guilmeau, E. Recent Developments in High-Performance Thermoelectric Sulphides: An Overview of the Promising

Synthetic Colusites. *J. Mater. Chem. C* **2021**, *9* (3), 773–795. https://doi.org/10.1039/D0TC05086E.

(91) Biswas, K.; Zhao, L.-D.; Kanatzidis, M. G. Tellurium-Free Thermoelectric: The Anisotropic n-Type Semiconductor Bi2S3. *Adv. Energy Mater.* **2012**, *2* (6), 634–638. https://doi.org/10.1002/aenm.201100775.

(92) Tan, G.; Hao, S.; Zhao, J.; Wolverton, C.; Kanatzidis, M. G. High Thermoelectric Performance in Electron-Doped AgBi 3 S 5 with Ultralow Thermal Conductivity. *J. Am. Chem. Soc.* **2017**, *139* (18), 6467–6473. https://doi.org/10.1021/jacs.7b02399.

(93) Powell, A. V. Recent Developments in Earth-Abundant Copper-Sulfide Thermoelectric Materials. *J. Appl. Phys.* **2019**, *126* (10), 100901. https://doi.org/10.1063/1.5119345.

(94) Baláž, P.; Achimovičová, M.; Baláž, M.; Chen, K.; Dobrozhan, O.; Guilmeau, E.; Hejtmánek, J.; Knížek, K.; Kubíčková, L.; Levinský, P.; Puchý, V.; Reece, M. J.; Varga, P.; Zhang, R. Thermoelectric Cu–S-Based Materials Synthesized via a Scalable Mechanochemical Process. *ACS Sustain. Chem. Eng.* **2021**, *9* (5), 2003–2016. https://doi.org/10.1021/acssuschemeng.0c05555.

(95) Snyder, G. J.; Toberer, E. S. Complex Thermoelectric Materials. *Nat. Mater.* **2008**, *7* (February), 105–114. https://doi.org/10.1038/nmat2090.

(96) Beretta, D.; Neophytou, N.; Hodges, J. M.; Kanatzidis, M. G.; Narducci, D.; Martin-Gonzalez, M.; Beekman, M.; Balke, B.; Cerretti, G.; Tremel, W.; Zevalkink, A.; Hofmann, A. I.; Müller, C.; Dörling, B.; Campoy-Quiles, M.; Caironi, M. Thermoelectrics: From History, a Window to the Future. *Mater. Sci. Eng. R Reports* **2018**, *138* (November 2018), 210–255. https://doi.org/10.1016/j.mser.2018.09.001.

(97) Zhang, X.; Bu, Z.; Shi, X.; Chen, Z.; Lin, S.; Shan, B.; Wood, M.; Snyder, A. H.; Chen, L.; Snyder, G. J.; Pei, Y. Electronic Quality Factor for Thermoelectrics. *Sci. Adv.* **2020**, *6* (46), eabc0726. https://doi.org/10.1126/sciadv.abc0726.

(98) Dias, S.; Kumawat, K.; Biswas, S.; Krupanidhi, S. B. Solvothermal Synthesis of Cu 2 SnS 3 Quantum Dots and Their Application in Near-Infrared Photodetectors. *Inorg. Chem.* **2017**, *56* (4), 2198–2203. https://doi.org/10.1021/acs.inorgchem.6b02832.

(99) Pavan Kumar, V.; Lemoine, P.; Carnevali, V.; Guélou, G.; Lebedev, O. I.; Boullay, P.; Raveau, B.; Al Rahal Al Orabi, R.; Fornari, M.; Prestipino, C.; Menut, D.; Candolfi, C.; Malaman, B.; Juraszek, J.; Guilmeau, E. Ordered Sphalerite Derivative Cu 5 Sn 2 S 7 : A Degenerate Semiconductor with High Carrier Mobility in the Cu–Sn–S Diagram. *J. Mater. Chem. A* **2021**, *9* (17), 10812–10826. https://doi.org/10.1039/D1TA01615F.

(100) Deng, T.; Qiu, P.; Song, Q.; Chen, H.; Wei, T.-R.; Xi, L.; Shi, X.; Chen, L. Thermoelectric Properties of Non-Stoichiometric Cu2+ XSn1− XS3 Compounds. *J. Appl. Phys.* **2019**, *126* (8), 085111. https://doi.org/10.1063/1.5115195.

(101) Aihara, N.; Matsumoto, Y.; Tanaka, K. Exciton Luminescence from Cu 2 SnS 3 Bulk Crystals. *Appl. Phys. Lett.* **2016**, *108* (9), 092107. https://doi.org/10.1063/1.4943229.

(102) Baranowski, L. L.; McLaughlin, K.; Zawadzki, P.; Lany, S.; Norman, A.; Hempel, H.; Eichberger, R.; Unold, T.; Toberer, E. S.; Zakutayev, A. Effects of Disorder on Carrier Transport in Cu2SnS3. *Phys. Rev. Appl.* **2015**, *4* (4), 044017. https://doi.org/10.1103/PhysRevApplied.4.044017.

(103) Dahule, R.; Raghav, A.; Hanindriyo, A. T.; Hongo, K.; Maezono, R.; Panda, E. Surface Study of Cu 2 SnS 3 Using First-Principles Density Functional Theory. *Adv. Theory Simulations* **2021**, *4* (6), 2000315. https://doi.org/10.1002/adts.202000315.

(104) Baláž, P.; Dutková, E.; Levinský, P.; Daneu, N.; Kubíčková, L.; Knížek, K.; Baláž, M.; Navrátil, J.; Kašparová, J.; Ksenofontov, V.; Möller, A.; Hejtmánek, J. Enhanced Thermoelectric Performance of Chalcopyrite Nanocomposite via Co-Milling of Synthetic and Natural Minerals. *Mater. Lett.* **2020**, *275* (June), 128107. https://doi.org/10.1016/j.matlet.2020.128107.

(105) Lohani, K.; Isotta, E.; Ataollahi, N.; Fanciulli, C.; Chiappini, A.; Scardi, P. Ultra-Low Thermal Conductivity and Improved Thermoelectric Performance in Disordered Nanostructured Copper Tin Sulphide (Cu2SnS3, CTS). *J. Alloys Compd.* **2020**, *830* (C), 154604. https://doi.org/10.1016/j.jallcom.2020.154604.

(106) Scardi, P.; Leoni, M. Diffraction Line Profiles from Polydisperse Crystalline Systems. *Acta Crystallogr. Sect. A Found. Crystallogr.* **2001**, *57* (5), 604–613. https://doi.org/10.1107/S0108767301008881.

(107) Black, D. R.; Mendenhall, M. H.; Brown, C. M.; Henins, A.; Filliben, J.; Cline, J. P. Certification of Standard Reference Material 660c for Powder Diffraction. *Powder Diffr.* **2020**, *35* (1), 17–22. https://doi.org/10.1017/S0885715620000068.

(108) Yang, Y.; Ying, P.; Wang, J.; Liu, X.; Du, Z.; Chao, Y.; Cui, J. Enhancing the Thermoelectric Performance of Cu3SnS4-Based Solid Solutions through Coordination of the Seebeck Coefficient and Carrier Concentration. *J. Mater. Chem. A* **2017**, *5* (35), 18808–18815. https://doi.org/10.1039/c7ta05253g.

(109) Deng, T.; Qiu, P.; Xing, T.; Zhou, Z.; Wei, T. R.; Ren, D.; Xiao, J.; Shi, X.; Chen, L. A Low-Cost and Eco-Friendly Br-Doped Cu7Sn3S10thermoelectric Compound WithzTaround Unity. *J. Mater. Chem. A* **2021**, *9* (12), 7946–7954. https://doi.org/10.1039/d0ta12042a.

(110) Narducci, D.; Selezneva, E.; Cerofolini, G.; Frabboni, S.; Ottaviani, G. Impact of Energy Filtering and Carrier Localization on the Thermoelectric Properties of Granular Semiconductors. *J. Solid State Chem.* **2012**, *193*, 19–25. https://doi.org/10.1016/j.jssc.2012.03.032.

(111) Kim, H.-S.; Gibbs, Z. M.; Tang, Y.; Wang, H.; Snyder, G. J. Characterization of Lorenz Number with Seebeck Coefficient Measurement. *APL Mater.* **2015**, *3* (4), 041506. https://doi.org/10.1063/1.4908244.

(112) Xie, H.; Su, X.; Yan, Y.; Liu, W.; Chen, L.; Fu, J.; Yang, J.; Uher, C.; Tang, X. Thermoelectric Performance of CuFeS2+2x Composites Prepared by Rapid Thermal Explosion. *NPG Asia Mater.* **2017**, *9* (6), e390–e390. https://doi.org/10.1038/am.2017.80.

(113) Deng, T.; Qiu, P.; Xing, T.; Zhou, Z.; Wei, T.-R.; Ren, D.; Xiao, J.; Shi, X.; Chen, L. A Low-Cost and Eco-Friendly Br-Doped Cu 7 Sn 3 S 10

Thermoelectric Compound with ZT around Unity. *J. Mater. Chem. A* **2021**, *9* (12), 7946–7954. https://doi.org/10.1039/D0TA12042A.

(114) Wei, Y.; Zhou, Z.; Jiang, P.; Zheng, S.; Xiong, Q.; Zhang, B.; Wang, G.; Lu, X.; Han, G.; Zhou, X. Phase Composition Manipulation and Twin Boundary Engineering Lead to Enhanced Thermoelectric Performance of Cu 2 SnS 3. *ACS Appl. Energy Mater.* **2021**, acsaem.1c01483. https://doi.org/10.1021/acsaem.1c01483.

(115) Nautiyal, H.; Lohani, K.; Mukherjee, B.; Isotta, E.; Malagutti, M. A.; Ataollahi, N.; Pallecchi, I.; Putti, M.; Misture, S. T.; Rebuffi, L.; Scardi, P. Mechanochemical Synthesis of Sustainable Ternary and Quaternary Nanostructured Cu2SnS3, Cu2ZnSnS4, and Cu2ZnSnSe4 Chalcogenides for Thermoelectric Applications. *Nanomaterials* **2023**, *13* (2), 366. https://doi.org/10.3390/nano13020366.

(116) Koskela, K. M.; Mora Perez, C.; Eremin, D. B.; Evans, J. M.; Strumolo, M. J.; Lewis, N. S.; Prezhdo, O. V; Brutchey, R. L. Polymorphic Control of Solution-Processed Cu 2 SnS 3 Films with Thiol–Amine Ink Formulation. *Chem. Mater.* **2022**. https://doi.org/10.1021/acs.chemmater.2c01612.

(117) Syafiq, U.; Isotta, E.; Ataollahi, N.; Lohani, K.; Luong, S.; Trifiletti, V.; Fenwick, O.; Scardi, P. Facile and Low-Cost Fabrication of Cu/Zn/Sn-Based Ternary and Quaternary Chalcogenides Thermoelectric Generators. *ACS Appl. Energy Mater.* **2022**, *5* (5), 5909–5918. https://doi.org/10.1021/acsaem.2c00268.

(118) Hu, L.; Luo, Y.; Fang, Y. W.; Qin, F.; Cao, X.; Xie, H.; Liu, J.; Dong, J.; Sanson, A.; Giarola, M.; Tan, X.; Zheng, Y.; Suwardi, A.; Huang, Y.; Hippalgaonkar, K.; He, J.; Zhang, W.; Xu, J.; Yan, Q.; Kanatzidis, M. G. High Thermoelectric Performance through Crystal Symmetry Enhancement in Triply Doped Diamondoid Compound Cu2SnSe3. *Adv. Energy Mater.* **2021**, *11* (42). https://doi.org/10.1002/aenm.202100661.

(119) Zhang, D.; Zhang, B.; Zhou, Z.; Peng, K.; Wu, H.; Wang, H.; Wang, G.; Han, G.; Wang, G.; Zhou, X.; Lu, X. Ultralow Lattice Thermal Conductivity of Cubic CuFeS 2 Induced by Atomic Disorder. *Chem. Mater.* **2021**. https://doi.org/10.1021/acs.chemmater.1c03785.

(120) Zhai, H.; Xiao, Y.; Zhao, L.-D.; Tan, G.; Tang, X. Large Effective Mass and Low Lattice Thermal Conductivity Contributing to High Thermoelectric Performance of Zn-Doped Cu5Sn2Se7. *J. Alloys Compd.* **2020**, *826*, 154154. https://doi.org/10.1016/j.jallcom.2020.154154.

(121) Isotta, E.; Mukherjee, B.; Bette, S.; Dinnebier, R.; Scardi, P. Static and Dynamic Components of Debye–Waller Coefficients in the Novel Cubic Polymorph of Low-Temperature Disordered Cu 2 ZnSnS 4 . *IUCrJ* **2022**, *9* (2), 1–14. https://doi.org/10.1107/s2052252522000239.

(122) Isotta, E.; Mukherjee, B.; Fanciulli, C.; Ataollahi, N.; Sergueev, I.; Stankov, S.; Edla, R.; Pugno, N. M.; Scardi, P. Origin of a Simultaneous Suppression of Thermal Conductivity and Increase of Electrical Conductivity and Seebeck Coefficient in Disordered Cubic Cu2ZnSnS4. *Phys. Rev. Appl.* **2020**, *14* (6), 1. https://doi.org/10.1103/PhysRevApplied.14.064073.

(123) Ataollahi, N.; Bazerla, F.; Malerba, C.; Chiappini, A.; Ferrari, M.; Di Maggio, R.; Scardi, P. Synthesis and Post-Annealing of Cu2ZnSnS4 Absorber Layers

Based on Oleylamine/1-Dodecanethiol. *Materials (Basel).* **2019**, *12* (20), 3320. https://doi.org/10.3390/ma12203320.

(124) Zhao, Q.; Qin, B.; Wang, D.; Qiu, Y.; Zhao, L. D. Realizing High Thermoelectric Performance in Polycrystalline SnSe via Silver Doping and Germanium Alloying. *ACS Appl. Energy Mater.* **2020**, *3* (3), 2049–2054. https://doi.org/10.1021/acsaem.9b01475.

(125) Sharma, S. D.; Khasimsaheb, B.; Chen, Y. Y.; Neeleshwar, S. Enhanced Thermoelectric Performance of Cu 2 ZnSnS 4 (CZTS) by Incorporating Ag Nanoparticles. *Ceram. Int.* **2019**, *45* (2), 2060–2068. https://doi.org/10.1016/j.ceramint.2018.10.109.

(126) Ballikaya, S.; Chi, H.; Salvador, J. R.; Uher, C. Thermoelectric Properties of Ag-Doped Cu2Se and Cu2Te. *J. Mater. Chem. A* **2013**, *1* (40), 12478–12484. https://doi.org/10.1039/c3ta12508d.

(127) Zhang, L.; Wang, J.; Cheng, Z.; Sun, Q.; Li, Z.; Dou, S. Lead-Free SnTe-Based Thermoelectrics: Enhancement of Thermoelectric Performance by Doping with Gd/Ag. *J. Mater. Chem. A* **2016**, *4* (20), 7936–7942. https://doi.org/10.1039/c6ta01994c.

(128) Jin, Z.; Mao, T.; Qiu, P.; Yue, Z.; Wang, L.; Zhao, K.; Ren, D.; Shi, X.; Chen, L. Thermoelectric Properties and Service Stability of Ag-Containing Cu2Se. *Mater. Today Phys.* **2021**, *21*, 100550. https://doi.org/10.1016/j.mtphys.2021.100550.

(129) Cheng, X.; Yang, D.; Su, X.; Xie, H.; Liu, W.; Zheng, Y.; Tang, X. Synergistically Enhanced Thermoelectric Performance of Cu2SnSe3-Based Composites via Ag Doping Balance. *ACS Appl. Mater. Interfaces* **2021**, *13* (46), 55178–55187. https://doi.org/10.1021/acsami.1c17460.

(130) Mehmood, F.; Wang, H.; Su, W.; Khan, M.; Huo, T.; Chen, T.; Chebanova, G.; Romanenko, A.; Wang, C. Enhanced Power Factor and Figure of Merit of Cu2ZnSnSe4-Based Thermoelectric Composites by Ag Alloying. *Inorg. Chem.* **2021**, *963* (February), 0–8. https://doi.org/10.1021/acs.inorgchem.1c00079.

(131) Lohani, K.; Nautiyal, H.; ataollahi, narges; Maji, K.; Guilmeau, E.; Scardi, P. Effects of Grain Size on the Thermoelectric Properties of Cu_2SnS_3: An Experimental and First-Principles Study. *ACS Appl. Energy Mater. 4* (11), 12604–12612. https://doi.org/10.1021/acsaem.1c02377.

(132) Mukherjee, B.; Isotta, E.; Malagutti, M. A.; Lohani, K.; Rebuffi, L.; Fanciulli, C.; Scardi, P. Thermoelectric Performance in Disordered Cu2ZnSnSe4 Nanostructures Driven by Ultra-Low Thermal Conductivity. *J. Alloys Compd.* **2023**, *933*, 167756. https://doi.org/10.1016/j.jallcom.2022.167756.

(133) Ming, H.; Zhu, G.; Zhu, C.; Qin, X.; Chen, T.; Zhang, J.; Li, D.; Xin, H.; Jabar, B. Boosting Thermoelectric Performance of Cu2SnSe3via Comprehensive Band Structure Regulation and Intensified Phonon Scattering by Multidimensional Defects. *ACS Nano* **2021**, *15* (6), 10532–10541. https://doi.org/10.1021/acsnano.1c03120.

(134) Scardi, P. Diffraction Line Profiles in the Rietveld Method. *Cryst. Growth Des.* **2020**, *20* (10), 6903–6916. https://doi.org/10.1021/acs.cgd.0c00956.

(135) Scardi, P. Chapter 13. Microstructural Properties: Lattice Defects and Domain Size Effects. *Powder Diffr.* **2008**, 376–413. https://doi.org/10.1039/9781847558237-00376.

(136) Heyd, J.; Scuseria, G. E. Efficient Hybrid Density Functional Calculations in Solids: Assessment of the Heyd-Scuseria-Ernzerhof Screened Coulomb Hybrid Functional. *J. Chem. Phys.* **2004**, *121* (3), 1187–1192. https://doi.org/10.1063/1.1760074.

(137) Zhou, W.; Dwivedi, P.; Shijimaya, C.; Ito, M.; Higashimine, K.; Nakada, T.; Takahashi, M.; Mott, D.; Miyata, M.; Ohta, M.; Miwa, H.; Akatsuka, T.; Maenosono, S. Enhancement of the Thermoelectric Figure of Merit in Blended Cu 2 Sn 1– x Zn x S 3 Nanobulk Materials. *ACS Appl. Nano Mater.* **2018**, *1* (9), 4819–4827. https://doi.org/10.1021/acsanm.8b01017.

(138) Lohani, K.; Fanciulli, C.; Scardi, P. Effects of Preparation Procedures and Porosity on Thermoelectric Bulk Samples of Cu2SnS3 (CTS). *Materials (Basel).* **2022**, *15* (3), 1–15. https://doi.org/10.3390/ma15030712.

(139) Deng, T.; Qiu, P.; Song, Q.; Chen, H.; Wei, T.-R.; Xi, L.; Shi, X.; Chen, L. Thermoelectric Properties of Non-Stoichiometric Cu2+ x Sn1− x S3 Compounds. *J. Appl. Phys.* **2019**, *126* (8), 085111. https://doi.org/10.1063/1.5115195.

(140) Snyder, G. J.; Snyder, A. H.; Wood, M.; Gurunathan, R.; Snyder, B. H.; Niu, C. Weighted Mobility. *Adv. Mater.* **2020**, *32* (25), 1–5. https://doi.org/10.1002/adma.202001537.

(141) Xie, H.; Su, X.; Hao, S.; Zhang, C.; Zhang, Z.; Liu, W.; Yan, Y.; Wolverton, C.; Tang, X.; Kanatzidis, M. G. Large Thermal Conductivity Drops in the Diamondoid Lattice of CuFeS2 by Discordant Atom Doping. *J. Am. Chem. Soc.* **2019**, *141* (47), 18900–18909. https://doi.org/10.1021/jacs.9b10983.

(142) Li, Y.; Liu, G.; Cao, T.; Liu, L. M.; Li, J.; Chen, K.; Li, L.; Han, Y.; Zhou, M. Enhanced Thermoelectric Properties of Cu2SnSe3 by (Ag,In)-Co-Doping. *Adv. Funct. Mater.* **2016**, *26* (33), 6025–6032. https://doi.org/10.1002/adfm.201601486.

(143) Baláž, P.; Achimovičová, M.; Baláž, M.; Chen, K.; Dobrozhan, O.; Guilmeau, E.; Hejtmánek, J.; Knížek, K.; Kubíčková, L.; Levinský, P.; Puchý, V.; Reece, M. J.; Varga, P.; Zhang, R. Thermoelectric Cu–S-Based Materials Synthesized via a Scalable Mechanochemical Process. *ACS Sustain. Chem. Eng.* **2021**, *9* (5), 2003–2016. https://doi.org/10.1021/acssuschemeng.0c05555.

(144) Kumar, V. P.; Lemoine, P.; Carnevali, V.; Guélou, G.; Lebedev, O. I.; Raveau, B.; Al Rahal Al Orabi, R.; Fornari, M.; Candolfi, C.; Prestipino, C.; Menut, D.; Malaman, B.; Juraszek, J.; Suekuni, K.; Guilmeau, E. Local-Disorder-Induced Low Thermal Conductivity in Degenerate Semiconductor Cu 22 Sn 10 S 32. *Inorg. Chem.* **2021**, *60* (21), 16273–16285. https://doi.org/10.1021/acs.inorgchem.1c02105.

(145) Liu, W.; Shi, X.; Hong, M.; Yang, L.; Moshwan, R.; Chen, Z. G.; Zou, J. Ag Doping Induced Abnormal Lattice Thermal Conductivity in Cu 2 Se. *J. Mater. Chem. C* **2018**, *6* (48), 13225–13231. https://doi.org/10.1039/c8tc04129f.

(146) Cao, L.; Du, X.; Guo, X.; Yuan, Z. The Enhanced Electrical Transport Properties of Fe3+ Doped Cu2SnS3. *Electron. Mater. Lett.* **2021**, No.

0123456789. https://doi.org/10.1007/s13391-021-00309-5.

(147) Tan, Q.; Sun, W.; Li, Z.; Li, J. F. Enhanced Thermoelectric Properties of Earth-Abundant Cu2SnS3via In Doping Effect. *J. Alloys Compd.* **2016**, *672*, 558–563. https://doi.org/10.1016/j.jallcom.2016.02.185.

(148) Zhao, Y.; Gu, Y.; Zhang, P.; Hu, X.; Wang, Y.; Zong, P.; Pan, L.; Lyu, Y.; Koumoto, K. Enhanced Thermoelectric Performance in Polymorphic Heavily Co-Doped Cu2SnS3 through Carrier Compensation by Sb Substitution. *Sci. Technol. Adv. Mater.* **2021**, *22* (1), 363–372. https://doi.org/10.1080/14686996.2021.1920821.

(149) Xing, W.; Zhao, Z.; Pan, L.; Chen, C.; Li, D.; Wang, Y. Thermoelectric Properties and Magnetoelectric Coupling in Dually Doped Cu2Sn1−2xZnxFexS3. *J. Mater. Sci. Mater. Electron.* **2020**, *31* (14), 11801–11809. https://doi.org/10.1007/s10854-020-03732-w.

(150) Gu, Y.; Ai, W.; Zhao, Y.; Hu, X.; Pan, L.; Zong, P.; Lu, C.; Xu, Z.; Wang, Y. Remarkable Thermoelectric Property Enhancement in Cu2SnS3-CuCo2S4 Nanocomposites via 3D Modulation Doping. *J. Mater. Chem. A* **2021**, No. 207890, 121. https://doi.org/10.1039/D1TA02812J.

(151) Narducci, D. Thermoelectric Harvesters and the Internet of Things: Technological and Economic Drivers. *J. Phys. Energy* **2019**, *1* (2), 024001. https://doi.org/10.1088/2515-7655/ab0c3a.

(152) Shi, X.; Yang, J.; Salvador, J. R.; Chi, M.; Cho, J. Y.; Wang, H.; Bai, S.; Yang, J.; Zhang, W.; Chen, L. Multiple-Filled Skutterudites: High Thermoelectric Figure of Merit through Separately Optimizing Electrical and Thermal Transports. *J. Am. Chem. Soc.* **2011**, *133* (20), 7837–7846. https://doi.org/10.1021/ja111199y.

(153) Zhao, L. D.; Lo, S. H.; Zhang, Y.; Sun, H.; Tan, G.; Uher, C.; Wolverton, C.; Dravid, V. P.; Kanatzidis, M. G. Ultralow Thermal Conductivity and High Thermoelectric Figure of Merit in SnSe Crystals. *Nature* **2014**, *508* (7496), 373–377. https://doi.org/10.1038/nature13184.

(154) Nielsen, M. D.; Ozolins, V.; Heremans, J. P. Lone Pair Electrons Minimize Lattice Thermal Conductivity. *Energy Environ. Sci.* **2013**, *6* (2), 570–578. https://doi.org/10.1039/c2ee23391f.

(155) Biswas, K.; He, J.; Blum, I. D.; Wu, C. I.; Hogan, T. P.; Seidman, D. N.; Dravid, V. P.; Kanatzidis, M. G. High-Performance Bulk Thermoelectrics with All-Scale Hierarchical Architectures. *Nature* **2012**, *489* (7416), 414–418. https://doi.org/10.1038/nature11439.

(156) Zhao, X.; Zhu, X. H.; Zhang, R. Z. Evaluation of Energy Filtering Effect from First Principles Calculations. *Phys. Status Solidi Appl. Mater. Sci.* **2016**, *213* (12), 3250–3253. https://doi.org/10.1002/pssa.201600546.

(157) Abdel-Motaleb, I. M.; Qadri, S. M. Thermoelectric Devices: Principles and Future Trends. **2017**, 1–20.

(158) Isotta, E.; Andrade-Arvizu, J.; Syafiq, U.; Jiménez-Arguijo, A.; Navarro-Güell, A.; Guc, M.; Saucedo, E.; Scardi, P. Towards Low Cost and Sustainable Thin Film Thermoelectric Devices Based on Quaternary Chalcogenides. *Adv. Funct. Mater.* **2022**, 2202157. https://doi.org/10.1002/adfm.202202157.

(159) Fiss, B. G.; Richard, A. J.; Douglas, G.; Kojic, M.; Friščić, T.; Moores, A. Mechanochemical Methods for the Transfer of Electrons and Exchange of Ions: Inorganic Reactivity from Nanoparticles to Organometallics. *Chemical Society Reviews*. Royal Society of Chemistry July 2021, pp 8279–8318. https://doi.org/10.1039/d0cs00918k.

(160) Malagutti, M. A.; de Fátima Ulbrich, K.; Winiarski, J. P.; Paes, V. Z. C.; Geshev, J.; Jost, C. L.; Maduro de Campos, C. E. Mechanochemical Synthesis of γ-CoTe2 Nanocrystals and Their Application for Determination of Ferulic Acid. *Mater. Today Commun.* **2022**, *31* (March). https://doi.org/10.1016/j.mtcomm.2022.103481.

(161) Malagutti, M. A.; Paes, V. Z. C.; Geshev, J.; De Campos, C. E. M. Polymorphism of the Co – Te Nanophases in Mechanochemical Synthesis †. *RSC Adv.* **2022**, *12*, 33488–33500. https://doi.org/10.1039/d2ra05757c.

(162) Moores, A. Bottom up, Solid-Phase Syntheses of Inorganic Nanomaterials by Mechanochemistry and Aging. *Curr. Opin. Green Sustain. Chem.* **2018**, *12*, 33–37. https://doi.org/10.1016/j.cogsc.2018.05.004.

(163) Isotta, E.; Pugno, N. M.; Scardi, P. Nanostructured Kesterite (Cu2ZnSnS4) for Applications in Thermoelectric Devices. *Powder Diffr.* **2019**, *34* (S1), S42–S47. https://doi.org/10.1017/S0885715619000277.

(164) Jathar, S. B.; Rondiya, S. R.; Jadhav, Y. A.; Nilegave, D. S.; Cross, R. W.; Barma, S. V.; Nasane, M. P.; Gaware, S. A.; Bade, B. R.; Jadkar, S. R.; Funde, A. M.; Dzade, N. Y. Ternary Cu2SnS3: Synthesis, Structure, Photoelectrochemical Activity, and Heterojunction Band Offset and Alignment. *Chem. Mater.* **2021**, *33* (6), 1983–1993. https://doi.org/10.1021/acs.chemmater.0c03223.

(165) Lokhande, A. C.; Yadav, A. A.; Lee, J. Y.; He, M.; Patil, S. J.; Lokhande, V. C.; Lokhande, C. D.; Kim, J. H. Room Temperature Liquefied Petroleum Gas Sensing Using Cu2SnS3/CdS Heterojunction. *J. Alloys Compd.* **2017**, *709*, 92–103. https://doi.org/10.1016/j.jallcom.2017.03.135.

(166) Mathur, A. S.; Upadhyay, S.; Singh, P. P.; Sharma, B.; Arora, P.; Rajput, V. K.; Kumar, P.; Singh, D.; Singh, B. P. Role of Defect Density in Absorber Layer of Ternary Chalcogenide Cu2SnS3 Solar Cell. *Opt. Mater. (Amst).* **2021**, *119* (April), 111314. https://doi.org/10.1016/j.optmat.2021.111314.

(167) Deng, T.; Qiu, P.; Song, Q.; Chen, H.; Wei, T. R.; Xi, L.; Shi, X.; Chen, L. Thermoelectric Properties of Non-Stoichiometric Cu2+ XSn1- XS3 Compounds. *J. Appl. Phys.* **2019**, *126* (8). https://doi.org/10.1063/1.5115195.

(168) Gu, Y.; Ai, W.; Zhao, Y.; Pan, L.; Lu, C.; Zong, P.; Hu, X.; Xu, Z.; Wang, Y. Remarkable Thermoelectric Property Enhancement in Cu2SnS3-CuCo2S4nanocompositesvia3D Modulation Doping. *J. Mater. Chem. A* **2021**, *9* (31), 16928–16935. https://doi.org/10.1039/d1ta02812j.

(169) Lohani, K.; Nautiyal, H.; Ataollahi, N.; Maji, K.; Guilmeau, E.; Scardi, P. Effects of Grain Size on the Thermoelectric Properties of Cu2SnS3: An Experimental and First-Principles Study. *ACS Appl. Energy Mater.* **2021**, *4* (11), 12604–12612. https://doi.org/10.1021/acsaem.1c02377.

(170) Ahmoum, H.; Sukor Su'ait, M.; Ataollahi, N.; Ubaidah Syafiq Mustaffa, M.; Boughrara, M.; Chelvanathan, P.; Sopian, K.; Li, G.; Kerouad, M.; Scardi, P.;

Wang, Q. Suppressing the Secondary Phases via N2 Preheating of Cu2ZnSnS4 Thin Films with the Addition of Oleylamine and/or 1-Dodecanethiol Solvents. *Inorg. Chem. Commun.* **2021**, *134* (September), 109031. https://doi.org/10.1016/j.inoche.2021.109031.

(171) Syafiq, U.; Ataollahi, N.; Scardi, P. Progress in CZTS as Hole Transport Layer in Perovskite Solar Cell. *Sol. Energy* **2020**, *196* (December 2019), 399–408. https://doi.org/10.1016/j.solener.2019.12.016.

(172) Liu, M. L.; Huang, F. Q.; Chen, L. D.; Chen, I. W. A Wide-Band-Gap p -Type Thermoelectric Material Based on Quaternary Chalcogenides of Cu2ZnSnQ4 (Q=S,Se). *Appl. Phys. Lett.* **2009**, *94* (20), 3–6. https://doi.org/10.1063/1.3130718.

(173) Yang, H.; Jauregui, L. A.; Zhang, G.; Chen, Y. P.; Wu, Y. Nontoxic and Abundant Copper Zinc Tin Sulfide Nanocrystals for Potential High-Temperature Thermoelectric Energy Harvesting. *Nano Lett.* **2012**, *12* (2), 540–545. https://doi.org/10.1021/nl201718z.

(174) Jiang, Q.; Yan, H.; Lin, Y.; Shen, Y.; Yang, J.; Reece, M. J. Colossal Thermoelectric Enhancement in Cu2+xZn1−xSnS4solid Solution by Local Disordering of Crystal Lattice and Multi-Scale Defect Engineering. *J. Mater. Chem. A* **2020**, *8* (21), 10909–10916. https://doi.org/10.1039/d0ta01595d.

(175) Dong, Y.; Wang, H.; Nolas, G. S. Synthesis and Thermoelectric Properties of Cu Excess Cu2ZnSnSe4. *Phys. Status Solidi - Rapid Res. Lett.* **2014**, *8* (1), 61–64. https://doi.org/10.1002/pssr.201308274.

(176) Raju, C.; Falmbigl, M.; Rogl, P.; Yan, X.; Bauer, E.; Horky, J.; Zehetbauer, M.; Chandra Mallik, R. Thermoelectric Properties of Chalcogenide Based Cu2xZnSn 1-XSe4. *AIP Adv.* **2013**, *3* (3). https://doi.org/10.1063/1.4794733.

(177) Li, Z.; Zhang, W.; Gu, B.; Zhao, C.; Ye, B.; Xiao, C.; Xie, Y. Vacancy Cluster-Induced Local Disordered Structure for the Enhancement of Thermoelectric Property in Cu2ZnSnSe4. *J. Mater. Chem. A* **2021**, *9* (2), 1006–1013. https://doi.org/10.1039/d0ta09866c.

(178) Nagaoka, A.; Yoshino, K.; Masuda, T.; Sparks, T. D.; Scarpulla, M. A.; Nishioka, K. Environmentally Friendly Thermoelectric Sulphide Cu2ZnSnS4single Crystals Achieving a 1.6 Dimensionless Figure of MeritZT. *J. Mater. Chem. A* **2021**, *9* (28), 15595–15604. https://doi.org/10.1039/d1ta02978a.

(179) Xiao, C.; Li, K.; Zhang, J.; Tong, W.; Liu, Y.; Li, Z.; Huang, P.; Pan, B.; Su, H.; Xie, Y. Magnetic Ions in Wide Band Gap Semiconductor Nanocrystals for Optimized Thermoelectric Properties. *Mater. Horizons* **2014**, *1* (1), 81–86. https://doi.org/10.1039/c3mh00091e.

(180) Wei, K.; Beauchemin, L.; Wang, H.; Porter, W. D.; Martin, J.; Nolas, G. S. Enhanced Thermoelectric Properties of Cu2ZnSnSe4 with Ga-Doping. *J. Alloys Compd.* **2015**, *650*, 844–847. https://doi.org/10.1016/j.jallcom.2015.08.046.

(181) Isotta, E.; Mukherjee, B.; Bette, S.; Dinnebier, R.; Scardi, P. Static and Dynamic Components of Debye-Waller Coefficients in the Novel Cubic Polymorph of Low-Temperature Disordered Cu2ZnSnS4. *IUCrJ* **2022**, *9*, 272–285. https://doi.org/10.1107/S2052252522000239.

(182) Scardi, P.; Azanza Ricardo, C. L.; Perez-Demydenko, C.; Coelho, A. A. Whole Powder Pattern Modelling Macros for TOPAS. *J. Appl. Crystallogr.* **2018**, *51* (6), 1752–1765. https://doi.org/10.1107/S160057671801289X.

(183) Scardi, P.; Leoni, M. Whole Powder Pattern Modelling. *Acta Crystallogr. Sect. A Found. Crystallogr.* **2002**, *58* (2), 190–200. https://doi.org/10.1107/S0108767301021298.

(184) Heyd, J.; Scuseria, G. E.; Ernzerhof, M. Hybrid Functionals Based on a Screened Coulomb Potential. *J. Chem. Phys.* **2003**, *118* (18), 8207–8215. https://doi.org/10.1063/1.1564060.

(185) Syafiq, U.; Ataollahi, N.; Maggio, R. Di; Scardi, P. Solution-Based Synthesis and Characterization of Cu2ZnSnS4 (CZTS) Thin Films. *Molecules* **2019**, *24* (19), 3454. https://doi.org/10.3390/molecules24193454.

(186) Baláž, P.; Achimovičová, M.; Baláž, M.; Chen, K.; Dobrozhan, O.; Guilmeau, E.; Hejtmánek, J.; Knížek, K.; Kubíčková, L.; Levinský, P.; Puchý, V.; Reece, M. J.; Varga, P.; Zhang, R. Thermoelectric Cu-S-Based Materials Synthesized via a Scalable Mechanochemical Process. *ACS Sustain. Chem. Eng.* **2021**, *9* (5), 2003–2016. https://doi.org/10.1021/acssuschemeng.0c05555.

(187) Ataollahi, N.; Malerba, C.; Cappelletto, E.; Ciancio, R.; Edla, R.; Di Maggio, R.; Scardi, P. Control of Composition and Grain Growth in Cu2ZnSnS4 Thin Films from Nanoparticle Inks. *Thin Solid Films* **2019**, *674* (February), 12–21. https://doi.org/10.1016/j.tsf.2019.02.004.

(188) Malagutti, M. A.; De Fátima Ulbrich, K.; Paes, V. Z. C.; Geshev, J.; Maduro De Campos, C. E. Structural, Microstructural and Magnetic Characterization of the β-CoTe Nanophase Synthesized by a Novel Mechanochemical Method. *RSC Adv.* **2021**, *11* (9), 5027–5034. https://doi.org/10.1039/d0ra10716f.

(189) Ardila-Fierro, K. J.; Hernández, J. G. Sustainability Assessment of Mechanochemistry by Using the Twelve Principles of Green Chemistry. *ChemSusChem* **2021**, *14* (10), 2145–2162. https://doi.org/10.1002/cssc.202100478.

(190) Ortiz, B. R.; Peng, W.; Gomes, L. C.; Gorai, P.; Zhu, T.; Smiadak, D. M.; Snyder, G. J.; Stevanović, V.; Ertekin, E.; Zevalkink, A.; Toberer, E. S. Ultralow Thermal Conductivity in Diamond-Like Semiconductors: Selective Scattering of Phonons from Antisite Defects. *Chem. Mater.* **2018**, *30* (10), 3395–3409. https://doi.org/10.1021/acs.chemmater.8b00890.

(191) Chen, S.; Gong, X. G.; Walsh, A.; Wei, S. H. Defect Physics of the Kesterite Thin-Film Solar Cell Absorber Cu 2 ZnSnS4. *Appl. Phys. Lett.* **2010**, *96* (2), 4–7. https://doi.org/10.1063/1.3275796.

(192) Walsh, A.; Chen, S.; Wei, S. H.; Gong, X. G. Kesterite Thin-Film Solar Cells: Advances in Materials Modelling of Cu 2 ZnSnS 4. *Adv. Energy Mater.* **2012**, *2* (4), 400–409. https://doi.org/10.1002/aenm.201100630.

(193) Chen, S.; Walsh, A.; Gong, X. G.; Wei, S. H. Classification of Lattice Defects in the Kesterite Cu2ZnSnS 4 and Cu2ZnSnSe4 Earth-Abundant Solar Cell Absorbers. *Adv. Mater.* **2013**, *25* (11), 1522–1539. https://doi.org/10.1002/adma.201203146.

(194) Momma, K.; Izumi, F. VESTA: A Three-Dimensional Visualization System

for Electronic and Structural Analysis. *J. Appl. Crystallogr.* **2008**, *41* (3), 653–658. https://doi.org/10.1107/S0021889808012016.

(195) Isotta, E.; Syafiq, U.; Ataollahi, N.; Chiappini, A.; Malerba, C.; Luong, S.; Trifiletti, V.; Fenwick, O.; Pugno, N. M.; Scardi, P. Thermoelectric Properties of CZTS Thin Films: Effect of Cu-Zn Disorder. *Phys. Chem. Chem. Phys.* **2021**, *23* (23), 13148–13158. https://doi.org/10.1039/d1cp01327k.

(196) Zoppi, G.; Forbes, I.; Miles, R. W.; Dale, P. J.; Scragg, J. J.; Peter, L. M. Cu 2 ZnSnSe 4 Thin Film Solar Cells Produced by Selenisation of Magnetron Sputtered Precursors. *Prog. Photovoltaics Res. Appl.* **2009**, *17* (5), 315–319. https://doi.org/10.1002/pip.886.

(197) Suresh Babu, G.; Kishore Kumar, Y. B.; Uday Bhaskar, P.; Raja Vanjari, S. Effect of Cu/(Zn+Sn) Ratio on the Properties of Co-Evaporated Cu2ZnSnSe4 Thin Films. *Sol. Energy Mater. Sol. Cells* **2010**, *94* (2), 221–226. https://doi.org/10.1016/j.solmat.2009.09.005.

(198) Ahn, S.; Jung, S.; Gwak, J.; Cho, A.; Shin, K.; Yoon, K.; Park, D.; Cheong, H.; Yun, J. H. Determination of Band Gap Energy (Eg) of Cu2 ZnSnSe4 Thin Films: On the Discrepancies of Reported Band Gap Values. *Appl. Phys. Lett.* **2010**, *97* (2). https://doi.org/10.1063/1.3457172.

(199) Kapusta, K.; Drygas, M.; Janik, J. F.; Jelen, P.; Bucko, M. M.; Olejniczak, Z. From Magnetic Cubic Pre-Kesterite to Semiconducting Tetragonal Kesterite Cu2ZnSnS4 Nanopowders via the Mechanochemically Assisted Route. *J. Alloys Compd.* **2019**, *770*, 981–988. https://doi.org/10.1016/j.jallcom.2018.08.135.

(200) Mukherjee, B.; Isotta, E.; Fanciulli, C.; Ataollahi, N.; Scardi, P. Topological Anderson Insulator in Cation-Disordered Cu2ZnSnS4. *Nanomaterials* **2021**, *11* (10). https://doi.org/10.3390/nano11102595.

(201) Feng, J.; Wang, W.; Huang, S.; Jiang, B.; Zhu, B.; Zhou, Y.; Cui, J.; Lin, P.; Xie, L.; He, J. Porous Thermoelectric Zintl: YbCd 2 Sb 2. *ACS Appl. Energy Mater.* **2021**, *4* (1), 913–920. https://doi.org/10.1021/acsaem.0c02825.

(202) Goldsmid, H. Porous Thermoelectric Materials. *Materials (Basel).* **2009**, *2* (3), 903–910. https://doi.org/10.3390/ma2030903.

(203) Kuo, J. J.; Kang, S. D.; Imasato, K.; Tamaki, H.; Ohno, S.; Kanno, T.; Snyder, G. J. Grain Boundary Dominated Charge Transport in Mg3Sb2-Based Compounds. *Energy Environ. Sci.* **2018**, *11* (2), 429–434. https://doi.org/10.1039/c7ee03326e.

(204) Ming, H.; Zhu, C.; Qin, X.; Jabar, B.; Chen, T.; Zhang, J.; Xin, H.; Li, D.; Zhang, J. Improving the Thermoelectric Performance of Cu2SnSe3: Via Regulating Micro-and Electronic Structures. *Nanoscale* **2021**, *13* (7), 4233–4240. https://doi.org/10.1039/d0nr08045d.

(205) Nautiyal, H.; Scardi, P. First Principles Study of SnX2(X = S, Se) and Janus SnSSe Monolayer for Thermoelectric Applications. *Nanotechnology* **2022**, *33* (32). https://doi.org/10.1088/1361-6528/ac6c37.

(206) Bell, L. E. Cooling, Heating, Generating Power, and Recovering Waste Heat with Thermoelectric Systems. *Science (80-.).* **2008**, *321* (5895), 1457–1461. https://doi.org/10.1126/science.1158899.

(207) Heremans, J. P. Low-Dimensional Thermoelectricity. *Acta Phys. Pol. A* **2005**, *108* (4 PART 1), 609–634. https://doi.org/10.12693/aphyspola.108.609.

(208) Fan, F. R.; Wu, W. Emerging Devices Based on Two-Dimensional Monolayer Materials for Energy Harvesting. *Research* **2019**, *2019*, 1–16. https://doi.org/10.34133/2019/7367828.

(209) Kanahashi, K.; Pu, J.; Takenobu, T. 2D Materials for Large-Area Flexible Thermoelectric Devices. *Adv. Energy Mater.* **2020**, *10* (11), 1–23. https://doi.org/10.1002/aenm.201902842.

(210) Peres, N. M. R. Colloquium: The Transport Properties of Graphene: An Introduction. *Rev. Mod. Phys.* **2010**, *82* (3), 2673–2700. https://doi.org/10.1103/RevModPhys.82.2673.

(211) K. S. Novoselov, A. K. Geim, S. V. Morozov, D. Jiang, Y. Zhang, S. V. Dubonos, I. V. G. and A. A. F. Electric Field Effect in Atomically Thin Carbon Films. **2016**, *306* (5696), 666–669. https://doi.org/10.1126/science.1102896.

(212) Butler, S. Z.; Hollen, S. M.; Cao, L.; Cui, Y.; Gupta, J. A.; Gutiérrez, H. R.; Heinz, T. F.; Hong, S. S.; Huang, J.; Ismach, A. F.; Johnston-Halperin, E.; Kuno, M.; Plashnitsa, V. V.; Robinson, R. D.; Ruoff, R. S.; Salahuddin, S.; Shan, J.; Shi, L.; Spencer, M. G.; Terrones, M.; Windl, W.; Goldberger, J. E. Progress, Challenges, and Opportunities in Two-Dimensional Materials beyond Graphene. *ACS Nano* **2013**, *7* (4), 2898–2926. https://doi.org/10.1021/nn400280c.

(213) Sun, M.; Hu, Y.; Shen, B.; Zhai, J.; Song, S.; Song, Z. Si/SnSe2 Multilayer Films for Phase Change Memory Applications. *Integr. Ferroelectr.* **2012**, *140* (1), 1–7. https://doi.org/10.1080/10584587.2012.741363.

(214) Sun, Y.; Cheng, H.; Gao, S.; Sun, Z.; Liu, Q.; Leu, Q.; Lei, F.; Yao, T.; He, J.; Wei, S.; Xie, Y. Freestanding Tin Disulfide Single-Layers Realizing Efficient Visible-Light Water Splitting. *Angew. Chemie - Int. Ed.* **2012**, *51* (35), 8727–8731. https://doi.org/10.1002/anie.201204675.

(215) Pan, T. S.; De, D.; Manongdo, J.; Guloy, A. M.; Hadjiev, V. G.; Lin, Y.; Peng, H. B. Field Effect Transistors with Layered Two- Dimensional SnS2−xSex Conduction Channels: Effects of Selenium Substitution. *Appl. Phys. Lett.* **2013**, *103* (9). https://doi.org/10.1063/1.4819072.

(216) Ou, J. Z.; Ge, W.; Carey, B.; Daeneke, T.; Rotbart, A.; Shan, W.; Wang, Y.; Fu, Z.; Chrimes, A. F.; Wlodarski, W.; Russo, S. P.; Li, Y. X.; Kalantar-Zadeh, K. Physisorption-Based Charge Transfer in Two-Dimensional SnS2 for Selective and Reversible NO2 Gas Sensing. *ACS Nano* **2015**, *9* (10), 10313–10323. https://doi.org/10.1021/acsnano.5b04343.

(217) Lee, M. J.; Ahn, J. H.; Sung, J. H.; Heo, H.; Jeon, S. G.; Lee, W.; Song, J. Y.; Hong, K. H.; Choi, B.; Lee, S. H.; Jo, M. H. Thermoelectric Materials by Using Two-Dimensional Materials with Negative Correlation between Electrical and Thermal Conductivity. *Nat. Commun.* **2016**, *7* (May), 1–7. https://doi.org/10.1038/ncomms12011.

(218) Su, G.; Hadjiev, V. G.; Loya, P. E.; Zhang, J.; Lei, S.; Maharjan, S.; Dong, P.; M. Ajayan, P.; Lou, J.; Peng, H. Chemical Vapor Deposition of Thin Crystals of Layered Semiconductor Sns2 for Fast Photodetection Application. *Nano Lett.* **2015**, *15* (1), 506–513. https://doi.org/10.1021/nl503857r.

(219) Huang, Y.; Sutter, E.; Sadowski, J. T.; Cotlet, M.; Monti, O. L. A.; Racke, D. A.; Neupane, M. R.; Wickramaratne, D.; Lake, R. K.; Parkinson, B. A.; Sutter, P. Tin Disulfide-an Emerging Layered Metal Dichalcogenide Semiconductor: Materials Properties and Device Characteristics. *ACS Nano* **2014**, *8* (10), 10743–10755. https://doi.org/10.1021/nn504481r.

(220) Wickramaratne, D.; Zahid, F.; Lake, R. K. Electronic and Thermoelectric Properties of Few-Layer Transition Metal Dichalcogenides. *J. Chem. Phys.* **2014**, *140* (12). https://doi.org/10.1063/1.4869142.

(221) Xiang, H.; Xu, B.; Xia, Y.; Yin, J.; Liu, Z. Strain Tunable Magnetism in SnX 2 (X = S, Se) Monolayers by Hole Doping. *Sci. Rep.* **2016**, *6* (December), 1–8. https://doi.org/10.1038/srep39218.

(222) Gonzalez, J. M.; Oleynik, I. I. Layer-Dependent Properties of SnS2 and SnSe2 Two-Dimensional Materials. *Phys. Rev. B* **2016**, *94* (12), 1–10. https://doi.org/10.1103/PhysRevB.94.125443.

(223) Lu, A. Y.; Zhu, H.; Xiao, J.; Chuu, C. P.; Han, Y.; Chiu, M. H.; Cheng, C. C.; Yang, C. W.; Wei, K. H.; Yang, Y.; Wang, Y.; Sokaras, D.; Nordlund, D.; Yang, P.; Muller, D. A.; Chou, M. Y.; Zhang, X.; Li, L. J. Janus Monolayers of Transition Metal Dichalcogenides. *Nat. Nanotechnol.* **2017**, *12* (8), 744–749. https://doi.org/10.1038/nnano.2017.100.

(224) Guo, S. D. Phonon Transport in Janus Monolayer MoSSe: A First-Principles Study. *Phys. Chem. Chem. Phys.* **2018**, *20* (10), 7236–7242. https://doi.org/10.1039/c8cp00350e.

(225) Dimple; Dimple; Mohanta, M. K.; Rawat, A.; Jena, N.; Ahammed, R.; De Sarkar, A. Ultra-Low Lattice Thermal Conductivity and Giant Phonon-Electric Field Coupling in Hafnium Dichalcogenide Monolayers. *J. Phys. Condens. Matter* **2020**, *32* (31). https://doi.org/10.1088/1361-648X/ab7e5f.

(226) Khosa, G. S.; Tripathi, S. K.; Alshaikhi, A. A.; Gupta, S.; Kumar, R. Janus Al2STe Monolayer: A Prospective Thermoelectric Material. *Solid State Commun.* **2022**, *341* (November 2021), 114579. https://doi.org/10.1016/j.ssc.2021.114579.

(227) Vu, T. V.; Vi, V. T. T.; Phuc, H. V.; Nguyen, C. V.; Poklonski, N. A.; Duque, C. A.; Rai, D. P.; Hoi, B. D.; Hieu, N. N. Electronic, Optical, and Thermoelectric Properties of Janus In-Based Monochalcogenides. *J. Phys. Condens. Matter* **2021**, *33* (22). https://doi.org/10.1088/1361-648X/abf381.

(228) Shi, W.; Wang, Z. Mechanical and Electronic Properties of Janus Monolayer Transition Metal Dichalcogenides. *J. Phys. Condens. Matter* **2018**, *30* (21). https://doi.org/10.1088/1361-648X/aabd59.

(229) Nguyen, H. T. T.; Tuan, V. V.; Nguyen, C. V.; Phuc, H. V.; Tong, H. D.; Nguyen, S. T.; Hieu, N. N. Electronic and Optical Properties of a Janus SnSSe Monolayer: Effects of Strain and Electric Field. *Phys. Chem. Chem. Phys.* **2020**, *22* (20), 11637–11643. https://doi.org/10.1039/d0cp01860k.

(230) Zhang, J.; Jia, S.; Kholmanov, I.; Dong, L.; Er, D.; Chen, W.; Guo, H.; Jin, Z.; Shenoy, V. B.; Shi, L.; Lou, J. Janus Monolayer Transition-Metal Dichalcogenides. *ACS Nano* **2017**, *11* (8), 8192–8198. https://doi.org/10.1021/acsnano.7b03186.

(231) Zhou, C.; Lee, Y. K.; Yu, Y.; Byun, S.; Luo, Z. Z.; Lee, H.; Ge, B.; Lee, Y. L.; Chen, X.; Lee, J. Y.; Cojocaru-Mirédin, O.; Chang, H.; Im, J.; Cho, S. P.; Wuttig, M.; Dravid, V. P.; Kanatzidis, M. G.; Chung, I. Polycrystalline SnSe with a Thermoelectric Figure of Merit Greater than the Single Crystal. *Nat. Mater.* **2021**, *20* (10), 1378–1384. https://doi.org/10.1038/s41563-021-01064-6.

(232) James D. Pack, H. J. M. Special Points for Brillonln-Zone Integrations"—a Reply. *J. Chem. Inf. Model.* **1977**, *16* (4), 1748–1749.

(233) Shafique, A.; Samad, A.; Shin, Y. H. Ultra Low Lattice Thermal Conductivity and High Carrier Mobility of Monolayer SnS2 and SnSe2: A First Principles Study. *Phys. Chem. Chem. Phys.* **2017**, *19* (31), 20677–20683. https://doi.org/10.1039/c7cp03748a.

(234) Csonka, G. I.; Perdew, J. P.; Ruzsinszky, A.; Philipsen, P. H. T.; Lebègue, S.; Paier, J.; Vydrov, O. A.; Ángyán, J. G. Assessing the Performance of Recent Density Functionals for Bulk Solids. *Phys. Rev. B - Condens. Matter Mater. Phys.* **2009**, *79* (15), 1–14. https://doi.org/10.1103/PhysRevB.79.155107.

(235) Choudhary, K.; Cheon, G.; Reed, E.; Tavazza, F. Elastic Properties of Bulk and Low-Dimensional Materials Using van Der Waals Density Functional. *Phys. Rev. B* **2018**, *98* (1), 1–12. https://doi.org/10.1103/PhysRevB.98.014107.

(236) Gutiérrez Moreno, J. J.; Cao, J.; Fronzi, M.; Assadi, M. H. N. A Review of Recent Progress in Thermoelectric Materials through Computational Methods. *Mater. Renew. Sustain. Energy* **2020**, *9* (3), 1–22. https://doi.org/10.1007/s40243-020-00175-5.

(237) Patel, A.; Singh, D.; Sonvane, Y.; Thakor, P. B.; Ahuja, R. High Thermoelectric Performance in Two-Dimensional Janus Monolayer Material WS-X (X = Se and Te). *ACS Appl. Mater. Interfaces* **2020**, *12* (41), 46212–46219. https://doi.org/10.1021/acsami.0c13960.

(238) Xiao, Y.; Zhao, L. D. Charge and Phonon Transport in PbTe-Based Thermoelectric Materials. *npj Quantum Mater.* **2018**, *3* (1). https://doi.org/10.1038/s41535-018-0127-y.

(239) Toberer, E. S.; Baranowski, L. L.; Dames, C. Advances in Thermal Conductivity. *Annu. Rev. Mater. Res.* **2012**, *42* (1), 179–209. https://doi.org/10.1146/annurev-matsci-070511-155040.

(240) Deng, S.; Li, L.; Guy, O. J.; Zhang, Y. Enhanced Thermoelectric Performance of Monolayer MoSSe, Bilayer MoSSe and Graphene/MoSSe Heterogeneous Nanoribbons. *Phys. Chem. Chem. Phys.* **2019**, *21* (33), 18161–18169. https://doi.org/10.1039/c9cp03639c.

(241) Tao, W. L.; Zhao, Y. Q.; Zeng, Z. Y.; Chen, X. R.; Geng, H. Y. Anisotropic Thermoelectric Materials: Pentagonal PTM2 (M = S, Se, Te). *ACS Appl. Mater. Interfaces* **2021**, *13* (7), 8700–8709. https://doi.org/10.1021/acsami.0c19460.

First-principles calculations are an effective means of investigating the complex thermoelectric phenomena involved in the direct conversion of heat into electricity. By simulating the fundamental interactions between electrons and phonons within a material, these calculations can yield valuable insights into its thermoelectric properties. Moreover, they can reveal the underlying mechanisms responsible for these properties, paving the way for more efficient and effective development of thermoelectric devices. In essence, the ability to conduct first-principles calculations represents a major breakthrough in our capacity to harness thermoelectricity and unlocks exciting possibilities for energy harvesting and conversion across various applications.

Himanshu Nautiyal was born on 14 December 1995 in Delhi, India. He obtained B.Sc. (Hons.) Physics in 2016 from University of Delhi and M.Sc. Physics in 2018 from Central University of Haryana, India. In his master's thesis work, he studied glass formation and statistical analysis of plastic events in steady state through molecular dynamics simulation. Himanshu, started his Ph.D. Project in December 2019 at Department of Civil, Environmental and Mechanical Engineering, University of Trento, Italy. During which, he investigated properties of thermoelectric materials using first principle simulation.